

Beam-Machine Interaction Studies for the Phase II LHC Collimation System

THÈSE N° 4910 (2010)

PRÉSENTÉE LE 13 DÉCEMBRE 2010

À LA FACULTÉ SCIENCES DE BASE

LABORATOIRE DE PHYSIQUE DES ACCÉLÉRATEURS DE PARTICULES

PROGRAMME DOCTORAL EN PHYSIQUE

ÉCOLE POLYTECHNIQUE FÉDÉRALE DE LAUSANNE

POUR L'OBTENTION DU GRADE DE DOCTEUR ÈS SCIENCES

PAR

Luisella LARI

acceptée sur proposition du jury:

Prof. N. Baluc, présidente du jury

Prof. L. Rivkin, directeur de thèse

Dr R. Assmann, rapporteur

Prof. A. Bay, rapporteur

Dr V. Vlachoudis, rapporteur



ÉCOLE POLYTECHNIQUE
FÉDÉRALE DE LAUSANNE

Suisse
2010

Abstract

Collimation is essential in a high Energy and Intensity hadron collider with Superconducting magnets, like the LHC at CERN. To improve the cleaning efficiency and to reduce the LHC impedance budget in stable condition and at top Energy, additional 30 Phase II collimators are foreseen to be installed.

The work of this PhD analyses the beam-machine interactions in the LHC Betatron Cleaning Insertions for its upgrade with the Phase II collimators. These studies aim at optimizing the collimation system layout from the machine protection point of view, considering different options for the Phase II collimator design and focusing on heating damage and activation problems. The outcomes of this PhD work have been used to support the Phase II design evolution and their prototype mechanical integration, and to point out possible critical points along the Betatron Cleaning Straight Section. Emphasis is on studying several configurations and material choices for nominal and failure scenarios.

Keywords: LHC, collimation, FLUKA, machine protection.

Résumé

Le système de collimation est essentiel dans un collisionneur de hadrons d'énergie et d'intensité élevées comprenant des aimants supraconducteurs comme le LHC au CERN. Afin d'améliorer l'efficacité du système de nettoyage du faisceau et de réduire la marge d'impédance du LHC dans des conditions stables et à des énergies maximales, 30 collimateurs supplémentaires de type Phase II seront installés.

L'objectif de cette thèse est d'analyser les interactions du faisceau de particules avec la matière au niveau des inserts de nettoyage bétatronique du LHC pour sa nouvelle phase après l'installation des collimateurs de Phase II. Une telle étude vise à optimiser la disposition des collimateurs de Phase II pour une meilleure protection de la machine. Les différentes options liées à leur conception, les détériorations causées par l'échauffement ainsi que les problèmes d'activation sont considérés et évalués. Les résultats de cette étude ont été utiles non seulement pour le suivi de la conception et l'intégration mécanique du prototype concerné par la Phase II, mais aussi pour mettre en évidence des éventuels points critiques au niveau du nettoyage bétatronique de la Section Droite. L'accent est mis sur l'étude de plusieurs configurations et matériaux pour des scénarios aussi bien nominaux que critiques.

Mot-clé: LHC, collimation, FLUKA, protection de la machine.

*To my parents Jole & Gino
To my origins Giovanni, Maria & Teresa
To my friends Amalia and Beppe
...and to myself*

Contents

1	Introduction	1
2	The Large Hadron Collider	3
2.1	The LHC accelerator chain	3
2.2	The LHC experiments	4
2.3	The LHC main ring	6
2.4	The LHC Superconducting Magnets	7
2.5	The LHC Cleaning Insertion Regions	9
2.5.1	The Momentum Cleaning Insertion IR3	9
2.5.2	The Betatron Cleaning Insertion IR7	9
3	The LHC Collimation System	11
3.1	Why is the LHC collimation essential?	11
3.2	The LHC Collimation System requirements	12
3.2.1	Beam loss rates during regular operation	12
3.2.2	Abnormal proton losses	13
3.2.3	Cleaning Inefficiency	14
3.2.4	Impedance	14
3.2.5	Radiation constraints	16
3.2.6	Additional requirements	16
3.3	The multi-stage LHC Collimation System	16
3.4	The multi-phase LHC Collimation System	18
3.4.1	The Phase I Collimation System	19
3.4.2	The Phase II Collimation System	24
3.4.3	Further Phases	28
4	Simulation Framework	29
4.1	Purpose of the simulations	29
4.2	The simulation chain	30
4.2.1	The MAD-X code	31
4.2.2	The SixTrack code	33
4.2.3	The FLUKA code	35
4.2.4	The FEM analysis	38

5	An overview of the FLUKA physics models	39
5.1	Proton-matter interaction: main framework	39
5.2	The FLUKA code: main features	40
5.2.1	Hadron-Nucleus and hadron-nucleon interactions	41
5.2.2	E-M showers	43
5.2.3	Multiple Scattering	45
5.2.4	Energy loss by particle in matter	45
5.2.5	Residual nuclei production and Decay	47
5.2.6	Transport of neutrons	49
5.2.7	Variance reduction techniques	49
6	Simulations of the IR7 region	51
6.1	The FLUKA Combinatorial Geometry	51
6.2	The FLUKA modular approach used for IR7	52
6.3	The IR7 FLUKA prototypes	52
6.3.1	The IR7 magnet models	53
6.3.2	The Phase I collimator models	58
6.3.3	The BLM models	61
6.4	The Phase II collimators FLUKA prototypes	62
6.5	The IR7 input file and executable	62
7	First exploratory studies on Phase II collimators	65
7.1	Collimator materials	65
7.2	Preliminary Phase II designs	67
7.3	Loss maps	68
7.4	First Phase II results	69
7.5	Simulation accuracy	72
7.6	Conclusions on Phase II first results	73
8	The SLAC Phase II design	75
8.1	The evolution of the SLAC Phase II design	75
8.1.1	The actual SLAC Phase II design	77
8.2	The SLAC Phase II FLUKA model	78
8.3	FLUKA results for the most advanced SLAC Phase II design	81
8.3.1	Operation conditions	82
8.3.2	Asynchronous dump scenario	87
8.4	The SLAC Phase II jaw rotation mechanism	91
8.5	Conclusions on the SLAC Phase II design	95
9	The CERN Phase II design	97
9.1	Main features of the CERN Phase II design	97
9.1.1	The back stiffener	98
9.1.2	The cooling system	98

9.1.3	The jaw	98
9.2	The evolution of the CERN Phase II Copper based design	99
9.2.1	FLUKA results for operation conditions	103
9.3	CERN Phase II jaw material comparison	108
9.4	Conclusion on the CERN Phase II design	114
10	Collimator setting errors	117
10.1	Beam-based alignment of the collimator jaws	117
10.2	FLUKA results for operation conditions	120
10.3	Conclusion	124
11	Activation of collimator materials	127
11.1	CERN radiation limits and constraints	127
11.2	Details of FLUKA calculations	128
11.3	FLUKA results	129
11.4	Conclusion	133
12	Optimization of the IR7 layout	135
12.1	New proposed IR7 Phase II layout	135
12.2	FLUKA results for operation conditions	138
12.3	Conclusion	140
13	The prompt radiation effects	141
13.1	Overview of LHC critical areas	141
13.1.1	Radiation effects on electronics	144
13.2	Radiation to electronics FLUKA results	145
13.2.1	Radiation to electronics in UJ76 and RR77 (& RR73)	145
13.3	The BPMs integration studies	151
13.4	Conclusion	152
14	Displacement Per Atom (DPA) calculations	153
14.1	Brief description of theoretical background	153
14.2	The BNL experiment	157
14.2.1	Simulation results with MCNPX	161
14.2.2	The BNL experiment simulated with FLUKA	161
14.2.3	Results comparison	163
14.3	DPA calculations for LHC collimators	164
14.4	Conclusions on DPA calculations	165
15	Conclusions	167
A	The principle of 2 stage Betatron and Momentum collimation	171
A.1	One-Dimensional Betatron Collimation	171
A.2	One-Dimensional Momentum Collimation	174

B	Phase I and Phase II collimator database	177
B.1	Beam 1	177
B.2	Beam 2	180
C	Database of LHC Beam 1 collimators with tilt jaws	183
C.1	Operational conventions for the collimator jaws	183
C.2	Operational conventions for the collimator jaws	184

List of Figures

2.1	LHC accelator chain.	4
2.2	LHC Schematic layout.	6
2.3	LHC Main dipole.	8
3.1	View along the beam line in a horizontal secondary collimator	15
3.2	Illustration of the multi-stage LHC cleaning concept	17
3.3	View into an open vacuum tank of a LHC Phase I collimator	20
3.4	Mechanical integration of a horizontal secondary collimator	21
3.5	Stability diagram at top energy to compare Phase I and Phase II collimators	23
3.6	Illustration of the multi-stage LHC cleaning concept with the Phase II secondary collimators	25
3.7	Inefficiency versus tune shift for Phase II	26
3.8	LHC tunnel view with the ready empty Phase II slots	27
4.1	The simulation chain	30
4.2	MAD-X output plot	31
4.3	Beam distribution at the TCP.C6L7.B1 location for the asynchronous beam dump scenario	32
4.4	Space distribution of Beam 1 losses for a perfect LHC machine at TCSM.A6L7.B1 location for the nominal horizontal scenario	34
4.5	LHC perfect machine loss map at low beta, including the Copper jaws Phase II collimators and without cryo-collimators	35
4.6	Example of a 3D power deposition map	36
5.1	Traces of a 6 GeV proton in liquid argon	40
5.2	FLUKA and experimantal data of p-p and p-n cross sections	42
5.3	Examples of particle production from inelastic interaction at different energies	42
5.4	A schematic view of an electromagnetic shower caused by an electron hitting a target	44
5.5	Stopping power for positive muons in Copper	46
5.6	Ionization fluctuation for 2 GeV/c protons after a 100 μm Si layer. FLUKA and experimental data	46

5.7	Residual nuclei production from $1\text{ GeV }^{208}\text{Pb} + \text{p}$ reaction	48
5.8	Dose rate benchmark	48
6.1	Real view and FLUKA model of a MBW warm magnet	54
6.2	Real view, technical drawing and FLUKA model of a MQW warm magnet	54
6.3	Real view, technical drawing and FLUKA model of a MB cold magnet	55
6.4	FLUKA model showing the MQTL cold magnets and a MCBC corrector	56
6.5	Transverse sections of geometry and magnetic fields as implemented in FLUKA	57
6.6	Cross plots of TCP, TCSG and TCLA FLUKA prototypes	59
6.7	Real view and cross FLUKA plots of the longest Passive Absorber	60
6.8	BLM real views and FLUKA model	61
6.9	FLUKA geometry of the IR7 Straight Section	64
7.1	Deposited energy density for one 7 TeV proton with 100 nm impact parameter versus mass length for different possible collimator jaw materials	66
7.2	Metallic and Foil Collimator FLUKA descriptions	67
7.3	Transverse view of the skew TCSM.A6L7.B1 jaws, where the loaded losses are shown for all (z) values along the collimator length both for the standard design and for the foil one	68
7.4	The $\sim 500\text{ kW}$ power distribution for the 0.2 h beam lifetime scenario in the IR7 SS region for different Phase II collimator jaws	69
7.5	Peak power density longitudinal profile at the most loaded Phase II location (TCSM.A6L7.B1) referring to the 1 h 7 TeV low beta horizontal losses scenario for the different materials	70
8.1	Jaw-Hub-Shaft concept to minimize the jaw deflection toward the beam	76
8.2	Cutaway of SLAC jaw	78
8.3	Evolution of the SLAC FLUKA model and comparison with the Catia technical drawing	79
8.4	SLAC jaw prototype and FLUKA model	80
8.5	FLUKA model evolution of the SLAC tank	81
8.6	Cut of the IR7 FLUKA model showing the Phase I primary collimators and the first 3 Phase II ones	82
8.7	Power deposition map at 20 cm longitudinal depth and along the collimator length for the horizontal halo scenario	84
8.8	Comparison between the power density peak values on the Glidcop jaws and on the Molybdenum shafts for the 3 halo distributions in the 1 h steady-state case	85
8.9	Power maps and cumulative power values inside the jaws and shafts	86

8.10	Geometrical and phase space distributions of protons coming from an asynchronous dump at the entrance of the indicated horizontal collimators	88
8.11	Energy density peaks along the jaw length in the case of the primary horizontal collimator impacted in consequence of an asynchronous dump accident	90
8.12	View of the shaft support showing the Geneva Mechanism for precision jaw rotation	92
8.13	Schematic view at one jaw end of the Phase I movement control and instrumentation	93
8.14	Picture of the additional limit switch for one SLAC jaw during the feasibility tests at SLAC laboratory	93
8.15	Schematic view of the actions performed by the additional routine created to rotate the SLAC jaws	94
8.16	Jaw sagitta and temperature distribution under 9 kW heat load, simulated by ANSYS, on the basis of the FLUKA 3D model results	95
9.1	CERN Phase II design modular design	99
9.2	FLUKA model of the preliminary CERN Phase II design version . . .	100
9.3	Evolution of the CERN Phase II FLUKA model with the jaw cut in 3 pieces	101
9.4	Current CERN Phase II FLUKA model components	102
9.5	Evolution of the elastic deflections for the CERN Phase II copper based jaw design	103
9.6	Power load distribution on the 11 Phase II Copper based jaw collimators CERN design (1 h beam lifetime scenario, horizontal losses distribution)	104
9.7	TCSM.A6L7.B1 3D power deposition map cuts	104
9.8	LHC loss maps for the Beam 1 horizontal scenario with and without cryo-collimators	105
9.9	Comparison between power density peaks for the most loaded Phase II collimator using loss maps with and without cryo-collimators . . .	106
9.10	Power density peak profile for the most loaded Phase II collimator (1 h beam lifetime)	107
9.11	FLUKA model of the CERN non conductive jaw design for Phase II collimators	108
9.12	Instantaneous energy deposition due to asynchronous dumps using different Phase II CERN design jaw materials	109
9.13	Energy deposition distributions along the IR7 line for the 3 scenarios of impact on horizontal collimators due to an asynchronous dump accident	110

9.14	Energy deposition peak comparison between the Phase II TCSM.B4L7.B1 directly impacted on the external jaw for the considered asynchronous dump scenario and the resulting most loaded element (i.e. Phase II TCSM.A4L7.B1)	111
9.15	Comparison between different jaw material energy deposition peaks for the most loaded Phase II TCSM.A6L7.B1 resulting from the asynchronous dump scenario of TCP.C6L7.B1 directly impacted	112
9.16	Basic CERN Phase II jaw prototype	114
10.1	Procedure to centre the collimator jaws around the circulating beam .	118
10.2	Sketch of a horizontal Phase I secondary collimator installed in the LHC tunnel	118
10.3	Illustration of set-up errors for the LHC collimation jaws used as input for FLUKA simulations	119
10.4	Comparison between power deposition on the SS IR7 Beam 1 elements with and without LHC collimator jaw tilts	120
10.5	Reductions and increments on power deposition for the 11 Phase II collimators in case of misaligned jaws	121
10.6	Reductions and increments on power deposition for each Phase I primary and Phase II jaw in case of misalignment.	122
10.7	Top: Total loads along the most impacted part of the IR7 Beam 1 line. Middle: Absolute reductions and increments. Bottom: Absolute percentage reductions and increments (tilted jaw case vs. ideal jaw case)	123
10.8	Local Cleaning Inefficiency for various imperfection scenarios	124
11.1	Irradiation profile assumed during residual dose rate FLUKA simulations	129
11.2	Ambient dose equivalent distribution after 185 days of continuous operation and 1 day of cooling time along the all IR7 straight section	130
11.3	Ambient dose equivalent distribution for different Phase II designs after 185 days of continuous operation and 1 day of cooling period . .	131
11.4	Ambient dose equivalent peaks for the 2 different Phase II designs at the most loaded TCSM.A6L7.B1 location and using different cooling times	132
12.1	Proposed optimized layout for Phase II collimators along IR7 Beam 1 line	137
12.2	Optimized layout vs. layout envisaging 11 Phase II CERN design Cu jaw collimators: power deposition along the LSS7	139
12.3	Sketch of IR7 line in which the tunnel service areas UJ76 and RR77 are shown	140

13.1	A LHC graphical area classification by radiation levels, as well as, when known, by criticality of installed electronics	143
13.2	High Energy Hadrons Fluence ($> 20 \text{ MeV}$) along IR7 averaged in the orange area, close to the LHC tunnel wall	146
13.3	High Energy Hadrons Fluence ($> 20 \text{ MeV}$) in the UJ76 cavern, due to Beam 1 line simulations	147
13.4	High Energy Hadrons Fluence ($> 20 \text{ MeV}$) in the UJ76 cavern, due to Beam 1 and Beam 2 line simulations	148
13.5	High Energy Hadrons Fluence ($> 20 \text{ MeV}$) in the RR77 cavern . . .	149
13.6	Location of electronic racks in the RR77 and UJ76 caverns	150
14.1	Comparison between the partition functions for α particles on Silicon, calculated using the Lindhard (black line) or the Zieler (blue line) approximations	157
14.2	BNL experimental facility used in the material irradiation study . . .	158
14.3	Cross section of the irradiated targets	159
14.4	Specimen design for mechanical and physical property studies	159
14.5	Front view of the target with the integration of different types of specimens into the irradiation space	160
14.6	Real cross view of target irradiation assembly and the FLUKA model implemented	162
14.7	DPA peak values along the target assembly	163
14.8	DPA values along the CERN design Glidcop jaws for the most loaded Phase II collimator location	165
14.9	DPA results form different MonteCarlo code for $130 \text{ MeV}/u$ ^{76}Ge impacting on 1.2 mm thick Tungsten target	166
A.1	Proton hitting the primary collimator	172
A.2	Secondary particles intercepted by secondary collimators	173
A.3	Phase space at primary collimator for momentum collimation	174
C.1	Operational naming conventions for the collimator jaws	183

List of Tables

2.1	LHC beam parameters	5
2.2	List of LHC Superconducting magnets	7
3.1	Specified beam lifetimes during operation	12
3.2	Overview on expected physical LHC aperture limits	18
3.3	Quantities and LHC locations for Phase I Collimation System components	19
7.1	Density, Atomic number, Radiation length and Inelastic scattering length for possible Phase II candidate materials	66
7.2	Integral values of power on the most loaded Beam 1 Phase II collimator (TCSM.A6L7.B1)	71
8.1	Simulated evolution performance of the different SLAC collimator concepts	77
8.2	Summary of Power deposition results on the collimator TCSM.A6L7.B1 for the 3 halo scenarios	83
8.3	Summary of Power deposition results on the collimator TCSM.A6L7.B1 components for the horizontal halo scenario	84
8.4	Energy deposition on the most loaded Beam 1 elements in the case of TCP.C6L7.B1 directly impacted	89
8.5	Energy deposition on the most loaded Beam 1 elements in the case of TCSM.B4L7.B1 directly impacted	89
8.6	Energy deposition on the most loaded Beam 1 elements in the case of TCSM.6R7.B1 directly impacted	89
8.7	Energy density peaks and instantaneous increases of temperature for the most loaded device for the 3 asynchronous dump scenarios	90
9.1	Physical properties of the most promising jaw materials for the CERN Phase II design	99
9.2	Energy density peaks and instantaneous increases of temperature (T) for asynchronous beam dump scenarios. Results refer only to CERN design Phase II collimators and to their most loaded jaw	113

12.1	Proposed layout for the 11 Phase II collimators located in IR7 along the Beam 1 line	136
13.1	High Energy Hadrons Fluence ($> 20 \text{ MeV}$), 1 MeV equivalent neutron Fluence and Dose values in the UJ76 and RR77 racks for Beam 1 simulations with Glidcop jaw Phase II collimation	151
13.2	High Energy Hadrons Fluence ($> 20 \text{ MeV}$), 1 MeV equivalent neutron Fluence and Dose values in the most exposed Rack1 in both UJ76 and RR77 for Beam 1 simulations with Glidcop jaw Phase II and optimized Phase II layout	151
14.1	Typical values used in NJOY99 code	156
14.2	DPA values for the BNL irradiation experiment calculated by MCNPS and FLUKA MonteCarlo codes	164
B.1	List of Phase I and Phase II (in red) collimators in the main ring for Beam 1	177
B.2	List of Phase I and Phase II (in red) collimators in the main ring for Beam 2	180
C.1	List of Beam 1 Phase I and Cu Phase II collimators with jaw tilted at low beta	184

Chapter 1

Introduction

CERN's Large Hadron Collider (LHC) has become on November 2009 the world's highest energy particle accelerator, having accelerated its proton beams to an energy of 1.18 TeV each. It marks an important milestone on the road toward the collisions at nominal energy of 14 TeV (7 TeV per beam), aiming at the discovery of the Higgs particle and the study of rare events.

A characteristic of the LHC is its large stored energy of 362 MJ per proton beam at nominal scenario. The very intense LHC beam must be handled in a Superconducting (SC) environment with *quench* limits of the order of 10 mWcm^{-3} , which represents a tiny fraction of the stored power. In order to prevent that unavoidable proton beam losses can bring to reach these limits in SC magnets, a sophisticated system of collimators is needed to provide beam cleaning and passive machine protection.

The LHC Collimation System is installed and commissioned in different phases, following the natural evolution of the machine performance. The full Collimation System (including the transfer lines) foresees more than 150 locations with the design goal not only of avoiding *quenches* of SC magnets but also of protecting other LHC equipments from radiation damage and of minimizing the halo induced background in the particle physics experiments. Due to the high beam power, LHC is the first machine which requires collimation through its whole operation cycle: from injection up to physics and extraction.

The installation of the full first stage (Phase I) was completed for 2009 operation of the LHC, after the incident in Sector 3-4. This system is adequate for beam commissioning but will not allow nominal beam Intensity. To improve Cleaning Efficiency toward the end of the low beta squeeze at 7 TeV , and in stable physics conditions, it is foreseen to complement the 30 highly robust Phase I secondary collimators with low impedance Phase II collimators. The Phase II collimators will be located in the two insertions regions IR3 for the momentum cleaning, and IR7 for the betatron cleaning, about 4-5 years after the first physics runs. These locations, where important beam losses are expected, will be among the most radioactive areas of LHC.

As part of the evaluation of the different designs, the application of a particle transport and interaction Monte-Carlo code, like FLUKA, is fundamental to estimate, before any Phase II collimator is installed in the machine, key physical quantities such as the energy deposition in the irradiate materials, the dose released in delicate components and the environmental activation. These predictions have a crucial impact on the performance and luminosity of LHC.

This PhD thesis is addressing the issues of high power deposition (up to 500 *kW* impacting power for continuous losses in nominal conditions) for their possible use in the LHC Collimator System upgrade. Using as input accelerator physics calculations, the FLUKA Monte Carlo code was extensively used to evaluate the energy deposition due to the interaction of high energy protons with the various materials of the collimators, the other beam elements and the surrounding tunnel environment by performing full shower studies.

The first part of this PhD is dedicated to the description of the Collimation System as it is now installed, its limitations and the upgrade foreseen. Chapters 4 and 5 describe the simulation set-up employed and the FLUKA physic models underneath. Chapter 6 shows how the LHC Betatron cleaning insertion is described in FLUKA. Results predicting the maximum equipment heating during the operation scenario and for abnormal beam losses, from the preliminary exploratory studies through the most promising Phase II designs and prototypes evolution, are presented in Chapters 7, 8 and 9. Additional effects related to the reduction of the jaw active length, due to misalignment setting errors, are evaluated in Chapter 10. Chapter 11 describes the activation of the collimator materials. On the basis of these results, a combination of different Phase II designs is proposed in Chapter 12 for the eleven positions foreseen along the IR7 Straight Section. Finally, to estimate the radiation damage amount in the Phase II jaws and in the surrounding areas, Prompt Dose and Displacements Per Atom (DPA) calculations are performed and reported in Chapters 13 and 14. To validate the DPA model used, the results are compared to the available data from the Brookhaven National Laboratory (BNL) radiation damage experiment.

The PhD results have been used by mechanical engineers as input for designing collimators, shielding and optimizations at CERN and at SLAC National Accelerator Laboratory in USA inside the framework of the international collaboration in charge of the Collimation System Upgrade project.

On January the 8th (2010), the first basic Phase II prototype was installed in the SPS accelerator to test the feasibility of Beam Position Monitor buttons (BPMs) installed in the jaws.

Chapter 2

The Large Hadron Collider

The construction of the LHC machine and its detectors has been a project spanning almost 15 years and involving scientists and engineers from all over the world [1]. It consists in a two-ring, SuperConducting accelerator and collider installed in a 27 km long circular tunnel at a depth ranging from 50 to 175 m underground, between France and Switzerland. The LHC is designed to accelerate and collide two counterrotating proton beams up to 7 TeV and, during a smaller part of the machine operating time, heavy ion beams up to 574 TeV . Each beam is guided around its circular orbit by powerful SC magnets cooled in a bath of superfluid helium and brought into collision in four huge detectors.

2.1 The LHC accelerator chain

No single machine can accelerate all alone a proton beam up to 7 TeV : one needs a cascade of accelerators. Before reaching the LHC main ring, the protons are accelerated in stages through 4 machines as it is shown in Fig.2.1. After being extracted from the source called Duoplasmatron at an energy of 50 keV , the protons enter in the 35 m long linear accelerator (LINAC), where their energy is increased up to 50 MeV . The next step is the BOOSTER synchrotron accelerator, which the protons leave at 1.4 GeV to being injected in the Proton Synchrotron (PS). In this machine the particles are grouped into a train of bunches at the right nominal spacing of 25 ns . Each bunch are accelerated up to $26\text{ GeV}/c$ in the PS. The last machine in which the protons have to pass through is the Super Proton Synchrotron (SPS), where they are further accelerated up to 450 GeV and then injected into the LHC, balancing the filling in both clockwise and counterclockwise rings. When the two rings are filled, the beams are accelerated by the radio frequency system and simultaneously the magnetic field of the LHC is slowly ramped up to keeps them in the center of the vacuum chamber. After about 20 minutes the beams reach the nominal collision energy of 7 TeV and they are steered into collision in each of the 4 detectors.

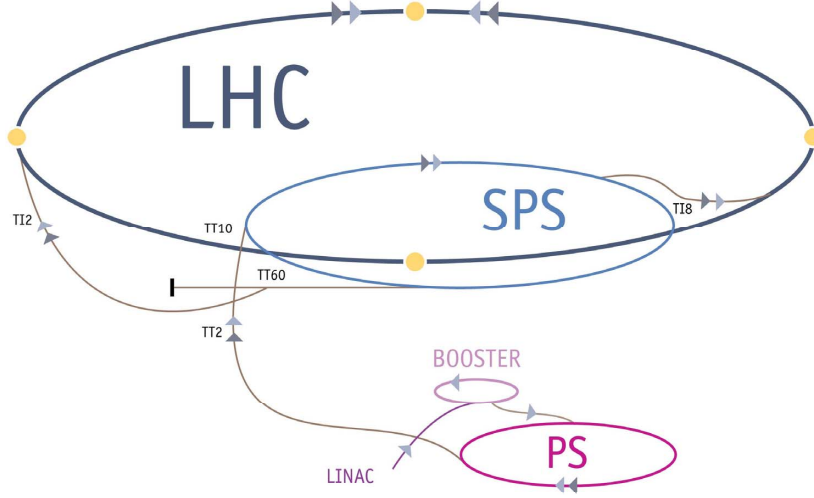


Figure 2.1: The LHC proton accelerator chain. Collisions take place in the four Interaction Points (IP), the yellow dots.

When the LHC is used to collide heavy ions, they will be first accelerated by the linear accelerator LINAC 3 and into the Low-Energy Ion Ring (LEIR) before being injected in the PS, SPS and finally in LHC, as for the proton beams.

2.2 The LHC experiments

The LHC provides extraordinary opportunities in particle physics based both on its high beam Energies and high beam Intensities. It hosts six experiments to detect events generated in its collisions.

The rate of these events is given by:

$$\mathcal{N}_{\text{event}} = \mathcal{L} \sigma_{\text{event}} \quad (2.1)$$

where σ_{event} is the cross section of the event under study and \mathcal{L} the machine Luminosity. The Luminosity is an important value to characterize the performance of an accelerator. The machine Luminosity is determined by a set of beam parameters and it can be written for a Gaussian beam distribution as:

$$\mathcal{L} = \frac{N_b^2 n_b f_{\text{rev}} \gamma_r}{4\pi \epsilon_n \beta^*} F, \quad (2.2)$$

where N_b is the number of particles per bunch, n_b the number of bunches per beam, f_{rev} the revolution frequency, γ_r the relativistic gamma factor, ε_n the normalized transverse beam emittance, β^* the beta function at the collision points and F the geometric Luminosity reduction factor due to the crossing angle that is imposed to the colliding bunches in order to avoid parasitic collisions at the Interaction Points (IP).

The LHC design Luminosity of $\mathcal{L} = 10^{34} cm^{-2}s^{-1}$ leads to around 1 billion proton-proton interactions per second. Summary of the main parameters for the nominal proton beam operation is given in Table 2.1.

Table 2.1: LHC proton beam parameters (see Fig. 2.2 for IP numbering legend).

Proton Beam Data		
	Injection	Collision
Energy [GeV]	450	7000
Stored energy per beam [MJ]	23.3	362
Peak Luminosity in IP1 and IP5 [$cm^{-2}s^{-1}$]	-	10^{34}
Number of particles per bunch	1.15x10 ¹¹	
Number of bunches	2808	
Revolution frequency [kHz]	11.245	
Relativistic gamma factor	479.6	7461
Normalized Transverse beam emittance [$\mu m rad$]	3.75	
β^* at IP1 and IP5 [m]	18	0.55
β^* at IP2 [m]	10	10
β^* at IP8 [m]	10	1 \leftrightarrow 50
Geometrical Luminosity reduction factor	-	0.836

The LHC has two high Luminosity experiments: CMS [2] and ATLAS [3]. They are multi-purpose detectors to explore physics at an unprecedented energy scale and to discover the Higgs Boson. The study of the asymmetry between matter and antimatter by investigating the Beauty-quark physics is addressed in particular by the LHCb experience [4]. LHCb is a low Luminosity experiment (peak luminosity of $\mathcal{L} = 10^{32} cm^{-2}s^{-1}$). Two further experiences LHCf [5] and TOTEM [6] share the IPs with the two high Luminosity experiments, being installed upstream and downstream of the ATLAS and CMS detectors respectively. They are intended to detect particles coming out from the experiments with small deviation angles, in order to measure cross sections of peripheral collision events. They are both low Luminosity experiences. Finally, ALICE [7] is a dedicated heavy-ion detector. It studies the physics of strongly interacting matter at extreme energy densities, where the formation of a new phase of matter, the quark-gluon plasma, is expected (peak luminosity of $\mathcal{L} = 10^{27} cm^{-2}s^{-1}$ for nominal Pb-Pb ion operation).

2.3 The LHC main ring

The LHC is divided into eight Sectors. The eight curved parts, called Arcs, are connected each other by the Long Straight Sections (LSS). Each LSS is composed by a Straight Section (SS) and two Dispersion Suppressor (DS) regions. The aim of the Dispersion Suppressor is to cancel the horizontal Dispersion arising in the Arc and to help in matching the insertion optics to the periodic solution of the Arc [8].

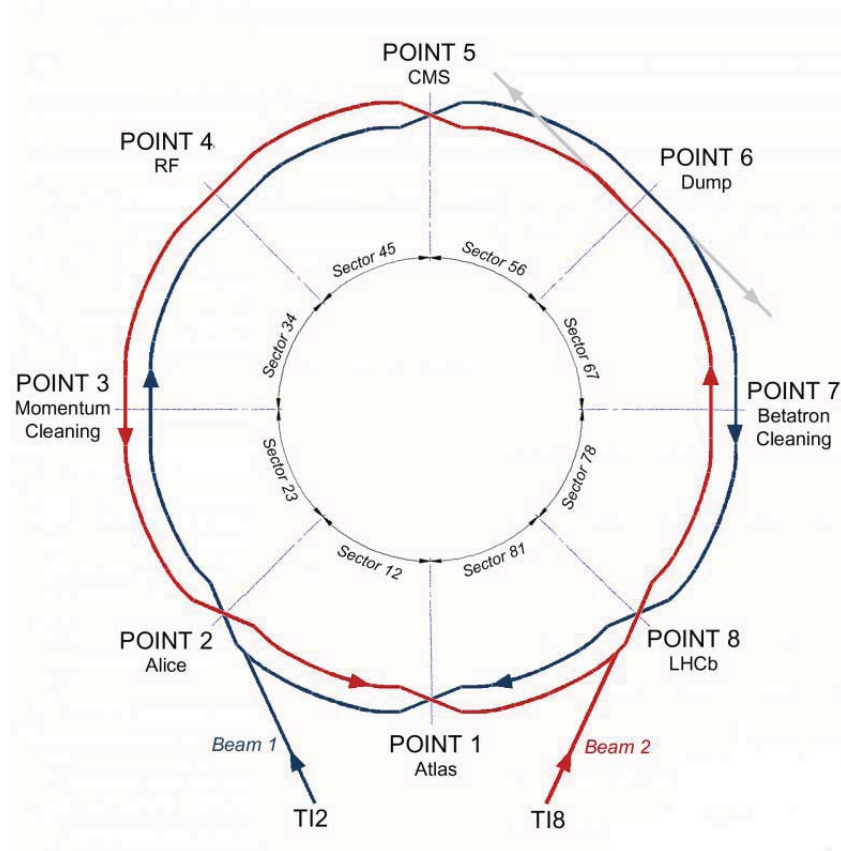


Figure 2.2: LHC Schematic Layout. Beam 1 circulates clockwise and Beam 2 counter-clockwise.

Each LSS is approximately 528 m long and can serve as an experimental or utility insertion. The two high Luminosity experiments are located at diametrically opposite SSs: the ATLAS experiment is located at Point 1 and the CMS at Point 5. Two more experimental insertions are located at Point 2 and Point 8, which also contain the injection systems for Beam 1 and Beam 2 respectively. The remaining four SSs do not have beam crossing. Insertions 3 and 7 contain the collimation system, for capturing stray particles. Insertion 4 contains the Radio Frequency (RF) Superconducting acceleration cavities. Each LHC beam has one RF independent

system. Acceleration is obtained by a longitudinal oscillating electric field at a frequency of 400 MHz in a set of resonant cavities. The SS at Point 6 contains the beam abort systems for the two beams, which allows the beams to be extracted safely and deposited onto external dumps capable of absorbing the considerable stored energy.

Protons injected in the LHC main ring have to increase their energy from 0.45 to 7 TeV . SC magnets are necessary to steer, bend and focus the particle beams.

2.4 The LHC Superconducting Magnets

In Table 2.2 are summarized the functions of the more than 6500 SC magnets installed in the LHC main ring. They range from the large 15 m long, 35 ton main dipoles (see Fig. 2.3), to the 11 cm long, 5 kg decapole-octupole correctors inside the dipole cold mass which correct for unwanted multipoles of the dipole field. They operate at cryogenic temperature of 1.9 K and 4.5 K .

Table 2.2: List of SC magnets installed in the LHC main ring and their function.

Type	Number	Function
MB	1232	Main Bending dipole
MQ	392	Main Arc Quadrupole
MBX/MBR	16	Separation and Recombination dipoles
MSCB	376	Combined chromaticity and closed orbit Correctors
MCS	2464	Sextupole Correctors for persistent current at inj.
MCDO	1232	Octu/Decapole Correctors for persistent current at inj.
MO	336	Landau damping octupoles
MQT/MQTL	248	Tuning quadrupole
MCB	190	Orbit Correction dipoles
MQM	86	Dispersion suppressor/Matching section quadrupoles
MQY	24	Enlarged-aperture quadrupoles in insertions
MQX	32	Low-beta insertion quadrupoles

The SC magnets are sensitive to heating from beam or other sources. A quench, (i.e. the transition from the SC state to the normal resistive one) occurs in the accelerator magnets if the temperature exceeds a critical value. Power deposited in the superconductor by the particle beams may provoke quenches. It is such the case if, for example, they impact on the vacuum chamber and their secondary showers deposit energy in the magnet coils over the quench limit for a given duration of time.

The value of quench limits are strongly dependent by the timescale of the loss process. The protection systems, such as the beam dumps or the magnet quench protection, or simply the cooling in the cables need time to react to the energy

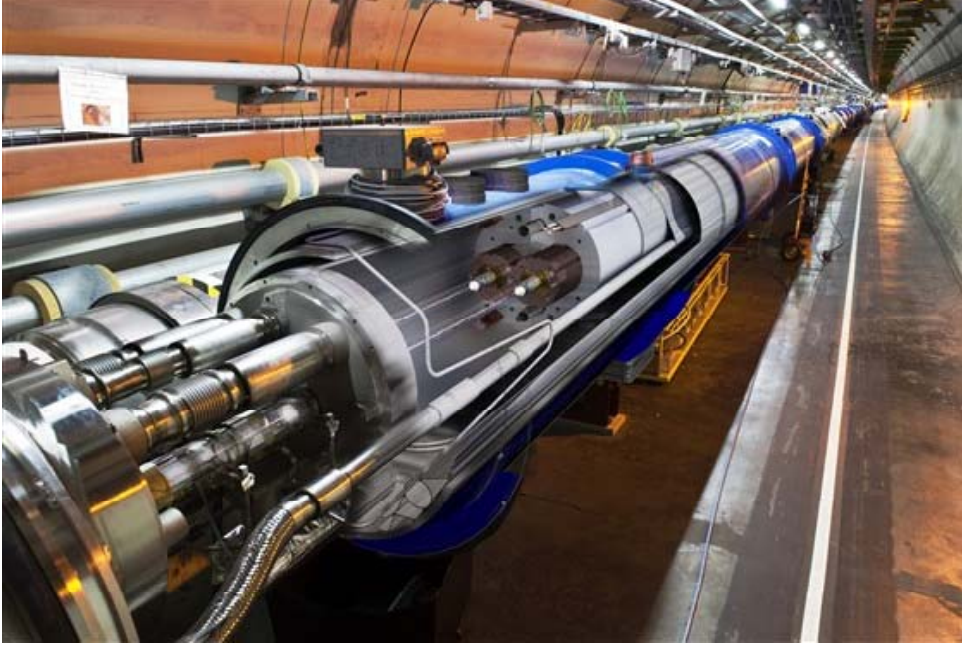


Figure 2.3: LHC main dipole cryo-magnet assembly.

deposited to ensure the safety of the LHC elements from damages. Timescale for particle losses ranges from few ns (i.e. single bunch injected with a bad angle, which might touch the vacuum chamber beyond the collimation system) to several seconds (i.e. RF losses at ramping), depending on the specific failure mode. Moreover, a continuous heating is produced by continuous losses, mainly due by the debris of the proton-proton interactions at experimental insertions, by the nonlinearities in the magnetic field, and by the interactions with the residual beam gas.

In the case of continuous heating, the SC magnets quench for a power density of the order of 10 mWcm^{-3} , when operating at the nominal field (i.e. 8.33 T for the main dipole) for 7 TeV optics. For local transient losses, for example, if an energy of about 30 mJcm^{-3} is deposited for less than 8 ms in the SC coils in 7 TeV nominal condition, it is expected to cause a quench. This happens because the duration of the loss is fast compared to the thermal diffusion time of the cable.

A detailed analysis is reported in [9]. So far, the results of [9] have been used as reference.

2.5 The LHC Cleaning Insertion Regions

Particle losses can be minimized but cannot be completely eliminated. As the beams are stored for many hours, a so-called *primary beam halo* of particles slowly builds up around the core due to various dynamic processes and to magnetic field errors. If it is left uncontrolled, eventually particles would hit the vacuum chamber wall, producing unacceptable background in the detectors and risking a quench in some of the magnets.

It is thus necessary to "clean" the beam by this halo, removing it locally. This is done by a sophisticated system of collimators, mainly installed in the two LHC cleaning Insertions Regions (IR).

2.5.1 The Momentum Cleaning Insertion IR3

The Insertion Region IR3 houses the Momentum Cleaning system for both beams. Particles with a large momentum offset are intercepted here.

The Momentum deviation of the nominal circulating beam does not exceed $\pm 10^{-3}$. Particles which are in the RF-bucket and have stable betatron oscillations below the cut of the betatron cleaning are not intercepted.

In order to fulfill this requirement and to decouple the momentum collimation from the betatron collimation in IR7, the primary collimator jaws in IR3 were located in a position with large Dispersion, generated ad-hoc in IR3 by over compensating the natural dispersion suppression in the DSs. The primary collimator intercept directly the *primary beam halo*.

Since the off-momentum losses are all in the horizontal plane, the IR3 collimators are mostly horizontal.

2.5.2 The Betatron Cleaning Insertion IR7

The Betatron system allows to limit the transverse extension of the beam halo by "cleaning" particles with large Betatron oscillation amplitude. This is optimised by installing primary collimators in a low Dispersion region, in order to reduce the effect of the off-momentum motion on the collimation.

It has to be noted that, while a pure betatron cleaning is achievable in regions of the machine with Dispersion close to zero, like IR7, off-momentum particles has generally a non negligible betatron component as well.

Chapter 3

The LHC Collimation System

In nominal conditions the LHC foresees to store 362 MJ in each proton beam and up to 1 GJ in some upgrade scenarios. This is far beyond the present world record of 2-3 MJ in storage rings like HERA or TEVATRON. The high beam intensity in the LHC requires a careful control of the beam losses around the ring. Stored energy of the order of $mJcm^{-3}$ in the SC magnets can cause a quench.

A sophisticated multi-stage Collimation System is implemented with the main functionality of **beam cleaning** to intercept efficiently the unavoidable losses during operation, **passive machine protection** to protect the accelerator elements against abnormal beam losses and radiation, and **minimization of halo-induced background in the particle physics experiments** to ensure a clear data acquisition [10].

3.1 Why is the LHC collimation essential?

The evolution of the loss rate can be quantified by the so-called *beam lifetime* τ . The beam lifetime plays an important role in the storage rings.

For a beam containing N particles, τ is defined through its relative loss rate at a given time as:

$$\frac{1}{\tau} = -\frac{1}{N} \frac{dN}{dt} \quad (3.1)$$

τ represents the time needed to reduce the number of particles to a fraction $1/e$ of the initial intensity.

In operating conditions, the number of the LHC beam protons at initial nominal intensity is about 3.2×10^{14} (equal to 1.15×10^{11} particles per bunch, times 2808 bunches (see Table 2.1)). Different beam lifetimes τ of 1 h , 20 h , 100 h correspond to beam loss rates $\frac{dN}{dt}$ of the order of 10^{11} , 5×10^9 , 10^9 *protons/s*, respectively.

It is quite likely that all these protons hit the vacuum chamber at one azimuthal position, where the beam, due to a combination of closed orbit, misalignment and

other errors, makes its closest approach to the pipe wall. It is unpredictable where this can occur and whether they will hit the vertical or the horizontal side of the chamber or both together in different locations where the beta function happens to be large. However, it is beyond doubt that the worst case of losses in a single location is on a SC magnet, where they can cause a quench.

During steady physics conditions at 7 TeV , combining the effects of collisions, residual gas and emittance growth, beam lifetimes of the order of 100 h are unrealistic [11]. In this case, the losses are still two orders of magnitude by above the reference SC quench limit $\sim 10^7$ reported in [9].

A beam cleaning system is thus *essential* to avoid that this can happen.

For its high intense beams, LHC requires that collimators are used from the injection until nominal operation conditions.

3.2 The LHC Collimation System requirements

The LHC is entering an unknown territory as far as are concerned beam losses and collimation. The destructive potential of the LHC beams has imposed several requirements and constraints in designing its Collimation System [12].

3.2.1 Beam loss rates during regular operation

Regular operation of the LHC beams requires a reasonable range of acceptable beam lifetimes without the collimators being damaged or the beam being dumped. Low beam lifetimes can occur due to orbit and optics changes during the whole operation cycle. The range of acceptable lifetimes for LHC is defined on the base of operational experience with various colliders (LEP, RHIC, TEVATRON and HERA). It must be large enough to allow commissioning of the machine and performance tuning in nominal running.

Table 3.1 summarizes the specific lifetimes and the corresponding maximum power deposition in the cleaning insertions. For period of up to 10 s , a beam lifetime of 0.1 h (injection) and 0.2 h (top energy) has to be accepted. For continuous losses a minimum possible lifetime of 1 h is specified for both injection and top energy.

Table 3.1: Specified beam lifetimes τ during operation and corresponding duration T , proton loss rate R_{loss} and maximum power deposition P_{loss} .

Energy	τ [h]	T [s]	R_{loss} [p/s]	P_{loss} [kW]
Injection 450 GeV	1.0	cont.	0.86×10^{11}	6
	0.1	10	8.6×10^{11}	63
Top Energy 7 TeV	1.0	cont.	0.86×10^{11}	97
	0.2	10	4.3×10^{11}	487

3.2.2 Abnormal proton losses

Abnormal losses result from failure or irregular behaviour of accelerator components. Primary proton losses will occur at the collimators if they are at nominal positions and they will be continuously monitored with the fast Beam Loss Monitor (BLM). About 4000 BLMs are installed along the ring [15]. When irregular beam losses are detected, a beam abort is initiated and completed within 2-3 turns in about $150\text{-}300\ \mu\text{s}$, without damages on any accelerator elements including collimators.

Here it is assumed that in case of equipment failure the disturbed beam will always end up in the beam dump. However, this machine protection philosophy does not protect against single turn problems, like irregularities of the beam dump itself at top energy and at injection, or abnormal injected beam.

In these accidental scenarios, several bunches may be deflected on a collimator jaw. The collimators jaws have to withstand these impacts.

3.2.2.1 Abnormal injected beam

During injection, transverse and longitudinal mis-matching between the end of the transverse line and the injection point can cause the deflection of the full injected batch (288 bunches) on any downstream aperture limit.

3.2.2.2 Irregularities of the beam dump

Two causes of abnormal proton losses are identified for the faulty operation of the extraction resistive dump kickers magnets (i.e. MKDs) [16]:

- *Asynchronous beam dump due to the all 15 MKDs mis-firing.* In this case, all the 15 MKDs are triggered simultaneously but with the uncorrect phase respect to the beam abort gap. Part of the LHC beam is thus swept across the machine aperture by the rising kicker voltage.
- *Asynchronous beam dump due to a spontaneous firing of 1 of the 15 MKDs.* When this happens, the remaining 14 MKDs are re-triggered. Times of $1.2\ \mu\text{s}$ at injection and of $0.7\ \mu\text{s}$ at top energy are necessary for retriggering and restoring the synchronized beam abort.

At 7 TeV , the second case is the most severe one on the downstream components, since the deflection is smaller and more intensity will impact per σ , where $\sigma = \sqrt{\beta\epsilon}$ is the local beam size calculated from beta function and the emittance ϵ .

For Phase I it was required to withstand the hit of 8 nominal bunches on one collimator jaw, in case of primary collimators not in their nominal position but at a distance of $5\sigma_x$ from the center of the beam. The range of the impact was from $5\sigma_x$ to $10\sigma_x$. Above $10\sigma_x$, local dump protection devices were assumed to intercept all beam. Improvement on the protection devices has reduced the requirement to about 5 impacting bunches.

The abnormal beam dump scenarios considered only affect the horizontal beam distribution, so only horizontal collimators (and a few skew ones to a certain extent) are concerned by the dump errors.

3.2.3 Cleaning Inefficiency

The performance of the collimation system is measured by the *global Cleaning Inefficiency* η_c . At a given amplitude A_i of betatron motion, η_c is defined as the ratio between the number of particles N_p with an amplitude above A_i and the total number of particles absorbed in the collimation system N_{abs} :

$$\eta_c = \frac{N_p(A > A_i)}{N_{abs}} \quad (3.2)$$

For the LHC $A_i=10\sigma$ is considered a typical case (equal to the aperture of the absorbers, see Appendix B). In case of LHC operating at top energy, η_c should be smaller than 10^{-3} , corresponds to 99.9% *Efficiency* (Collimation Efficiency = $1-\eta_c$) [13].

However, even if the requirement for global η_c is satisfied, the surviving particles may get lost locally in the machine and cause quenches. The so-called *local Cleaning Inefficiency* $\tilde{\eta}_c$ [m^{-1}] is thus introduced as:

$$\tilde{\eta}_c = \frac{1}{\Delta s} \frac{N_{loss}}{N_{abs}} \quad (3.3)$$

where N_{loss} is the number of particles lost along a Δs length.

Powerful tracking tools [14] are used to calculate $\tilde{\eta}_c$ every 10 cm along the whole LHC ring. The value of $\tilde{\eta}_c$ in critical regions (i.e. the locations of SC magnets) has to be compared with the local inefficiency at the quench limit:

$$\tilde{\eta}_c^q = \frac{R_q \tau}{N_{tot}} \quad (3.4)$$

where R_q is the maximum allowed loss rate of protons per meter, τ is the beam lifetime and N_{tot} is the total beam intensity [13].

The most stringent value for $\tilde{\eta}_c^q$ is at top energy. In such a case, using the R_q reference value of $7.8 \times 10^6 m^{-1} s^{-1}$ reported in [10], for the minimum beam lifetime of 0.2 h and with $N_{tot}=3.2 \times 10^{14} s^{-1}$, $\tilde{\eta}_c^q$ is equal to $1.7 \times 10^{-5} m^{-1}$. This is the design value for Cleaning Inefficiency in case of ideal LHC machine (i.e. without imperfections).

3.2.4 Impedance

The collimator jaws are the material closest to the LHC beam, separated one from the other by a gap as small as 2-3 mm at 7 TeV. When they are at their nominal

positions, the machine aperture is equivalent to the size of the Iberian Peninsula on a one euro coin (see Fig. 3.1) [10].

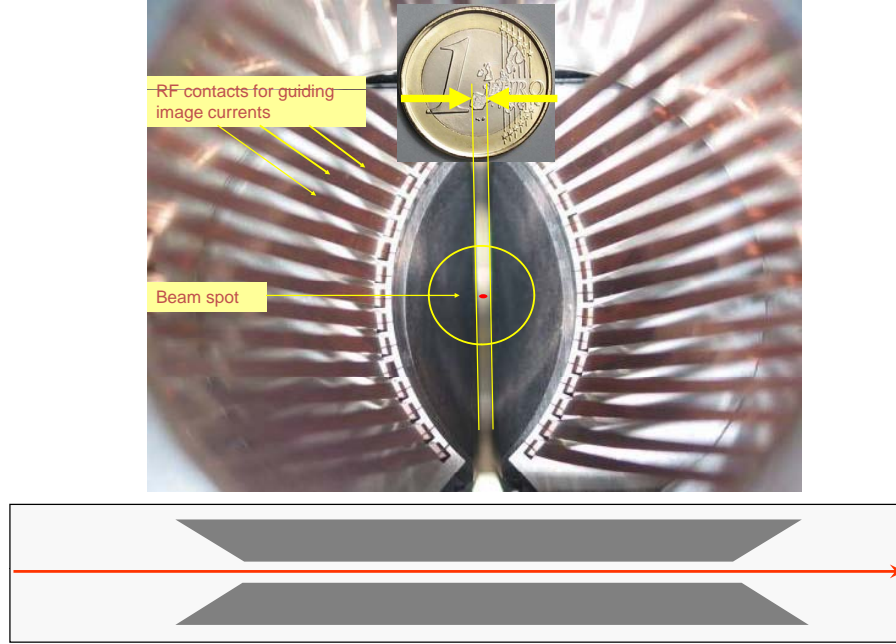


Figure 3.1: View along the beam line in a horizontal secondary collimator. A typical LHC gap size is shown. The RF fingers are used to guide image currents.

Their approaching to the beam can introduce intolerable wake fields (i.e. impedance) that might compromise beam stability.

The collimation impedance budget is due by the resistive jaw wall and by the geometrical and electrical discontinuity contributions. It has to be minimized in order to prevent the onset of beam instabilities.

In particular, collimators can produce a significant transverse resistive impedance [17]. It scales approximatively as $1/b^3$, where b is the distance from the beam axis to the collimator jaw surface. Especially its real part has to be carefully evaluated, playing with different collimator apertures or jaw materials. The resistive wall-transverse impedance of the jaws can generate tune shifts [18]. Landau damping [19] or transverse feedback [20] provide a possible cure against tune spread instabilities.

In addition to the main, resistive wall collimator impedance, impedance peaks can be observed due to transverse geometric and electrical discontinuities of the vacuum tank cross section. These result in longer term wakes or "trapped mode". These trapped modes can cause beam energy loss and local heating as well as coupled bunch instabilities [22]. In particular, the problem of the trapped mode is addressed

by the tapering of the jaw ends and by adding RF fingers [21], allowing for a smooth geometrical transition from the flat jaws to the round flanges and beam pipe, while guaranteeing electrical continuity for the beam image currents.

3.2.5 Radiation constraints

Under the assumption of about 180 days per year of nominal operation, proton losses are estimated 1.15×10^{16} and 3.15×10^{15} for each beam in IR7 and IR3 respectively [11].

The collimators and the neighboring accelerator elements should survive the beam-induced prompt radiation. In addition, the induced radiation in the collimator area shall be fully compatible with the maintenance work in the tunnel. Of particular importance for human interventions are estimates of residual dose rates from induced radioactivity to foresee fast and remote handling where needed.

3.2.6 Additional requirements

Particular attention is given to the mechanical tolerances for collimation production, since they must act as precision devices with safe and accurate settings that are remotely controlled and reproducible over weeks or even months. This translates into strict requirements for surface flatness, step size in jaw movements and reproducibility of jaw settings in the $5\text{--}30\ \mu\text{m}$ range.

In addition, the choice of collimator materials has to be compatible with the ultra-high vacuum of LHC (e.g. outgassing rates must remain acceptable).

Constraints related to the tunnel space availability also apply to the LHC Collimation System.

3.3 The multi-stage LHC Collimation System

The collimation of high energy rings, like the LHC, is based on the so-called *multi-stage collimation system*. The above mentioned goal for Cleaning Inefficiency can only be achieved with a cleaning system that has at least two stages [23] [25].

The principle of multi-stage cleaning is the following. The jaws inserted closest to the beam are called primary collimators and define the primary aperture which is normally chosen to be larger or equal to the dynamic aperture in order not to intercept stable particles. At LHC energies, not all the protons of the primary halo are absorbed by the primary collimators, which intercept them. By multiple Coulomb scattering many of these protons are scattered off with larger angular divergence. In addition, by inelastic processes, secondary particles may be produced, generating hadronic showers. All these particles form the so-called *secondary halo*, which can also induce quenches. Secondary jaws, installed downstream of the primary ones, are thus necessary to intercept the secondary halo and to remove it. The residual halo

(i.e. the so-called *tertiary halo* produced by the secondary collimators) is captured by additional absorbers or collimators, located close to the most sensitive elements and to the particle physics detectors. Fig. 3.2 illustrates schematically this system.

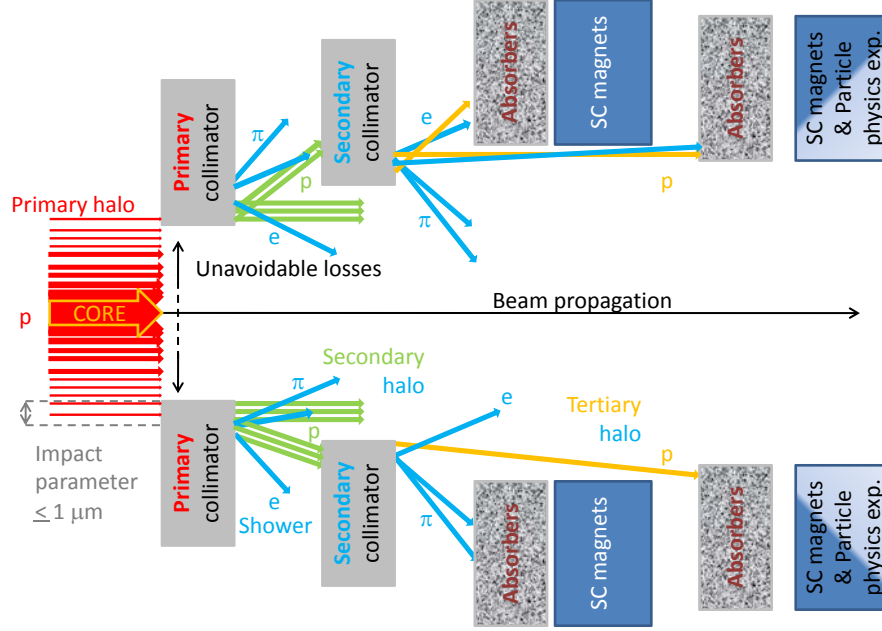


Figure 3.2: Schematic illustration of the multi-stage cleaning concept of the LHC.

In the Betatron Cleaning, three primary jaws for each beam are located in a low Dispersion region, forming an octagonal primary aperture. In contrast to the Betatron halo, which may drift away from the beam in all the transverse directions, momentum losses are concentrated in the horizontal plane, so only one primary horizontal collimators for each beam is installed in a position with large Dispersion in the Momentum Cleaning region. Once these locations are fixed, the position of the secondary collimators are constrained by the required phase advance in order to achieve the best coverage in the transverse phase space (see Appendix A) as well as by actual integration availabilities. The LHC foresees about 4 secondary collimators per primary ones.

The physical aperture of the collimators is expected to shadow the bottlenecks of the accelerator, without interfering the motion of the core particles. In injection, the aperture is limited by the arc SC magnets, while for the 7 TeV scenario the LHC Collimation System must efficiently shadow the triplets. The aperture is here

limited by the SC triplets, where, for squeezed optics ($\beta^* = 0.55\text{ m}$), β function values in the final focus quadrupoles as large as about 4500 m are implied to achieve small beam size at the interaction points IP1 and IP5.

The limits at injection and at top energy are summarized in Table 3.2 [24].

Table 3.2: Overview on expected physical LHC aperture limits at injection and top energy. Minimal horizontal and vertical apertures in σ for cold elements.

Energy		Beam 1		Beam 2	
		Horizontal	Vertical	Horizontal	Vertical
450 GeV	SC Arc	7.88	7.78	7.70	7.60
7 TeV	SC Triplet	8.90	8.43	8.13	8.75

Protecting the triplets imposes to close the half gap (i.e. the distance between one collimator jaw surface and the beam axis) n_3 of the tertiary collimators down to about 8σ in such a way to intercept as much as possible of the tertiary halo. The half gaps of the secondary jaws n_2 (that generate the tertiary halo) must be smaller of n_3 but larger than the primary n_1 , so that only protons which experience an interaction with the primary are caught. On the other hand, n_1 must fit to external parameters like the dynamic aperture of the ring.

Numerical simulations allowed to define the number of collimators, their relative phase advance, azimuthal positions and relative gaps [23].

The LHC implements a 3 stage cleaning for the SC arc downstream the cleaning insertions, including primary, secondary collimators and the active absorbers. The latter are geometrically equal to secondary collimators but with tungsten jaws at the place of Carbon-Carbon ones. For the protection of the triplets in the experimental insertions, a 4 stage cleaning is foreseen, including primary, secondary, tertiary collimators and active absorbers.

3.4 The multi-phase LHC Collimation System

The listed LHC Collimation System requirements impose various conflicting constraints. For example, a collimation system with sufficient robustness, based only on Graphite jaws collimators, would introduce peak performance limitations for LHC (i.e. reduced intensity, increased β^*). A system with sufficiently low impedance, like the Copper based one, would likely experience regular damage to the collimator jaws with resulting loss in cleaning efficiency of LHC operation. A Beryllium based system would not resist the specified one turn beam load due to the mechanical stresses and in addition would introduce concerns about toxic materials [26].

Since all the requirements cannot be satisfied simultaneously, it was defined a phased approach for LHC collimators, addressing the different needs in steps [27].

3.4.1 The Phase I Collimation System

A first sub-set of the Phase I Collimation System has been installed for the 2008 first beam commissioning of the LHC. It included 88 collimators and absorbers around the ring and along the two injection lines. It constituted the largest and most complex collimation system ever put into operation [28]. During the reparation of Sector 3-4, additional devices were installed in order to maximize the LHC Intensity and Luminosity achievable. In June 2009, the Phase I installation was totally completed and ready for the LHC 2009 restart.

The Phase I Collimation System is composed by 108 collimators and absorbers, out of which 97 are precision movable devices (i.e. collimators), being controlled by 388 stepping motors in total. Table 3.3 summarizes the Phase I components giving quantities per functional type and their specific locations along the ring.

Table 3.3: Quantities and LHC locations for Phase I Collimation System components in both beam lines.

Functional Type	Phase I
IR3 Primary Collimators	2
IR3 Secondary Collimators	8
IR3 Passive Absorbers	2
IR3 High-Z Collimators	8
IR7 Primary Collimators	6
IR7 Secondary Collimators	22
IR7 Passive Absorbers	6
IR7 High-Z Collimators	10
Injection Protection Collimators (IR2, IR8 and transfer lines TI2, TI8)	20
Dump Protection Collimators and Diluter Elements (IR6)	4
High-Z Collimators in experimental regions (IR1, IR2, IR5, IR8)	20
Total	108
<i>Total (movable only)</i>	97

A number of design variations were developed. Primary (TCP), secondary (TCSG) and absorbing (TCLA) collimators are the main devices. They are located in the LHC cleaning insertion IR3 and IR7 for each beam line. In the same regions are installed the different length passive absorbers (TCAP). They are immediately upstream of warm magnets that need protection from damage by particle showers created by the collimators. Injection protectors (TDI, TCLI, TCDD) are installed in IR2 for Beam 1 and in IR8 for Beam 2. The TCLI type A, have a "two beams in one tank" design, since they are installed in region with common beam pipe. Diluter elements (TCDQ) plus a TCSG protect the machine against miss-kicked beams in the dumping region IR6. Tertiary collimators (TCT) are installed upstream of the

interaction regions to protect the triplet magnets. Tertiary vertical collimators in IR1 and IR5 have the classical one-beam design, while in IR2 and IR8 they have the "two beams in one tank" design. In addition, absorbers (TCL) are located downstream of the IPs to catch the physics debris coming out from the experiments. The Transfer Injection (TI) line collimators (TCDI) complete the Phase I Collimator System.

Robust collimators (primary, secondary and some protection collimators) use a special fiber-reinforced Carbon material (CFC), which combines extreme robustness with good thermal, electrical and mechanical properties. Collimators for absorbing showers use high-Z materials of Copper and/or Tungsten. They enhance efficiency while being sensitive to beam damage. Therefore, they are only used at larger distances from the beam.

3.4.1.1 The Phase I Collimator design

A Phase I collimator houses two parallel jaws inside a vacuum box (see Fig. 3.3).

The flange-to-flange length of a collimator is standardized at 1.48 m . The rotation of the tank is used to define a horizontal, vertical or skew collimator. The vertical, horizontal and skew collimators perform cleaning in the vertical, horizontal, skew

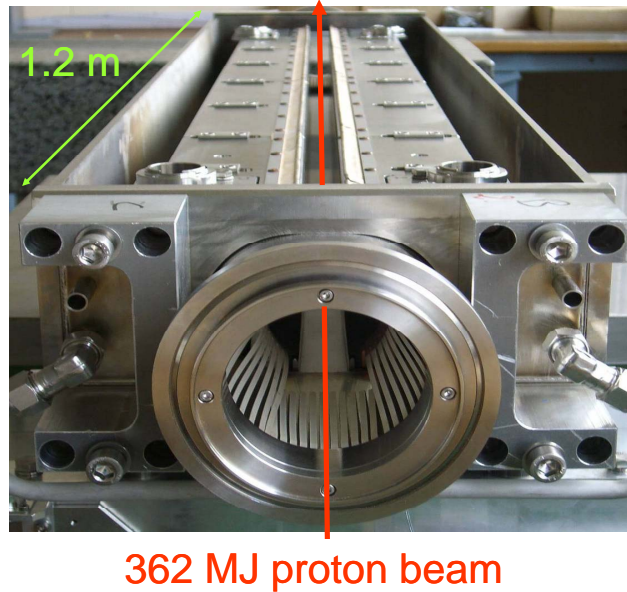


Figure 3.3: View into an open vacuum tank of an LHC Phase I collimator. The two parallel jaws are visible. The total jaw length is 1.2 m with a tapering at the front and the back of the jaws.

plane through jaws placed perpendicular to the cleaning plane.

The jaws are the material blocks put closest to the beam. Different jaw materials identify different collimation types. The jaw is constituted by a flat part, determining the jaw *active length*, and by 10 cm tapering at both ends to minimize impedance effects. The flat top length of the jaws is always 1.0 m, except for primary (0.6 m) and transfer line collimators (1.2 m). Each jaw is supported at its two extremities and movable in order to be centered and aligned with respect to the beam envelope and to follow the change of beam dimensions as a function of the energy.

Precise stepping motors are used to move the jaws. Four of these, located at each jaw ends, are used for aperture and angular adjustments, while a fifth motor shifts transversally the whole collimator tank. Movements are monitored independently with precision sensors (LVDT's, resolvers) [30]. Excessive tilt of the jaw is prevented by a rack and pinion system. The return springs ensure a semi-automatic back-driving of the jaw in case of motor failure.

Jaws and tank are cooled for extracting loads of up to 3 kW by the water of the general cooling circuit of LHC. The heat exchanger is constituted by two OFE-Copper pipes per jaw brazed on one side to a Copper plate and on the other to the Glidcop bar. Each pipe has three turns to increase the heat exchange capability. The clamping system allows to enhance the thermal contact between jaw and heat exchanger without creating mechanical constraints between materials having different thermal expansion coefficient.

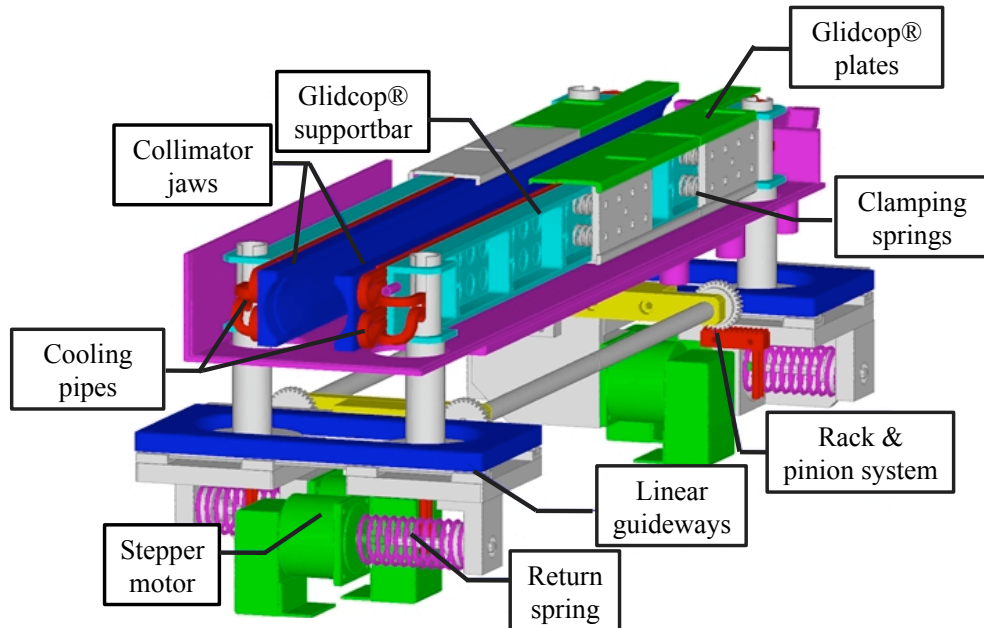


Figure 3.4: Mechanical Integration of a horizontal secondary collimator. Components including motorization and actuation system are shown.

The vacuum pressure after bake-out is smaller than $4 \times 10^{-8} \text{ mbar}$ [29].

Fig. 3.4 shows the collimator mechanical integration described above.

Once installed in the LHC tunnel over special supports, the collimators can be replaced thanks their fast plug-in-time, using a remote control for appropriate robotics. This was foreseen in view of the radioactive environment due by the collimators themselves.

3.4.1.2 Protection devices

The Phase I Collimation System includes devices with little or significant design differences from the collimators described above.

In particular, in case of the passive absorbers installed in the cleaning regions, significant differences can be found. They consist of about 1 cm thick hollow Tungsten cylinder of different active length surrounding the beampipe. Copper cooling plates in between the cylinders ensure the heat transfer from the Tungsten to the cooling water (see Fig. 6.7).

In the insertion regions, the injector beam stoppers TDIs are vertical collimators with extremely long carbon-carbon jaws (4.2 m). The upper jaw should intercept bunches not sufficiently deflected by the injection kickers, while the lower jaw should catch miskicked beam. Downstream the TDI is installed the TCDD absorber (1 m Copper jaw) used to protect the SC beam separation dipole D1 from damage and quench. The asymmetry of the TI lines required this special device only at the end of TI8.

The TCDD and the passive absorbers are employed to intercept only shower particles.

Finally the TCDQs installed in the extraction region are 3 m long horizontal single-side mobile elements, used to absorb the beam swept over the machine aperture. Each couple of TCDQ is counted as 1 collimator.

3.4.1.3 The limitations of the Phase I

The Phase I collimators define a system that offers maximum robustness against beam damage. It will be used, for the whole lifetime of LHC, from injection up to the end of energy ramp for any beam intensity and during the more unstable moments of operation.

The choice of materials for the LHC collimator jaws is not so much driven by the standard collimation procedure during the operation, but rather by possible malfunctions of the components. Only the usage of the non-metallic low-Z material, like Carbon-Carbon or Graphite, for primary and secondary collimator jaws can ensure a sufficient mechanical robustness against fast bursts of multi-hundred GeV beams [31].

However, this choice has limited the performance of the Collimation System, in terms of:

- *Proton Cleaning Inefficiency.*

The simulated ideal performance of the Phase I Collimation System is about $5 \times 10^{-5} m^{-1}$. This value has to be compared with the local inefficiency at quench limit for the same bin size, which is $1.7 \times 10^{-5} m^{-1}$ for nominal beam Intensity (see Section 3.2.3). This means that, since the LHC intensity is in inverse proportion to the cleaning inefficiency, the ideal intensity reachable by the Phase I collimation system is limited to about 40 % of the nominal LHC one.

The limitation is related to a physics process (single-diffractive scattering) in the CFC primary and secondary collimator jaws. A fraction of protons receive a small transverse kick which brings them to be lost after the first strong bending dipoles in the downstream SC arc.

In case of the real machine, unavoidable imperfections (i.e. machine misalignments, deformed jaws, tilt, offset and gap errors) further reduce the performance by a factor of up to 11 [32].

- *Resistive Impedance.*

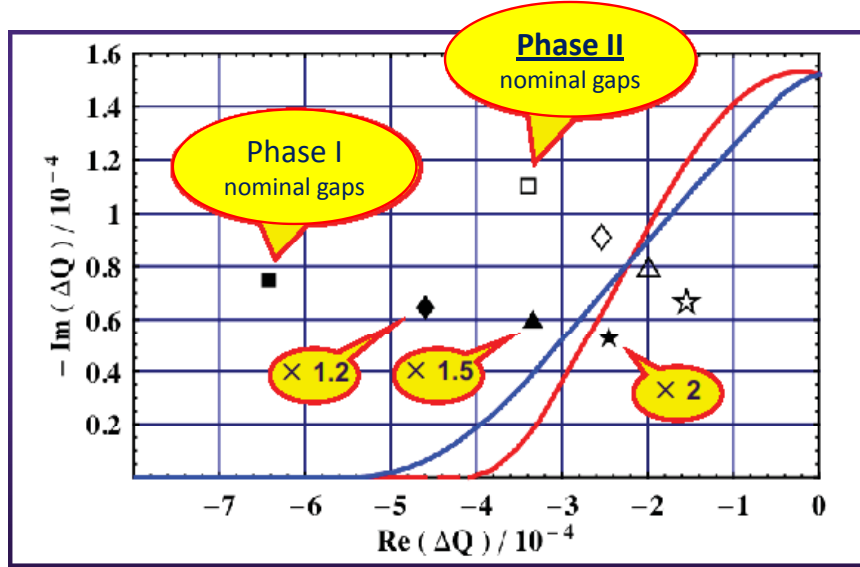


Figure 3.5: Stability diagram at top energy. Red and blue lines represent the stability limit for maximum Landau octupole. Comparison between Phase I and Phase II with Copper secondary collimators and cryogenic collimators included is shown.

The overall resistive wall impedance of the LHC is dominated by the collimator contributions. It is predicted that the LHC beam will be unstable even with the maximum Landau damping (fully powered octupoles) above 50 % of nominal design intensity. Even if the transverse feedback will be used to actively stabilize the beam at higher intensity, Phase I collimators at nominal settings are farther away from the stability limit than a collimation system built up of Phase I primary and Phase II with metallic jaws (secondary and cryo-collimators with Copper jaws).

However, since the best way to reduce the collimator impedance remains to open the collimator gaps (see Fig. 3.5), this means that the Phase I system has to sacrifice more in term of Cleaning Efficiency in order to be in a stable working area.

- *Ion Cleaning Inefficiency.*

Ions experience fragmentation and dissociation in the primary jaws. The effect is the loss of ion fragments in the same SC DS region. Ion intensity is predicted to be limited by Phase I Cleaning Inefficiency to about 30-50 % of its nominal design value [33].

3.4.2 The Phase II Collimation System

The Phase II collimators will not replace but complement the Phase I System. They are supposed to remove the Intensity limitations just discussed. For this reason, the use of low impedance and higher-Z materials (to improve the Cleaning Efficiency) is foreseen for the Phase II collimator jaws. Since this choice results in higher energy deposition, in particular with serious consequences in the case of direct impact, they will be used only at the end of the β squeeze and in stable physics conditions.

It relies on adding 30 collimators (TCSM) behind the secondary TCSGs in the IR3 and IR7 regions. They will be closed in stable parts of operation (stable beams), while the Phase I secondaries will be kept at larger gaps (see Fig. 3.6).

Besides the Phase II secondary collimators, recent studies have demonstrated that 8 new collimators are required in the SC DS around the cleaning insertions IR3 and IR7, in order to absorb protons that experience single-diffractive scattering and ions fragmented produced by interaction with Phase I CFC collimators. These are referred to as "cryo-collimators", which are part of the collimation Phase II upgrade, too.

Settings and main parameters of the Phase I collimation system installed in the main ring and of Phase II secondary and cryo-collimators for Beam 1 and Beam 2 at injection and top energy in case of pure Betatron Cleaning at IR7 are reported in Appendix B.

To complement the Phase II collimation system, 4 hollow electron-beam lenses [34] [38] are foreseen, but still under study. They should allow safe removal of beam

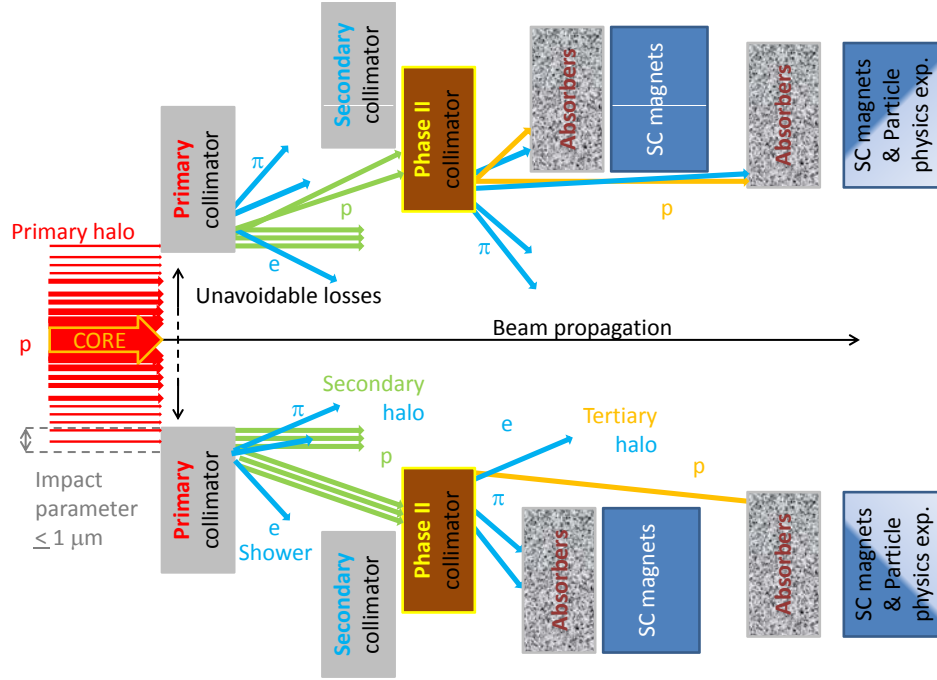


Figure 3.6: Schematic illustration of the multi-stage cleaning concept of the LHC with the Phase II secondary collimators.

tails and halo below collimators settings, reducing peak losses at the collimators.

The Phase II collimation work is performed in collaboration between CERN, several US labs (through the LHC Accelerator Research Program (LARP)) and several European partners in research institutes and universities (ColMat work package in the EuCARD program funded by the EU through FP7).

3.4.2.1 Benefits of the Phase II secondary implementation

The study on Phase I performance with imperfections [32] has pointed out that the only Phase II secondary collimator implementation is not sufficient to reach the nominal Intensity in a realistic case.

It was predicted that the introduction of cryo-collimators in the cryogenic region, in addition to the secondary Phase II, improves the Cleaning Efficiency by a factor 15 for a perfect machine and to a factor 90 for an imperfed machine [35].

Apart from the higher local radiation, due to the use of high-Z materials for the collimator jaws (double dose peak to the cables running along both sides of the tunnel wall), the only implementation of secondary Phase II collimators is expected

to add various benefits:

- *Lower Impedance.*

The 60 Phase II jaws if all in Copper based material reduce the collimator induced impedance of about a factor 2. It might be crucial for removing the limit on β^* .

In addition, the gain in Cleaning Inefficiency could be used to open the collimator gaps, in such a way to reach a stable working point during operation, without using any damping system (see Fig. 3.7).

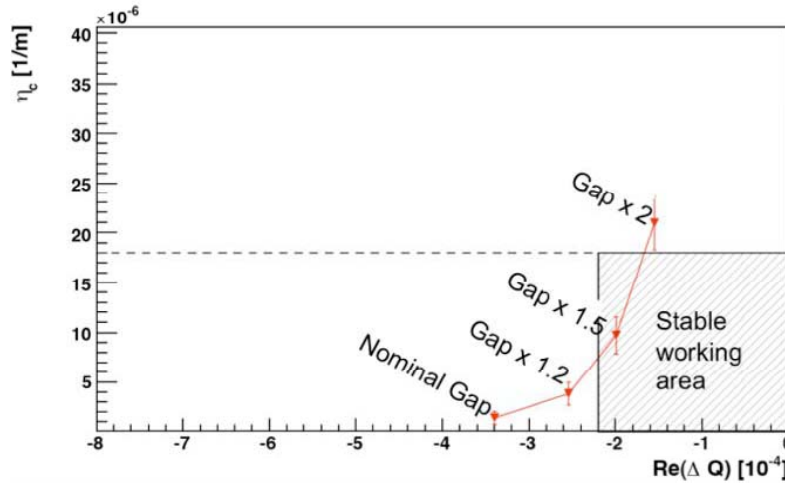


Figure 3.7: Inefficiency versus tune shift (induced by the impedance) for Phase II with secondary collimators in copper opened at different gaps. The stable working area for nominal Intensity is shown.

- *Longer collimator lifetime.*

Adding devices, that intercept losses, improves the lifetime of all the LHC Collimation System and of neighboring equipments, because the radiation load will be distribute on more objects.

- *Longer magnet lifetime.*

For the same reason reported above, the improvement of lifetime for warm magnets (order of tens *MGy* are supposed to break some coil insulators) in

cleaning insertion regions is about of a factor 3. It is to be noted that the limited lifetime of warm magnets is not addressed elsewhere.

- *Lower radiation to electronic equipment.*

The complexity of the LHC accelerator demands the installation of the control electronics close to the beam lines. It is essential that the electronics does not severely degrade or fail due to irradiation. In particular the Single Event Errors (SEE) are to be avoided. These errors are a flip of a logical gate value induced by an energetic particle traversing the electronics. The flip occurs if a sufficient amount of energy is deposited in the active volume of the transistor in question. In addition, any electronic device operating in strong radiation fields such as that of IR7 will undergo degradation through ionizing and nonionizing processes.

The radiation to the electronic equipment, installed close to the IR7 main tunnel, is reduced by the Phase II collimators (see Chapter 13 for more details).

- *Faster and more accurate set-up.*

Empty Phase II TCSM slots are ready in the LHC tunnel (see Fig. 3.8). They will reduce substantially the time needed for the Phase II installation, since water supply, long cables, supports, pumping domes, BLM's are all already installed.

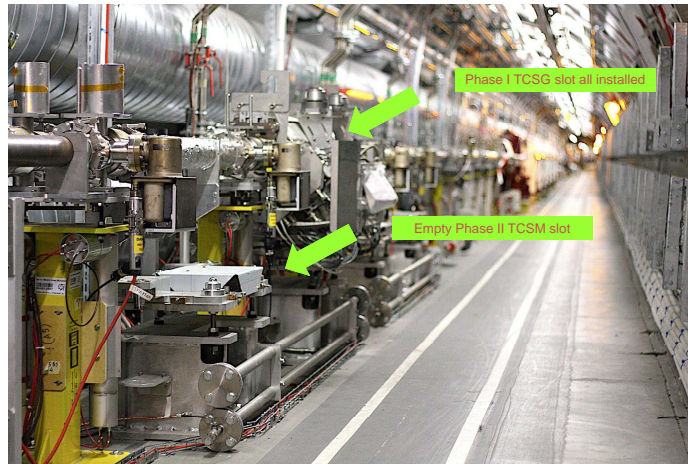


Figure 3.8: LHC tunnel view with the ready empty slots for the installation of secondary Phase II collimators.

- *Higher operation efficiency.*

On January 2010, the first basic Phase II collimator was installed in the SPS. The purpose is to test the BPMs which are integrated in the jaws. This is not the case of Phase I collimators that use the BLMs for their beam alignment. In such a way, Phase II collimators can improve the operation efficiency, helping the collimator setup with fewer special calibration fills.

3.4.3 Further Phases

The LHC upgrade program foresees a further increase of the beam Intensity. At this time it cannot be guaranteed that the Phase II of the LHC collimator is sufficient for supporting up to 1 GJ stored per beam. A further upgrade of the LHC collimation beyond Phase II has therefore been envisaged.

Novel techniques are pursued for further improved cleaning, for example crystal collimation [36], non-linear solutions [37] and hollow e-beam lenses used as primary collimators [38].

Chapter 4

Simulation Framework

In order to evaluate the performance of the LHC Phase II Collimation System in terms of energy deposition and radiation issues, the distribution of the losses along the collimators and beam elements has to be as much realistic as possible.

The predictions on collimator thermal and radiation loads and on the induced activation are strongly dependent on inputs. They define the particle distribution during the nominal beam operation conditions as well as during abnormal scenarios.

For these reasons, a simulation framework was built up to provide outputs such as the expected thermal deformations, quantities for assessing the radiation damages (Dose, peak dose, DPA, etc.) and the evaluation of residual dose rates, starting from the MAD-X optic model.

4.1 Purpose of the simulations

The collimator design must comply with the very demanding functional specifications resulting from the highly energetic beams handled in the LHC rings.

Their design imposes that important questions are addressed:

- 1) Which are the effects of particles showers generated by the inelastic interactions of the primary protons on different jaw materials?
- 2) Can the Phase II collimators withstand the energy density deposition induced by the particle losses in the nominal operation scenarios?
- 3) Which is the distribution of the thermal loads in the collimator components during the most destructive possible failure mode?
- 4) How high are the temperature peaks and where are they localized?
- 5) Which are the consequences of different Phase II designs on the adjacent equipments?
- 6) How much is the influence of collimators on the residual ambient dose equivalent levels in the region?
- 7) How can we evaluate the degradation of the collimator materials, due by radiation?

This PhD work addresses for the proton beam these questions, the answer to which will have a crucial impact on the performance of the LHC for physics at low beta optics.

4.2 The simulation chain

In order to evaluate the mechanical strengths on the collimators and the effect of these devices on the surrounding environment during operation and failure scenarios, a chain of simulations was build up (see Fig. 4.1).

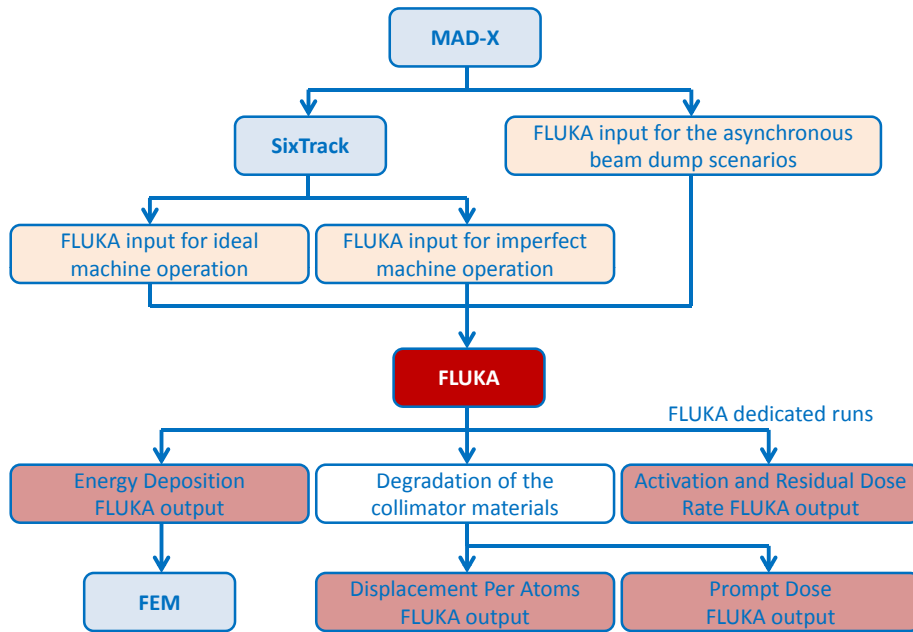


Figure 4.1: The simulation chain where the inputs and outputs of the FLUKA code are pointed out.

The chain starts with the MAD-X optics sequence model, which defines the LHC layout and the magnetic strengths of the LHC elements. In particular, beam distributions for the abnormal scenarios are directly deduced by the MAD-X outputs.

The distributions of the halo particles during the operation scenarios are produced by the LHC beam loss simulation tools. They consist of a 6D single particle tracking through a MAD-X thin lens lattice approximation, using the SixTrack code extended for simulating a large number of halo particles and combined with special

routines describing the proton scattering processes within the collimators jaws (i.e. the COLLTRACK/K2 routines). The recorded particle non-inelastic interactions with arbitrarily placed collimators are the input for the FLUKA calculations.

The FLUKA Monte Carlo code performs full shower simulation and provides as output power distributions for further Finite Element Method (FEM) calculations as well as quantities relevant for the radiation damage and activation evaluation.

4.2.1 The MAD-X code

The MAD-X accelerator design code [39] is used to generate the official LHC beam optics and the LHC lattice (each arc is composed of 23 FODO cells plus one Dispersion Suppressor at each end). It delivers relevant values like the closed orbit coordinates in each transverse plane and, for each element, the Twiss parameters (i.e. $\beta(s)$, $\alpha(s)$ ($\alpha(s) = -\beta'(s)/2$) and $\gamma(s)$ ($\gamma(s) = (1 + \alpha^2(s))/\beta(s)$) optical functions at s locations along the ring which give a complete and compact description of particle trajectories). Fig. 4.2 shows an example of MAD-X outputs. The β function

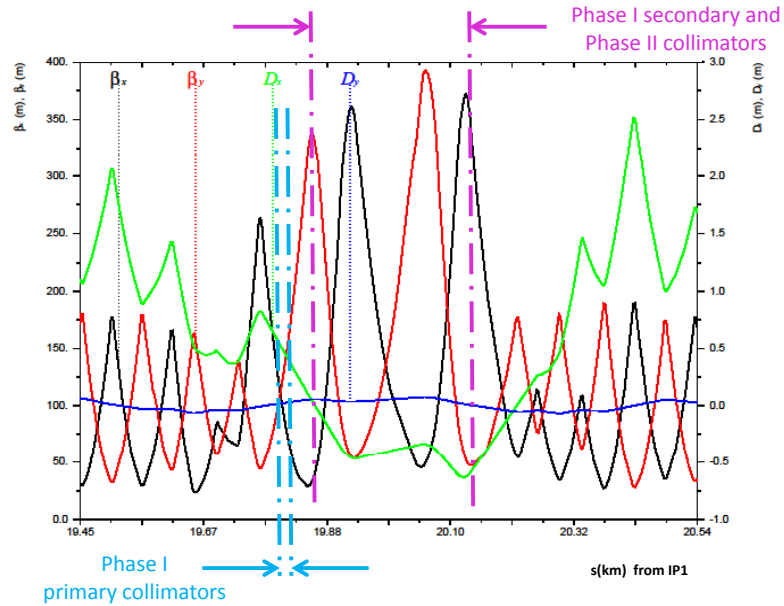


Figure 4.2: MAD-X output plot. Horizontal and vertical β -functions (β_x , β_y) and Dispersion (D_x , D_y) in the betatron cleaning insertion are shown as well as the positions of the primary and secondary Phase I and Phase II collimators.

and the Dispersion in the x and y planes are plotted for Beam 1 considering the low beta scenario in the IR7 region.

The particle tracking for a large number of turns requires excessive CPU resources using the most detailed lattice description in MAD-X. It is therefore needed to approximate long magnetic elements with drifts and point-like kicks. This relies on a special model of the considered lattice, called the thin lens formalism.

The SixTrack results refer to the LHC Optics and Lattice Version V6.500, thin lens approximation and including the Phase II collimators.

4.2.1.1 Beam distribution for the asynchronous beam dump scenario

The input for FLUKA simulations in case of asynchronous beam dump is directly deduced by the MAD-X code results at top energy optics, this time starting from the thick lens approximation (i.e. the most accurate lattice description). It refers to the worst scenario of a spontaneous firing of 1 of the 15 MKDs.

The bunch amplitudes versus time was calculated at the worst location downstream the kicker, that is at $\pi/2$ phase advance in the IR7 region. Since the kickers

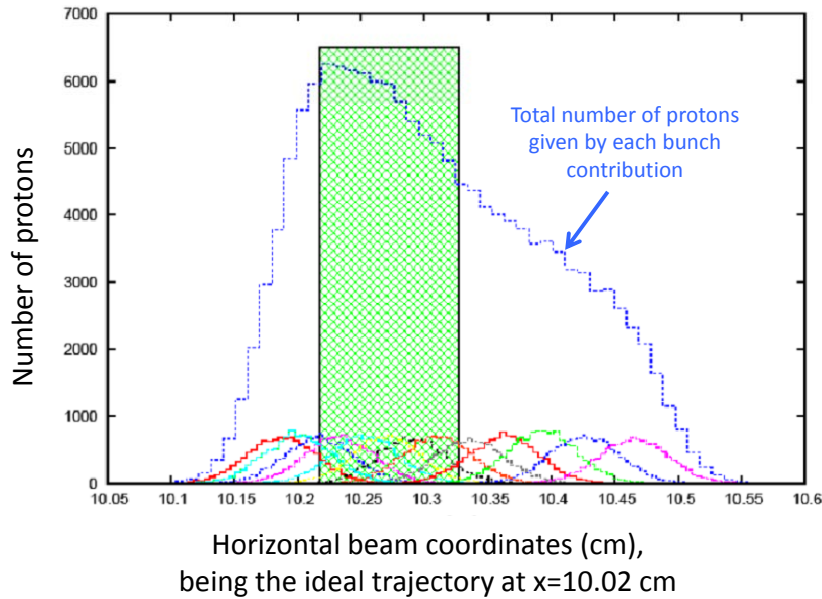


Figure 4.3: Beam distribution at the TCP.C6L7.B1 location for the asynchronous beam dump scenario.

act in the horizontal plane, it was supposed that any horizontal collimator may be at $\pi/2$ phase advance from the kicker when the mis-firing occurs, in such a way to intercept the maximum number of particles [42].

The horizontal Phase I collimator TCP.C6L7.B1 and the horizontal Phase II collimators TCSM.B4L7.B1 and TCSM.6R7.B1 were considered. In these collimator positions, each bunch is translated horizontally because of the mis-firing.

Fig. 4.3 gives an example of the bunches distribution on the front face of the primary TCP.C6L7.B1 collimator. It is supposed to be hit up to $10\sigma_x$ (as already mentioned in Section 3.2.2.2, above $10\sigma_x$ local protections intercept all beam). A Gaussian distribution is assumed for each bunch. The protons, which are in the green area, are impacting the primary collimator jaw. The 11500 particles contained in each bunch are representative of the 1.15×10^{11} protons of a real LHC bunch.

Similar beam distributions are produced for the Phase II collimators TCSM.B4L7.B1 and TCSM.6R7.B1, taking into account the different value of the Twiss parameters at their locations.

4.2.2 The SixTrack code

Collimation and beam cleaning studies are carried out with the SixTrack code [40]. It track particles which are transported through the lattice, element by element, and their phase space coordinates are transformed according to the type of beam line device met. When a particle hits a collimator jaw, it potentially could interact with the material and it is randomly scattered through matter. The effect of collimator scattering is modeled using the COLLTRACK/K2 [41] [14] routines, now embedded in the last version of the SixTrack code. This improvement makes possible to track a large number of particles over hundreds of turns (typically 5×10^6 halo particles which are followed for 200 turns), to include the proton scattering in various collimator materials, to simulate various halo and diffusion models and to take care of multiple imperfections of the beam and the collimator properties (setting errors, tilts, orbit errors, beta beat, etc.).

MAD-X produces "ready to use" input file for SixTrack, in which is defined the lattice of the machine without magnetic field errors. An input file called *Collimation database* contains the details of collimator geometry, materials and settings (i.e. aperture of the collimators). The introduction of the optic parameter β in this file allows studies of error scenarios. Tracking parameters like number of particles per turns, type of beam and type of halo are specified in another SixTrack input file. In particular, for Phase II collimation studies, the halo considered is a flat distribution in a selected plane, horizontal, vertical or transverse (for the skew case), plus a Gaussian distribution cut at 3σ in the other planes and a longitudinal component defined through a rms bunch length (nominally 7.55 cm at 7 TeV) and a rms energy spread ($1.13 \times 10^{-4} \Delta E/E$ at 7 TeV). The real distribution of losses is an average of the above three halo limit cases in the three planes.

Outputs of the SixTrack code are the trajectories of lost particles along the whole accelerator. After the tracking process, an aperture analysis program allows to find the location where a given recorded trajectory intercepts the LHC aperture within a specified resolution.

The positions and directions of primary protons which experience inelastic interactions in the collimator jaws are stored in a file used as input for FLUKA studies. Fig. 4.4 shows the space coordinates of these input FLUKA data along a collimator in case of 7 TeV horizontal distribution. The FLUKA input file is produced for ideal as well as imperfect machine operation by the team in charge of LHC collimation tracking simulations.

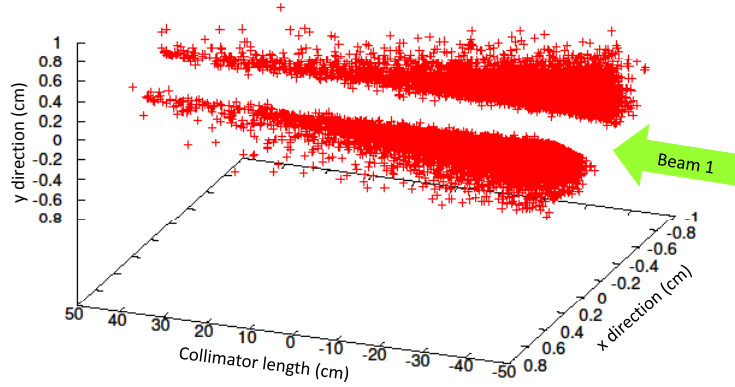


Figure 4.4: Space distribution of Beam 1 losses for a perfect LHC machine at the first Phase II collimator location (TCSM.A6L7.B1) with Copper jaws for the 7 TeV horizontal scenario.

4.2.2.1 The Loss Maps

Precise maps of losses location along the whole LHC ring are produced by the SixTrack code, applying the local cleaning inefficiency \tilde{n}_c definition (see Equation 3.3). By counting the number of particles (N_{lost}) within each 10 cm (Δs) and the total number of particles absorbed in the collimation system (N_{abs}) is possible to visualize where the critical regions are, that is the location s of possible quenches. Fig. 4.5 shows one of these loss maps all along the ring for a low beta scenario in case of perfect LHC machine. Losses in SC magnets (blue line) must be below the

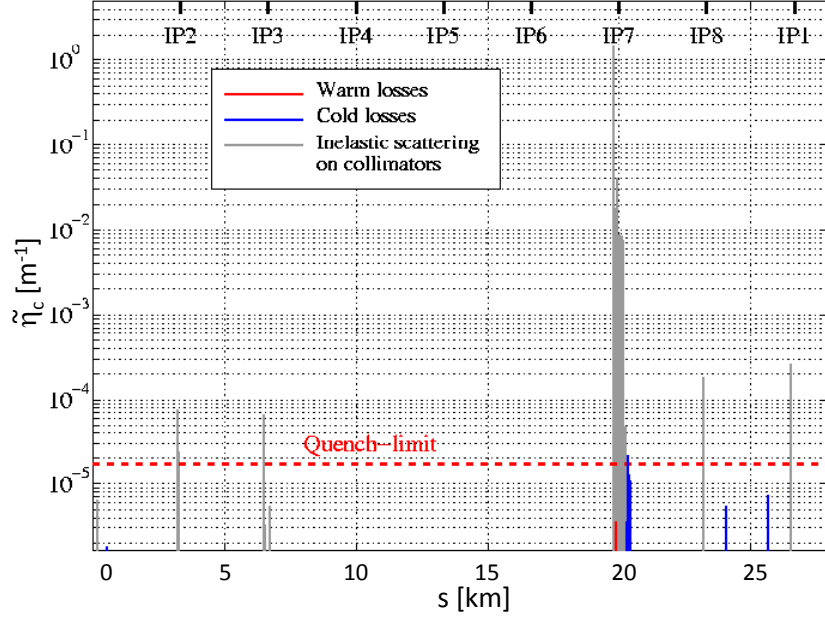


Figure 4.5: LHC perfect machine loss map at low beta energy, including the Copper jaws Phase II collimators and without cryo-collimators.

quench limit.

The loss maps show the foreseen losses in the LHC bottleneck regions where following investigation with FLUKA is required. Loss maps are produced both for perfect and imperfect LHC machine.

4.2.3 The FLUKA code

Designing and operating accelerator devices require the application of a particle transport and interaction Monte Carlo code, like FLUKA [43], [44].

In particular, FLUKA was used to support the Phase II collimator studies, starting from the maps of primary non-elastic collisions. The cascade starts by forcing the FLUKA code to simulate an inelastic nuclear interaction of a proton inside the collimator jaw at the position given by the tracking program. The FLUKA code samples randomly one proton with its space and direction coordinates from the provided loss list, and initiates the hadronic shower. Generally about 10000 primary particles per 10 following runs and per 10 parallel jobs are required to reach the statistical FLUKA convergence for the evaluation of the peak power in the first IR7 Phase II collimators for the adopted biasing settings. It corresponds to 6 days of

CPU time.

The high energetic LHC protons produce secondary particles with a large spectra of energies. Their effects vary from the heating of collimator components (mainly due to the electromagnetic shower), to the perturbation of electronics and the displacement damage. FLUKA allows to load magnetic field maps in the different beam line element, so assuring accurate tracking also outside the aperture.

Different outputs are produced by FLUKA, to answer at different questions about the Phase II collimators. The FLUKA results are per primary particle or, in other world, per lost interacting proton. The main outcomes are listed below.

4.2.3.1 Energy deposition output

FLUKA simulates the proton interaction and the resulting cascade in a material where energy deposited density is scored. Power deposition 3D distributions and integrated power values are typical outcomes.

- *Power deposition 3D distributions.*

These maps visualize the hotspots due by the particle shower interaction with the materials. They give important indications such as the peaks of energy density and its localization as well as how the thermal load is distributed in

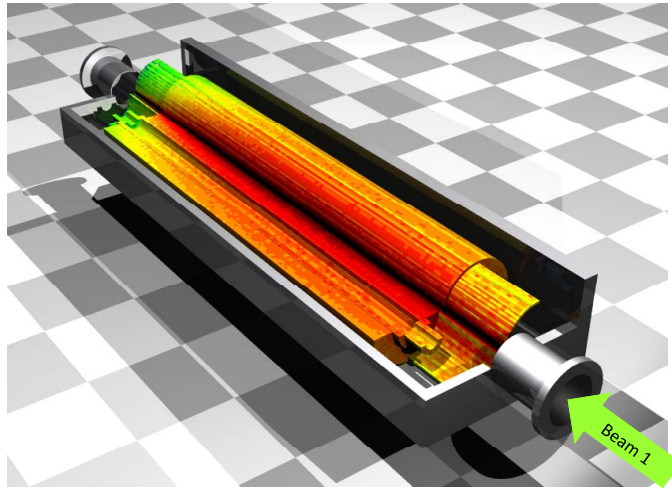


Figure 4.6: Example of a 3D power deposition map for the SLAC design with Copper cylindrical jaws. The scale is in Wcm^{-3} . Red spots are of the order of $10 Wcm^{-3}$. Close to the beam passage, brown spots on the jaws are of the order of $100 Wcm^{-3}$.

the device under study. Fig. 4.6 shows an example of these maps applying to a specific Phase II collimator design.

- *Integrated power values.*

Integral values of power deposition are calculated in order to be better compared with the available cooling capacity. In particular, since the collimators have an active cooling system, rating the total power to be removed is a basic requirement for their design.

4.2.3.2 Radiation damage output

Any device operating in strong radiation fields such as those expected in the LHC tunnel will undergo degradation due by radiation damage effects.

The FLUKA simulations allow to evaluate the impact of cumulative effects, like the total dose in the materials and the damages due by dislocation of atoms in the material structure.

- *Prompt Dose.*

The Prompt Dose is the dose released during irradiation. Long time irradiation at high intensity induces, over an operation given time, high dose values in the material through the shower propagate. This represents a concern for delicate components which could experience breaks.

- *Displacement Per Atoms (DPA).*

Long term employment of collimators will unavoidably result in structural change in the materials due to the displacement of atoms from their normal position. The produced lattice defects can manifest themselves as dimensional changes (jaw surface quality) and change in electrical resistivity. In particular, the latter is responsible for the collimator induced impedance that can modify in turn the LHC peak performance.

The lattice defects are evaluated in terms of DPA produced through elastic and inelastic scattering reactions, in which projectile protons or secondary particles and nuclear fragments impart some of their kinetic energy to a nucleus of the material under examination. The DPA is a function of the number of incident per secondary particles rather than the total energy. This can justify the employment of Monte Carlo algorithms tested on the data collected in high energy proton beams for evaluating number of displacement produced in the LHC proton beam if particle production and transport algorithms at the LHC energies can be considered as reliable. The FLUKA code is used to calculate the number of DPA which are used as reference to the evaluation of changes of material proprieties, important for the functionality of a specific device.

4.2.3.3 Activation and Residual Dose Rates

Nuclear reactions induced by beam particle losses lead to the activation of materials in the respective zone of the LHC. FLUKA is able to estimate the activity levels as a function of the cooling time after the irradiation end. This is possible thanks to the calculation of the produced radionuclide yields and of time evolution of their population.

Residual dose rates are due to the activated equipments. Three-dimensional maps of dose equivalent rates at different cooling times after operation of the LHC have been also calculated with FLUKA through the transport of the decay electromagnetic radiation.

An extended benchmark of the FLUKA prediction has been performed against experimental data acquired through a dedicated CERN beam test facility called CERF [45].

4.2.4 The FEM analysis

The thermo-mechanical analysis [29] provides informations about the possible permanent deformations and their shapes because of fast increase of temperature, in particular during the abnormal beam scenario.

The energy distribution on the 3D ANSYS model of the whole jaw assembly is provided by the FLUKA simulations on a 3D compatible model.

The size of the jaw deformations gives an estimate of the active length reduction of the collimators during operation (i.e. the so-called banana shape). Avoiding jaw deformations means to increase the LHC performance.

Chapter 5

An overview of the FLUKA physics models

The FLUKA code is a general purpose Monte Carlo code for the interaction and the transport of hadrons, heavy ions, and electromagnetic particles from few keV (or thermal energies for neutrons) to cosmic ray energies in whichever material. It is built and maintained with the aim of including the best possible physical models in terms of completeness and precision and it is continuously upgraded and benchmarked against experimental data.

At CERN, the FLUKA code is extensively used by different projects such as LHC, CNGS, LINAC-4 and n_TOF. In particular, FLUKA is the main tool to carry out beam-material interaction studies, e.g. for machine protection purposes.

5.1 Proton-matter interaction: main framework

When a proton hits a material block, all or part of its energy is dissipated through different processes. It could interact with a nucleus and produce many secondary particles, which later also interact, and so on, until the residual energy per particle is too small that is negligible for our studies. The result of this process is called hadronic shower. It is combined to electromagnetic showers through the decay of short-lived products, typically neutral pions decaying into two photons. Or the proton, such as any other charged particle, could ionise atoms along its path. Electrons are set free and release their kinetic energy to the lattice, or are excited and emit photons in the atomic range of energy, which are absorbed and converted to phonons locally. Finally almost all the deposited energy is converted to heat.

The spatial distribution of heat deposition cannot be computed analytically with a good accuracy, but is calculated thanks to Monte Carlo programs, like FLUKA.

5.2 The FLUKA code: main features

FLUKA is based, as far as possible, on original and well tested microscopic models. Consistency among all the reaction steps and/or reaction types is ensured, conservation laws are enforced at each step and results, when possible, are checked against experimental data at single interaction level. Outcomes are obtained with a minimal set of free parameters, fixed for all energies and target/projectile combinations. Predictions are provided where no experimental data are directly available, like for the LHC 7 TeV scenario, and correlations within interactions and among shower components are preserved.

All events or "histories" are initiated by primary particles, which are monoenergetic 7 TeV protons in the specific case of this PhD studies.

Fig. 5.1 shows the traces produced by a 6 GeV proton in liquid argon. Different kinds of processes are visible: hadron-nucleus interaction (hA interaction), electron-magnetic showers (E-M showers), decay of unstable nuclei, multiple scatterings, ionization (dE/dx and δ) and low energy neutron interactions.

All these processes are taken into account in the FLUKA simulations performed for the Phase II collimators.

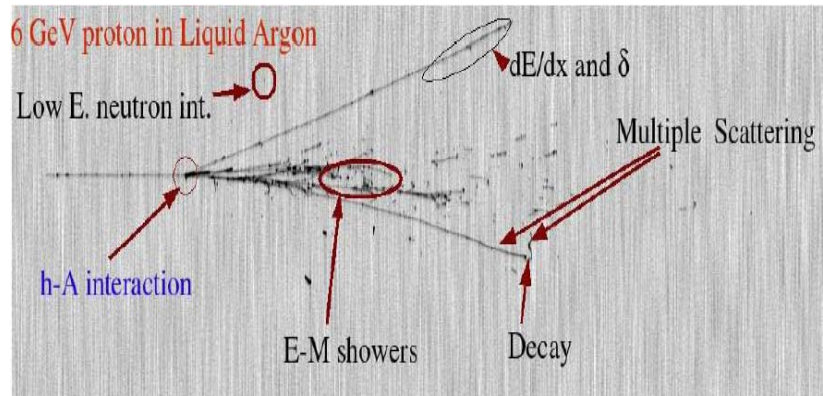


Figure 5.1: Traces of a 6 GeV proton in liquid argon. Different physical processes taking place are indicated. Through its embedded models, the FLUKA code is able to accurately simulate each of them.

5.2.1 Hadron-Nucleus and hadron-nucleon interactions

Hadron-Nucleus (hN or hA) non-elastic interactions are described mostly in the framework of the IntraNuclear Cascade (INC) model. This model was developed at the very beginning of the history of the energetic nuclear interaction modelling (the original ideas go back at the end of the fourties). The model is intrinsically a Monte Carlo one, well suited for numerical applications. In the energy range going from the pion π production threshold (about 290 MeV for a free nucleon, down to 200 MeV for nucleons in nuclei because of the Fermi motion) to high energies, INC models are practically the only available tools to model hN interactions. At lower energies, a variety of pre-equilibrium models can do a good job. However, INC models, like those developed in the seventies, become unreliable both at lower ($< 100\text{--}200\text{ MeV}$) and higher ($> 2\text{--}3\text{ GeV}$) ends of the energy scale, and show limitations also when used in the proper energy range. The basic assumption in calculations of INC is that nuclear reaction involving incident particles of high energy can be described in terms of hadron-nucleon (hn) collisions within the nucleus. Once suitable models for describing hn interactions were available, the high energy regime was properly handled, provided the spacetime characteristics of high energy interactions and multiple primary collisions, according to the Glauber approach, were taken into account. Important changes to the original INC approach were done also at the lowest energies. They are mainly related with quantum nuclear effects and multibody interactions, besides the introduction of a pre-equilibrium stage. The latter is a transition between the first step of the reaction and the final thermalization at energies lower than the π production threshold. INC approaches which make use both of the high energy and low energy extensions are called Generalized IntraNuclear Cascade (GINC) models.

The FLUKA hn interaction models are based on resonance production and decay below few GeV (i.e. isobar model) and on Dual Parton model (DPM) based on interacting strings above.

Two models are also used for the hN interactions. Up to $3\text{--}5\text{ GeV}$ the FLUKA PEANUT (Pre-Equilibrium Approach to NUClear Thermalization) package includes a very detailed GINC, based on "resonance" production and decay with smooth transition to a pre-equilibrium stage performed with standard assumptions on exciton number or excitation energy. At high energies the Gribov-Glauber multiple collision mechanism applies (also included in the FLUKA PEANUT). It is based on quark/parton string models, which provide reliable results up to several tens of TeV .

In addition, to extend the higher FLUKA energy limit for hadronic interactions, the DPMJET-III package is implemented in the code. DPMJET-III is also used as event generator for nucleus-nucleus (AA) interactions above $5\text{ GeV}/c$, whereas a Relativistic Molecular Dynamics (RQMD) approach and a model based on the Boltzmann Master Equation (BME) theory apply to AA reactions at intermediate (down to $100\text{ MeV}/c$) and low (down to the Coulomb barrier) energies, respectively.

Fig. 5.2 shows the proton-proton and proton-neutron cross sections and the dis-

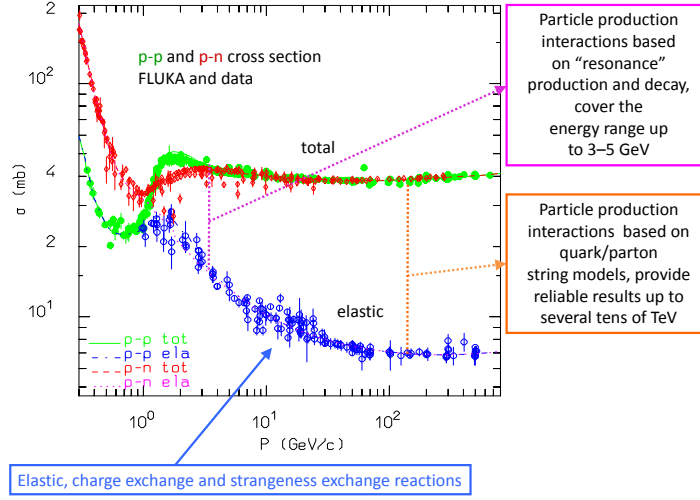


Figure 5.2: FLUKA total and elastic cross sections for p-p and p-n scattering, together with experimental data.

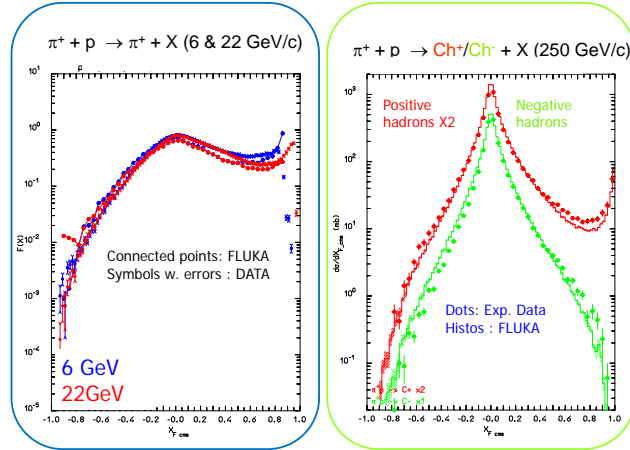


Figure 5.3: Examples of particle production from inelastic interaction at different energies. Left side: Feynman x_F distribution of positive pions emitted for π^+ on proton at various momenta (6 and 22 GeV/c). Data from [46] and FLUKA results. Right side: the longitudinal distribution of positive and negative hadrons produced by 250 GeV/c π^+ on Hydrogen. Data from [47] and FLUKA results.

tribution of elastic and charge/strangeness exchange (data and FLUKA predictions). Below the π production threshold, the only possible interaction between two nucleons is just elastic scattering. The neutron-proton (n-p) and proton-proton (p-p) cross sections are different by about a factor 3 at the lowest energies, as expected on the basis of symmetry and isospin considerations, while at high energies they tend to be equal. The difference between the two lines (total and elastic) gives the cross section of inelastic interactions responsible for secondary particle production.

The examples in Fig. 5.3 shows the ability of the FLUKA models to reproduce the features of particle production at different energies.

As soon as the energy of a primary hadron exceeds few tens of MeV , inelastic interactions start to play a major role and secondaries have enough energy to trigger further interactions, giving rise to a hadronic shower. Whenever the beam energy is such that pion production plays a major role, a fraction of the energy is transferred from the hadronic to the electro-magnetic (E-M) sector due to production of mesons (mainly π^0 and η) which quickly decay into E-M particles (e^+ , e^- and γ).

Hadron and electro-magnetic showers are very complex phenomena. There are two basic differences between hadronic and E-M showers. The first is that, while energetic hadronic showers are always giving rise to significant E-M ones and such E-M component is more and more important with increasing primary energy, E-M showers develop independently without further hadronic particle production, neglecting the (small) probability of electro and photonuclear interactions. The second difference is that, while E-M interactions are in principle well understood and described by the Quantum ElectroDynamics (QED) theory, the same does not apply to hadronic nuclear interactions, where such a complete theory does not exist.

The development of hadron initiated showers is determined both by atomic process (dE/dx , multiple Coulomb scattering, etc.), which take place very frequently, and by the relatively rare nuclear interactions (both elastic and inelastic). E-M showers are determined by the same atomic processes (dE/dx , multiple Coulomb scattering, etc.), plus other atomic processes (bremsstrahlung, pair production, Compton scattering, etc.), which are specific of e^+ , e^- and photons, while nuclear interactions play a minor role and usually can be safely neglected.

5.2.2 E-M showers

When high-energy electrons interact with matter, only a small fraction of the energy is dissipated as a result of collision processes. A large fraction is spent in the production of high-energy photons (bremsstrahlung). These photons produce further electrons through pair production or Compton collisions. These new electrons radiate more photons, which in turn interact to produce more electrons.

At each new step, the number of particles increases, and the average energy decreases. This process continues until the electrons fall into the energy range where radiation losses no longer compete with collision losses and then dissipate their energy by ionization and excitation of the target atoms resulting in heat production

rather than by generation of more shower particles. This entire process results in a cascade of photons, electrons, and positrons called an electromagnetic shower. Fig. 5.4 illustrates the various processes that take place within an electromagnetic shower.

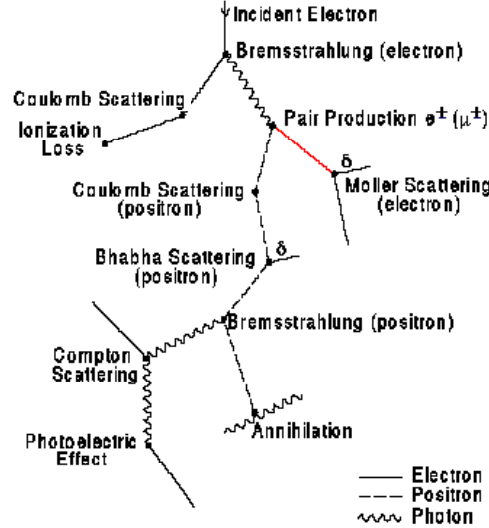


Figure 5.4: A schematic view of an electromagnetic shower caused by an electron hitting a target.

A shower is produced when the primary beam energy is much greater than the *critical energy*. The latter is the electron energy at which the average energy loss due to radiation equals that due to ionization.

The distance needed to reduce, by radiation, the average electron's energy to $1/e$ of its original value is called *radiation length*, X_0 . X_0 is also defined as $7/9$ of the mean free path for pair production by a high-energy photon. The longitudinal development is governed by the high-energy part of the cascade, and therefore scales as the X_0 in the material. The radiation length is a measure of the penetration of the electro-magnetic shower into the material. Its main dependencies are on the atomic number Z and the density ρ of the material.

The transverse development of electromagnetic showers in different material scales fairly accurately with the *Molière radius* (R_M).

The simulation of the electromagnetic cascade in FLUKA is very accurate, including the Landau-Pomeranchuk-Migdal effect and a special treatment of the tip of the bremsstrahlung spectrum. The electromagnetic part of FLUKA allows a reliable physics in the range from 1 keV up to 1000 TeV , including a precise database of photonuclear cross sections.

Pair production and bremsstrahlung are treated sampling from the proper double differential energy-angular distributions improving the common practice of using average angles. In a similar way the three-dimensional shape of the electromagnetic cascades is reproduced in detail by a rigorous sampling of correlated energy and angles in decay, scattering and multiple Coulomb scattering.

5.2.3 Multiple Scattering

A charged particle traversing a medium is deflected by many angle scatters.

Most of these deflections is due to Coulomb scattering from nuclei. The particle experience numerous small deviations, the distribution of which is well represented by the theory of Molière [48]. It is roughly Gaussian for small deflection angles, while at larger angles it behaves like Rutherford scattering, with larger tails than does a Gaussian distribution.

However, the Gaussian is sufficient for many application for the central 98 % of the projected angular distribution, with a width given by:

$$\Theta_0(x) = \frac{13.6 \text{ MeV}}{\beta c p} z \sqrt{\frac{x}{X_0}} [1 + 0.038 \ln(\frac{x}{X_0})] \quad (5.1)$$

where p , βc and z are the momentum, velocity and charge number of the incident particle and X_0 the radiation length of the target.

Transport of charged particles is performed in FLUKA through an original Multiple Coulomb scattering algorithm, supplemented by an optional single scattering method.

Multiple scattering with inclusion of nuclear form factors is applied also to heavy ion transport.

5.2.4 Energy loss by particle in matter

Moderately relativistic protons, and in general charged particles other than electrons, lose their energy primarily by ionization and excitation of the atoms of the material they pass through. The average rate of energy loss, the so-called *stopping power*, is given by the Bethe-Bloch equation [49]:

$$-\frac{dE}{dx} = K z^2 \frac{Z}{A} \frac{1}{\beta^2} \left[\frac{1}{2} \ln \frac{2 m_e c^2 \beta^2 \gamma^2 T_{max}}{I^2} - \beta^2 - \frac{\delta}{2} \right] \quad (5.2)$$

Where K is a constant, Z and A are atomic number and atomic mass of the target material, z , β and γ are charge and relativistic factors of the incident particle, and m_e is the electron mass. I is the ionization potential, T_{max} the maximum kinetic energy that an electron can gain in one single collision and δ is a correction factor depending on the density of the target.

The stopping power for muons on copper, considering all the different regimes, is shown by the solid curve in Fig. 5.5. At higher energies, radiative effects begin to be important.

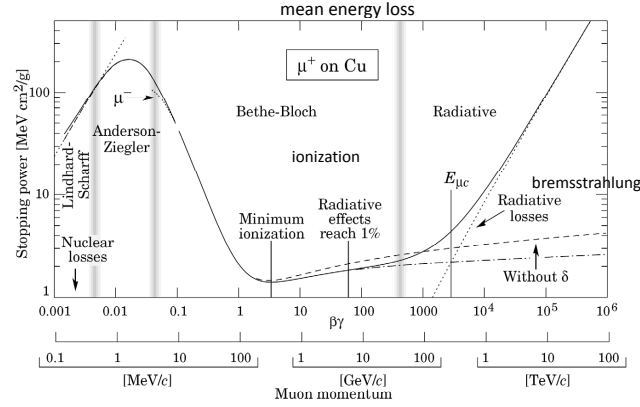


Figure 5.5: Stopping power for positive muons in Copper. Vertical bands indicate boundaries between different regimes.

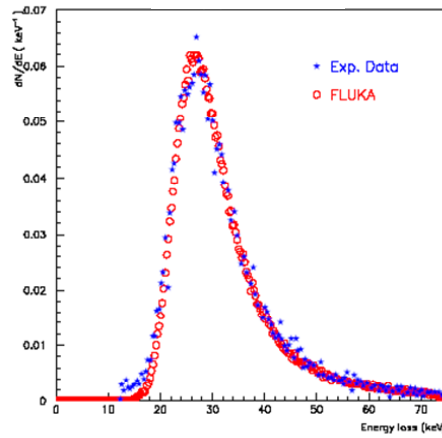


Figure 5.6: Ionization fluctuation for $2\text{ GeV}/c$ protons after a $100\text{ }\mu\text{m}$ Si layer. FLUKA and experimental data from [50].

The treatment of ionization energy loss in FLUKA is based on a stochastic approach alternative to the standard Landau and Vavilov ones that provides a very good reproduction of average ionization and fluctuations. Fig. 5.6 shows the good agreement between FLUKA and experimental data for $2\text{ GeV}/c$ protons traversing a $100\text{ }\mu\text{m}$ thick Silicon target.

5.2.5 Residual nuclei production and Decay

At the end of the reaction chain, the nucleus is a thermally equilibrated system characterized by its excitation energy U . If U is higher than the separation energy, nucleons and light fragments can still be emitted. The emission process can be well described as an evaporation from a hot system. The evaporation stage ends when the nuclear excitation energy becomes lower than all separation energies for nucleons and fragments. This residual excitation energy is then dissipated through emission of photons. In reality, γ emission occurs even during the pre-equilibrium and evaporation stages, in competition with particle emission, but its relative probability is low. Gamma deexcitation proceeds through a cascade of consecutive photon emissions, until the ground state is reached.

The evaporation process is in competition with another equilibrium process, that is fission. A fraction of the excitation energy may be spent to induce a collective deformation. The potential energy reaches a maximum at the deformation stage that is called *saddle point*. Once a nucleus reaches the saddle points, the fission occurs, and the nucleus separates, most of the times into two heavy fragment.

All these equilibrium processes are critical for a correct calculation of residual nuclei distributions. They represent the last stage of a nuclear interaction and are responsible for the exact nature of the residuals left after the interaction, which play the main role in activation and residual dose rate studies.

The FLUKA evaporation model is based on the Weisskopf-Ewing approach. For light residual nuclei, where the excitation energy may overwhelm the total binding energy, a statistical fragmentation (Fermi break-up) model is implemented in the code. The FLUKA evaporation/fission/break-up routines are used for the final deexcitation and "low" (in the excited residual rest frame) energy particle production.

Fig. 5.7 shows the experimental data and FLUKA prediction of the residual nuclei production in $1\text{ GeV }^{208}\text{Pb} + \text{p}$ reaction. Residual mass distributions are very well reproduced by FLUKA.

The time evolution of activation and residual dose rates, as given by FLUKA, has been extensively benchmarked. Samples of different materials have been irradiated in a CERN facility called CERF. Comparison (of dose rate curves) with FLUKA simulations show a very nice agreement (see Fig. 5.8).

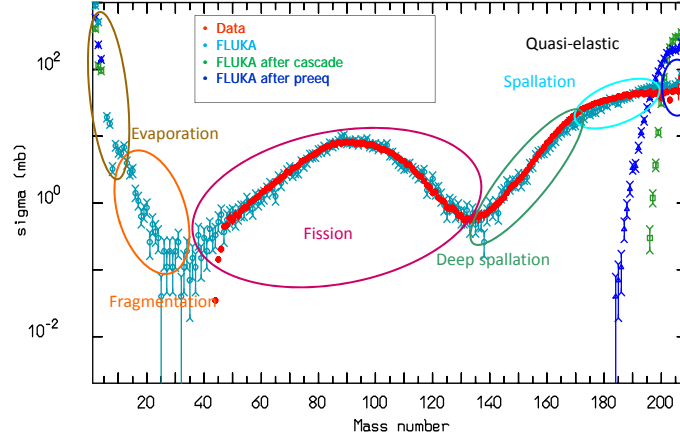


Figure 5.7: Residual nuclei production from $1\text{ GeV } ^{208}\text{Pb} + p$ reaction. Data from [51]. The green dots are the the FLUKA prediction before of pre-equilibrium and the evaporation/fission processes, while the blue dots are the FLUKA prediction before only the evaporation/fission processes.

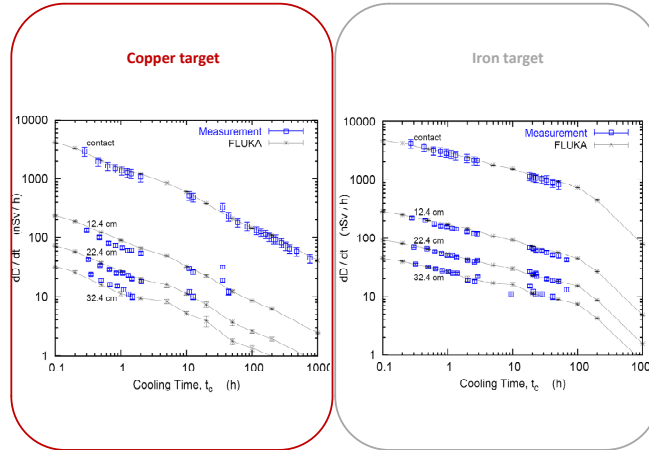


Figure 5.8: Dose rate benchmark [45]. Dose rate as a function of cooling time at different distances between copper (left side) and iron (right side) samples and detector.

5.2.6 Transport of neutrons

Above 20 MeV the neutrons are transported in FLUKA as any other particles, using the PEANUT and DPNJET-III packages.

Otherwise, transport of neutrons with energies lower than 20 MeV is performed in FLUKA by a multi-group algorithm, because of uncertainties on cross sections, particularly in the resonance region. The multi-group technique, widely used in low-energy neutron transport programs, consists in dividing the energy range of interest in a given number of intervals, called *energy groups*. In the FLUKA cross section library, the energy range is divided into 260 energy groups of approximately equal logarithmic width (31 of which are thermal).

Gamma generation by low energy neutrons (but not gamma transport) is treated in the frame of a multigroup scheme too. A downscattering matrix provides the probability, for a neutron in a given energy group, to generate a photon in each of 42 gamma energy groups, covering the range 1 keV to 50 MeV . In all cases, the generated gammas are transported in the same way as all other photons in FLUKA.

5.2.7 Variance reduction techniques

FLUKA makes available several biasing options. They are used in many applications to improve the simulation efficiency FLUKA, converging faster to the correct expectation values by reducing the variance or the CPU time, or both. The central idea of the biasing is to assign a weight to the particles, in order to compensate the particle fluence attenuation in regions far away from the shower development.

In particular for these PhD studies, it was used the region-importance biasing which is based on two complementary techniques: Surface Splitting and Russian Roulette (RR). The number of particles at the boundary from a region to another will increase by splitting or decrease via RR according to the ratio of region importances and the particle statistical weight will be modified inversely so that the total weight will remain unchanged.

In addition the weight window option was used, in order to prevent fluctuations due to rare particles with very large weight and time wasting due to transport of particles with very low weight (or unable to affect results). It is based on the absolute value of particle weight. It is set an upper and a lower limit for the particle weight in each region, tuned per particle type and energy. Splitting and RR will be applied so that the weight of all relevant particles will have a value between the two limits.

Chapter 6

Simulations of the IR7 region

The dump caverns, the inner triplets, the experiments and the cleaning insertions, where the Phase II collimators are foreseen to be installed, are the LHC regions for which the highest loss densities are expected. In particular, the loss rate at the Betatron Cleaning region is higher by about a factor of 7 when compared to that at the Momentum Cleaning one. The focus is thus put on the simulation of the IR7 insertion which is the most critical region of LHC.

The SS and the DSs of IR7 are fully implemented in FLUKA up to a high degree of sophistication, including all relevant components and details up to a realistic limit. A modular approach in the geometry definition and an extensive use of user-written programs allowed the detailed implementation of all magnets, collimators and absorbers, including the beam instrumentation, the beam pipeline, the interconnections between SC magnets, the cables on each side of the LHC tunnel, steel supports, and naturally the tunnel with its service caverns and bypasses.

6.1 The FLUKA Combinatorial Geometry

The Combinatorial Geometry (CG) used by FLUKA is based on the original one by MAGI (Mathematical Application Group, Inc.) [52] [53]. Two concepts are fundamental in CG: bodies and regions. In FLUKA the bodies are defined as finite portion of space completely delimited by surfaces of first or second degree. Moreover, infinite planes and cylinders are also available. The regions are combinations of bodies through boolean operations. Each region is not necessary simply connected (it can be made of two or more non contiguous parts), but must be of homogeneous material composition. All the regions must be contained within a surrounding *blackhole* so that all escaping particles are there absorbed.

6.2 The FLUKA modular approach used for IR7

The IR7 description in FLUKA consists of a 1.5 *km* long LHC tunnel section composed of the SS, the dispersion suppressor region and a part of the LHC arc on the right side of the IP7. It includes more than 220 elements of about 30 different types, such as SC bending magnets, SC quadrupoles, warm magnets, orbit correctors, beam loss monitors, primary and secondary collimators, passive and active absorbers. Each LHC magnet model has an associated magnetic field map.

Most of these elements appear several times in the IR7 layout. Sometimes all elements of the same type are completely identical (e.g. the MB) although commonly they show some differences, like the orientation (e.g. the collimators), material (e.g. active absorbers and Phase I secondary collimators) and beam pipes (e.g. MBW). For this reason, it was decided to place all prototypes (i.e. each model representative of all elements similar in IR7) in a *parking* area near the simulated geometry and replicate them along the tunnel via the *Lattice* option of FLUKA. The cloning is performed by allocating a bounding body in the input file for the replicated item and defining the transformation to superimpose it on the prototype [54].

Whenever a particle enters a replica in the tunnel, it is virtually transported to the prototype in the parking. The change of reference system, including translation, rotation and reflection, is defined by the user in a routine (i.e. *lattice.f*). As soon as the particle escapes from the prototype, it is transported back to the replica boundary in the tunnel. It is obviously possible to distinguish at scoring between events occurring in two different replicas of the same prototype.

It has to be pointed out that all replicas of the same prototype share the same properties. In the special case of both Phase I and Phase II collimators, a dedicated prototype is not created for each jaw gap, but their aperture, which follows the actual value of the β function, is adapted runtime through the same *lattice.f* routine.

6.3 The IR7 FLUKA prototypes

The layout of the IR7 geometry is in continuous development by the members of the FLUKA team, following the needs of new investigations with the addition of prototypes where necessary. For example, in consequence of the LHC accident in Sector 3-4, the possibility of a simultaneous magnet and busbar quench was investigated thanks to the addition of the interconnection and busbar models in the DS region of IR7. Or following the radiation induced electronic equipment failure in the CNGS experiment, a campaign of simulations has been built up to investigate if the same could happen at the electronic devices installed in the IR7 tunnel or in its service caverns, and to add protecting shieldings or plan relocation (see Chapter 13).

The main IR7 prototypes are described in detail below.

6.3.1 The IR7 magnet models

The DS segment extends from the SC quadrupole Q8 to Q11 (Q is a generic SC quadrupole identification in the optics files) on each side of the IP7. In addition to the DS, the first LHC arc cells 12 and 13 are also included in the FLUKA IR7 description, since they are used for the matching procedure between the DS and the LHC arc. The DS cold quadrupoles Q8, Q9 and Q10 (plus the Q7 in the SS) are made of an assembly including a main quadrupole MQ plus a long tuning quadrupole MQTL (MQ+2MQTLs for Q9). In between the DS quadrupole assemblies, 2 SC main bending magnets (MB) are installed, while for the arc cell 3 MBs are placed in between the quadrupoles. Orbit correctors (MCB), sextupoles (MCS), octupole and decapoles (MCDO) correctors are also implemented in the FLUKA geometry.

The straight section of the Betatron Cleaning insertion is mirror symmetric with respect to the IP7. It includes mainly resistive magnets, to avoid quenches and high heat loads on cryogenics. Starting from Q7 left, the quadrupole Q6, made of 6 SC MQTL modules, is followed by a dog-leg structure made of two sets of MBW warm single bore wide aperture dipole magnets (2 warm modules each) which increase the inter-beam distance from 19.4 cm to 22.4 cm . Two further MBW pairs after 340 m restore the nominal distance. Four quadrupole (MQW) sets are installed in the SS. Each MQW set is in turn composed of 5 MQWA and 1 MQWB modules. Horizontal and vertical correctors (the MCBW dipoles) complete the total budget of the 114 magnets included in the IR7 FLUKA description.

6.3.1.1 The warm magnet models

A total of 40 warm magnets of 3 different design families: MBW, MQW and MCBW, are implemented in the FLUKA geometry of the IR7 SS.

- *Warm dipole magnets.*

A MBW is a warm dipole and it is often referred as a *dogleg bending magnet*. The MBW are 3.8 m long, 1.08 m wide and 0.74 m high. Their magnetic length is 3.4 m (see Fig. 6.1). The dipole is perfectly symmetric in x and y .

The first and the last pairs are described by the same prototype in the parking region. The central axes of the vacuum chambers are at 19.4 cm distance from each other. The remaining pairs are described by another FLUKA prototype and associated to a different magnetic field map. The distance between the beams is in this case 22.4 cm .

The MCBWs are also warm dipole magnets but they are used as correctors and they act only on one beam. They can be vertical and horizontal, both having a magnetic length of 1.7 m . In the horizontal one the other beam pass through a passive aperture and outside the magnet in the vertical version. A total of 8 MCBW are installed in the straight section.

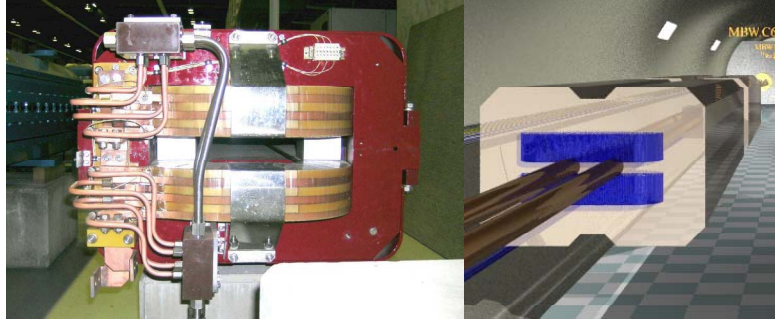


Figure 6.1: Real view (left) and FLUKA model (right) of a MBW warm magnet.

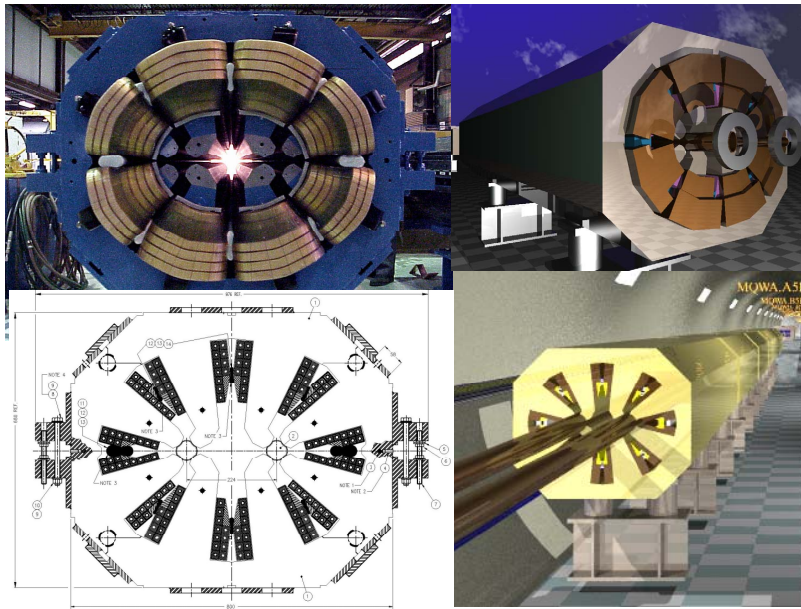


Figure 6.2: Real view, technical drawing (left) and FLUKA model (right) of a MQW warm magnet.

- *Warm quadrupole magnets.*

The MQW is a warm quadrupole with elliptical beam chambers (see Fig. 6.2).

There are two types of MQW: MQWA and MQWB, which have the same mechanical design but a different magnetic field. In addition, there are 2 classes of prototype, depending on the orientation (horizontal or vertical) of the vacuum chambers of the two beams.

All the MQWs have a magnetic length of 3.108 m . Their model is implemented in FLUKA, splitting the geometrical description in four quadrants.

6.3.1.2 The cold magnet models

The total number of the cold magnets implemented in the FLUKA IR7 model is 74 of 9 different prototype families.

- *Cold main dipole magnets.*

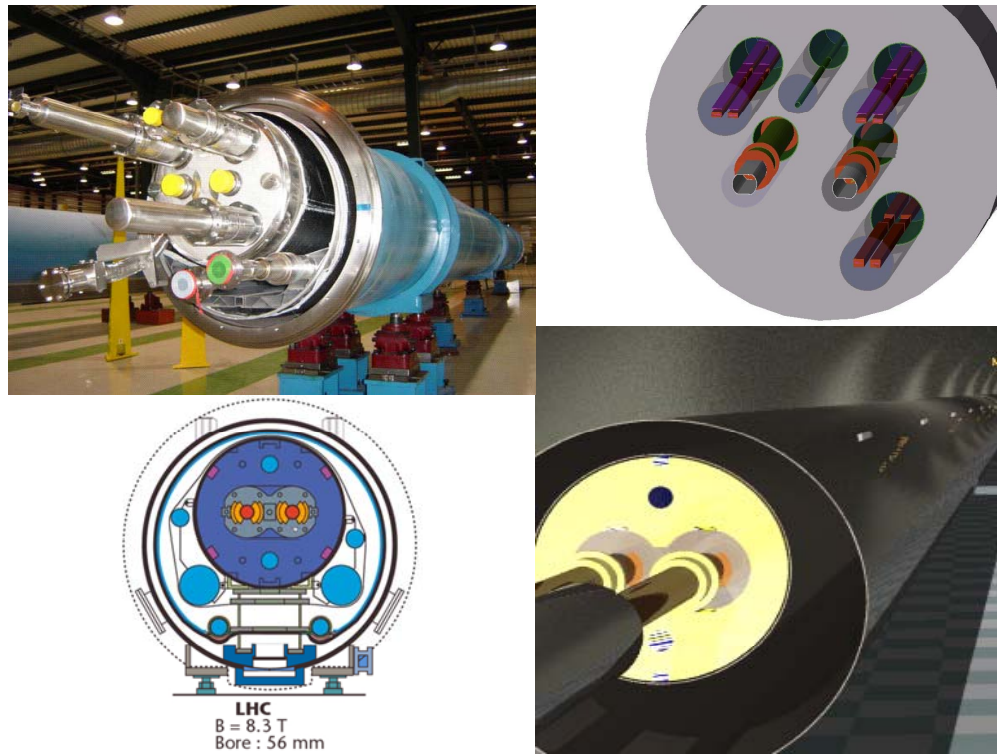


Figure 6.3: Real view, technical drawing (left) and FLUKA model (right) of a MB cold magnet. The FLUKA model of interconnections is also shown (left up).

The MB are 14.3 m long SC dipoles (see Fig. 6.3) with a magnetic field of about 8 T at top energy, each bending the beam by 5 mrad . Their sagitta is $9,14\text{ mm}$. The FLUKA MB prototype is modelled by splitting the beam lines into 4 tilted segments, in order to approximate the beam curvature.

- *Cold quadrupole magnets.*

The 3.1 m long MQs are the LHC main quadrupoles. There are 11 MQs implemented with all the details in the FLUKA IR7 description.

Upstream of each MQ in the LHC arc part considered in the FLUKA description, the 36.5 cm long tuning SC quadrupoles MQT is placed.

Additional 1.3 m long tuning quadrupoles MQTL (see Fig. 6.4) are present in the DS and SS regions. The MQTL magnets are SC quadrupoles grouped one next to the other sharing the same cryostat at each end of the SS. The MQTLs are also present in the DS and in the LHC arc part close to the MQs.

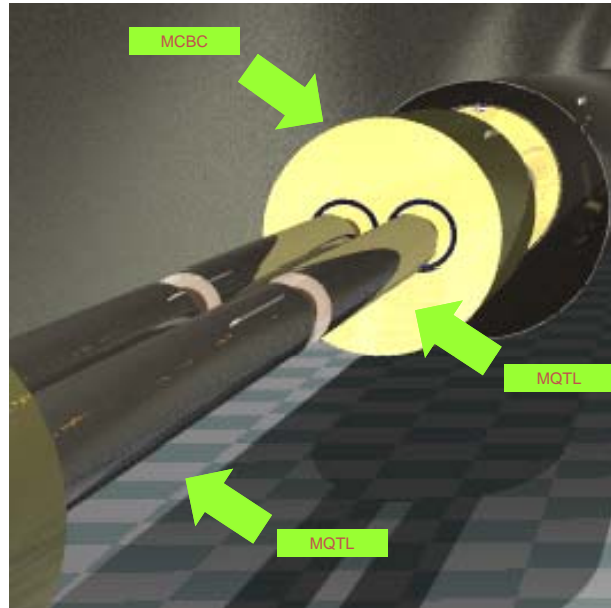


Figure 6.4: FLUKA model showing the MQTL cold magnets and a MCBC corrector.

- *Cold Correctors magnets.*

Different kinds of cold corrector magnets are described in the FLUKA IR7 geometry, for a total number of 40 devices.

Close to each of the MQTL magnets in the DS region, 90 cm long SC dipole orbit corrector magnets (MCBC) are installed. Vertical and horizontal 65 cm

long SC dipole correctors are also present in the first arc cells after the 36.9 cm long sextupole (MS) joined with the MQTL magnets. The MB magnets have a sextupoles (MCS) at one end and a nested decapole-octupole multipole (MCDO) correctors at the other end. These corrector magnets are also described in the FLUKA IR7 model.

6.3.1.3 The Magnetic fields

An accurate treatment of the magnetic field is essential in tracking particles along the machine, since it has a major impact on the interaction fluence distribution. In the FLUKA simulation, the nominal beam is kept into the right trajectory along the entire section, within a few micron accuracy.

Close to the beam axis the field is assumed to be analytical up to the quadrupole and only in the vacuum chambers (excluding the MB magnets because of their curvature), whereas farther away is calculated through a 2D interpolation from a pre-computed grid. Examples of magnetic field maps from ROXIE code [55] implemented in FLUKA are shown in Fig.6.5. The intensity or the gradient of each magnetic element pre-processing as well as the associated rotatraslation parameter are automatically assigned by the REXX script [56].

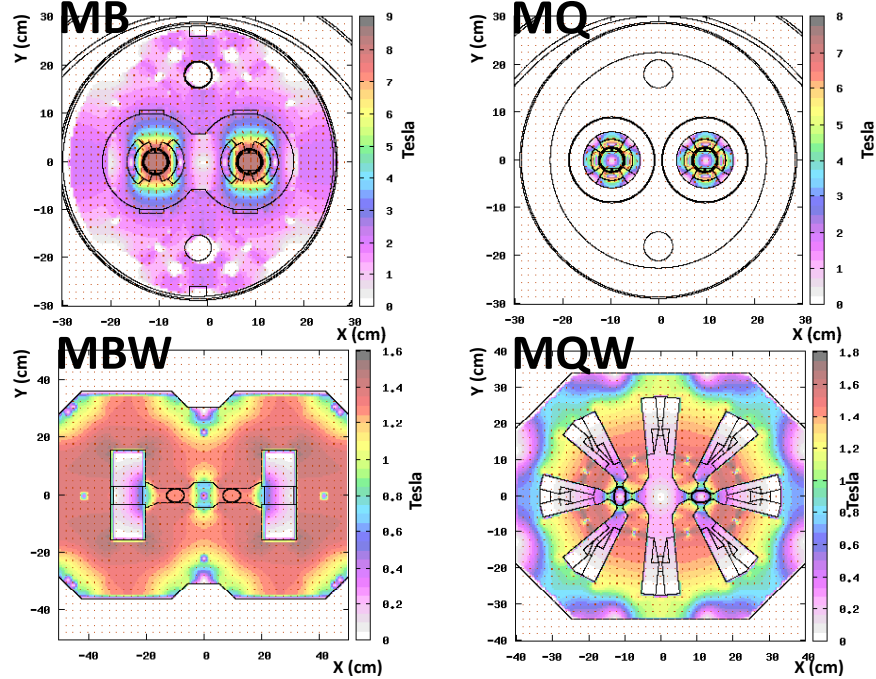


Figure 6.5: Transverse section of geometry and magnetic field for cold (MB, MQTL) and warm (MBW, MQW) magnet models as implemented in FLUKA.

6.3.2 The Phase I collimator models

Primary and secondary collimators as well as active absorbers are key elements in the halo cleaning system. To complete the Phase I collimators system models, the passive absorbers are also described below.

6.3.2.1 Phase I Primary collimator model

Three IR7 primary collimators (TCP) are located between the two dogleg warm bending magnet sets, on the left side of IP7 for Beam 1 and on the right side for Beam 2.

The TCP jaws are elongated blocks with conical tapering and about 12 *cm* superficial skimming, in order to leave an active length of 60 *cm*. The CFC jaws are sitting at 6σ from the beam axis for each TCP orientation. Moreover the tilt of the jaws follows the beam divergence at the location of the collimators. The first TCP is a vertical collimator, the second is horizontal and the third is a skew one (see Appendix B for more details). They are installed in cascade on each beam line.

The TCP jaws are contained in a steel tank, implemented in FLUKA with its entry and exit flanges for the connection with the beam pipeline.

Inside the tank the FLUKA TCP description includes two symmetric pieces composed by a jaw, a support plaque, 6 longitudinal cooling water pipes on top one of the other, a clamp support, a steel clamp, 5 *x*-transverse springs and RF fingers.

Two prototypes are implemented for the injection and the 7 *TeV* scenario respectively, because the jaw gap variation between these two configurations is significant. Taking the low beta aperture prototype, at injection the moving planes, used to cut the jaws in accordance with their actual gaps, would "eat" a good fraction of the jaw material, coming too deeply inside the jaw.

6.3.2.2 Phase I Secondary collimator model

The two FLUKA prototypes (for injection and 7 *TeV*) of the secondary collimators (TCSG) are almost identical to these of the primary ones, but in this case, they have 1 *m* long CFC jaws (and no shimmed layers because the active length is the full length). They are opened at 7σ from the beam orbit.

Eleven TCSGs for each beamline are implemented in the FLUKA LSS description with different orientations (see Appendix B for more details). The first of the secondary collimators is located 40 *m* downstream of the last primary.

6.3.2.3 Active absorber model

The two FLUKA active absorber (TCLA) descriptions are almost like the secondary ones, but the base material of the jaws is Copper instead of CFC and the jaws have 90 *cm* long and 3.4 *cm* wide Tungsten inserts. The jaws of the IR7 active absorbers are sitting at 10σ .

Fig. 6.6 shows the FLUKA cross plots of the TCP, the TCSG and TCLA, summarizing their similarities and differences.

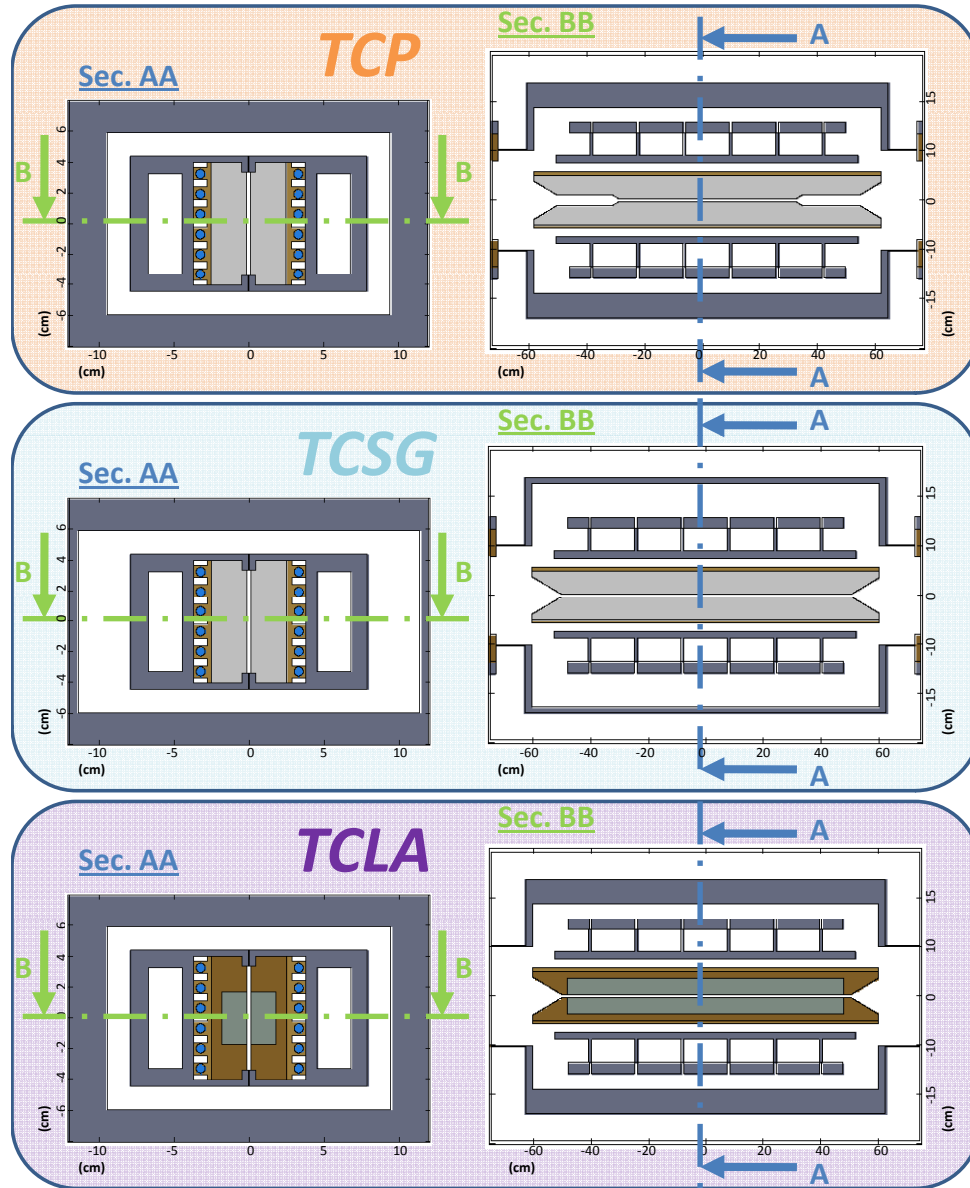


Figure 6.6: Cross plots of TCP, TCSG and TCLA FLUKA prototypes.

6.3.2.4 Passive absorber models

There are three different passive absorbers (see Fig.6.7) for each beam line. The differences between positioning the 3 FLUKA prototypes concern the length and the number of Copper plates for the cooling.

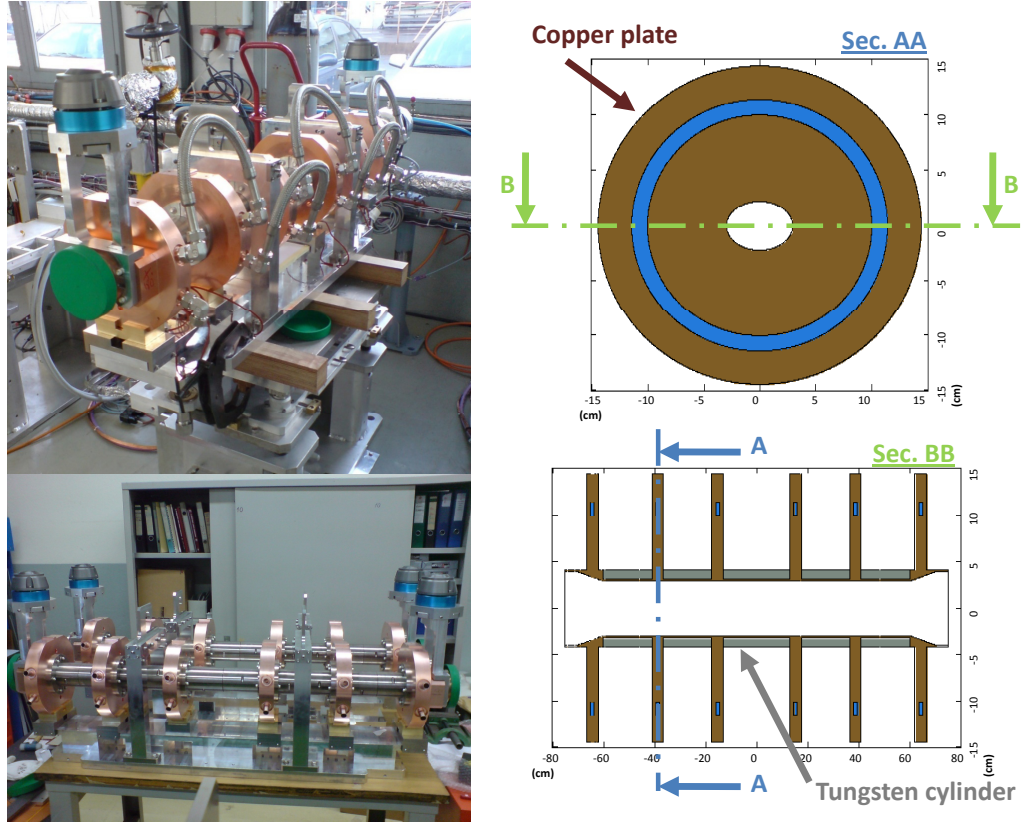


Figure 6.7: Real view and cross FLUKA plots of the longest Passive Absorber installed on each beam line downstream of the primary collimators (with respect to the beam direction) to shield the following MBW dogleg warm magnet.

The passive absorbers are intended to protect the warm magnet coils from damage by particle showers created in the collimators. So they are located upstream (with respect to the beam direction) of the most exposed elements, i.e. each of the two dipoles of the second MBW pair seen by each beam and the first quadrupole of the MQW group downstream of the first TCSG (which is also downstream of the TCP's).

6.3.3 The BLM models

In the FLUKA SS description the BLMs installed just after each collimators and below the beam pipe are modelled. This in principle allows to predict the longitudinal sequence of BLM signals associated to a given loss scenario.

Two different kind of BLMs are implemented in the IR7 line. The LHC BLM system uses Ionization chambers (i.e. BLMI) as standard detectors but in the areas where very high dose rates are expected, like in IR7 (the electronics of the BLMI saturates at about 23 Gy/s [57]), Secondary Emission Monitors (i.e. BLMS) are added because of their high linearity, low sensitivity and fast response [58].

Each collimator has one BLMS and one BLMI installed below it on a suitable support shared with the vacuum pumps (see Fig. 6.8). Three different models for the BLM are implemented in FLUKA: the first and second differ by relative positioning of BLMI and BLMS, reflecting the actual installation in the tunnel. The third one is a very detailed description of the ionization chamber used for specific simulations.

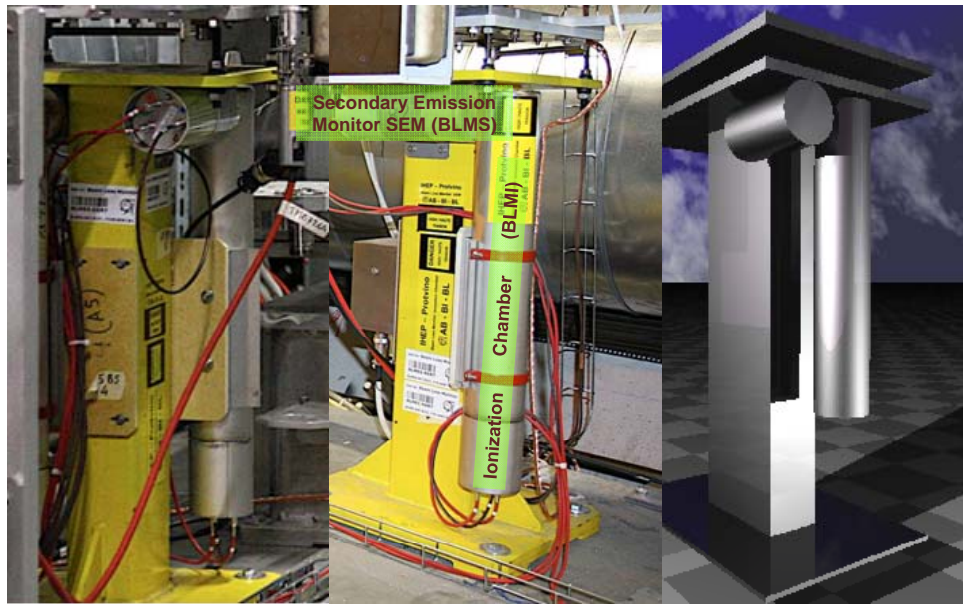


Figure 6.8: BLM real views and FLUKA model.

6.4 The Phase II collimators FLUKA prototypes

In the framework of this PhD, 11 Phase II collimators have been considered on each beam line, downstream of each of the 11 TCSGs.

In total 8 families of designs were investigated, starting with a preliminary model up to the very detailed implementation of the two first prototypes now in phase of production (see Chapter 8 and 9).

Each of the 8 Phase II FLUKA design types is contained in a 3D cylinder region in the parking area. In order to reduce the number of FLUKA prototypes, only one Phase II model was created for each design family and adapted for all energy scenarios. Each prototype jaw is set at an average aperture typical of the case under study. In addition, different jaw materials (e.g. Aluminum, Tungsten, Copper, etc) and different design details (e.g. jaw supports, tank shape, metallic foil onto the jaw, etc) are implemented for the same prototype and activated by the user during the pre-processing stage when a specific IR7 lay-out is produced through the script *go.sh*.

6.5 The IR7 input file and executable

All the prototypes described above are contained in a file called *ir7.fluka* which is the pre-processed version of the FLUKA input file. It includes all the IR7 geometry, the physics options and the scorings necessary for all the study cases.

In order to define the containers (i.e. the 3D volume portions where the prototypes are replicated), the respective transformations and the magnetic fields associated to each magnet element, the *mklattic.r* REXX script is used. It produces eventually the FLUKA input file, that is *ir7.inp* and the *lattic.f* user routine where all the rototranslations and the dynamic changes of the collimator gaps with the associated possible jaw tilts are coded.

The *mklattic.r* takes as input several files. They include the optics informations, which are the beam element sequence, position and magnetic parameters. All the IR7 prototype considered are listed in the *prototype.pos* file, which summarizes all FLUKA available models, their position in the parking area, their names and bounding boxes and the name of the Magnetic Field map files (from ROXIE) to be coupled with each corresponding FLUKA prototype. For collimators, input file includes their rotation, half gaps and possible jaw tilts. The *mklattic.r* calculates the magnetic field intensity/gradient for the dipoles/quadrupoles, as a function of the beam magnetic rigidity.

The *makefile* is the configuration file in which are specified all the user routines necessary for the simulations, in particular, the *source.f* and the *magfld.f* routines. The first routine is responsible of loading the inelastic scattering positions of primary protons from SixTrack and, sampling randomly from this distribution, to force their non elastic interaction at the specified location with the collimator materials. The

second routine defines the magnetic fields on each magnetic prototype.

In order to be flexible for different scenarios, the IR7 layout is not fixed but can be adapted during a pre-processing stage, following the goals of the simulation. In addition, since the prototypes used for IR7 are the same present in the IR3 Momentum Cleaning region, the simulation set-up can be used to perform the study of their impact on IR3 line as soon as corresponding loss maps will be available.

Through the use of the script *go.sh* is possible to select between:

- *The Cleaning region under study: IR7 or IR3.*
- *The primary proton losses in Beam 1 or in Beam 2 line (even if the FLUKA IR7 model foreseen to implement collimators in each beam line).*
- *The Loss Planes: horizontal, vertical or skew.*
- *The Energy of the beam: Injection (450 GeV), Low Beta (7 TeV) or Intermediate Energies (3.5 TeV, 5 TeV).*
- *The Layout of the Collimation System: only Phase I collimators (as the present machine), or Phase I and Phase II collimators with or without Cryo-collimators for the upgrade scenario studies.*
- *The different Phase II designs, in case of Phase II selection.*
- *The Operation scenario: all devices in their nominal setting position or setting errors/optimizations/special assumption (e.g. no TCLA installed, secondary Phase I collimators with different gaps in presence of Phase II collimators, etc).*
- *The simulation settings specifying the desired scoring options (in the DS or SS or in the service caverns regions) and the physics transport parameters. Simulations can be performed for evaluation of power deposition on beam elements and in the adjacent areas as well as for the estimation of radioactive nuclei and dose rates values. In addition, energy thresholds for particle transport are set for special cases. For example for studies of power deposition, the transport of charged particles, including electrons and positrons, has a cut off at 100 keV, considering that at that energy their residual range is quite small to be neglected. The photon energy threshold is set to 33 keV, whereas the neutrons are transported down to thermal energies.*

Fig. 6.9 shows a FLUKA cross plot of the IR7 SS.

During this PhD work, several modifications were introduced in the file structure described above and utilized by different users to generate FLUKA input files. This was done in order to increase the automation degree, to reduce the number of the ancillary files necessary to run a simulation, to collect all the geometries created by different users, to reproduce automatically most of the results already published and to be flexible for new scenarios studies (e.g. new intermediate energies).

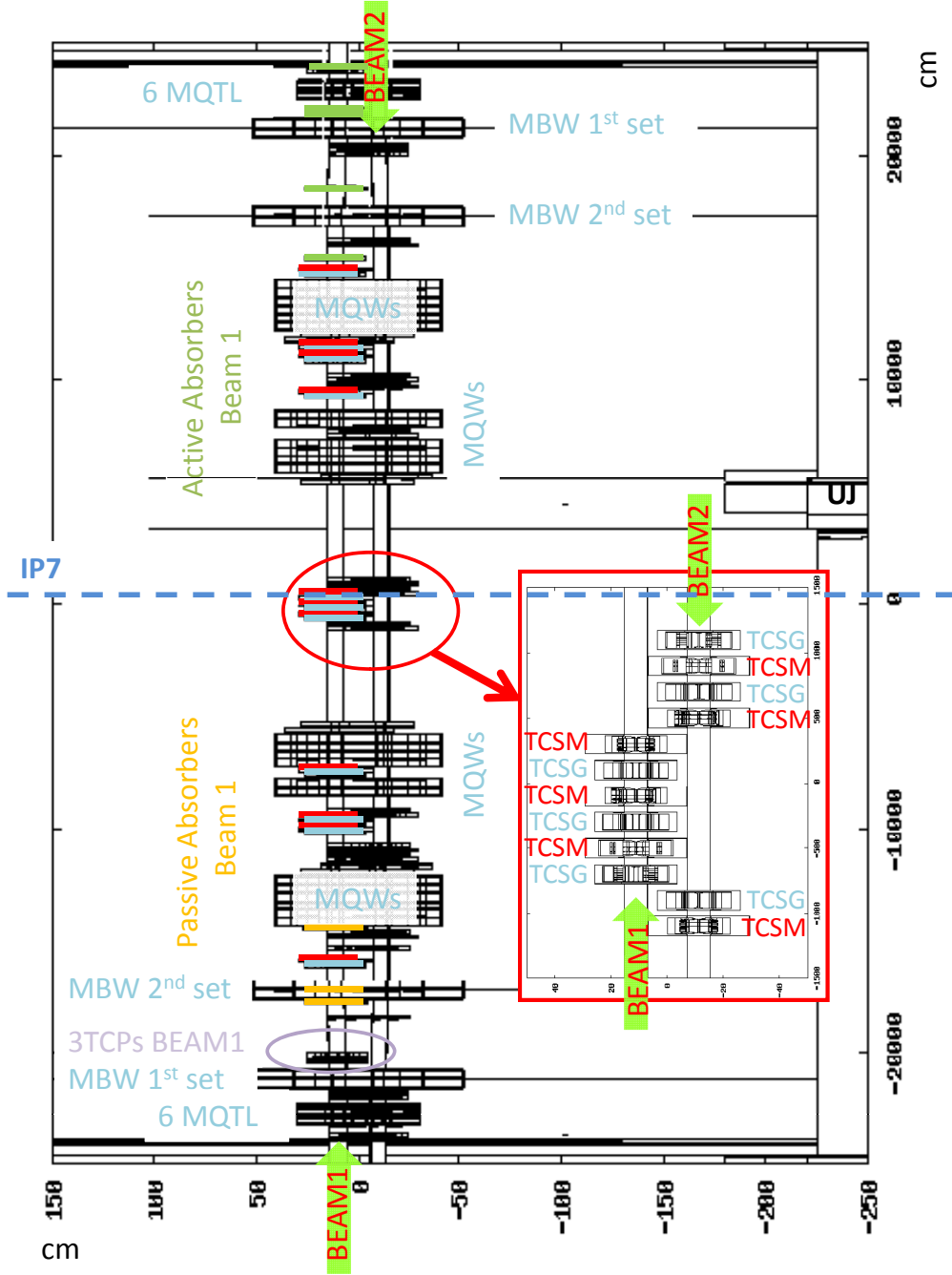


Figure 6.9: FLUKA geometry of the IR7 Straight Section. The location of the Phase I and Phase II collimators are underlined in this cross plot for Beam1. The Beam II is mirror symmetric with respect to the IP7, apart from the location of the collimators inside the red frame.

Chapter 7

First exploratory studies on Phase II collimators

A preliminary Phase II metallic collimator design proposed by CERN was investigated with different jaw materials. This step provided valuable informations not only for the power loads on the jaws themselves but also for those on the jaw support structures and on the collimator tanks, in the different SS locations.

The impacting power in the SS IR7 region in the $0.2h$ beam lifetime scenario for the 7 TeV low beta optics is up to 500 kW . The distribution of this load on the IR7 beam elements and on the surrounding devices is strongly dependent on the material of the jaws which are directly hit by the protons, determining the particle shower development.

General studies are thus necessary in order to evaluate these power distributions and to put the basis for further investigations.

7.1 Collimator materials

In order to compare candidate materials for collimator jaws, a simple exercise is enlightening. A single 92 cm long jaw of different homogeneous materials is impacted with a pencil beam of 7 TeV protons at 100 nm from the jaw surface [59].

Table 7.1 summarizes for the 6 materials considered the physical quantities ruling the energy deposition: Beryllium, Carbon-Carbon (or CFC, it is a 2D carbon fibre reinforced carbon composite, chosen for primary and secondary Phase I collimator jaws because of its low- Z number along with good thermal and mechanical properties), Aluminum, Titanium, Copper and Tungsten. In particular, values of radiation length X_0 (mainly dependent on the atomic number Z and density ρ) and of inelastic scattering length λ (mainly dependent on ρ) are reported.

Fig. 7.1 shows the deposited energy density versus mass length per impacting proton for the scenario under study. The effect of normalizing x axis to the material density is translated in an apparent different jaw length and pointed out the Z -

Table 7.1: Density, Atomic number, Radiation length and Inelastic scattering length for possible Phase II candidate materials.

	ρ [g/cm^3]	Z	X_0 [cm]	λ [cm]
Be	1.85	4	35.28	37.06
CC	1.77	6	24.12	42.09
Al	2.70	13	8.90	35.35
Ti	4.54	22	3.56	25.04
Cu	8.96	29	1.44	13.86
W	19.3	74	0.35	8.90

dependence for the peak positions. For low Z-density materials the peak is not reached within the length of a jaw, because these materials (CC and Be) confine only a small part of the cascade, while the rest escapes from the collimator.

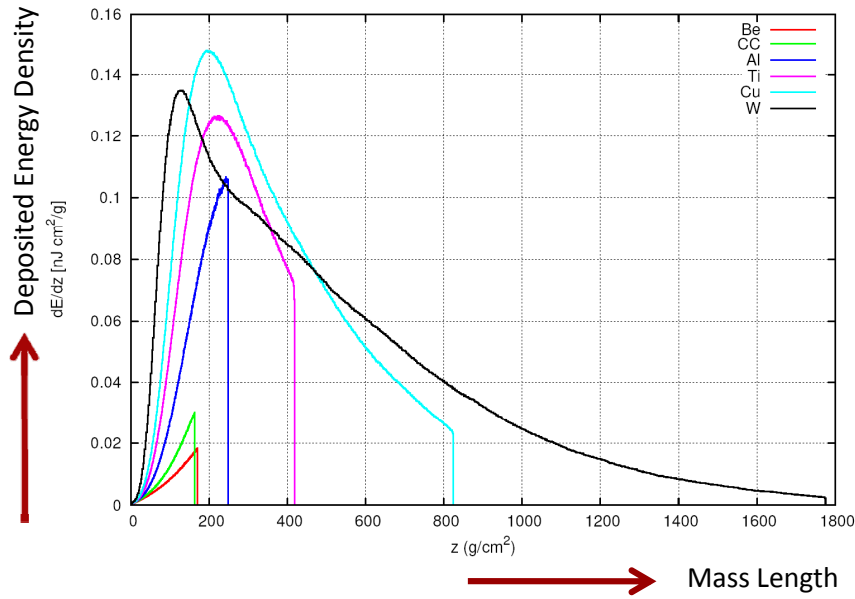


Figure 7.1: Deposited energy density for one $7 TeV$ proton with $100 nm$ impact parameter versus mass length for different possible collimator jaw materials.

7.2 Preliminary Phase II designs

A preliminary metallic collimator design was investigated with different jaw materials and integrated in the IR7 SS FLUKA description, with its cooling circuit (6 water pipelines located in the brazed jaw cover) and its C-shape Molybdenum support included in a stainless steel tank (see Fig. 7.2 left side).

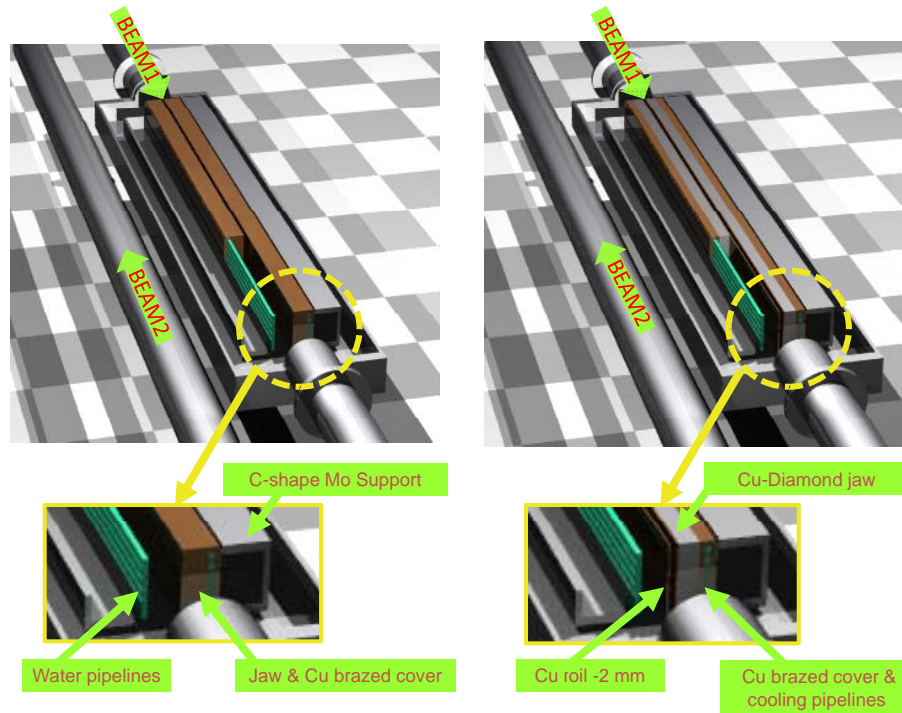


Figure 7.2: Metallic and Foil Collimator FLUKA descriptions. The left jaw is cut to show the water channels.

The geometry of the 1 *m* long metallic collimators has been implemented in the eleven IR7 SS locations. A set of simulations was needed in order to evaluate the feasibility of this collimators with Copper, Aluminum and Tungsten jaws with a fixed transversal thickness of 2.4 *cm*. Tungsten was considered for its optimal radiation absorption and benign damage in case of beam hit, because it is a brittle material and it doesn't explode when subjected to high thermal stresses. Copper was identified for good absorption and good electrical conductivity. Aluminum was investigated due to its past use for some of the Large Electron Positron (LEP) collider collimator jaws. On the other hand, Titanium was rejected for its poor thermal conductivity as well as Beryllium based composites because of their toxicity.

In addition, a metallic Foil design was evaluated. It represents a possible solution, proposed by CERN, to restore the functionality in case of beam damage without changing the whole *ensemble*. The idea is to move into place a 1-3 mm thick Copper foil onto a Carbon based jaw. Using a Carbon jaw behind guarantees a higher probability of collimator survival in comparison to a jaw made entirely of Copper. Indeed, since energy deposition depends strongly on the atomic number and on the density of the material, Carbon assures that only a small part of the cascade will be confined in the collimator jaws, implying an acceptable instantaneous temperature rise. For a first evaluation of this design, a FLUKA model with the foil fully adhering to the jaws (see Fig. 7.2 right side) has been set up. The material chosen for the 1 m jaw is Copper-Diamond (35% Cu and 65% C).

7.3 Loss maps

All the following results refer to an horizontal loss scenario at 7 TeV low beta optics for Beam 1: the largest fraction of primary proton interactions takes place thus in the second horizontal Phase I primary collimator (TCP.C6L7.B1).

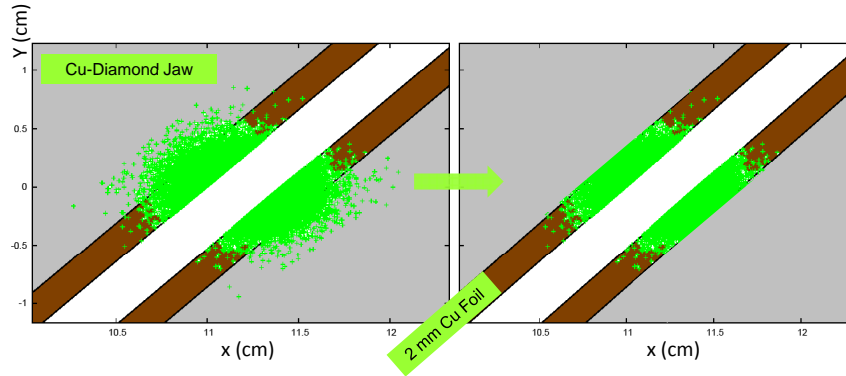


Figure 7.3: Transverse view of the skew TCSM.A6L7.B1 jaws, where the loaded losses are shown for all (z) values along the collimator length both for the standard design and for the foil one.

In the case of the Foil design, the study was performed by loading a loss map referring to a whole Copper jaw and neglecting primary inelastic events outside of the 2 mm thick foil considered (see Fig. 7.3). This cut corresponds to less than 1.5% of all losses and so it has a negligible impact on the integrated power calculation, shown in Fig. 7.4. However, the total power of specific Phase II device can be slightly underestimated.

The first Phase II location (TCSM.A6L7.B1) is the most loaded one, due to its position, it is expected that a significant part of the secondary shower developed in the primary collimators will impact on it.

7.4 First Phase II results

The FLUKA simulations were performed in the SS region only, between the two

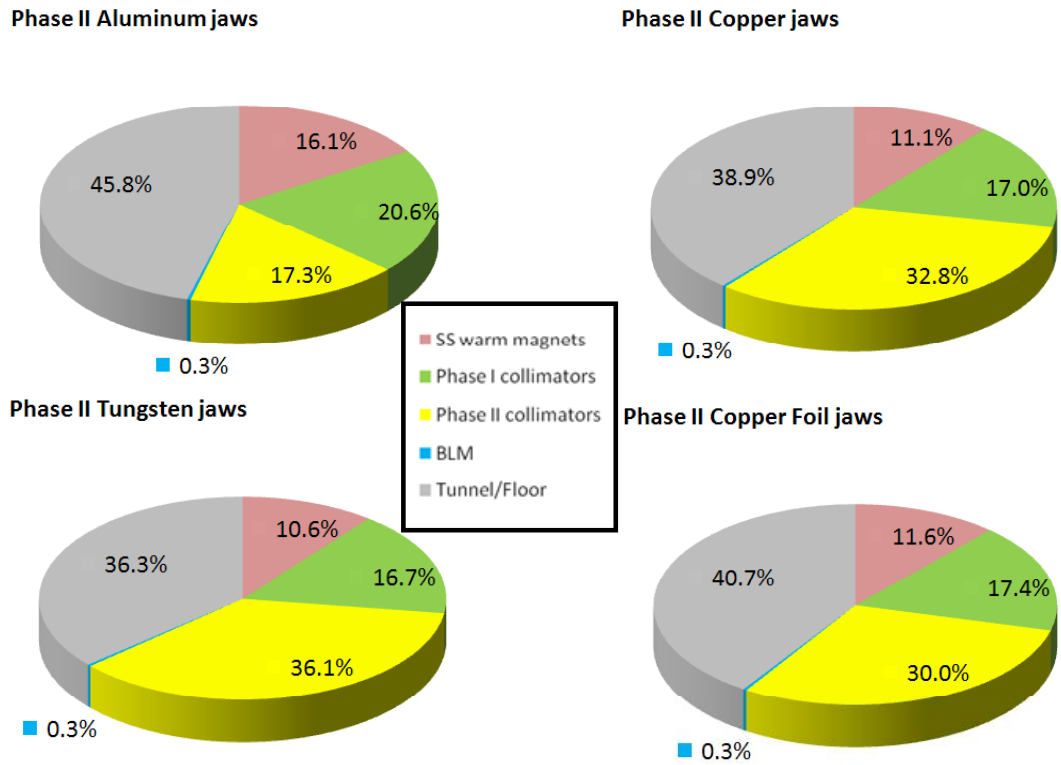


Figure 7.4: The $\sim 500\text{ kW}$ power distribution for the 0.2 h beam lifetime scenario in the IR7 SS region for different Phase II collimator jaws.

MQTL magnet groups. The Phase II collimators are introduced on the Beam 1 line, while all the other beam elements are present on both lines at their foreseen positions. The secondary Phase I collimators are set opened like at the injection energy. In correspondance of each Phase I primary and secondary collimators, the BLMs were considered.

The distribution of the about 500 kW power is shown in percentage in Fig. 7.4. Changing the Phase II collimator jaw materials significantly affects the power distribution. The highest Z material (W) for the jaw doubles the power deposited in the Phase II collimators in comparison to the case of the lowest Z one (Al). On the other hand the use of Phase II Tungsten jaws implies a reduction of 35 % for the power deposited in the IR7 magnets with respect to the Aluminum ones. Different thermal loads can be observed also on the Phase I collimators, due to the effect that Phase I secondary CFC collimators are more or less shielded by the Phase II jaw materials.

FLUKA binnings, that are spatial meshes independent on the geometry, designed to score average or event-by-event quantities, are generally defined as Cartesian structures parallel to the coordinate axes, or as cylindrical structures parallel to the z-axis. A bin size of $0.2 \times 0.2 \times 1\text{ cm}^3$ was found to be the minimum required

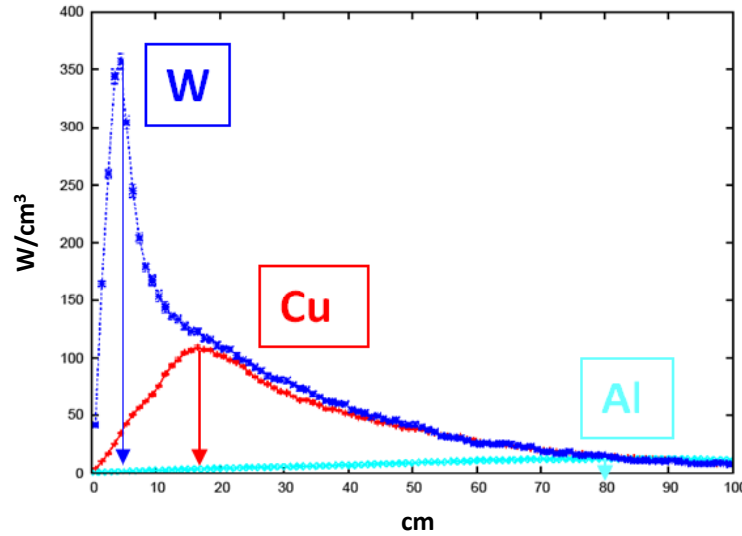


Figure 7.5: Peak power density longitudinal profile at the most loaded Phase II location (TCSM.A6L7.B1) referring to the $1\text{ h } 7\text{ TeV}$ low beta horizontal losses scenario for the different materials.

so as a further bin volume reduction doesn't significantly increase the estimated peak power density. The energy density in $\frac{\text{GeV}}{\text{cm}^3 p}$ per primary interacting proton p obtained as output from FLUKA simulation, was transformed into power density $\frac{W}{\text{cm}^3}$ by the following factors F_n in $\frac{Jp}{\text{GeV}s}$ for fully squeezed optics at top energy in nominal conditions (see Table 3.1):

- Loss rate = $4.3 \times 10^{11} \text{ protons/s}$ (0.2 h beam lifetime) $\Rightarrow F_n = 68.9$
- Loss rate = $0.86 \times 10^{11} \text{ protons/s}$ (1 h beam lifetime) $\Rightarrow F_n = 13.8$

These two operating scenarios define the thermal loading of the Phase II collimators.

Results for the three different collimator jaw materials are summarized in Fig. 7.5 in the case of 1 h beam lifetime.

Table 7.2: Integral values of power on the most loaded Beam 1 Phase II collimator (TCSM.A6L7.B1). In particular, the values refer to the most loaded jaw.

Jaw material	Region	Power 0.2 h [kW]	Power 1 h [kW]
Al	One jaw (only Al part)	15	3
	Cooling water	0.3	0.06
	Mo C-shape support	1.3	0.26
	Tank	9.5	1.9
	Whole collimator	60	12
Cu	One jaw (only Cu part)	45	9
	Cooling water	0.3	0.06
	Mo C-shape support	1.8	0.36
	Tank	8.6	1.7
	Whole collimator	115	23
W	One jaw (only W part)	55	11
	Cooling water	0.2	0.04
	Mo C-shape support	1.3	0.26
	Tank	5.6	1.1
	Whole collimator	120	25
Cu Foil	One jaw only 2 mm Cu Foil	10	2
	One jaw only Cu-Diam part	30	6
	Cooling water	0.3	0.06
	Mo C-shape support	1.9	0.4
	Tank	10	2
	Whole collimator	105	21

The position of the peak is on the jaw surface: at about 18 *cm* longitudinal depth for the Copper jaw and the Copper Foil collimator, at 80 *cm* for the Aluminum one and at 5 *cm* for the Tungsten one. The curves refer to the most loaded Phase II TCSM.A6L7.B1 jaw. The 1 *h* scenario represents the reference nominal steady state operation condition. The transient case results in a 5-fold increase in the heat load on the secondary collimators for a beam lifetime of about 12 minutes. However, after 10 *s* of the transient condition, it is assumed that the beam can be dumped.

Summary of integral power deposition results [60] for the most loaded Phase II collimator (TCSM.A6L7.B1) are reported in Table 7.2.

In addition, activation studies for collimators with different jaw materials [61] have shown that the activated cooling circuits, tank, and support structures contribute significantly to the residual dose rates (more than 60%). Nevertheless, the overall activation level depends on the jaw material and, for example, is 20-50% higher for collimators with Tungsten jaws compared to those with Copper jaws. On the other hand, the cooling time dependence is found to be similar for all jaw materials.

7.5 Simulation accuracy

The systematic error when simulating the cascade introduced by 7 *TeV* beams on the machine elements is a combination of several factors [62].

While the statistical uncertainties are generally below 10% for peak values and below 1% for integral values, further main sources of errors are systematic [63].

- *Physics modeling uncertainties.*

In particular these uncertainties are due to the extrapolation of the inelastic p-A cross-sections at 7 *TeV* and to the uncertainty in the interaction modelling. A factor 2.4 is to be taken into account for integral quantities scored like energy deposition, dose, and a factor 4 for peak values.

- *Assumption used in the geometry and material description.*

The approximation introduced in the geometry and material description brings to errors which are difficult to quantify. A factor 1.1 can be taken as a safe limit for integral values and a factor 1.5 for peak ones.

- *Jaw roughness.*

In particular this refers to having beams grazing the surfaces of the collimators, where the surface roughness is not taken into account. A factor of 1.5 has to be considered.

Furthermore, since the tracking loss pattern forms the basis of the FLUKA studies (see Chapter 4), errors due to the assumptions used to generate the loss maps have to be added to the uncertainties mentioned above.

7.6 Conclusions on Phase II first results

The first exploratory studies have identified the most loaded position independent of the jaw material for the Phase II collimators, that is the first location after the Phase I primary ones.

For this particular position, simulation results gives the order of magnitude of thermal loads distribution in the main collimator components. Preliminary evaluations of the major jaw deflection and of cooling requirements are calculated. Following Phase II collimators mechanical integration optimization are based on these calculations.

In addition the results outline that the possible choice of Tungsten jaws for this position has to be avoided. Indeed already in operation conditions, its functionality could be limited because of the high values of the peak power density on the jaw surface.

Choice is therefore limited to Copper or Aluminum. Since the latter has relatively poor cleaning efficiency and the water channel fabrication has shown to be difficult, further investigations are focalized in particular on Copper based materials such as Glidcop. It shows a good balance of cleaning efficiency, deflection and manufacturability, in addition to its good electrical conductivity (important from the impedance point of view).

However introduction of other possible strategies and further jaw materials will be not excluded at this stage. In particular, composite materials such as silicon carbide or copper diamond have been proposed in an advanced phase of the mechanical integration studies as possible solution (see Chapter 9, Section 9.3).

Chapter 8

The SLAC Phase II design

Due to the high beam power involved, special attention is given to develop Phase II collimators that allow a new jaw surface to be moved into place, after possible beam damage.

In the framework of this study, the SLAC laboratory, through the LARP program proposes a collimator built up of two cylindrical 91 *cm* long Glidcop jaws which can rotate, in order to move into place a new surface in case of beam damage.

This concept is an advanced development, specific for the LHC, of the Next Linear Collider (NLC) rotatable collimator [64]. The NLC project was a SLAC proposed electron-positron collider which has posed similar collimation problems, because of its high energy density. Following the decision of SLAC laboratory to pursue a next-generation linear collider using superconducting RF technology (i.e. International linear Collider (ILC)), the NLC project was cancelled in 2004. However, the considerable engineering, design and manufacturing efforts required to build and test the NLC collimator have been carried over to the design of rotatable collimators for LHC.

8.1 The evolution of the SLAC Phase II design

The most critical issue in the design of the collimator is the **non permanent** thermal deflection of the jaws due to the beam heat load, which brings to a reduction of the active length and thus to a possible reduction of the cleaning efficiency.

On the basis of the preliminary evaluations of different materials, the use of Glidcop instead of pure Copper was introduced.

Extensive simulations were performed using FLUKA and ANSYS to determinate the maximum realistic heating and deflection of the jaws under steady state and transient conditions. The ANSYS models were designed to duplicate the cylindrical cell structure of the FLUKA mesh for each jaw. At the beginning, the FLUKA model was composed only by two hollow cylindrical 75 *cm* and 14 *cm* diameter Glidcop jaws, set at 7σ from the axis of the beam at the TCSM.A6L7.B1 position. The jaw

dimensions were chosen in such a way to be located both in the Phase I collimator tank (see the technical drawing (left down corner) in Fig. 8.3) and to use most of the Phase I components (i.e. jaw motors, cooling and electrical connections, collimator handling robots, etc).

These preliminary studies bring to the evaluation of the deflection limits for this *baseline* configuration in the case of the most loaded jaw: $426\ \mu\text{m}$ for the $1\ h$ beam lifetime (i.e. steady-state) and $1260\ \mu\text{m}$ for the $0.2\ h$ beam lifetime (i.e. transient) scenarios, when the jaw is constrained to deflect away from beam. An helical cooling channel at about $2.5\ \text{cm}$ from the jaw surface was chosen for these evaluations, because it was demonstrated to result in less jaw deflection in comparison to an axial cooling channel option. However, the external jaw helical cooling tube connections have reduced the jaw length from $1\ \text{m}$ (as for the Phase I secondary collimators) to $75\ \text{cm}$, in order to reutilize the Phase I tank. Simulations show a reduction of the active length from $75\ \text{cm}$ to $43\ \text{cm}$ for the steady state and to $24\ \text{cm}$ for the transient conditions respectively.

In order to minimize the jaw deflection, in particular for the TCSM.A6L7.B1 position, different jaw design options were proposed [65].

As design work proceeded, it became evident that the jaw deflection, due to differential thermal expansion of the hot beam side relative to the cooler side away from the beam, can be relieved by providing a direct thermal path throught the jaw. The baseline configuration evolved into a so-called *refined baseline* design with a solid Copper shaft and a reduction of the pitch of the helical cooling tube.

A second conceptual brackthrough consisted of introducing a shaft and concentric jaw jointed only at the collimator center. This layout was called *Jaw-Hub-Shaft* concept. It allowed the jaw ends to deflect away from the beam, eliminating the

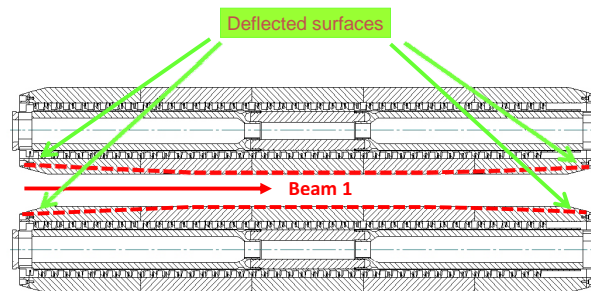


Figure 8.1: Jaw-Hub-Shaft concept to minimize the jaw deflection toward the beam.

need of flexible end supports (see Fig. 8.1).

A third step was the replacement of the external helical cooling tube connections at the jaw ends by twistable straight connections routed through the center of the shaft. This improvement allowed for longer jaws, from 75 to 91 *cm* active length, and eliminated concerns about interface between external helices and the shaft support and vacuum tank to jaw RF shielding.

The final design change was a decision to make the shaft in Molybdenum. The use of Molybdenum for the central shaft is to increase the structural rigidity.

Table 8.1 reports the simulated performance of the *baseline*, *refined baseline*, *Jaw-Hub-Shaft* (actual design) under the two heating conditions. It does not include the static deflection due to gravity, which is 68 μm in the case of the refined Jaw-Hub-Shaft concept. The table shows that the 1260 μm total deflection of the jaw relative to the shaft axis is reduced by roughly a factor of 5 to 236 μm , or, in other word, to one beam σ .

Table 8.1: Simulated evolution performance of the different SLAC collimator concepts at the most loaded jaw position (collimator TCSM.A6L7.B1) [65].

Operation condition	Jaw design	Deflection [μm]	Ideal active length [<i>cm</i>]	Actual active length [<i>cm</i>]
Steady state	Baseline	426	75	43
	Refined baseline	238	75	63
	Jaw-Hub-Shaft	84	91	74
Transient	Baseline	1260	75	24
	Refined baseline	853	75	31
	Jaw-Hub-Shaft	236	91	39

8.1.1 The actual SLAC Phase II design

The actual SLAC Phase II design features cylindrical Glidcop jaws, 13.6 *cm* diameter, 93 *cm* long, with 1 *cm*, 15 degree tapers at each end, and an internal helical cooling channel. Each Glidcop jaw consists of a Molybdenum shaft and concentric jaw joined via a Copper hub. There is a 2 *mm* gap between the shaft and the outer jaw. This allows the jaw ends to deflect mostly away from the beam during heating, reducing the jaw deflection toward the beam. The jaw shaft is supported on each end by a stainless steel post. Each jaw shows 20 flat facets on the cylindrical jaw surface (see Fig. 8.2). The SLAC collimator can thus support 20 local damages without changing the total *ensemble*, but by rotating the jaw to introduce a clean surface to the impacting beam halo.

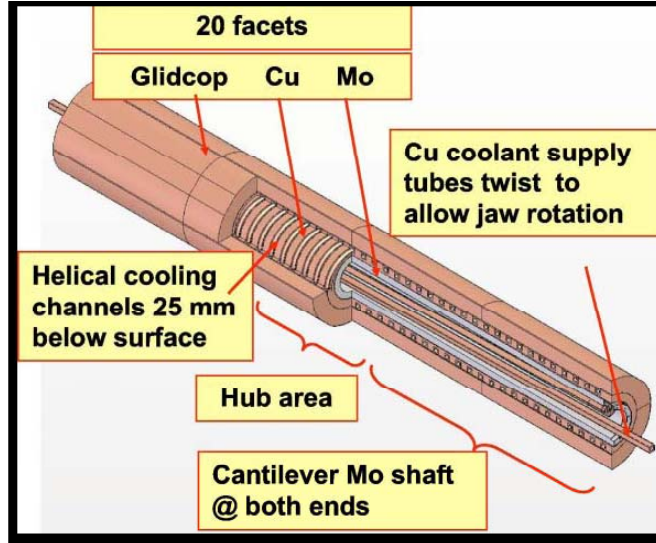


Figure 8.2: Cutaway of SLAC jaw showing outer jaw surfaces and cooling tube routed through the center of the Molybdenum shaft.

The cooling circuit is composed by a 16 m Copper tube, forming a helix within the jaw, with straight tails extending through the center of the shaft. This eliminates any vacuum to water joints and allows for the Copper tube to be twisted as the jaw rotates. It requires a vacuum tank slightly larger in width and depth than the Phase I unit.

8.2 The SLAC Phase II FLUKA model

Following the mechanical evolution of the SLAC Phase II design, a FLUKA description of the collimator was created and then modified at each integration step, starting with a model composed only by the two cylindrical jaws (see Fig. 8.3).

It was developed during this PhD work to obtain distributed heat loads, which were used as primary scope for the evaluation of the jaw deflections.

Additional studies on the jaw motion mechanism are responsible of the most recent evolution concerning the stainless steel jaw supports and the RF transition pieces (see Fig. 8.4). Fig. 8.4 shows the comparison between the jaw prototype built in the SLAC laboratory and the FLUKA model.

Since the cylindrical SLAC jaws are bigger than the rectangular Phase I ones, a semi-cylindrical cross section tank at the place of the Phase I box was developed. The new tank rotates using the same Phase I external supports without interferences with the Beam 2 line. Fig. 8.5 shows the set-up problems caused by using a bigger

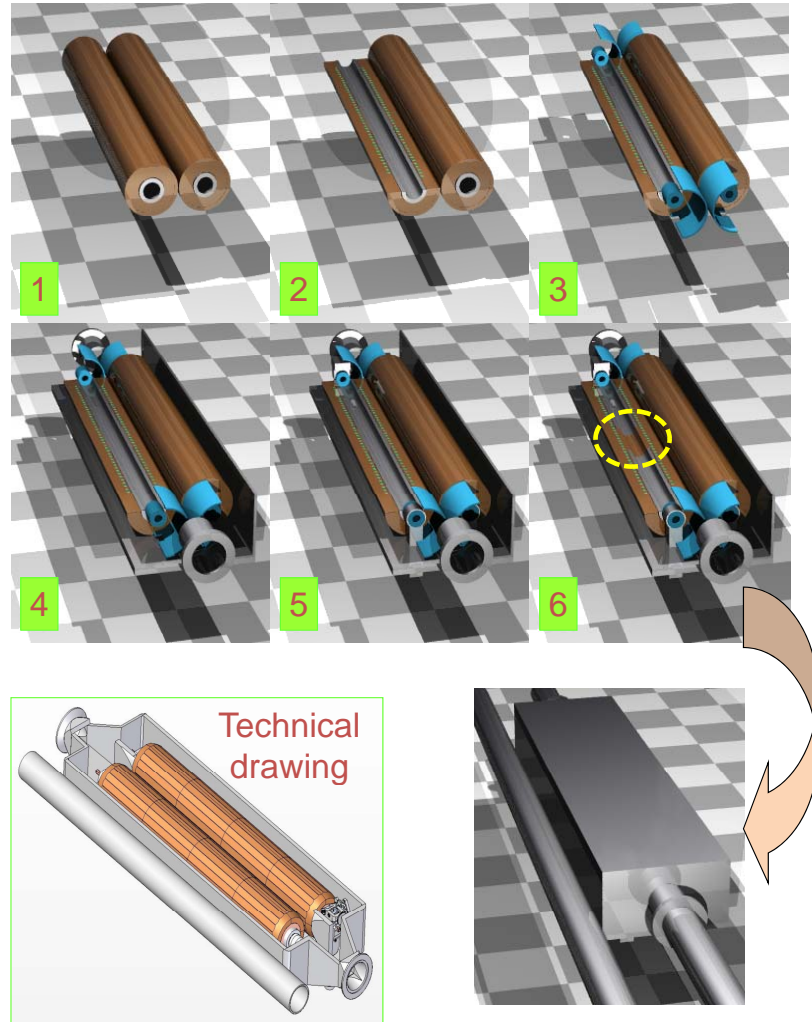


Figure 8.3: Evolution of the SLAC FLUKA model and comparison with the Catia technical drawing. At the beginning, the model was composed only by the two Glidcop jaws and the Molybdenum shaft (1). The cooling circuit was subsequently added (2), as well as the stub shaft for the RF connection (3), the tank (4), the jaw upbeam and downbeam asymmetric supports (5) and the refined Jaw-Hub-Shaft configuration with the 2 mm gap and the central copper hub (6). Each time the model was integrated in the IR7 FLUKA description to evaluate the collimator performance.

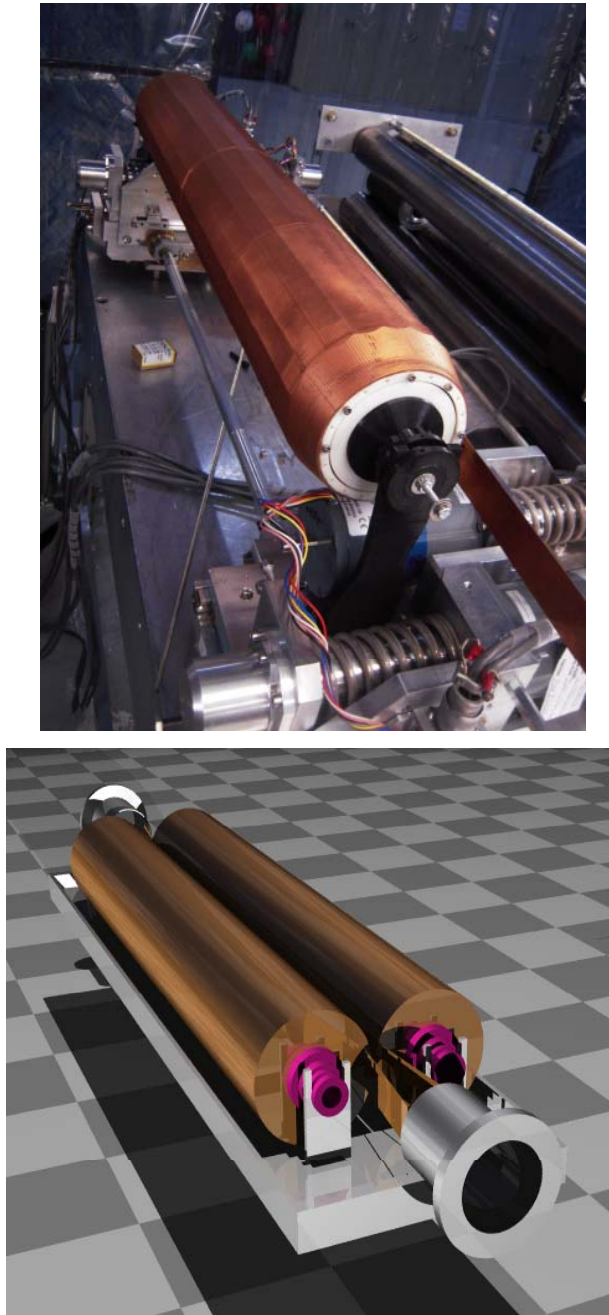


Figure 8.4: SLAC jaw prototype (top) and FLUKA model (bottom).

tank, in particular this is put in evidence in Fig. 8.5 (see up-left corner) for the skew collimator orientation.

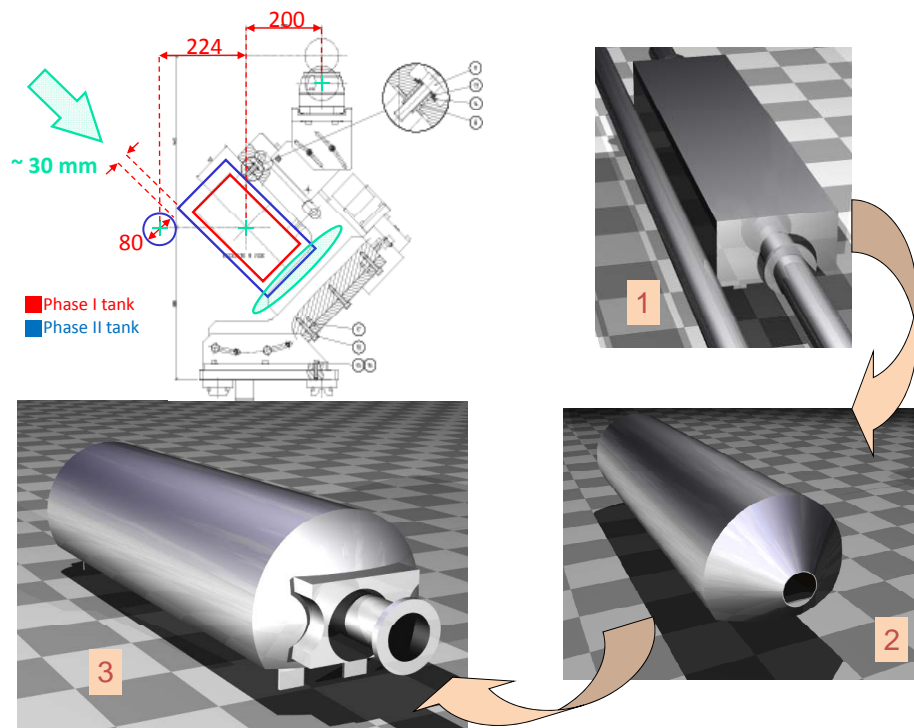


Figure 8.5: FLUKA model evolution of the SLAC tank: from the rectangular section tank (1) to the final semi-cylindrical tank (3) through a preliminary version (2).

8.3 FLUKA results for the most advanced SLAC Phase II design

A set of FLUKA simulations has been performed to score the power distribution at each SLAC design evolution step.

In the FLUKA runs cylindrical coordinates were used to score in the jaws, mandrel and shafts. Bin size were in average 1 mm^2 transverse and 1 cm along the jaw length. Cartesian coordinates were used in all other components, with an equivalent bin size.

The statistical error does not exceed few % for integral values, whereas for the power density peak is approximately 10 %.

The same SLAC FLUKA model is adapted runtime at the 11 IR7 locations of the Beam 1 line, through a customized routine which modifies the collimation aperture reducing or enlarging the jaw cylinder to match the beta function evolution. The 11 collimator apertures are different from each other by the order of hundred μm . The aperture setting introduces variations in the 22 jaw thickness around its real value, which however have a negligible impact for the evaluation of the power distribution in the collimator and their effect can be included in the statistical errors. The same routine is also responsible of the collimator different orientations in the IR7 line.

The following FLUKA simulation results refer to the current SLAC Phase II design.

8.3.1 Operation conditions

Since the largest fraction of halo protons is expected to be lost in the three Phase I primary collimators, three scenarios have been studied separately. Halo losses concentrated in the horizontal, vertical and skew Phase I primary collimators re-

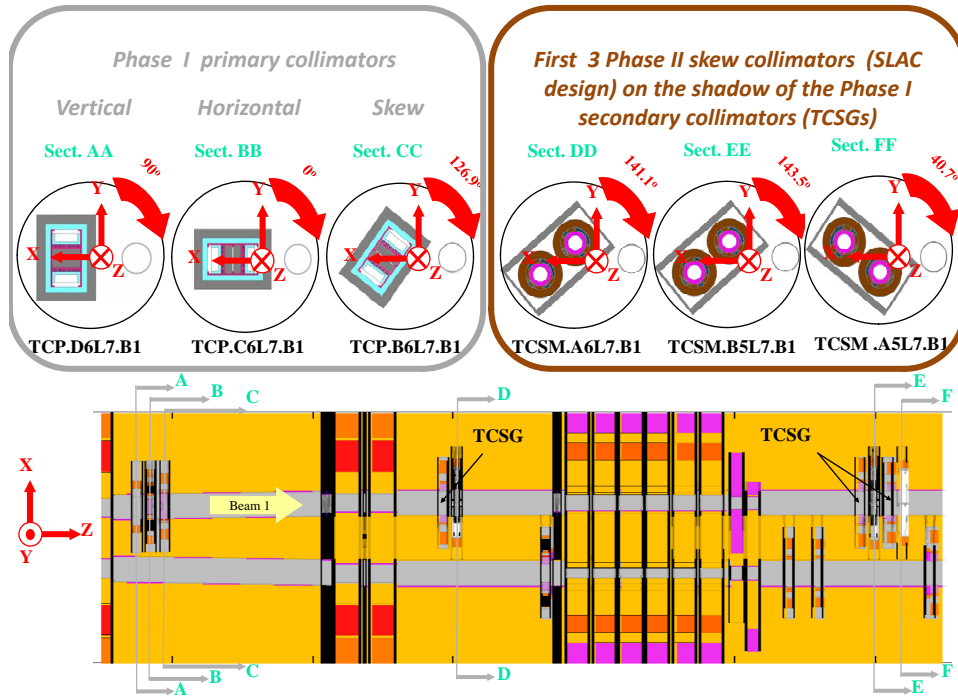


Figure 8.6: Cut of the IR7 FLUKA model showing the Phase I primary collimators with the respective orientations and the first 3 Phase II collimators along the IR7 line.

spectively, have been evaluated for both the steady-state and transient conditions at low beta 7 TeV . It has to be noted that the real distribution of losses is a combination of the above three halo limit cases. The spatial coordinates and the direction of the primary protons undergoing an inelastic interaction in the jaws are given by a multi-turn beam optics code (see Chapter 4, Section 4.2.2).

The most loaded collimator is the TCSM.A6L7.B1, which is the first skew oriented Phase II collimator located downstream from the primary Phase I ones (see Fig. 8.6). About 70 % of the total power on all the 11 Phase II collimators is on the TCSM.A6L7.B1. The FLUKA simulations take care of the contribution of primary proton losses in each collimator and of particle shower from the upstream devices. The studied scenarios refer to a Phase II system without cryo-collimators in place.

The fraction of power on both the TCSM.A6L7.B1 Glidcop jaws is about 70 % of the total amount on the whole collimator.

Table 8.2 summarizes the results for the three scenarios studied. The FLUKA results are normalized to the ratio between the number of protons impacting in the IR7 collimators and the total number of losses on the LHC machine (data from the tracking code), multiplied by the loss rate corresponding to the beam lifetime.

In addition, since the tracking was run for collimators modelled with rectangular jaw sections, the optics input file was cleaned by the losses outside the SLAC cylindrical profile, which corresponds to neglecting less than 3 % of the particles impacting on the 11 IR7 Phase II collimators.

Table 8.2: Summary of Power deposition results on the collimator TCSM.A6L7.B1 for the 3 halo scenarios [66]. Results refer to the whole collimator and to the most loaded jaw for the Glidcop part (from 4.4 to about 6.8 cm radius), leaving out the Molybdenum shaft, the cooling circuit and the jaw end supports.

Halo	Region	Power 0.2 h [kW]	Power 1 h [kW]
Horizontal	Whole collimator	110	22
	One jaw (only Glidcop part)	42.5	8.5
Vertical	Whole collimator	110	22
	One jaw (only Glidcop part)	42.5	8.5
Skew	Whole collimator	106.5	21.3
	One jaw (only Glidcop part)	43.5	8.7

Detailed analyses were also performed for the heat load deposited respectively on the shaft, cooling pipelines, jaw supports, flanges and tank to assure the proper functionality of these collimator components. Table 8.3 summarizes these values for one of the 3 halo distributions as a representative case (i.e. the horizontal one).

Improvements on the tank design have reduced the power load from 1.6 to 1.2 kW flanges included, while the heating on the most recent jaw supports shows about the

Table 8.3: Summary of Power deposition results on the collimator TCSM.A6L7.B1 components for the horizontal halo steady-state scenario.

Region	Power 1 h [kW]
Molybdenum shaft	0.5 (x2 jaws)
Copper mandrel and copper pipeline	0.8 (x2 jaws)
Cooling water	0.03 (x2 jaws)
Jaw support	0.04 (x2 jaws)
Tank and flanges	1.6 (square tank)

same value in comparison to the previous ones.

The FLUKA simulations show different peak power profiles in the jaws due for the horizontal and skew halo, whereas for the vertical one the peak load is pretty symmetric. On the other hand, the power density peak is sharply localized on the jaw surface, at about 20 cm longitudinal depth for all the three scenarios. The similar patterns for the peak results are typical for the Molybdenum shafts (see Fig. 8.8).

Fig. 8.7 shows the power map at the depth of the maximum and along the longitudinal plane.

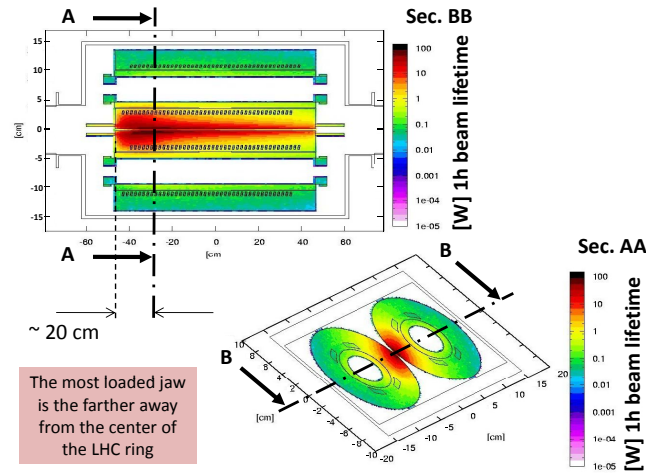


Figure 8.7: Power deposition map at 20 cm longitudinal depth and along the collimator length for the horizontal halo scenario. It has to be noted that the coordinate system refers to the prototype in the parking area which in the case of the TCSM.A6L7.B1 location undergoes a rotation of 141.1° as indicated in Fig. 8.6

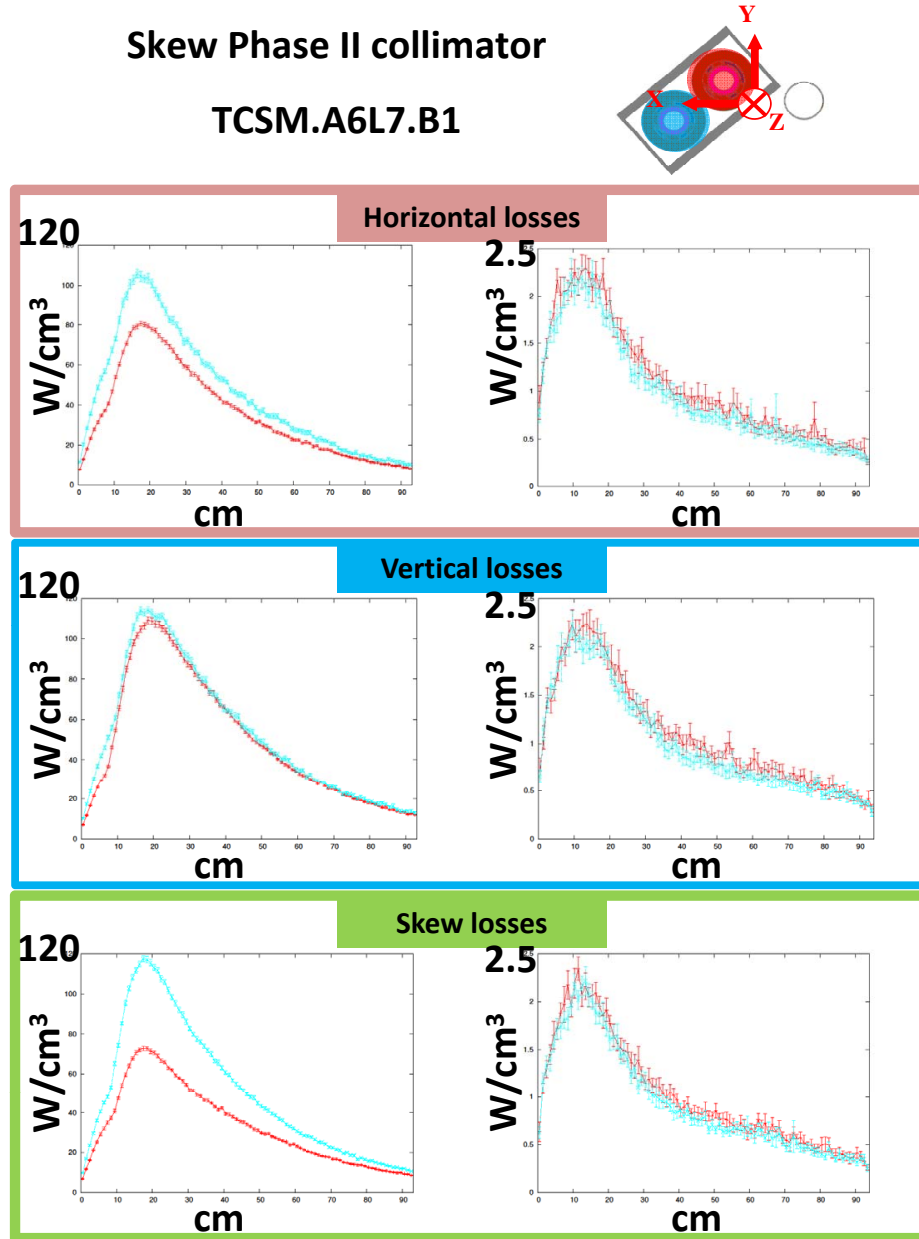


Figure 8.8: Comparison between the power density peak values on the Glidcop jaws (left side) and on the Molybdenum shafts (right side) for the 3 halo distributions in the 1 h steady-state case. Red and blue lines refer to the respective jaw as indicated on the picture top.

Fig. 8.9 shows the power maps and the cumulative power as a function of the jaw radial coordinate (integrated over 2π and a 1 cm z-slice) at the longitudinal peak location.

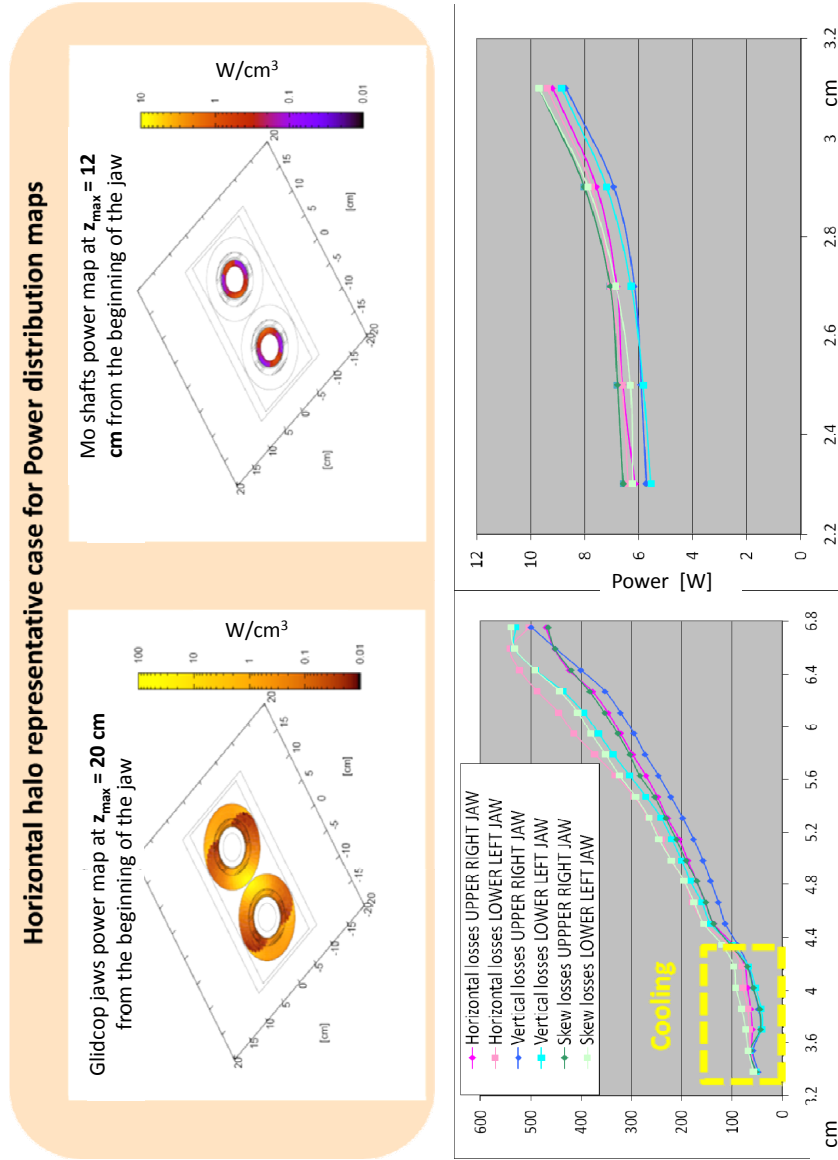


Figure 8.9: Power maps and cumulative power values inside the jaws (including the helical cooling circuits) and shafts.

8.3.2 Asynchronous dump scenario

The scenarios studied refer to the abnormal beam losses due to a mis-firing of the horizontal extraction kicker at top energy (see Chapter 4, Section 4.2.1.1). In particular, simulations have been run using a low probability accident case, which concerns the impact on the Phase II collimators, since it can happen only by-passing all the upstream beam line aperture restrictions along IR7.

This kind of failure affects mainly the horizontal collimators, as the dump kick acts on the horizontal plane. Since there are three horizontal collimators implemented in the IR7 line, three were the scenarios studied.

In the first scenario, it was assumed that proton between 6 and 10 σ_x impact on a Phase I primary CFC collimator, that is the TCP.C6L7.B1. In the second and third scenario, since the aperture of the Phase II collimators is fixed at 7σ , protons between 7 and 10 σ_x hit the two horizontal Phase II collimators. The first one is the TCSM.B4L7.B1, located in the middle of the IR7 LSS. The second one is the TCSM.6R7.B1, which is the last of the 11 Phase II collimators crossed by the Beam 1 before leaving the IR7 LSS, located at the end of the SS line before the dogleg bending magnets MBWs.

Local dump protection devices (TCDQs) are assumed to intercept all beam above $10\sigma_x$ (see Fig. 8.10). These scenarios correspond to an impact of 5.6 nominal LHC bunches within 1.1 mm from the edge of the TCP.C6L7.B1 collimator and of 4.2 bunches within 0.8 mm for the TCSM.B4L7.B1 and 4.1 bunches within 1.2 mm for the TCSM.6R7.B1. The difference of 0.1 between the numbers of bunches impacting the two Phase II collimators is due by the approximation errors of the half gap setting definition.

The spatial distributions in the transverse plane of the protons at the entrance of the collimators are shown in Fig. 8.10, where the penetration of the impact in the jaw is put in evidence for all the three cases. Fig. 8.10 also shows the phase space distributions in (x, x') and in (y, y') of the input data at the same longitudinal position. In the central plots of Fig. 8.10 the fraction of the impacting protons is delimited by the blue arrows. The incoming particles did not receive any kick in the vertical plane, as it is shown by the plots on the top side of Fig. 8.10.

It has to be pointed out that the Phase II collimator survival to the asynchronous dump doesn't represent a project requirement. For all the asynchronous cases studied, results show that a Glidcop Phase II collimator is always the most loaded one.

Since the time-scale of the accident scenario is of the order of hundred nanoseconds, results refer to the total instantaneous energy deposition. Tables 8.4, 8.5 and 8.6 report the respective value for the most loaded IR7 beam elements and their distance from the collimator directly impacted. Simulations refer to the case of Phase I secondary collimators (i.e. TCSGs) totally opened.

The difference of 9 kW between the two Phase II collimators directly impacted results from the 0.1 bunch neglected in the second case due to the halfgap approximation errors.

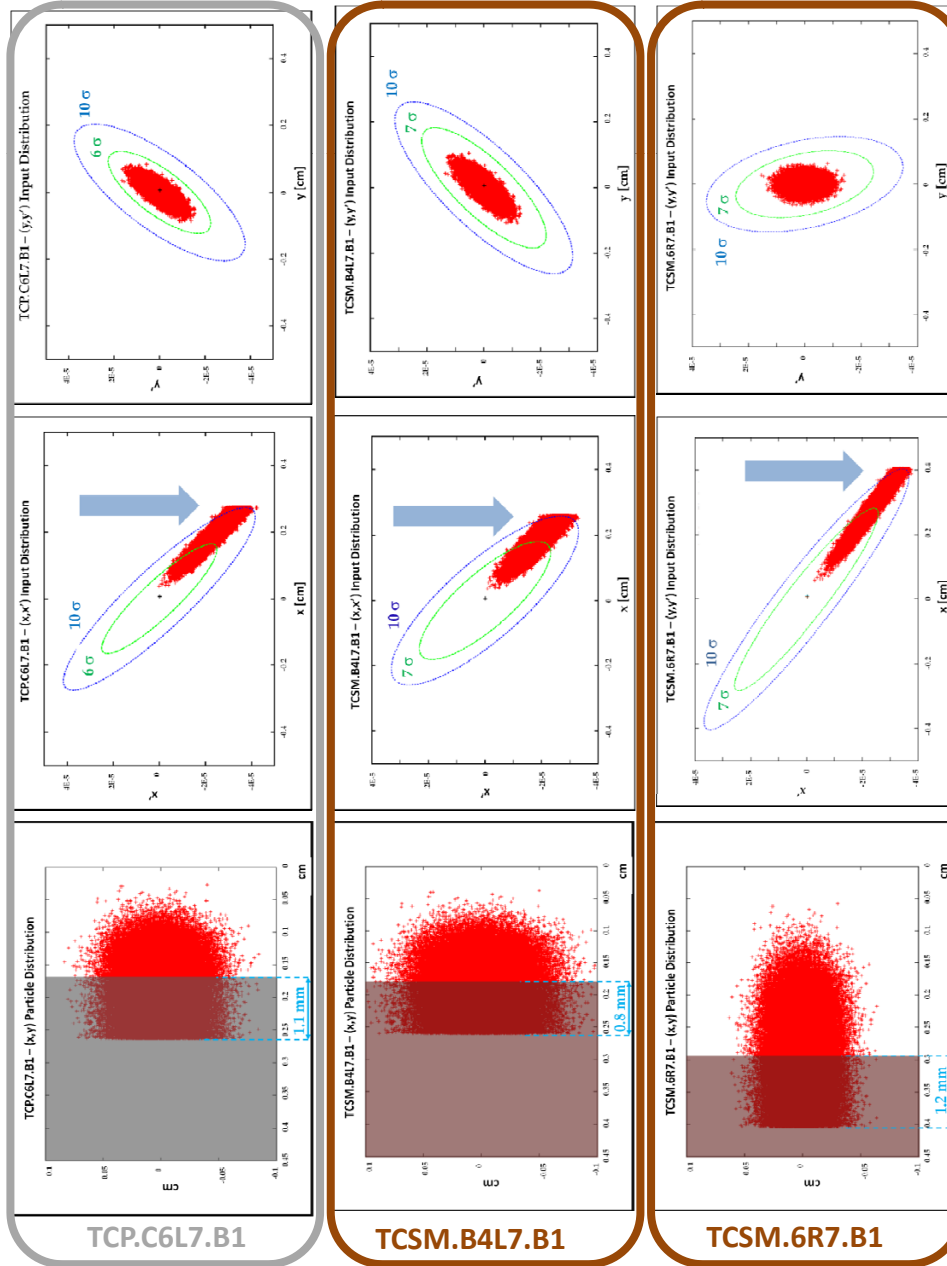


Figure 8.10: Geometrical and phase space distributions of protons coming from an asynchronous dump at the entrance of the indicated horizontal collimators. In the bottom plots, the beam direction is entering the page.

Table 8.4: Energy deposition on the most loaded Beam 1 elements in the case of TCP.C6L7.B1 directly impacted during an asynchronous dump.

Beam element name	Functional type	Energy deposition [kJ]	Distance from TCP.C6L7.B1 [m]
TCSM.A6L7.B1	Phase II collimator	132	42
TCP.B6L7.B1	Phase I primary	41	0.5
TCAP.A6L7.B1	Passive absorber	37	23
MBW.B6L7	Dogleg bending magnet	36	25
MBW.A6L7	Dogleg bending magnet	24	30
TCSM.B5L7.B1	Phase II collimator	22	101
TCP.C6L7.B1	Phase I primary	9	0

Table 8.5: Energy deposition on the most loaded Beam 1 elements in the case of TCSM.B4L7.B1 directly impacted during an asynchronous dump.

Beam element name	Functional type	Energy deposition [kJ]	Distance from TCSM.B4L7.B1 [m]
TCSM.B4L7.B1	Phase II collimator	294	0
TCSM.A4L7.B1	Phase II collimator	61	2.5
TCSM.A4R7.B1	Phase II collimator	16	6.5
TCSG.A4L7.B1	Phase I secondary	14	0.5
TCSG.A4R7.B1	Phase I secondary	4	4.5

Table 8.6: Energy deposition on the most loaded Beam 1 elements in the case of TCSM.6R7.B1 directly impacted during an asynchronous dump.

Beam element name	Functional type	Energy deposition [kJ]	Distance from TCSM.6R7.B1 [m]
TCSM.6R7.B1	Phase II collimator	285	0
TCLA.A6R7.B1	Active absorber	61	5
TCLA.C6R7.B1	Active absorber	6	69
MBW.A6R7	Dogleg bending magnet	4	20

Table 8.7: Energy density peaks and instantaneous increases of temperature for the most loaded device for the 3 asynchronous dump accident scenarios [66].

TCP.C6L7.B1 impacted → TCSM.A6L7.B1 most loaded	
Energy Density peak on the most loaded jaw	600 [J/cm^3]
Instantaneous increase of temperature	180 [$^{\circ}C$]
TCSM.B4L7.B1 impacted → TCSM.B4L7.B1 most loaded	
Energy Density peak on the most loaded jaw	50000 [J/cm^3]
Instantaneous increase of temperature	» melting point
TCSM.6R7.B1 impacted → TCSM.6R7.B1 most loaded	
Energy Density peak on the most loaded jaw	50000 [J/cm^3]
Instantaneous increase of temperature	» melting point

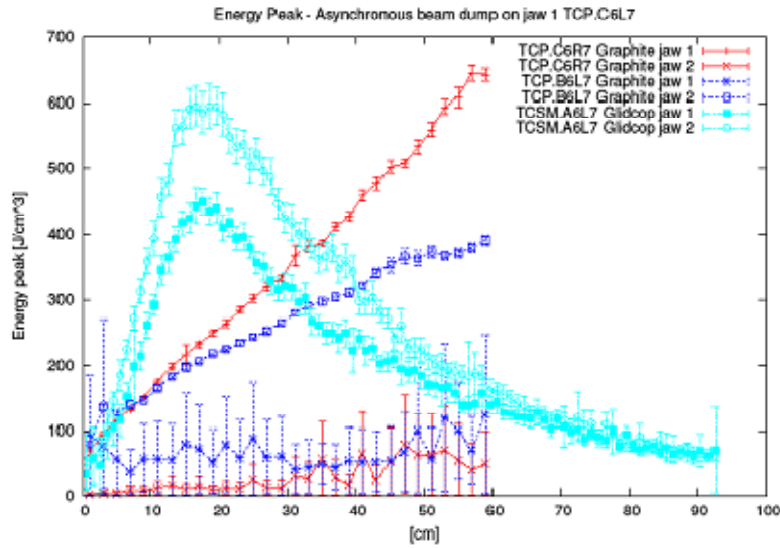


Figure 8.11: Energy density peaks along the jaw length in the case of the primary horizontal collimator (TCP.C6L7.B1) impacted in consequence of an asynchronous dump accident.

In addition, studies were performed for the evaluation of the energy density peak and the local instantaneous increase of temperature, calculated under adiabatic assumptions, for the most loaded Phase II collimators.

Since the impacting protons cover a small transverse area, suitable cylindrical three dimensional grids were used for the scoring (i.e. $0.25\text{ mm}^2 \times 1\text{ cm}$ (along z) bins on the jaw surface).

Table 8.7 reports the peak values for the three scenarios under study.

Fig. 8.11 shows the energy density peak profiles along the collimator jaws in the case of the TCP.C6L7.B1 directly impacted. The maximum peak values are almost the same for the 60 cm long TCP directly impacted jaw and for the most loaded 92 cm long Phase II jaw in the TCSM.A6L7.B1 position, but they are located at different places along the jaw, because of the different jaw material radiation length. While the Phase I jaws show a marked asymmetric heating (obvious for the TCP.C6L7.B1 directly impacted only on one jaw), in the Phase II jaws this asymmetry is less pronounced because of the propagation of the particle shower generated by the primary particle interactions.

The FLUKA simulations of the asynchronous dump scenario point out that the Glidcop Phase II collimators will be always the most loaded ones for this type of failure. Results show that, when a SLAC Phase II collimator is directly impacted, it is seriously damaged and most probably destroyed. Other possible design solutions shall be investigated for these special locations.

8.4 The SLAC Phase II jaw rotation mechanism

The current SLAC jaw rotation mechanism is set up by an internally actuated drive, which utilizes a ratchet attached to a *Geneva Mechanism*, or *Maltese cross* (see Fig. 8.12). It translates a continuous rotation into an intermittent rotary motion, allowing for the precise rotation of the jaw in increments of $1/20^{\text{th}}$ of a revolution, or one facet face. The mechanism effectively guarantees against the accidental over-rotating of the jaw because the jaw only begins to rotate after the 8^{th} ratchet past the last rotation.

The ratcheting is performed by over-retracting the jaw whereby the ratchet hits a *hammer* attached to the chamber wall. Successive over retracting rotates the jaw with a total of 512 ratchets resulting in one facet rotation when using a tri-lobed Geneva driver (see Fig. 8.12). The ratchet hammer must be pressed by roughly 3 mm in order to advance the ratchet gear, therefore, during a rotation one end of the jaw will successively move in and out by about 3 mm to ratchet the jaw. The other end of the jaw can remain still.

In the framework of this PhD, I have participated in the hardware upgrade and software commissioning to adapt the Phase I jaws movement control and instrumentation in order to perform the SLAC jaw rotation, working 3 months at the SLAC laboratory in USA.

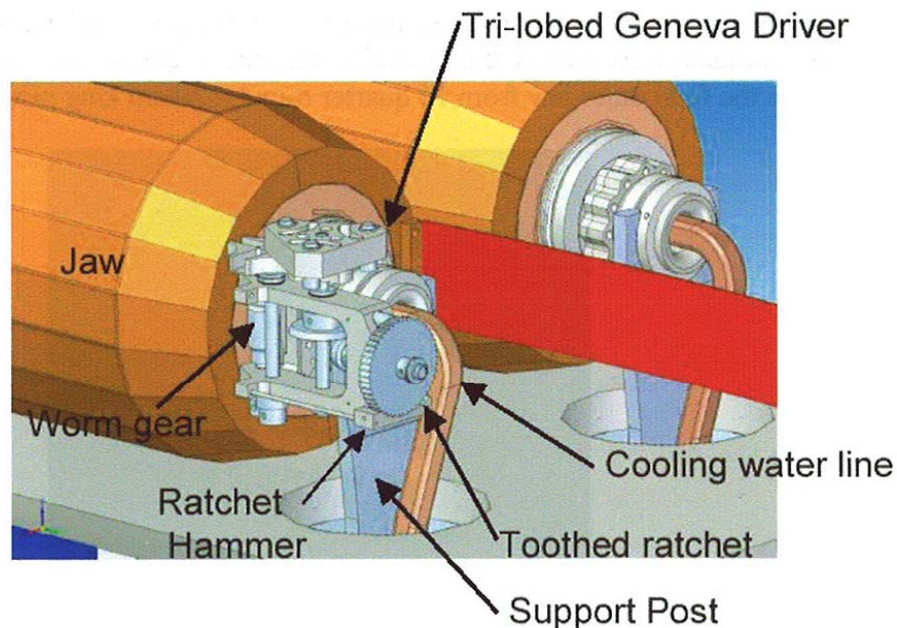


Figure 8.12: View of the shaft support showing the Geneva Mechanism for precision jaw rotation.

In Fig. 8.13 is shown the schematic view of the current precise system of motors and position sensors for the accurate setting of the Phase I collimator jaws. Actually, four stepping motors are used to move the corners of the two jaws. Four resolvers are connected to the stepping motors and monitor the number of steps performed. Six position sensor (four potentiometers and two linear variable differential transformers LVDT) are used to measure respectively the actual jaw positions and the upstream and downstream gaps. Ten switches (one full-in and one full-out at each corner plus two anti-collision switches) are installed to trigger motor steps and to protect the collimator mechanical system [30]. Metrology measurements showed that the system has mechanical plays of the order of $30\text{-}40\text{ }\mu\text{m}$, that can be taken into account for jaw movements. Jaws positions are monitored with about $\pm 20\text{ }\mu\text{m}$ accuracy (i.e. better than the collimator alignment in the tunnel).

To rotate the SLAC jaw facet by over-retraction, it was chosen not to add ex-

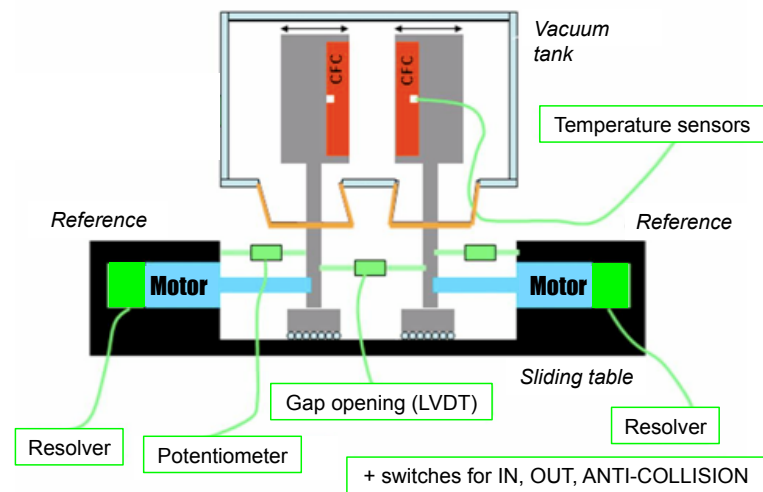


Figure 8.13: Schematic view at one jaw end of the Phase I movement control and instrumentation.

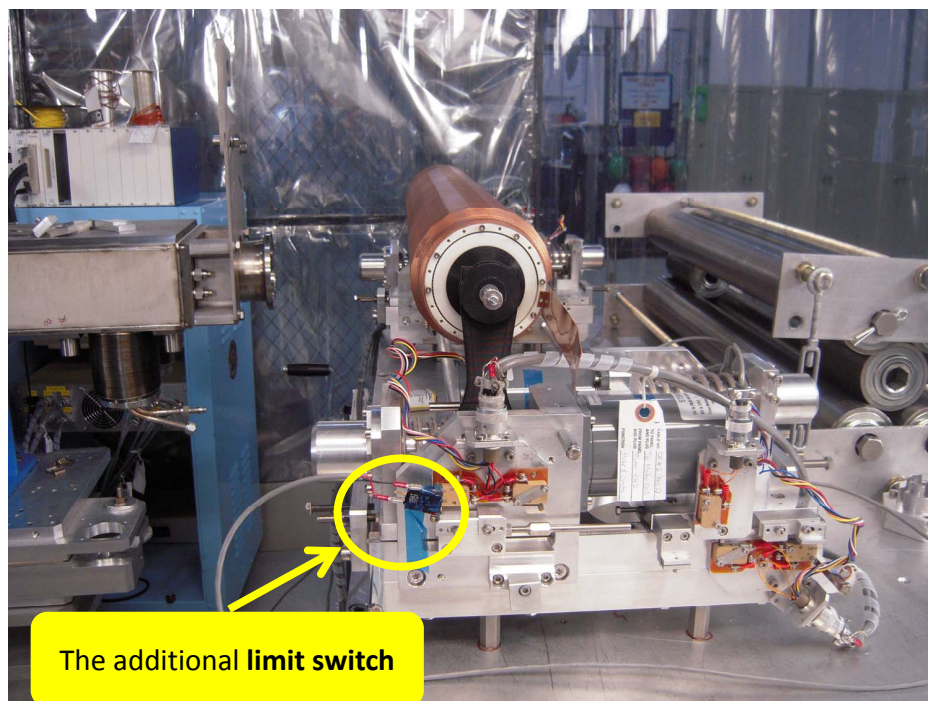


Figure 8.14: Picture of the additional limit switch for one SLAC jaw during the feasibility tests at SLAC laboratory.

tra moving parts to the CERN Phase I collimator drive hardware, but to use the same four step motors to insert and retract the jaws, inserting two additional limit switches, one for each jaw (see Fig. 8.14). Each limit switch is installed behind the current *end switch*. They are used to control the limit in motion of the jaw end to fully push the ratched hammer by 3 mm. Every time the jaw touches the hammer and then retracts, the jaw will be turned. One facet rotation requires 512 ratchets using this technique, which takes an extended period of time of the order of hours. Fortunately, the facet rotation is foreseen to occur roughly once per year and not during normal operation.

The CERN Labview program for the control setting was thus modified in order to integrate the additional "rotate jaw" option for the SLAC design. The scheme of the actions managed by the integrated routine is shown in Fig. 8.15.

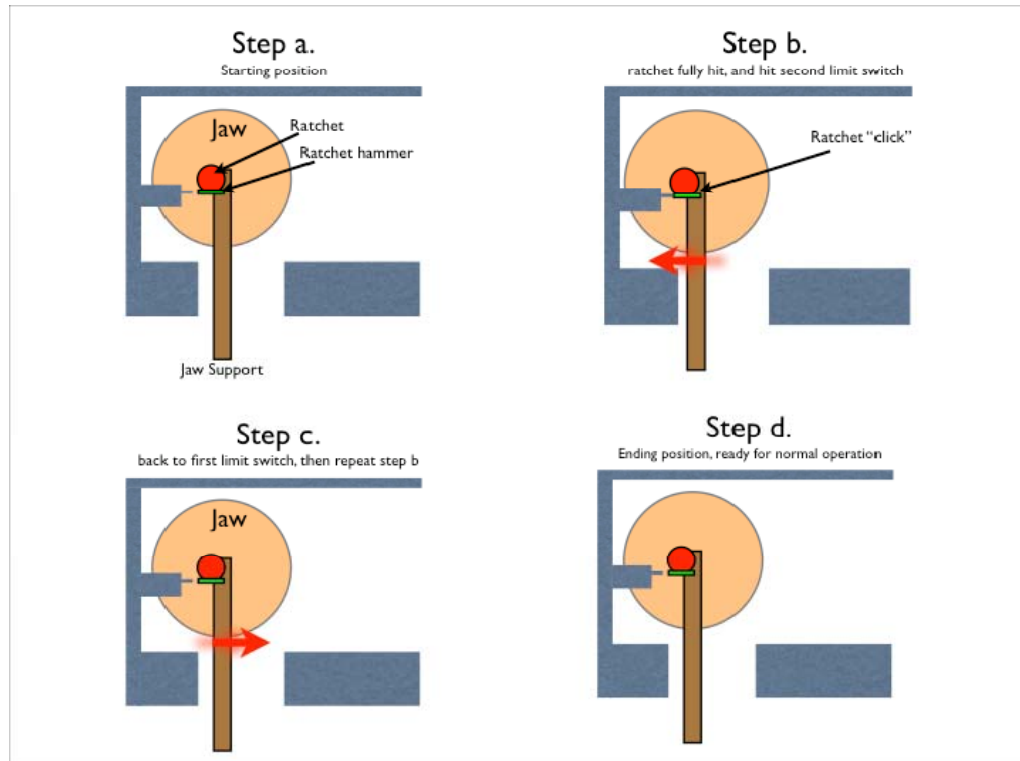


Figure 8.15: Schematic view of the actions performed by the additional routine created to rotate the SLAC jaws.

8.5 Conclusions on the SLAC Phase II design

On the basis of the FLUKA calculations, the *non permanent* jaw deflections of the SLAC collimator design were evaluated.

The heating due by the impacting beam losses during operation conditions is strictly connected with the collimator system performance, in particular for what concerns the first in line TCSM.A6L7.B1 collimator, which is taken as reference for the design.

However, the interaction between the mechanical engineering development and the FLUKA simulations performed during my PhD was brought from a factor 5 to 2 the active length reduction due by jaw heating from the ideal value of 91 cm , for the worst operation case in transient conditions (i.e. 0.2 h beam lifetime, see Table 8.1).

To support the mechanical integration of SLAC collimator components (e.g. tank, jaw support, cooling circuits, etc.), FLUKA simulations were also performed for specific studies, adding regions to the model, where necessary, until eventually reaching a high degree of realism.

At the heating value predicted by FLUKA for the steady state scenario (i.e. about 9 kW per jaw, see Table 8.2), a benchmarking test was set up at the SLAC laboratory to measure the sagitta at six azimuthal locations to be compared with the ANSYS predictions (see Fig. 8.16). The outcoming disagreement of 12% is small,

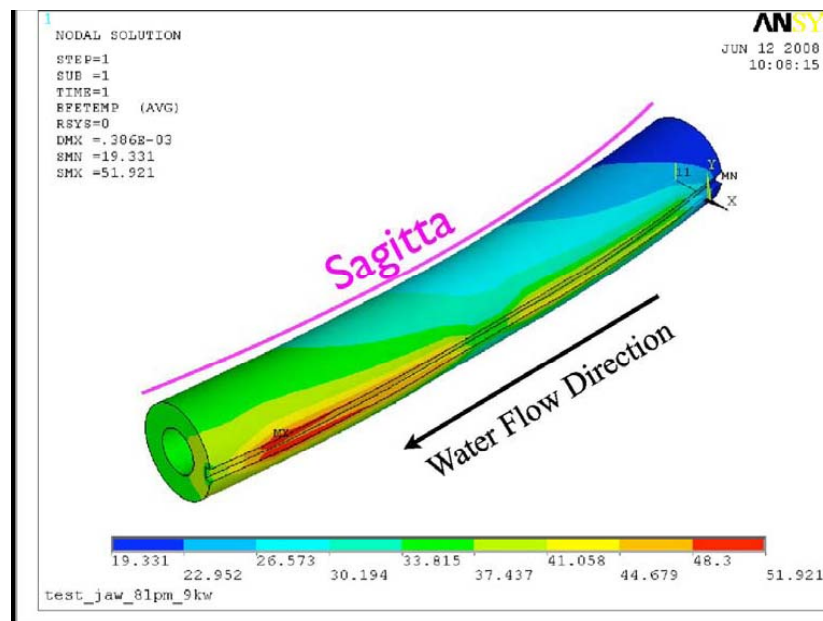


Figure 8.16: Jaw sagitta and temperature distribution under 9 kW heat load, simulated by ANSYS, on the basis of the FLUKA 3D model results.

considering that the simulations give the jaw deformation a realistic beam heating [67].

Two SLAC prototypes are under final production and they are foreseen to be at CERN at the beginning of the next year (2011). They will be installed one in the SPS accelerator, to evaluate its performance with beam, and the other in a High Radiation Material (HiRadMat) test facility, opportunely designed to perform beam shock and impact test for beam intercepting devices [68]. The aim is to evaluate the Phase II behaviour under extreme conditions similar to what was simulated for the asynchronous dump scenarios, in order to assure that even in the case of collimator destruction, the downstream beam line devices are safe.

Chapter 9

The CERN Phase II design

On the basis of experience gained with the development and production of Phase I, CERN proposes for the Phase II collimators a modular design concept which foresees a common baseline for the jaw assembly and allows the use of alternative materials for the jaws themselves. This approach permits the development of diverse solutions with a single supporting structure [69].

The CERN option focuses on the use of a linear collimator design (as for the Phase I) which can accommodate about 5 beam local damages in comparison to the 20 ones of the SLAC design, but improving the thermal shock resistance and reducing the jaw elastic deflections in the most critical collimator positions, with the investigation of different materials than Copper or Glidcop and jaw support solutions [70].

The challenges posed by the development, experimental characterization and industrialization of these advanced materials are tackled in a collaboration involving academic and industrial partners in the framework of the FP7 European research program.

9.1 Main features of the CERN Phase II design

An intense effort is being devoted at CERN to material investigation, in particular by the Design Team, in order to identify new solutions that could comply with extremely demanding specifications of Phase II collimators. In addition, the choice of promising materials was carried out considering the functionality of the different Phase II collimator components.

For all the design solutions, the jaw assembly is composed of a rigid back stiffener and an equipped jaw with the cooling circuit. The combined approach of material and design optimization allowed the identification of potential materials for each component of the jaw assembly.

9.1.1 The back stiffener

The main function of the back stiffener is to ensure, through the fine adjustment system, high geometrical stability to the jaw surface under thermal load. The adjustable system allows jaw flatness control to compensate gravity sag and minimize thermal deflection.

The back stiffener should ideally have a very high thermo-mechanical stability (i.e. a high ratio Ek/α , where E is the Young's modulus, k the thermal conductivity and α the Coefficient of Thermal Expansion (CTE)).

Upon these considerations and the FLUKA preliminary evaluations of the power load on the jaw support, Molybdenum was considered as a promising choice, not only for its suitable thermo-mechanical properties, but also from the manufacturing point of view and for its expected radiation hardness.

9.1.2 The cooling system

The use of higher-Z materials implies the increase of deposited energy.

Different options were investigated to improve the cooling efficiency. A jaw back casted pipe design as well as a cooling circuit directly machined from a solid block with brazed cover were evaluated as possible solutions.

In particular, in the latter proposal, OFE-Cu and Stainless Steel were considered to ensure high reliability of the brazed joint and to avoid any problem concerning Ultra-High-Vacuum (UHV) tightness of the cooler.

9.1.3 The jaw

Two options for the jaw material were identified in relation to the beam stabilization method to be employed.

The first one concerns the use of highly conductive jaws, coupled with a Landau octupoles stabilization system. This option requires the maximization of the electrical conductivity, therefore Copper or Glidcop represent typical solutions. However, in order to improve thermo-mechanical stability and thermal shock resistance while keeping a high electrical conductivity, advanced thermal management materials can represent valid candidates, particularly Copper-Diamond (Cu-CD).

The second option is focused on the investigation of jaw composed by a non conducting material to be bonded on a conductive support, coupled with the transverse feedback stabilization method. Tailored electrical resistivity in order to exploit at best the inductive by-pass effect (see [71] and [72] for details), together with good thermo-mechanical stability led to the choice of Silicon Carbide (SiC) material, which in addition has a better thermal shock resistance with respect to Cu-CD.

Properties of relevant materials for the jaws are collected in Table 9.1 in comparison with the CFC used for the Phase I jaws.

Table 9.1: Physical properties of the most promising jaw materials for the CERN Phase II design.

Jaw material	Density [kg/m^3]	Thermal conductivity [$Wm^{-1}K^{-1}$]	CTE [K^{-1}]	Electrical resistivity [Ωm]
Cu	8900	395	17×10^{-6}	17×10^{-9}
Cu-CD	5500	500-600	$6-7 \times 10^{-6}$	90×10^{-9}
SiC	3200	250	$3.5-5 \times 10^{-6}$	10^0-10^2
CFC	1650	60	1.5×10^{-6}	7×10^{-6}

9.2 The evolution of the CERN Phase II Copper based design

As already mentioned, the CERN design for Phase II is an evolution of Phase I, in which extensive re-designing has been carried out on jaw assemblies to respond to new requirements. Attention was devoted to flatness control, minimization of

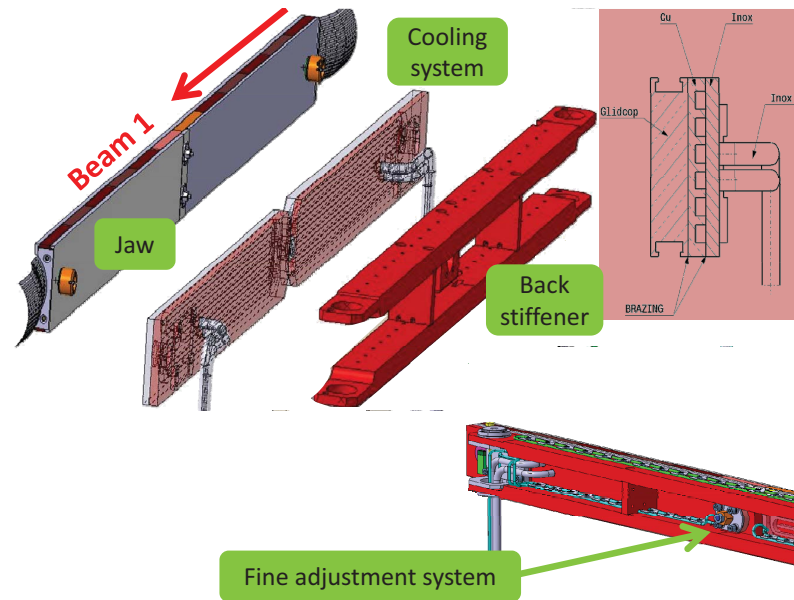


Figure 9.1: CERN Phase II design baseline. Modular design including (from left to right) equipped jaw, cooling system and back-stiffener. A cross section of the collimator jaw and the location of the fine adjustment system in the middle of the back stiffener are also shown.

induced deflection and heat evacuation, with particular attention in the case of Copper based jaws.

To limit the thermal deflection on the most loaded Phase II location along the Beam 1 line (i.e. TCSM.A6L7.B1), different mechanical designs and FLUKA models were created.

The preliminary one was based on using one intermediate adjustable support (see Fig. 9.1), in order to maximize the geometrical stability during heating. A realistic FLUKA description was created in order to provide a 3D energy deposition map to be used for the following FEM analysis. The model was developed in such a way to allow FLUKA simulations with the whole jaw in Copper (or Glidcop) or with a 2 mm Cu coating foil onto a Cu-CD based jaw (see Fig. 9.2).

In order to minimize the active length reduction due by jaw elastic deflection and thus improving the collimator cleaning efficiency, the design solution described above was modified introducing two intermediate jaw adjustable supports. The

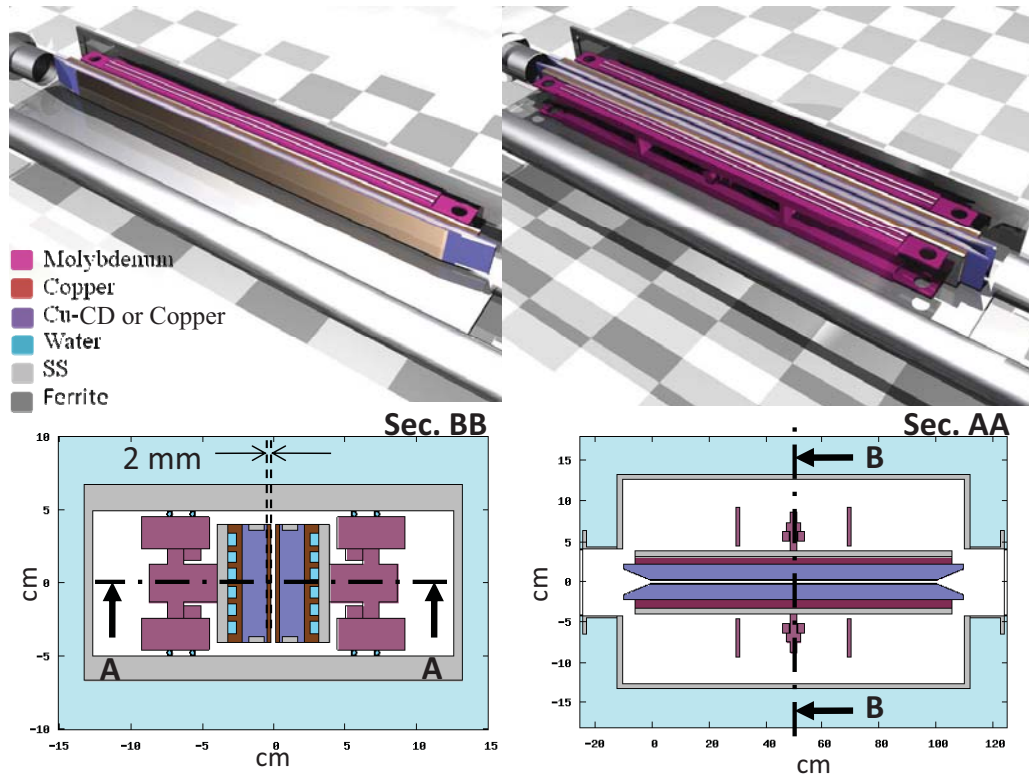


Figure 9.2: FLUKA model of the preliminary CERN Phase II design version. The violet jaw material can be Copper or Cu-CD in accordance with the simulation specifications.

collimator jaw was cut in 3 pieces independently supported on the back stiffener and independently cooled by 3 separate brazed coolers.

A preliminary analysis was performed using a FLUKA model with equal long cuts in a 1 m long jaw. Additional FLUKA and FEM optimization studies brought then to fix the lengths of the 3 jaw pieces.

As already shown by the preliminary FLUKA calculation (see Chapter 7, Section 7.4), the power density peak is calculated to be at about 20 cm from the jaw beginning, in the case of a copper based jaw. The first cut was fixed at 24.4 cm, while the second and third pieces are 30 cm and 44.4 cm long respectively. This jaw division was considered valid for all the Phase II replica along the IR7 SS line, because it is expected that the peak will be located at about 20 cm (or less) in every case. Between subsequent jaw pieces and between the lateral jaw pieces and the tapering parts, RF finger contacts were introduced to ensure electrical conductivity (see Fig. 9.3).

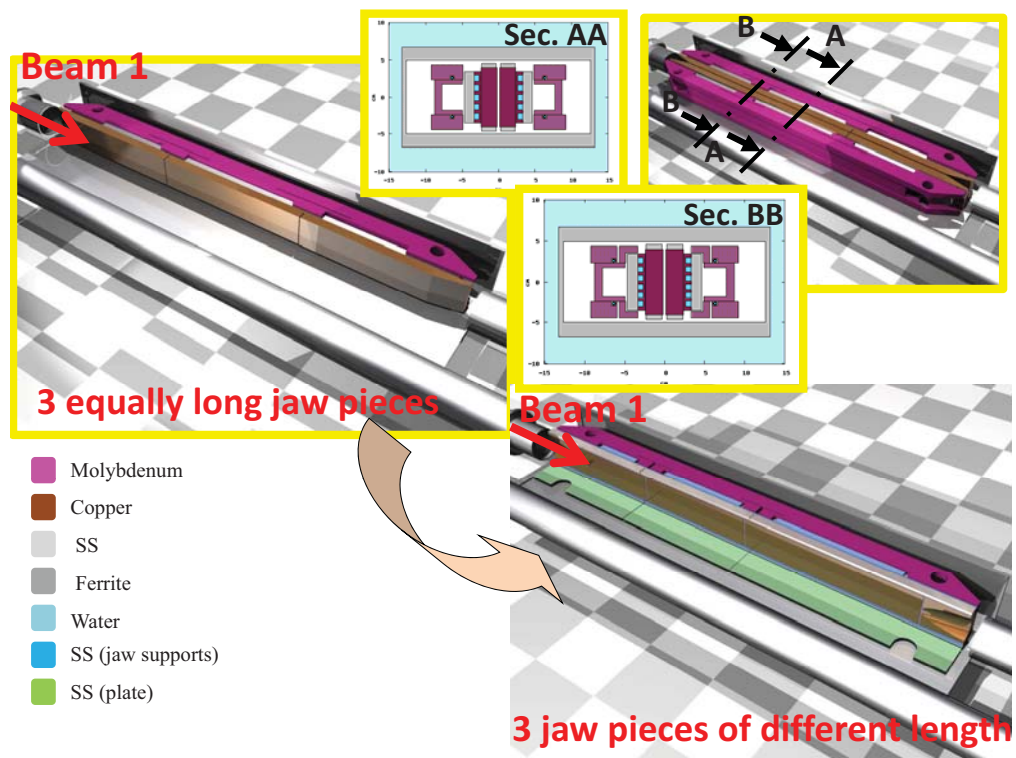


Figure 9.3: Evolution of the CERN Phase II FLUKA model with the jaw cut in 3 pieces.

Fig. 9.4 shows the detailed FLUKA model created for the current and last version of the CERN design, now in phase of prototyping.

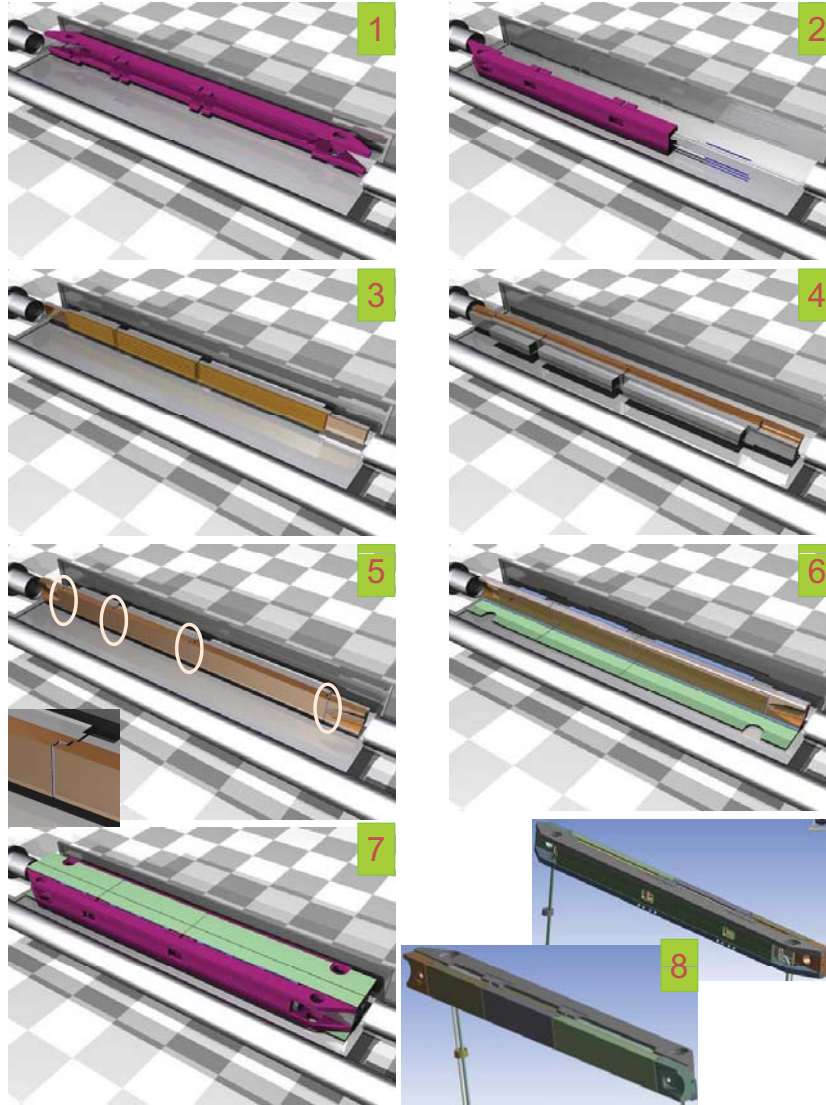


Figure 9.4: Current CERN Phase II FLUKA model components and comparison with the Ansys model (8). The back-stiffener (1) incorporates a cooling circuit (2) to maintain it at almost uniform temperature in order to maximize the geometrical stability. The jaw is also equipped with a cooling system brazed to it (3) for each composed piece (3) and with jaw stiffeners for each block (4). The RF system (i.e. Ferrite bars on SS jaw supports (6) coupled with SS plates) and the contact elements (i.e. RF fingers (5)) placed between each block are included. The whole collimator assembly is also shown (7).

The iterative process between FLUKA simulations and FEM analyses has brought to a reduction of a factor 3 of the largest deflection calculated for the Copper based jaw solution, as displayed in Fig. 9.5 [73].

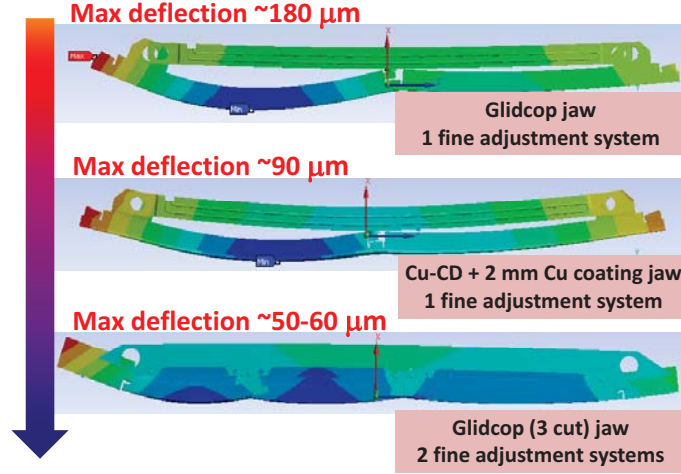


Figure 9.5: Evolution of the elastic deflections for the CERN Phase II copper based jaw design. Results refer to the 1 h beam lifetime scenario for horizontal beam losses distribution.

9.2.1 FLUKA results for operation conditions

The FLUKA results used for the evaluation of the jaw elastic deflections reported above are depending on the 7 TeV loss scenario used as input and the study is focused on the most loaded Phase II device, which in the case of Copper based jaw is the first Phase II met by each beam passing through the SS IR7 lines. In that particular position, the particle shower developed by the primary collimators brings to almost equal integral power values for the most loaded Phase II jaw in the 3 scenarios of losses (i.e. horizontal, vertical and skew). Moreover, power density peak values and their localizations on the most loaded jaw surface are similar (see as reference Fig. 8.8 and Table 8.2 in Chapter 8). For these reasons it was assumed that any distribution could be selected to perform the jaw deflection evaluations.

In these PhD studies it was chosen to use horizontal losses distribution as reference for the Phase II jaw deflection studies as well as to support the integration of the collimator components in the case of operation condition simulations.

Fig. 9.6 shows the total power deposited in each Phase II collimator assembly in the IR7 sequence order, where it is evident the factor of 5 between the first and second Phase II collimators located along the Beam 1 line.

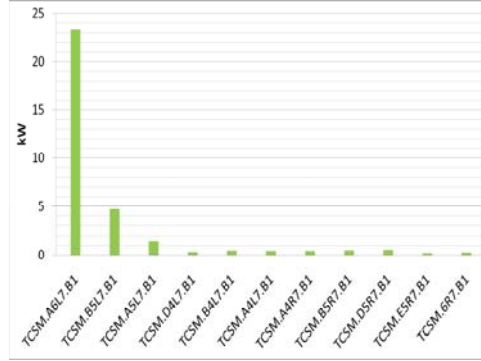


Figure 9.6: Power load distribution on the 11 Phase II Copper based jaw collimators CERN design (1 h beam lifetime scenario, horizontal losses distribution).

Fig. 9.7 shows two cuts of the power map used for the FEM analysis for the most loaded Phase II collimator.

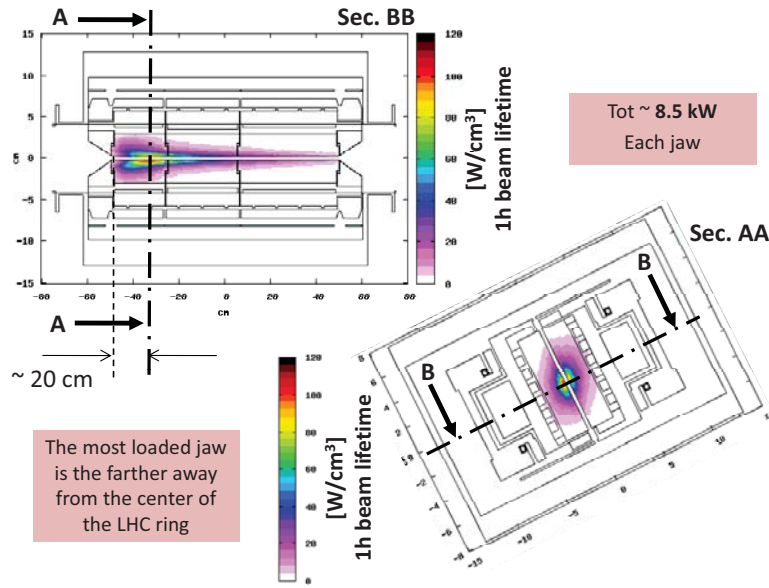


Figure 9.7: TCSM.A6L7.B1 3D power deposition map cuts (1 h beam lifetime scenario). Top (i.e. Sec.BB): longitudinal cut at the beam height. Bottom (i.e. Sec.AA): transverse cut at the depth of the maximum. It has to be noted that the coordinate system refers to the prototype in the parking, which in the case of this specific location undergoes a rotation of 142.5° as indicated in Appendix B.

The results shown in Fig.9.6 and in Fig.9.7 refer to the case in which cryo-collimators are set. The introduction of cryo-collimators in the LHC has the goal of providing the cold magnets in the DS with a local protection, and the effect of distributing the direct losses on more elements. Fig.9.8 shows the comparison between the two losses distributions along the LHC ring collimators for a horizontal halo scenario.

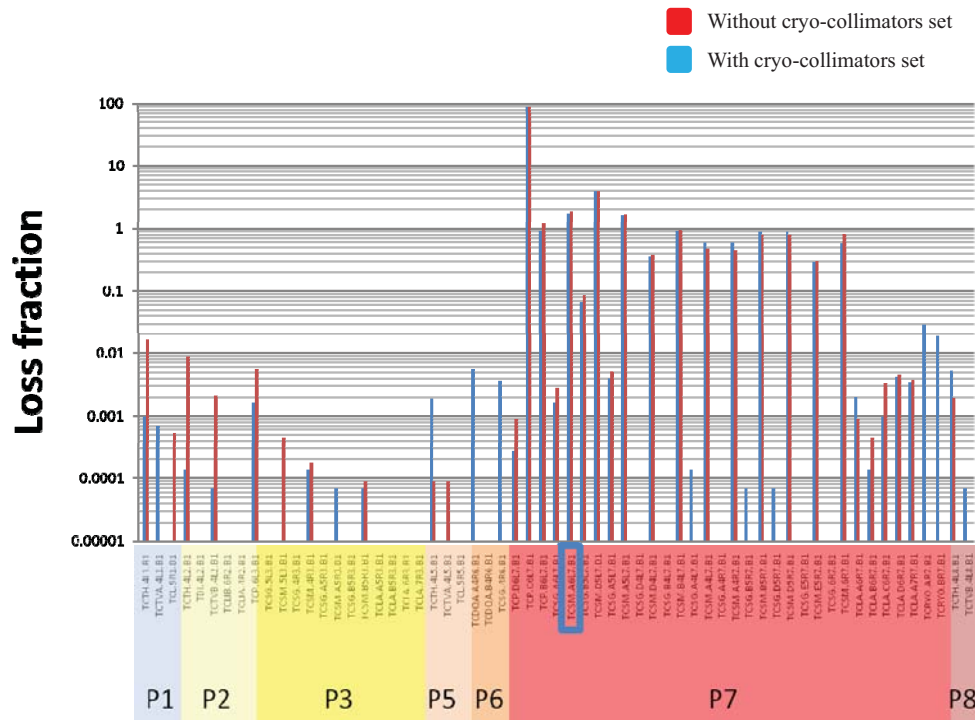


Figure 9.8: LHC loss maps for the Beam 1 nominal horizontal scenario with and without cryo-collimators. In particular the direct losses on TCSM.A6L7.B1 are put in evidence.

However, the addition of the cryo-collimators in the LHC optics simulations is negligible for what concerns the power deposited on the most loaded Phase II collimator, which is used as reference for the design. This is proven in Fig.9.9 in which, using the same binning mesh, the variation on the power density peak profile for the most loaded Phase II CERN design collimator between the cases of presence and absence of cryo-collimators turns out not to be significant.

In addition, the Fig.9.9 shows the impact of the tapering material on the peak density distribution along the collimator. This is a typical example of mechanical

integration support studies performed with FLUKA during this PhD in order to indicate solutions and to investigate different material choices. In this particular case, it was quantified how much Aluminum taperings are better than Copper ones, in order not to increase the power load in the first part of the jaw and especially on the upstream tapering, which is not cooled as well as the downstream one.

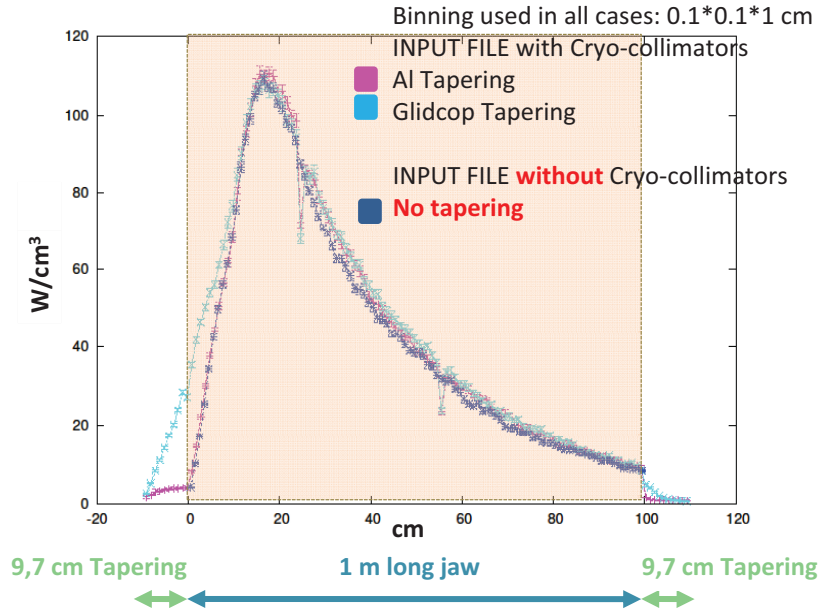


Figure 9.9: Comparison between power density peaks for the most loaded Phase II collimator using loss maps with and without cryo-collimators. The blu line refers to a preliminary CERN FLUKA model in which the tapering part was not yet added. The light blue and pink lines refer to the actual CERN Phase II design for which different materials for the tapering were evaluated.

Many power distribution maps, referring to different geometries, were provided to FEM experts and specific FLUKA analyses not reported here were performed during this PhD, before converging to the current CERN Phase II design.

9.2.1.1 The contribution of direct proton losses vs. upstream shower

In order to understand the origin of power load on the most loaded Phase II collimator, the contribution of direct 7 TeV proton losses has been disentangled from the one of the particle shower generated upstream.

The study was performed scoring the power deposited on the TCSM.A6L7.B1 for two different input loss maps. In the first case, horizontal halo distribution is used. In the second case, the direct losses on the Phase II collimator under study are removed from the horizontal halo loss map, in such a way to consider only the particles shower coming from the upstream elements.

Since the direct losses are localized close to the surface of the collimator jaws, their effect can be particularly appreciated in the evaluation of the power density peak, which is located on the jaw surface.

It has to be noted that the evaluation of the jaw elastic deformation is strictly dependent on the power density peak profile and in particular on its maximum.

Fig. 9.10 shows the power density peaks in the two cases. The contribution of the shower to the peak values is evidently higher in comparison with the contribution of the direct losses. The importance of the shower is even more evident when looking at the total power for which the contribution of the direct losses is negligible.

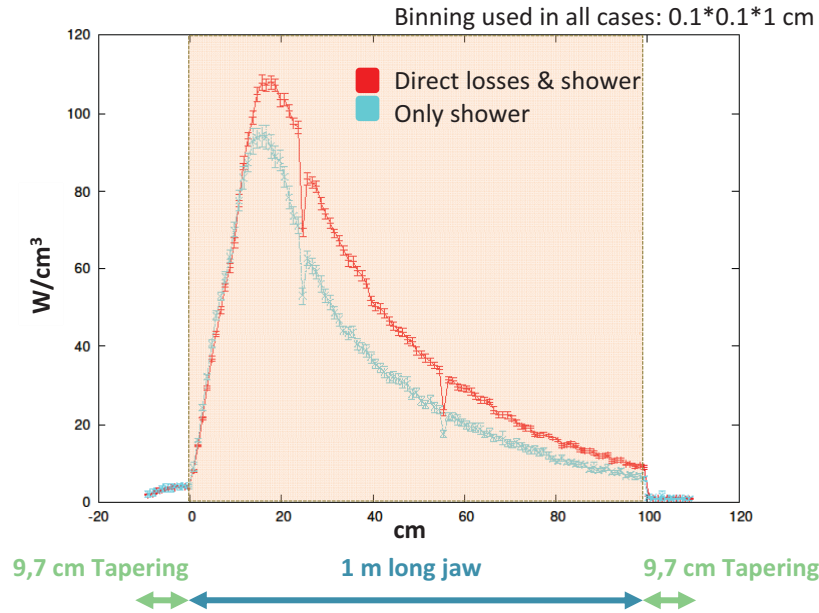


Figure 9.10: Power density peak profile for the most loaded Phase II collimator (1 h beam lifetime). The contribution of the shower generated upstream is shown, pointing out its dominant role with respect to the contribution of direct losses (i.e. beam protons lost in the collimator jaws).

Similar results are obtained with the investigation of different halo distributions.

9.3 CERN Phase II jaw material comparison

Different Phase II jaw materials imply different power loads on the collimator itself and on the LHC elements downstream, due to the different shower propagation.

To compare the behaviour of Phase II jaws composed by a non conductive material against the Copper based ones, the asynchronous dump scenario was used for a first evaluation (preliminary FLUKA calculations are reported in [74]).

The non conductive jaw, proposed by CERN, is composed by 47, 2 cm long, SiC tiles, with 1 mm gap between each other, bonded on a Copper or a Cu-CD support. The CERN modular approach allows the implementation of these jaws using the same design for what concerns the cooling system and the back stiffener (see Fig. 9.11).

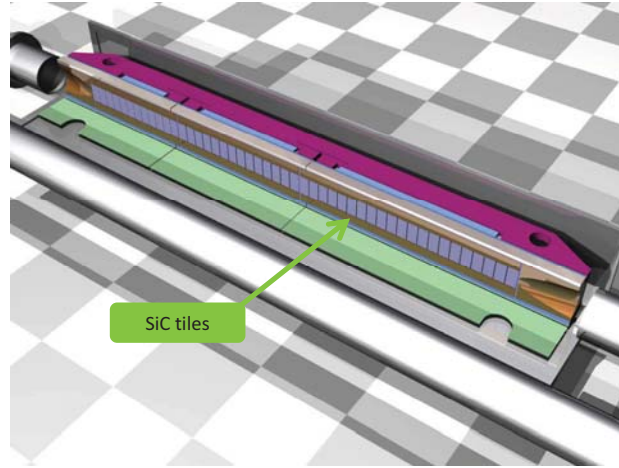


Figure 9.11: FLUKA model of the CERN non conductive jaw design for Phase II collimators.

The input files used refer to an impact of 5.4 nominal LHC bunches on the TCP.C6L7.B1 primary collimator, of 4.1 bunches on the TCSM.B4L7.B1 first Phase II horizontal collimator and of 4 bunches on the TCSM.6R7.B1 second and last (in the SS IR7 line) Phase II horizontal collimator.

The numbers of impacting bunches differ from those used in the SLAC design simulations (see Chapter 8, Section 8.3.2) because the aperture of the collimators refers here to the layout in which cryo-collimators are set in the Beam 1 line. The relaxed apertures in comparison to those calculated for the nominal 7 TeV layout without cryo-collimators, including approximation errors of the half gap setting,

bring to the reduction of impacting protons close to the edge of the jaw. However, this represents a realistic scenario for LHC beam at nominal conditions when Phase II and cryo-collimators will be installed.

Five design solutions were studied separately between the two limiting scenarios of Phase II CERN design with CFC jaws, as for the Phase I, and with Glidcop jaws. For the TCP.C6L7.B1 directly impacted, the instantaneous energy deposited on all the beam elements (excluding the Beam 1 pipeline in between) is between 345 kJ and 409 kJ . For the TCSM.B4L7.B1, it is between 276 kJ and 406 kJ , and finally for the TCSM.6R7.B1, results are between 284 kJ and 458 kJ .

Different Phase II jaw materials not only imply variations on the energy deposited on the beam elements, but are responsible of different instantaneous heat loads on the beam pipeline and on the cables installed above the beam lines close to the location of impacts. The values reported in Fig. 9.12 are representative of the shielding power owned by the Phase II collimators with different jaw materials.

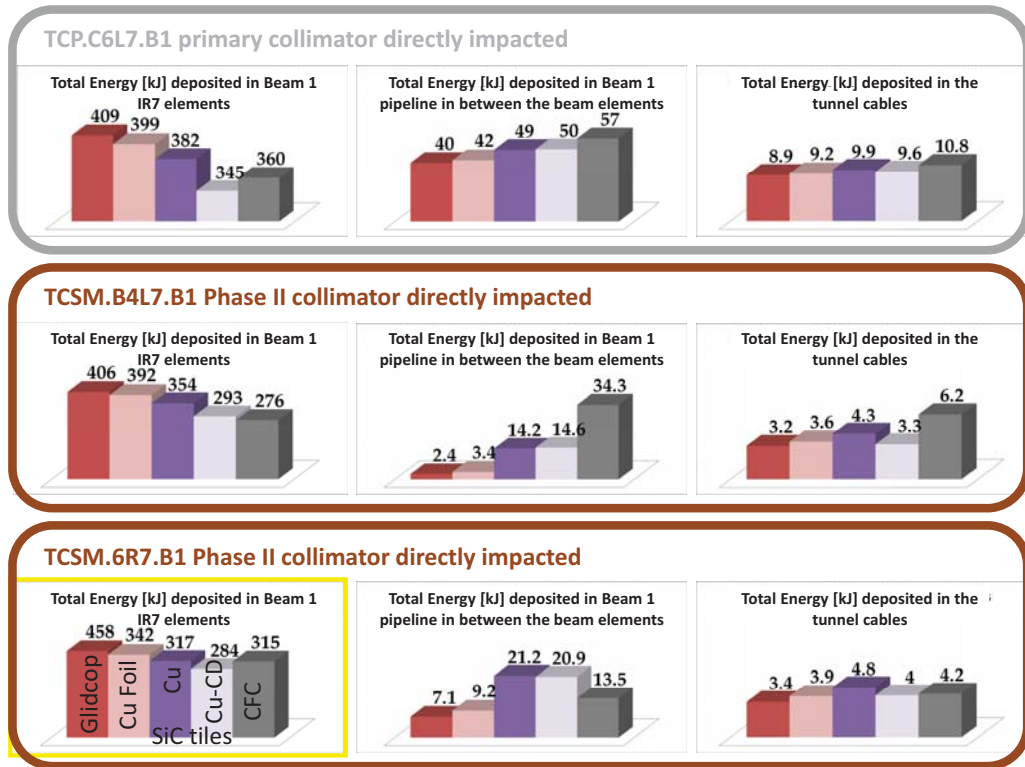


Figure 9.12: Instantaneous energy deposition due to asynchronous dumps using different Phase II CERN design jaw materials. The meaning of the different bar colors is indicated in the bottom-left frame (violet bars refer to the Phase II design with SiC tiles on Cu or Cu-CD supports, and the thickness of the Cu Foil considered here is 1 mm).

The distribution of the total energy amount (first column in Fig. 9.12) among the directly impacted collimator and the downstream beam elements is of course dependent on the different Phase II jaws.

Fig. 9.13 shows the energy deposition distribution for the three impact scenarios.

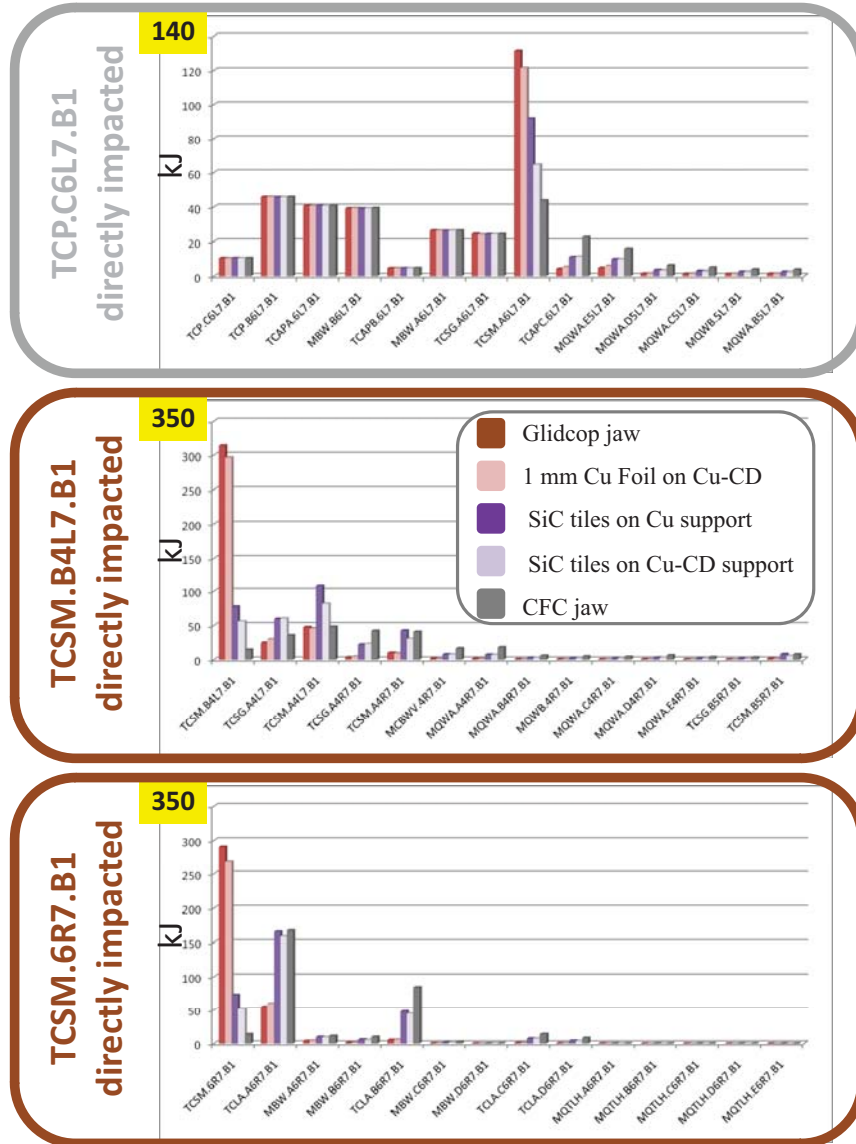


Figure 9.13: Energy deposition distributions along the IR7 line for the 3 scenarios of impact on horizontal collimators due to an asynchronous dump accident. Each color refers to a different material choice for the Phase II collimator jaws, as indicated.

When a Glidcop or Copper foil jaws is used, the most loaded element is always a Phase II collimator.

For the accidents in which a Phase II is directly impacted, if SiC tiles are used, the most loaded element is downstream, due to the particles shower propagation. In particular, when the TCSM.B4L7.B1 is impacted, the most loaded element is still a Phase II collimator (i.e. the skew TCSM.A4L7.B1), located about 3 m downstream, while in the case of TCSM.6R7.B1 (last of the 11 TCSM in the SS IR7 region for Beam 1) the most loaded device is an active absorber (i.e. the TCLA.A6R7.B1), installed just behind it to protect the cold magnets. It has to be pointed out that in these cases the energy deposition is spread over a bigger volume, in comparison to what happens on the collimator directly impacted. The asynchronous dump accident is thus less critical in terms of energy density peak in the downstream elements and in particular for the downstream Phase II collimators (see Fig. 9.14).

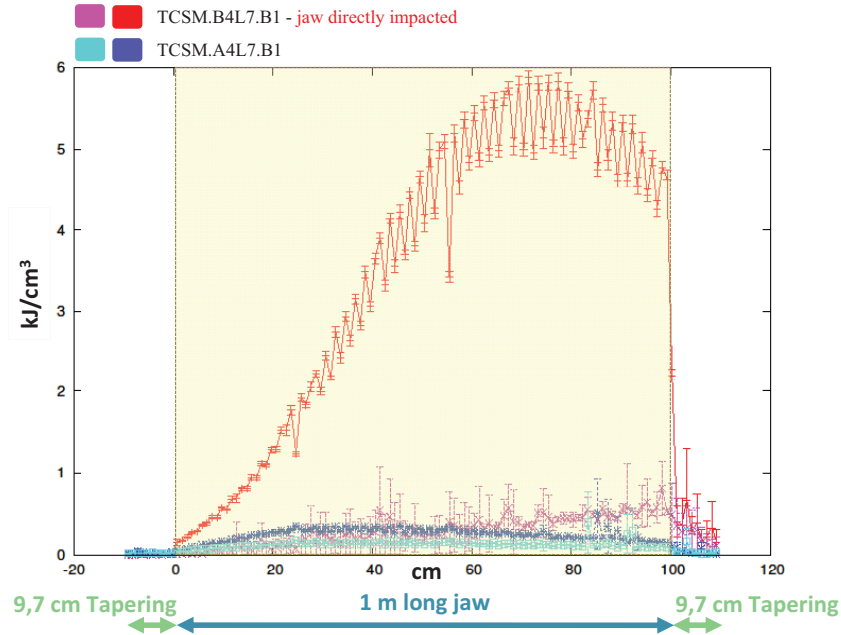


Figure 9.14: Energy deposition peak comparison between the Phase II TCSM.B4L7.B1 directly impacted on the external jaw (red curve) for the considered asynchronous dump scenario and the resulting most loaded element (i.e. Phase II TCSM.A4L7.B1). For each collimator, the peak profiles in the two jaws are shown separately. The oscillations, particularly visible in the red curve, are due to the inhomogenous surface, alternating tiles and vacuum, since the tiles overhang the Cu-CD support.

For the impact scenario on the primary collimator (i.e. the TCP.C6L7.B1), the most loaded element turns out to be the TCSM.A6L7.B1 for all the jaw design proposed, unless it is assumed to use CFC jaws, as for the Phase I. In this case, the maximum energy density is found on the skew primary collimator, installed behind the horizontal TCP.C6L7.B1 impacted. Fig. 9.15 compares the different peak profiles on the TCSM.A6L7.B1. While for the Glidcop and Copper foil jaws the localization of the maximum is at about 20 *cm* from the beginning of the jaw and on the jaw surface, using SiC tiles the energy density maximum can be reached on the tiles surface or directly on the tiles support depending on the support material used. For Copper behind the SiC tiles, it is localized at about 10 *cm* longitudinal depth in the support, while for more transparent material, like Cu-CD, it is found almost at the end of the jaw and on the SiC tiles surface.

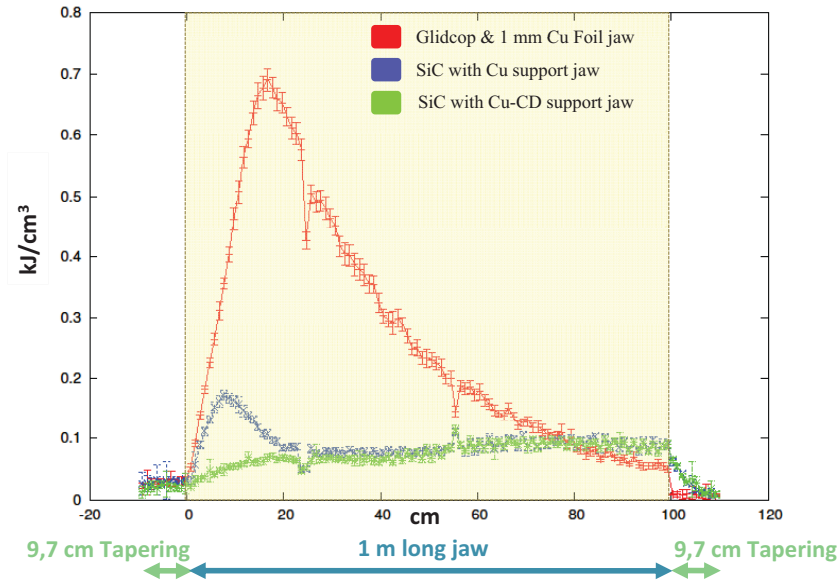


Figure 9.15: Comparison between different jaw material energy deposition peaks for the most loaded Phase II TCSM.A6L7.B1 resulting from the asynchronous dump scenario of TCP.C6L7.B1 directly impacted.

Table 9.2 summarizes the maximum values and the corresponding instantaneous increases of temperature on Phase II collimators, calculated under adiabatic conditions. In case of Phase II TCSM.6R7.B1 directly impacted, values are equivalent to those referring to the TCSM.B4L7.B1 case. In addition, since the TCSM.6R7.B1 is the last Phase II collimator on the SS IR7 line, no other Phase II devices are

Table 9.2: Energy density peaks and instantaneous increases of temperature (T) for asynchronous beam dump scenarios. Results refer only to CERN design Phase II collimators and to their most loaded jaw.

TCP.C6L7.B1 impacted → TCSM.A6L7.B1 most loaded		
Glidcop jaw	Energy on TCSM.A6L7.B1 jaw	49.5 [kJ]
	Energy density peak on the jaw	0.7 [kJ/cm ³]
	Istantaneous increase of T	180 [°C]
1 mm Cu Foil on Cu-CD base jaw	Energy on TCSM.A6L7.B1 jaw	41.3 [kJ]
	Energy density peak on the jaw	0.7 [kJ/cm ³]
	Istantaneous increase of T	180 [°C]
SiC inserts on Cu base jaw	Energy on TCSM.A6L7.B1 jaw	31.3 [kJ]
	Energy density peak on the jaw on Cu	0.18 [kJ/cm ³]
	Istantaneous increase of T on Cu	50 [°C]
SiC inserts on Cu-CD base jaw	Energy on TCSM.A6L7.B1 jaw	25.7 [kJ]
	Energy density peak on the jaw on SiC	0.1 [kJ/cm ³]
	Istantaneous increase of T on SiC	25 [°C]
TCSM.B4L7.B1 impacted → different most loaded Phase II collimators		
Glidcop jaw	Energy on TCSM.B4L7.B1 jaw	152.3 [kJ]
	Energy Density peak on the jaw	65 [kJ/cm ³]
	Istantaneous increase of T	» melting point
1 mm Cu Foil on Cu-CD base jaw	Energy on TCSM.B4L7.B1 jaw	133.9 [kJ]
	Energy Density peak on the jaw	65 [kJ/cm ³]
	Istantaneous increase of T	» melting point
SiC inserts on Cu base jaw	Energy on TCSM.B4L7.B1 jaw	35.3 [kJ]
	Energy Density peak on the jaw on SiC	6 [kJ/cm ³]
	Istantaneous increase of T on SiC	~melting point
	Energy on TCSM.A4L7.B1 jaw	39.6 [kJ]
	Energy Density peak on the jaw on SiC	0.36 [kJ/cm ³]
SiC inserts on Cu-CD base jaw	Istantaneous increase of T on SiC	150 [°C]
	Energy on TCSM.B4L7.B1 jaw	29.6 [kJ]
	Energy Density peak on the jaw on SiC	6 [kJ/cm ³]
	Istantaneous increase of T on SiC	~melting point
	Energy on TCSM.A4L7.B1 jaw	32.7 [kJ]
	Energy Density peak on the jaw on SiC	0.35 [kJ/cm ³]
	Istantaneous increase of T on SiC	145 [°C]

involved. For these reasons, it is not included in the table.

Results show that non conductive Phase II jaws could mitigate the sharp temperature peak, expected in Copper based jaws in case of direct beam impact on horizontal collimators. In particular for what concerns the SiC material, it has to be noted that the increasing of the Carbon amount in the SiC mixture obviously brings to a reduction of the temperature peak. In order to avoid that the SiC melting point is reached, special mixture of SiC must thus be investigated.

9.4 Conclusion on the CERN Phase II design

Different experimental tests are foreseen to be carried out in the next future on the CERN Phase II collimator prototypes.

Based on these PhD FLUKA calculations, promising results are obtained on Glidcop jaw elastic deformation (i.e. $50\text{-}60\ \mu\text{m}$ for $1\ h$ beam lifetime) and on integrating SiC tiles on the jaws to reduce the effects of asynchronous dump accidents. Future efforts are planned on investigating several different samples of SiC mixture, in order to identify suitable materials able to minimize thermal loads and to optimize RF performances (required range for electrical resistivity is $1\text{-}100\ \Omega\text{m}$), and on studying a longitudinal multi-layer jaw, in particular for the TCSM.A6L7.B1 position. This proposed jaw is a development of the last design in which the 3 pieces are composed by 3 different material blocks (e.g. SiC in the first 24.4 cm part and Glidcop in the last two pieces). All these studies are focused on preventing inelastic jaw deformations and, in the worst cases, on avoiding to reach the melting point in the jaw materials.

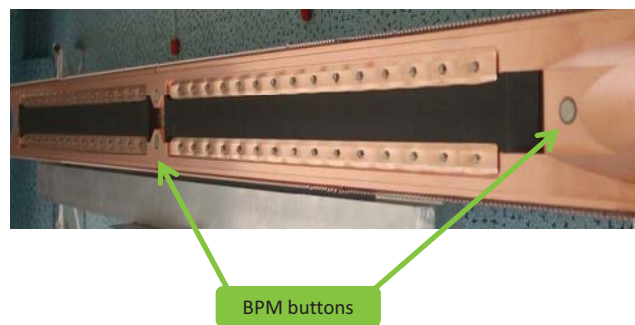


Figure 9.16: Basic CERN Phase II jaw prototype.

In addition, to support the final choice on CERN design jaw as regards collimation efficiency performance, a wide range of material tests and damage experiments are planned in the CERN HiRadMat facility. Experimental tests on the SPS accelerator at CERN are also foreseen.

Actually a basic CERN Phase II prototype (see Fig.9.16) is installed in the SPS to verify the effectiveness of the jaw assembly, especially concerning the fine adjustment system. Furthermore, the SPS tests support the feasibility study of integrating Beam Position Monitor (BPMs) buttons on the jaw center and on the tapering parts of the jaw, in order to reduce the set-up time. The impact of showers and the thermal effects on these BPMs are under study as well as their operational performance.

As for the SLAC design, the prototyping phase of these LHC devices is founded on these FLUKA results.

Chapter 10

Collimator setting errors

The results presented in the previous chapters refer to an ideal machine and perfect collimators. However, unavoidable errors in accuracy affect the beam based alignment for the set-up of the collimators.

On the basis of experimental evaluation from beam tests with Phase I collimators, specific set-up errors are identified and quantified. Namely rms and/or systematic jaw tilts, rms and/or systematic offsets of the collimator gap with respect to the ideal position (i.e. the beam center) and rms errors on the size of collimator gaps with respect to their ideal value have been evaluated [75].

In order to give a more realistic estimation of the power deposited during operation conditions on the IR7 collimators and beam elements, FLUKA simulations were performed focusing on symmetric and antisymmetric jaw tilts errors. Input files by the SixTrack experts were provided using random errors on both Phase I and Phase II jaw angles.

10.1 Beam-based alignment of the collimator jaws

The procedure for centering the collimator jaws with respect to the beam centre is the following. A jaw, e.g. the right one, is moved towards the beam until it touches it and left at a given distance from its center. Due to the betatron motion of the beam particles, both beam sides are scraped and this provides a *sharp* reference edge for the other jaw, which is then moved towards the beam in small steps. The downstream BLMs measure some proton losses only when the left jaw reaches the same distance from the beam centre as the right jaw (see Fig. 10.1). This procedure provides a centering of the jaw with a precision fixed by the motor step size. Smaller consecutive steps allow a finer centering of the two jaws with respect to the beam [76].

In addition, this method was also proposed to adjust the jaw angle with respect to the beam envelope by moving one jaw corner per time. However, tests with beam show that, when the second jaw corner is moved into place by adjustment stages (see

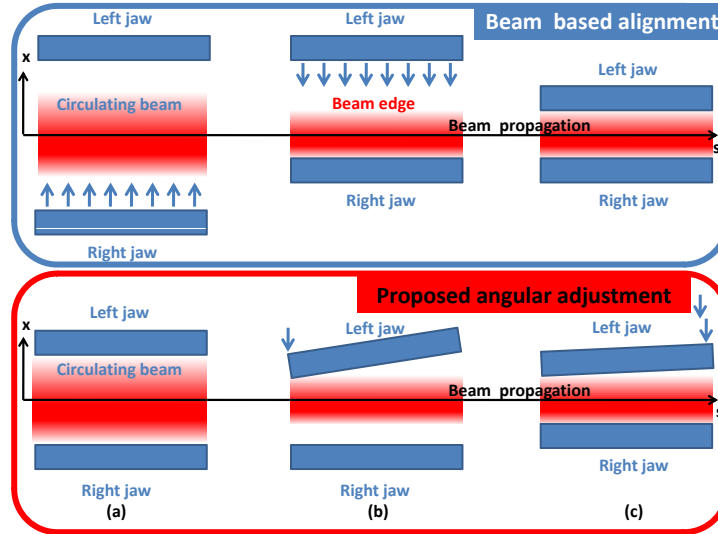


Figure 10.1: Procedure to centre the collimator jaws around the circulating beam. The beam is scraped with one jaw and the other jaw is moved towards the beam until new signals are recorded by the BLMs. The proposed and for the moment dropped angular alignment system is also shown.



Figure 10.2: Sketch of a horizontal Phase I secondary collimator installed in the LHC tunnel. The two reference points located on the tank are used for the alignment of the collimator with respect to the upstream and downstream elements of the machine.

the bottom right picture (c) in Fig. 10.1), unexpected BLM signals appear already at the first fine movement step. This effect is probably due to the change of the electromagnetic coupling field when varying the position of CFC collimator jaw resistive wall with respect to the proton beam. The angular alignment was thus performed using as reference the zero angle, relying on the collimator metrology during production and on the accuracy of the collimator alignment in the tunnel.

Using the last method described above, the maximum tilt errors of a collimator, sitting in the tunnel inside a 1.48 m long (flanges included) tank, was calculated to be $442\text{ }\mu\text{rad}$. This number includes the inaccuracies due to jaw to tank to external tank reference points (i.e. two points on the collimator tank at 64 cm distance used for the tank positioning. See Fig. 10.2) respective alignment as well as those coming from the setting of the collimator in the LHC tunnel (for details see pp 119-122 [32]).

It has to be noted that the angular alignment of the collimators is crucial in order to maximize the material seen by the beam (i.e. to maximize the actual active length for each collimator).

The idea of introducing BPMs in the jaw tapering parts and thus closer to the jaw surface, as proposed for the Phase II by the CERN Design Team, should reduce the set-up time and improving the precision on angle for the jaw alignment (tests in SPS are ongoing). On the basis of these considerations, the SLAC team is also exploring the possibility of implementing button or cavity BPMs into their design.

Fig. 10.3 illustrates the set-up errors studied with FLUKA simulations. For all the LHC Phase I and Phase II collimators, a random tilt of maximum $600\text{ }\mu\text{rad}$ is

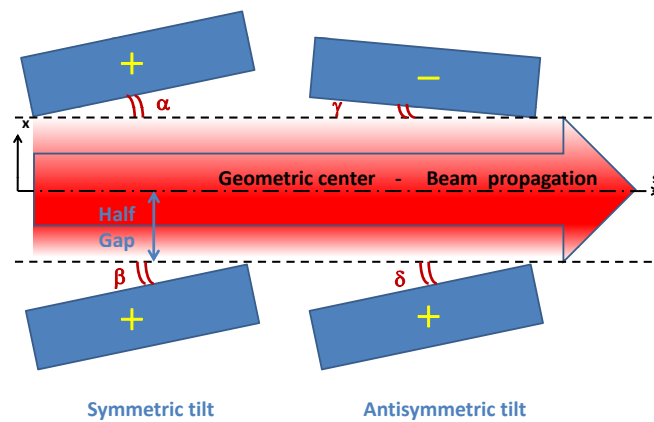


Figure 10.3: Illustration of set-up errors for the LHC collimation jaws used as input for FLUKA simulations.

assigned to each jaw by the SixTrack program. Each LHC collimator experiences thus a symmetric or an antisymmetric tilt with a different angle per jaw. Loss maps used as FLUKA input reflect these jaw tilting (see Appendix C as reference for the collimator setting used in the simulations).

The FLUKA collimator models were developed in order to allow these angular jaw variations.

10.2 FLUKA results for operation conditions

The purpose of this study is to evaluate the variation in terms of power deposited in the SS IR7 region Beam 1 line due to the collimator beam-jaw misalignments, during nominal operation conditions at low beta, in particular focusing on the tilt effects on the Phase II collimator loads.

The reference collimator design considered is the most recent CERN one with Aluminum tapering parts. The loss maps used refer to the horizontal halo distribu-

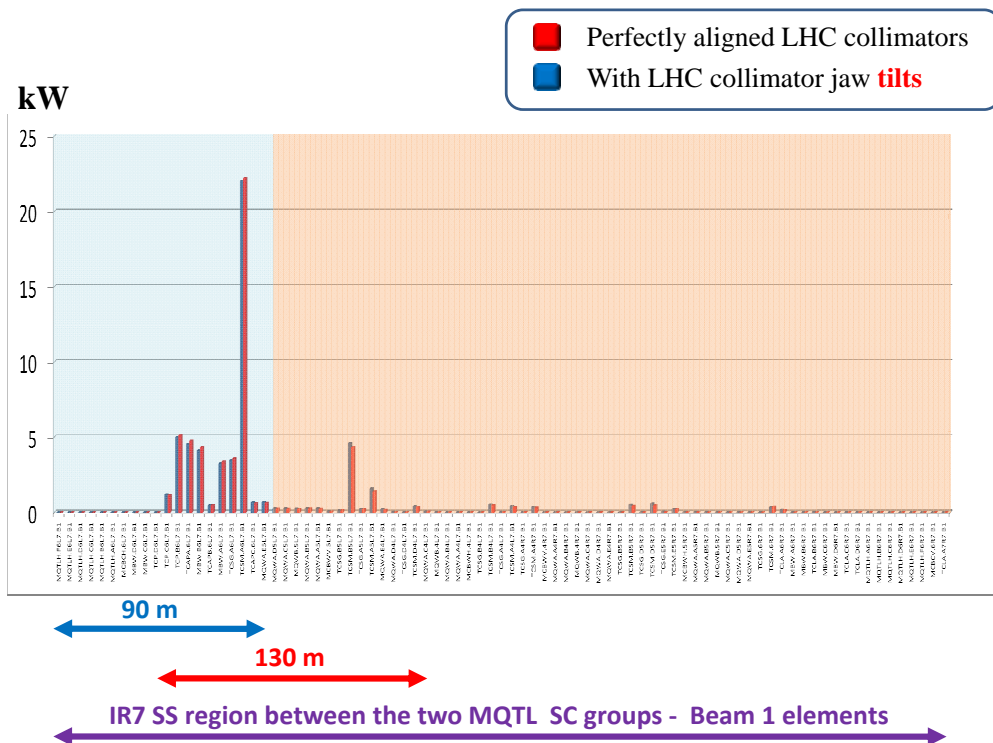


Figure 10.4: Comparison between power deposition on the SS IR7 Beam 1 elements with and without LHC collimator jaw tilts.

tion without cryo-collimators installed.

Results show that, as a consequence of the tilts, the thermal load is reduced on beam elements located in the first 90 m of the SS IR7 region, excluding the small increment on the TCP.C6L7.B1 primary horizontal collimator, and it is increased in the central and downstream SS parts (see Fig. 10.4).

Fig. 10.5 summarizes these effects on Phase II collimators for the 1 h beam lifetime steady state scenario. Negative W values have the meaning of reduction in terms of power deposited in case of tilting jaws in comparison with the perfect parallel collimator simulation results, while the positive ones represent the increments.

The jaw tilts mitigate the amount of power deposited on the most loaded Phase II collimator. However this reduction is only of about 1 % with respect to the no tilts case. An increment of about 300 W for the 1 h beam lifetime scenario is expected for the second Phase II collimator on the Beam 1 line (total heat load of about 6 % in average). Bigger percentage variations are found for Phase II collimators located in the central and downstream parts of the IR7 SS region. Nevertheless, since the

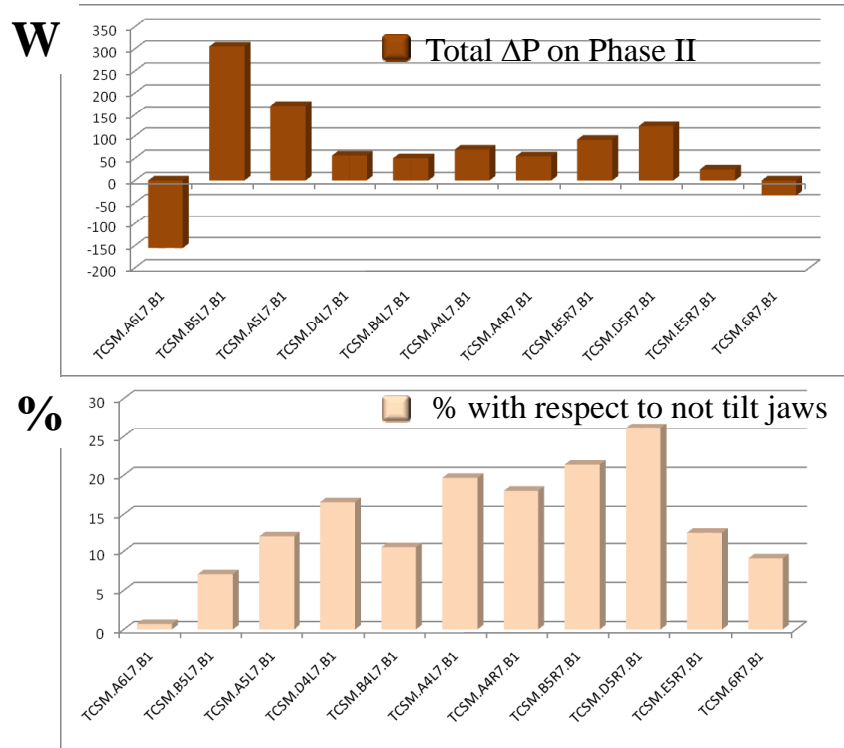


Figure 10.5: Reductions and increments on power deposition (absolute and absolute percentage) for the 11 Phase II collimators in case of misaligned jaws (1 h beam lifetime).

calculated power deposited in the other Phase II elements is significantly lower in comparison to what is evaluated for the TCSM.A6L7.B1 collimator (see Fig. 9.6), these variations cannot be the cause of plastic deflections which could bring to a mechanical Phase II design review.

In addition, a deeper analysis points out that each Phase II jaw experiments a different behaviour because of the tilts. In particular for what concerns the TCSM.A6L7.B1 collimator, the external jaw (with respect to the LHC ring center) undergoes a decrease in terms of power deposited of about 0.1 kW , while on the internal jaw, results point out a reduction ten times smaller (i.e. about 0.01 kW). Both values are calculated for the 1 h beam lifetime transient scenario.

Fig. 10.6 shows the tilt effect on each jaw for the steady state scenario. As before, differences are in absolute scale as well as in % (with respect to the parallel jaws case).

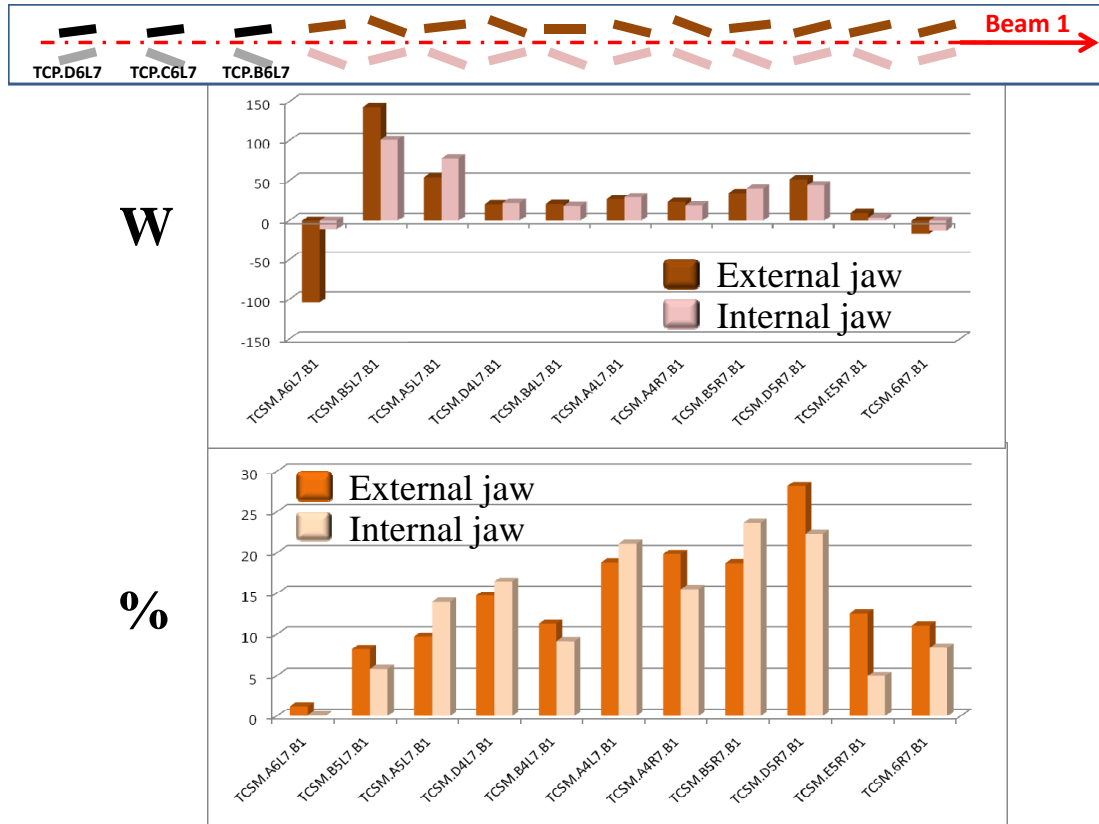


Figure 10.6: The same as in Fig. 10.5 for each jaw instead of the whole collimator. The tilt jaw orientation is also shows for the Phase II and Phase I primary colimators.

Fig. 10.7 shows the tilt consequences on the most loaded Beam 1 elements, zooming on the 130 m long region indicated in Fig. 10.4). Two primary Phase I collimators and all 3 passive absorbers are considered as well as the first 4 Phase II collimators with the respective upstream Phase I secondary ones. Warm dogleg magnets and the first SS group of resistive quadrupoles are also shown.

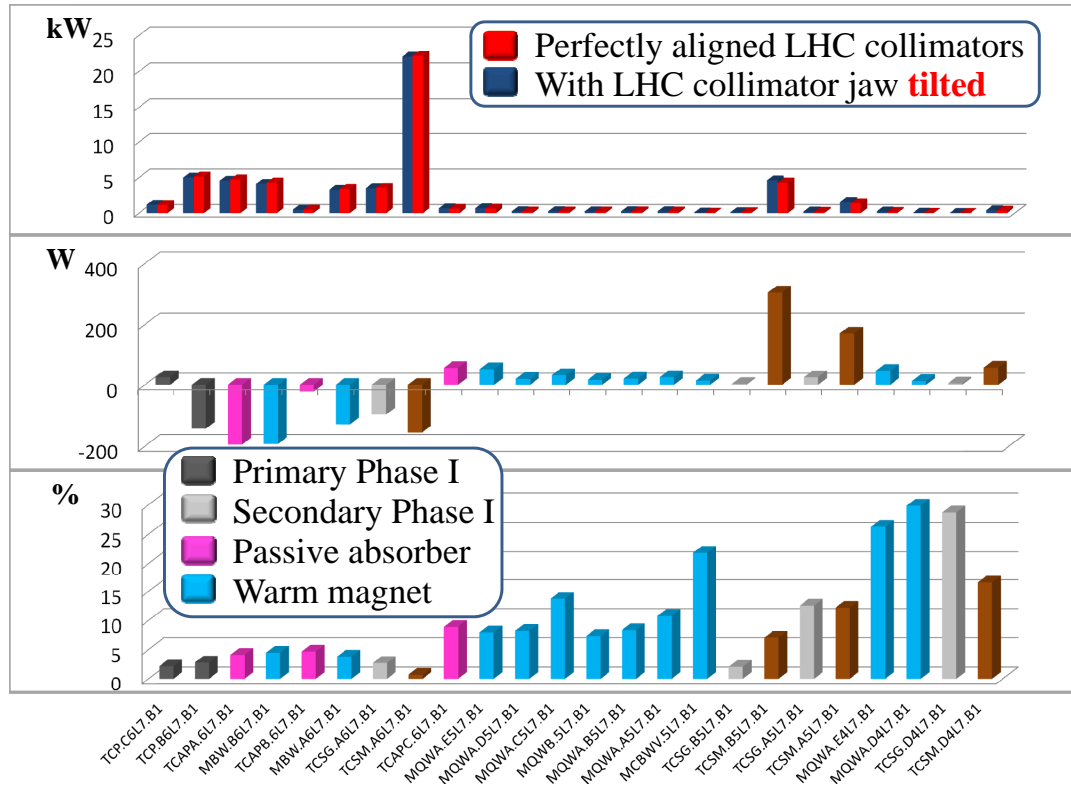


Figure 10.7: Top: Total loads along the most impacted part of the IR7 Beam 1 line (i.e. the 130 m long segment indicated in Fig. 10.4). Middle: Absolute reductions and increments. Bottom: Absolute percentage reductions and increments (tilted jaw case vs. ideal jaw case).

A beneficial effect of the collimator jaw tilts is found on the second set of the dogleg magnets at the beginning of the Beam 1 IR7 line, downstream the primary collimators. About 200 W for the 1 h beam lifetime scenario is the amount of the power reduction on the first MBW.B6L7.B1 and on the upstream passive absorber (i.e. the TCAPA.6L7.B1). However, this reduction corresponds to less than 5 % of the load on these elements.

10.3 Conclusion

Results show a minor effects on the thermal load of the Beam 1 elements along the warm section (i.e. the SS region).

In particular, the Phase II collimators are the most sensitive elements in terms of absolute increments in power deposition due to the beam-jaw misalignment. For the tilt scenario studied, the maximum growth is estimated to be of about 1.5 kW for the transient case, on the second Phase II collimators along the Beam 1 line (i.e. the TCSM.B5L7.B1). However, even with this increase, the total power deposited on this Phase II collimator represents only $\sim 20\%$ of the power deposited on the most loaded TCSM.A6L7.B1 for the same transient scenario.

It has to be pointed out that the beam-jaw misalignment evaluated in this chapter is only one of the possible errors which can affect an accelerator and in particular the Collimation System.

Fig. 10.8 shows the evolution of the Phase I collimation system performance when several imperfections are applied. The 5th scenario, which is considered the

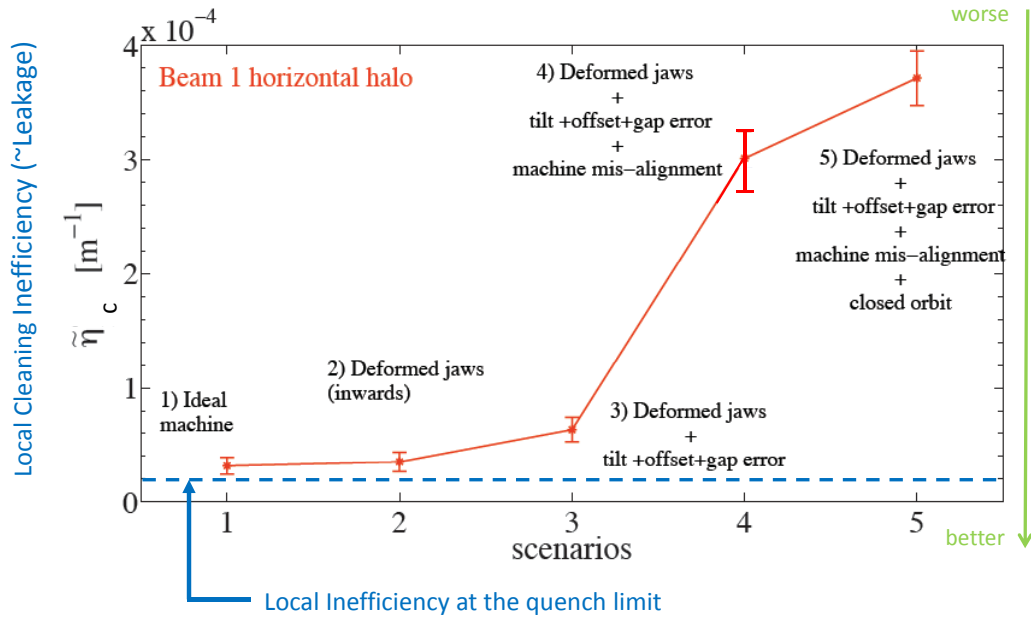


Figure 10.8: Local cleaning inefficiency for various imperfection scenarios.

most realistic one, could limit the maximum intensity reach in collimation to $< 5\%$ of nominal Intensity. In addition, further imperfections, which are not taken into account in the figure, have to be evaluated, namely effects for beta-beat, coupling and non-linearities in the LHC (for details see [32], Chapter 6).

Since, according to the beam tracking estimates of the imperfection impact reported in Fig. 10.8, the major role turns out to be played by the machine misalignment (i.e. magnet transverse displacement), the FLUKA team is actually working on assessing the change of peak power deposition in the cold section (i.e. the DS regions) for this scenario.

Chapter 11

Activation of collimator materials

Losses of the primary protons in beam line components generate nuclear reactions that produce unstable isotopes responsible of induced radioactivity.

Activation occurs mainly in beam line components exposed to large beam losses such as collimators. Depending on the average production cross section and on the half-life of the unstable nucleus produced, their radioactive decays contribute to the residual dose rate, after switching the machine off. In particular, since the highest number of proton losses are localized in the Betatron Cleaning insertion at Point 7, this region is the most critical one for what concerns its impact on radiological quantities.

In this Chapter, the focus is put on the assessment of radiation exposure of personnel during maintenance at IR7 when the Phase II collimators will be in place.

Residual dose rates to be expected during later repair or maintenance interventions must be considered already at an early design stage of each beam element and in particular for collimators. This can support the choice of Phase II materials to be used in their design as well as to give an indication of the cooling period duration to optimize access to the IR7 tunnel after LHC shutdown.

11.1 CERN radiation limits and constraints

CERN's guidelines for the protection of the environment and personnel are compiled in the CERN Radiation Safety Manual [77] which is related to the French and the Swiss National Legislation and to the European Council Directive 96/29/EU-RATOM [78]. They all base radiation protection on three general principles: *justification*, *limitation* and *optimization* of potential human exposure due to the use and operation of equipment emitting ionising radiation.

Therein the legal dose limit defines a value never to be exceeded nor to be reached and differentiates between category B workers and category A workers.

However, these limits and constraints cannot be directly applied during the construction and design work of any accelerator. It is therefore useful to introduce a

design criterion in order to ensure that the above mentioned limits and constraints will not be exceeded during operation. For high radiation areas a design criterion of 2 mSv per person and per intervention is applied. Estimated or calculated individual doses getting close to 2 mSv must raise awareness and imply further optimization of design and work procedures.

11.2 Details of FLUKA calculations

The simulation of residual dose rates employs the capability of FLUKA to simulate in the same calculation prompt particle showers as well as radioactive decay at different cooling times and the transport of the associated radiation.

Dose equivalent due to induced radioactivity was calculated by folding during the simulation (at scoring time) particle fluence with energy-dependent fluence-to-ambient dose equivalent conversion factors [80] [81].

In addition, during a first successful full scale Phase I collimator test in the SPS-LHC transfer line (TT40), the applied FLUKA simulation method was benchmarked with measurements of residual dose rates for two different cooling times of one week and one month [79]. Both agreed within 10% and confirmed the accuracy of the simulation approach not only for the already existing benchmark data of specific materials but also for complex objects and geometries like collimators.

In order to retrieve three dimensional maps of residual dose rate distributions for the Phase II collimators, FLUKA simulations were performed assuming 5 years in succession of LHC operation.

All results presented later in this chapter refer to the so-called loss at nominal Intensity of 1.15×10^{16} protons per beam per year. It has to be noted that one year of continuous operation means about 185 days of machine on, or irradiation, each 365 days. This number represents the loss intensity to be expected after the installation of Phase II collimators [11].

Results are presented for 4 different cooling times after each 185 days of machine operation: 1 day, 1 week, 1 month and 4 months (see Fig. 11.1). These cooling times represent typical situations during accelerator operation of fast inspections shortly after beam shutdown, minor repair during the operational period or at the beginning of a longer shutdown, and major work like machine upgrades, typically performed towards the end of an annual shutdown.

Actually, due to recent changes in the operation period timeframe, a 1 year long shutdown after 2 years of non-stop operation at different beam energy (e.g. 3.5 TeV and 5 TeV) is foreseen. However, even if this operation time slot is also applied when the Phase II collimators will be installed, results in case of Copper based jaws for the two different irradiation profiles will be equivalent after approximately 2 months cooling time.

The residual dose rates calculated reflect the horizontal losses halo distribution. As mentioned earlier, in reality losses will be distributed over all three primary

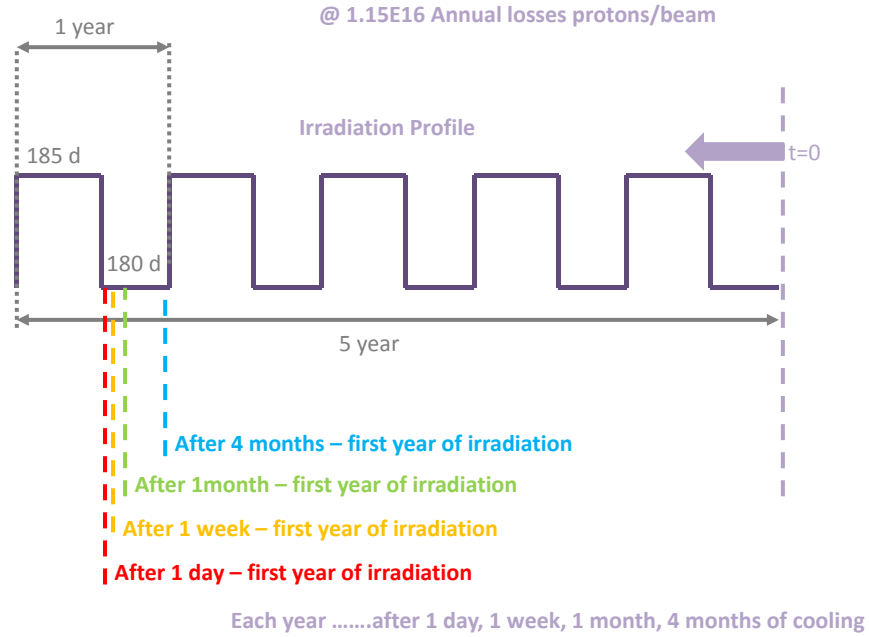


Figure 11.1: Irradiation profile assumed during residual dose rate FLUKA simulations. $t=0$ refers to the definition of decay (cooling) time with respect to the irradiation end.

collimators.

11.3 FLUKA results

Due to the secondary particle shower, the Phase II collimator in the TCSM.A6L7.B1 location becomes highly activated and constitute together with the primary collimators the main contributors to the ambient dose equivalent close to the beam line.

For short cooling times of the order of days, the residual dose rates close to the most radioactive objects range from 1 to 10 mSv/h (see Fig. 11.2).

Results are produced to compare the CERN and the SLAC design with Glidcop jaws in terms of residual dose rates. Spatial distributions are shown for horizontal sections in Fig. 11.3. The calculations can be also performed for all recently proposed Phase II designs with different jaw materials as soon as corresponding loss maps will be available.

In addition, in order to verify results of previous studies which were based on

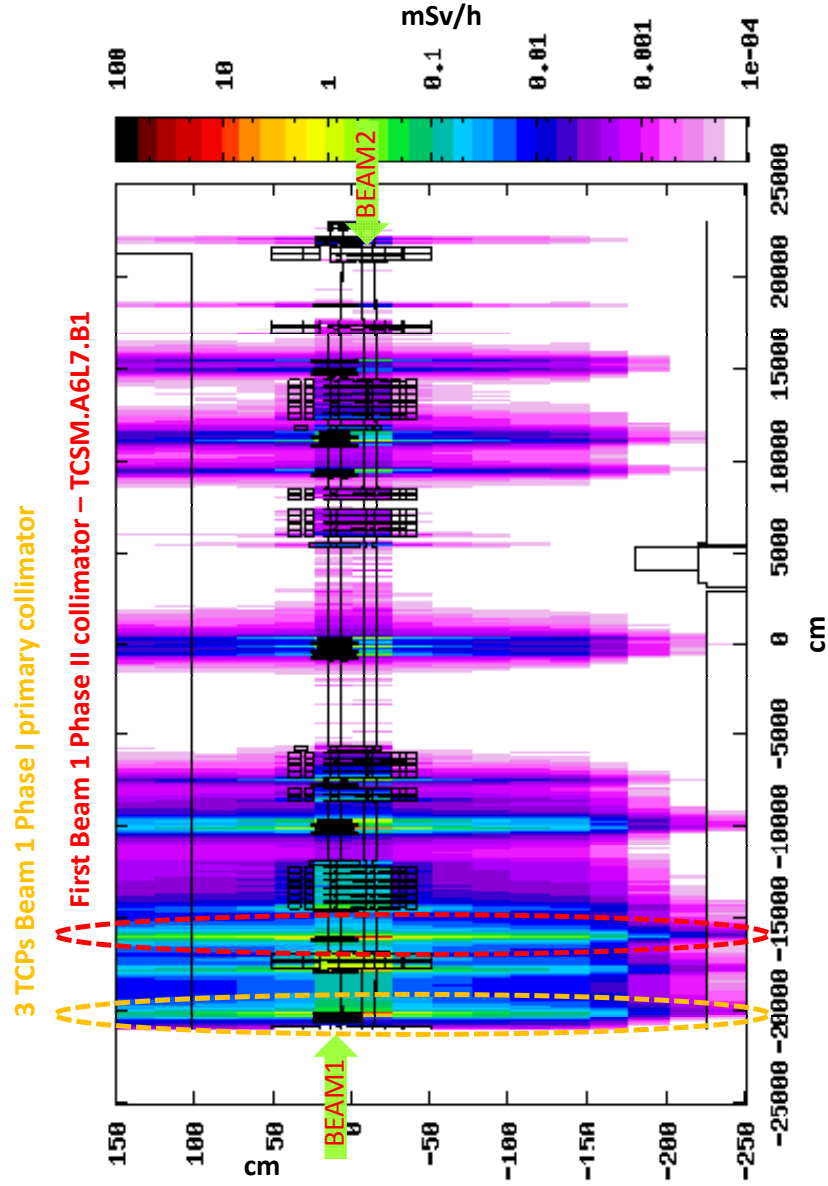


Figure 11.2: Ambient dose equivalent distribution after 185 days of continuous operation and 1 day of cooling time along the all IR7 straight section, shown for a horizontal cut through the geometry at the height of the beam axes.

a different geometry of IR7, dose equivalent rates were not only scored around the Phase II collimators but also around the horizontal Phase I primary collimator, the first Phase I secondary one and the 3 passive absorbers. These beam elements were chosen since they are the most loaded ones. The results agree with the previous calculations reported in [82].

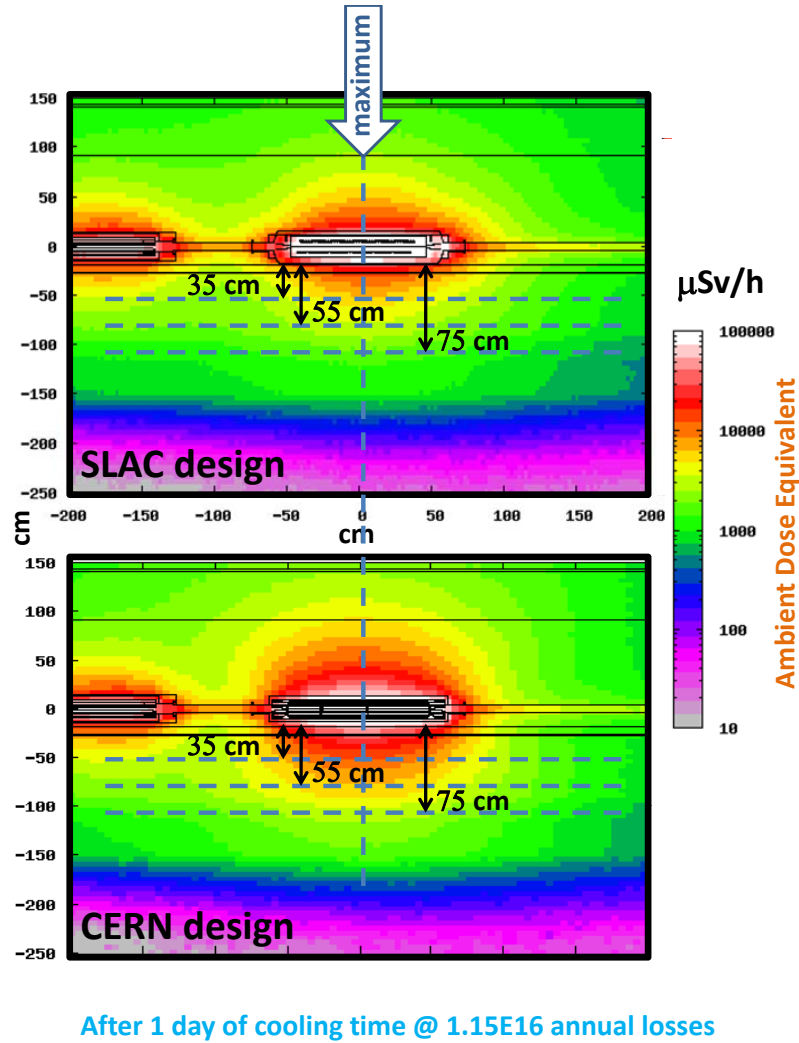


Figure 11.3: Ambient dose equivalent distribution for different Phase II designs after 185 days of continuous operation and 1 day of cooling period, shown for a horizontal cut through the geometry at the height of the beam axes for the most loaded Phase II collimator location (i.e. TCSM.A6L7.B1).

Fig. 11.4 shown the values of ambient dose equivalent at different distances (i.e. 35 cm, 55 cm and 75 cm) from the skew Phase II tank at the position of maximum, that is from the middle of the collimator itself (see Fig. 11.3). The distances take

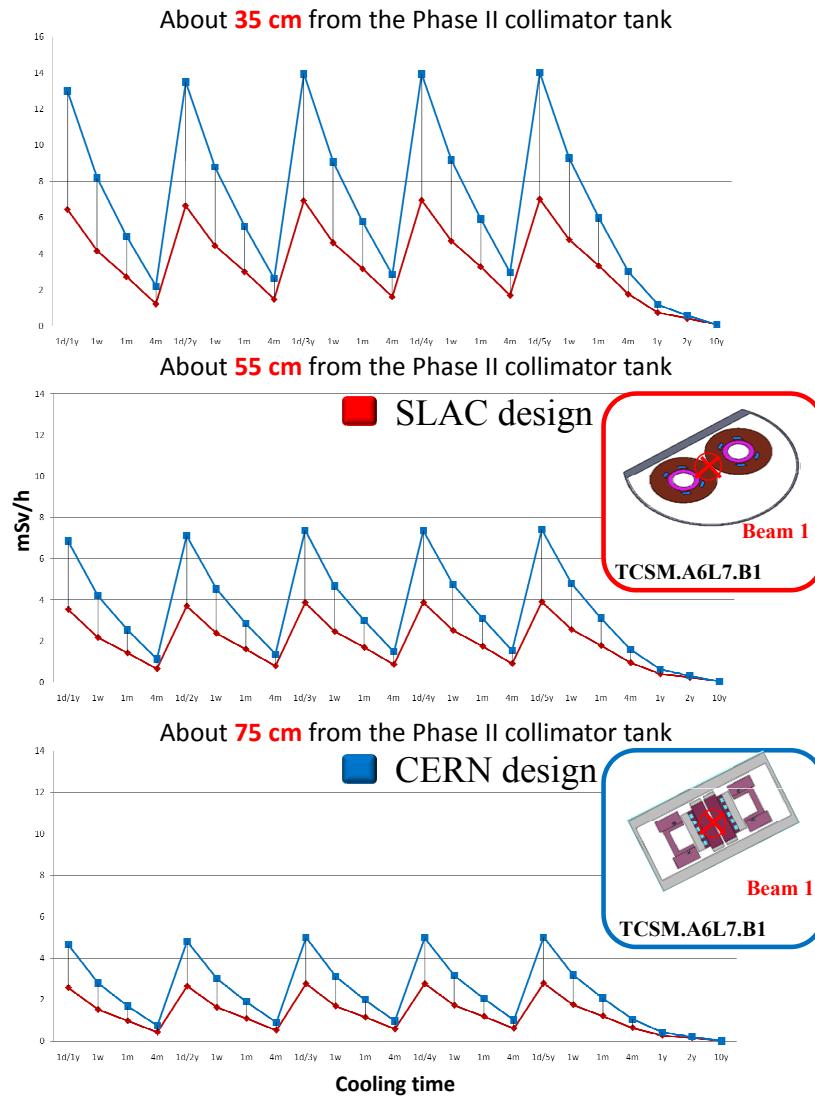


Figure 11.4: Ambient dose equivalent peaks for the 2 different Phase II designs at the most loaded TCSM.A6L7.B1 location and using different cooling times. The skew layout for each design is also shown.

in consideration are representative of possible working conditions at the collimators, or close to it, as well as of assuring a safe radiation passage for the personnel in the tunnel.

The results are shown for five years of operation, as well as after 1, 2 and 10 years at the end of the 5 cycle of irradiation. This last evaluation give an estimation of when the devices can be moved away from the tunnel.

Results show a different behaviour depending of the jaw designs and the different tank thickness. However, in these simulations the turning of the SLAC jaws was not taken into consideration, and thus the contribution could change and the gain of the SLAC design could be lost.

From the handling point of view a factor of about 2 is not changing remote handling requirements, because the dose rates is of the same order, that is several mSv/h .

In addition, since the orientation of the collimators varies in the different locations of the IR7 line, the shielding power of jaws and tank is different for different layout.

11.4 Conclusion

The ambient dose rate peaks calculated for Phase II exceed, at different distances from the most loaded location, the $2mSv/h$ value at different cooling times considered, and it is close to it after the longer ones, that is 4 months. The $2mSv/h$ triggers the highest level of ALARA (As Low As Reasonably Achievable) precautions as laid down in the corresponding procedure [83], which has to be followed during work on a radioactive component. Any work close to the Phase II collimators must thus be carefully planned and optimized. In particular, since the collimators have moving parts and motors, fewer repair works are already expected now to be required during their lifetime.

In order to identify and understand the source of radionuclides produced, generic studies were performed in FLUKA by the Radio Protection group at CERN, using different collimator jaw materials (i.e. Cu, C and W) at different beam energies, protons, and lead ion beams as well as different irradiation and cooling times [61]. Results have shown that the activated cooling circuits, tank, and support structures contribute significantly to the residual dose rates (i.e. more than 60 %). In particular, after a sufficiently long cooling time, a few radionuclides produced in the steel tank, such as ^{56}Co , ^{58}Co , ^{48}V , and ^{54}Mn , dominate the dose rate.

For this reason, a thinner tank or, using Aluminum at the place of Stainless Steel for it could be an option for Phase II colimators. However, it has to be noted that the bulk-numbers would most probably not change significantly, given the fact that the shielding effect of the tank is in competition with its source term. Indeed, the overall activation level depends on the jaw material. For example, residual dose rates around a collimator with Carbon jaws, like Phase I, are about a factor 5 lower

than around a collimator with Copper jaws [60].

Measurements of residual dose rates, foreseen to be performed in the HiRad-Mat facility, using the same two designs considered in my simulations, will allow a verification of the results.

In the meanwhile, an easy plug-in system for Phase II collimators is already foreseen, allowing a fast exchange with the remote bake-out equipment in case of damages.

In addition, all simulations presented in this chapter were performed only for Beam 1, as contribution to the residual dose rate coming from activation due to Beam 2 are negligible at the most loaded devices locations. The same remark is for Beam 2 at its most loaded locations, which are mirroring with respect to IP2. However, for what concerns the central region, results have to be multiplied by a factor of 2, since the contribution coming from the 2 beam lines is of the same order.

Finally, it has to be considered that the air in the accelerator tunnel will be activated during the beam operation, due to the direct interactions between hadronic particles and the stable nuclei of e.g. Oxygen, Nitrogen and Argon. For this reason, the air is monitored at the outlet and its confinement in the underground areas is achieved via pressure differences and static means (e.g. closing ducts, etc.). Because of Phase II collimators installation in the IR7 straight section, an increase of the air activation in the tunnel is expected. This is not been quantified within this PhD, but it will be the subject of further following studies.

Chapter 12

Optimization of the IR7 layout

A combination of different Phase II designs and jaw materials for the 11 positions foreseen in the IR7 Straight Section is proposed in this Chapter.

The purpose is to optimize the IR7 layout, on the basis of power deposition and activation results. Mechanical constraints and warnings coming from the FLUKA simulations for operation and abnormal beam losses scenarios are taken into account.

However, before any final decision could be taken, Cleaning Efficiency and collimator driven Impedance have to be further estimated as well as heat conducting and radiation protection analyses have to be carried out where necessary.

In addition, the performances of collimators have to be validated by the experiments or diagnostic foreseen in the CERN test facility or SPS, before choosing an implementation solution. Only tested and fully qualified materials/collimators can be installed into the operating LHC accelerator.

12.1 New proposed IR7 Phase II layout

In order to choose how to arrange the 11 Phase II collimators along the IR7 line, different criteria were applied. The main ones are:

- To minimize the jaw deflections, in particular in the most loaded locations.
- To assure the reliability of the Phase II collimators system during abnormal beam losses scenarios.
- To avoid frequent changes of the entire *ensemble* for collimators in the tunnel (i.e. to minimize the application of Radiation Protection constraints).
- To follow the mechanical characteristics of each design.

Table 12.1 summarizes the final proposed choice for each Phase II collimator, reported with respect to the sequence in the Beam 1 line. The justification for the choice is also reported for each location.

Table 12.1: Proposed layout for the 11 Phase II collimators located in IR7 along the Beam 1 line.

Name	Design	Justification
TCSM.A6L7.B1	CERN with Cu jaws	to limit the jaw deflection
TCSM.B5L7.B1	SLAC with Cu jaws	to avoid collimator change in a high radiation area
TCSM.A5L7.B1	SLAC with Cu jaws	to avoid collimator change in a high radiation area
TCSM.D4L7.B1	CERN with Cu jaws	because of mechanical constraints due to the vertical collimator position
TCSM.B4L7.B1	CERN with CFC jaws	to save the collimator against the asynchronous dump accident
TCSM.A4L7.B1	CERN with Cu jaws	-
TCSM.A4R7.B1	SLAC with Cu jaws	-
TCSM.B5R7.B1	CERN with Cu jaws	-
TCSM.D5R7.B1	SLAC with Cu jaws	-
TCSM.E5R7.B1	CERN with Cu jaws	-
TCSM.6R7.B1	CERN with CFC jaws	to save the collimator against the asynchronous dump accident

At the first location, the CERN design with Glidcop jaws is proposed, since the FEM calculations show lower values of jaw deflections with respect to the SLAC design in this most loaded Phase II location (see Table 8.1 and Fig. 9.5).

In the second and third position the SLAC design is set, because avoiding collimator changes was preferred to limiting the jaw deflections. It has to be pointed out that in these positions the power deposited on the most loaded jaw is lower by a factor 5 for the TCSM.B5L7.B1 and more than a factor 10 for the TCSM.A5L7.B1 with respect to the first location (see as reference Fig. 9.6). The jaw deflection values are converging for the two designs in those locations. The peculiarity of SLAC turning jaws design was thus preferred in order to accomodate more possible beam hits (20 against 5-7, see Chapter 9) before changing the collimator.

The fourth Phase II collimator in the line is a vertical one. Since the SLAC design jaws are heavier in comparison to the CERN ones, for safety and reliability reasons the CERN design is preferred.

The fifth TCSM.B4L7.B1 as well as the last one, that is the TCSM.6R7.B1, are horizontal collimators. In order to protect the machine from the asynchronous accident, Copper based jaw collimator are not considered here. In principle SiC collimators would be a good choice for these locations in terms of thermal load during the accident. For a first estimation, a preliminary study is here performed using CFC jaws, as for Phase I collimators. The reference design refers to entire

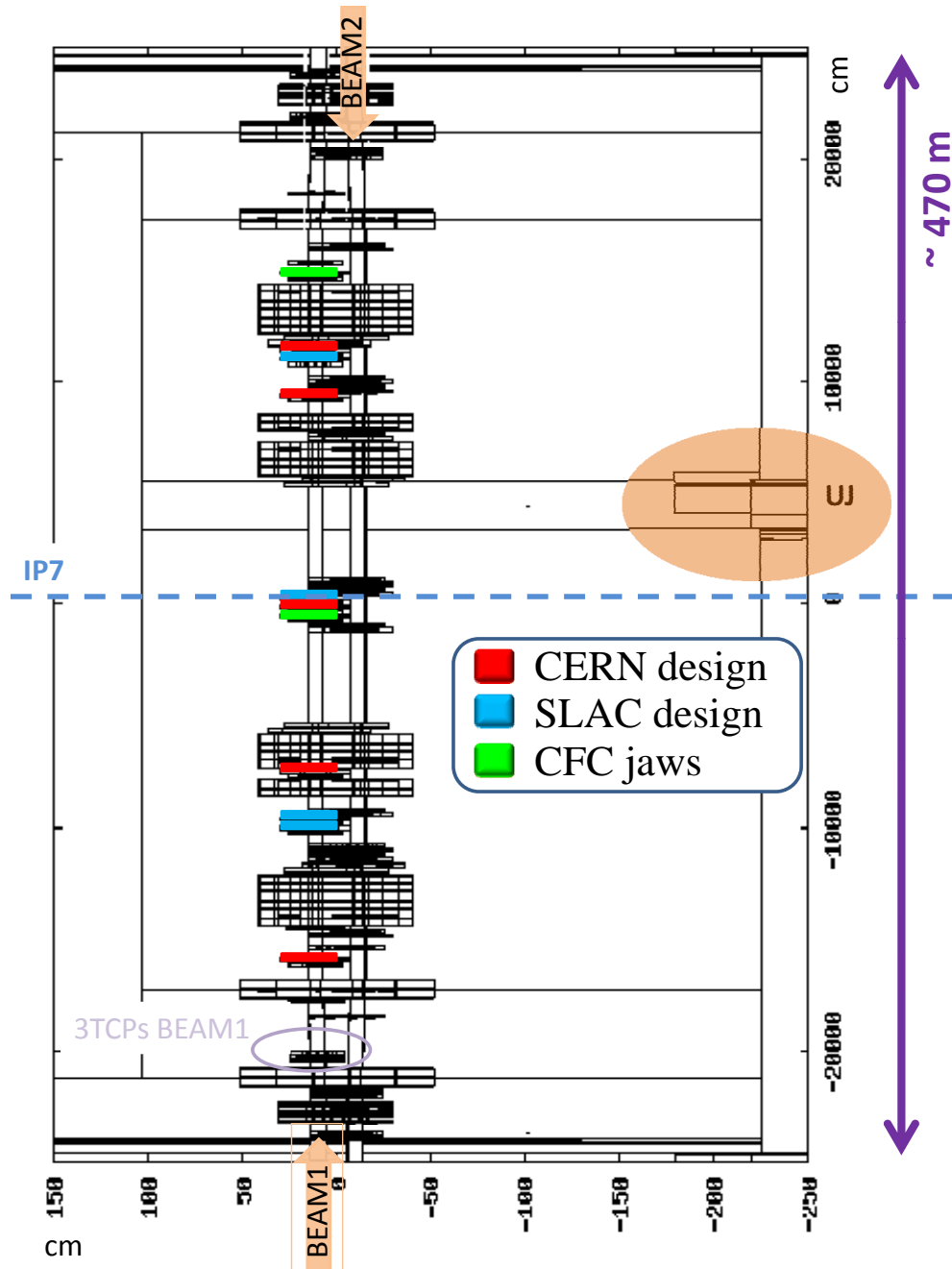


Figure 12.1: Proposed optimized layout for Phase II collimators along IR7 Beam 1 line. The UJ76 service cavern is also shown.

jaws on a Molybdenum support. This is the developed Phase I secondary design, which was studied for Phase II at the beginning (see Fig. 9.2). As soon as loss maps will be provided for SiC material, FLUKA simulations will be performed using the corresponding Phase II design model.

For all the other 5 locations along the IR7 line, the two designs with Glidcop jaws are equivalent, using as terms of comparison the criteria listed above. The CERN and SLAC collimators are thus alternating along the line, allowing to study the different behaviour in adjacent locations, where the thermal load is similar.

Fig. 12.1 shows the IR7 optimized layout studied for Phase II. Since the Phase II collimators on Beam 2 are mirror set with respect to the IP7, the same layout can be also applied to the Beam 2 line.

12.2 FLUKA results for operation conditions

The optimized IR7 layout proposed was studied using a horizontal loss map created for Beam 1 at low beta to match the Phase II jaw materials. The scenario refers to operation condition without cryo-collimators installed.

Results for 1 *h* beam lifetime are compared with the IR7 layout composed by Phase II CERN design collimators with Glidcop jaws in all the 11 foreseen locations.

In terms of power deposited, results on the TCSM.A6L7.B1 converge at about 22 *kW*. This means that the redistribution of primary losses along the LHC collimators due to the introduction of 2 Phase II with CFC jaws has no effect on the power deposited on the most loaded Phase II collimator.

The optimized layout proposed has its major effect downstream the most loaded devices. In particular, due to the different material density and atomic number, the value of power deposited in the first TCSM.B4L7.B1 horizontal Phase II collimator increases from 10 *W* to about 470 *W* from using CFC to Glidcop materials for the jaws. The decrease obtained with CFC jaws on this device is compensated by an increment on the following 3 Phase II with Glidcop jaws, up to a maximum of about 120 *W* on each.

In case of TCSM.6R7.B1, the effect of changing its jaws material (from Glidcop to CFC) is translated in a decrease from 370 *W* to about 10 *W* of power on it, compensated with increments on the downstream active absorbers. A variation of about 1-2 order of magnitude is the increment factor on the second one after the TCSM.6R7.B1, while smaller absolute increments are on the other 2 active absorbers at the end of the IR7 LSS line.

Fig. 12.2 summarizes all these results, with a focus on the region of major changes.

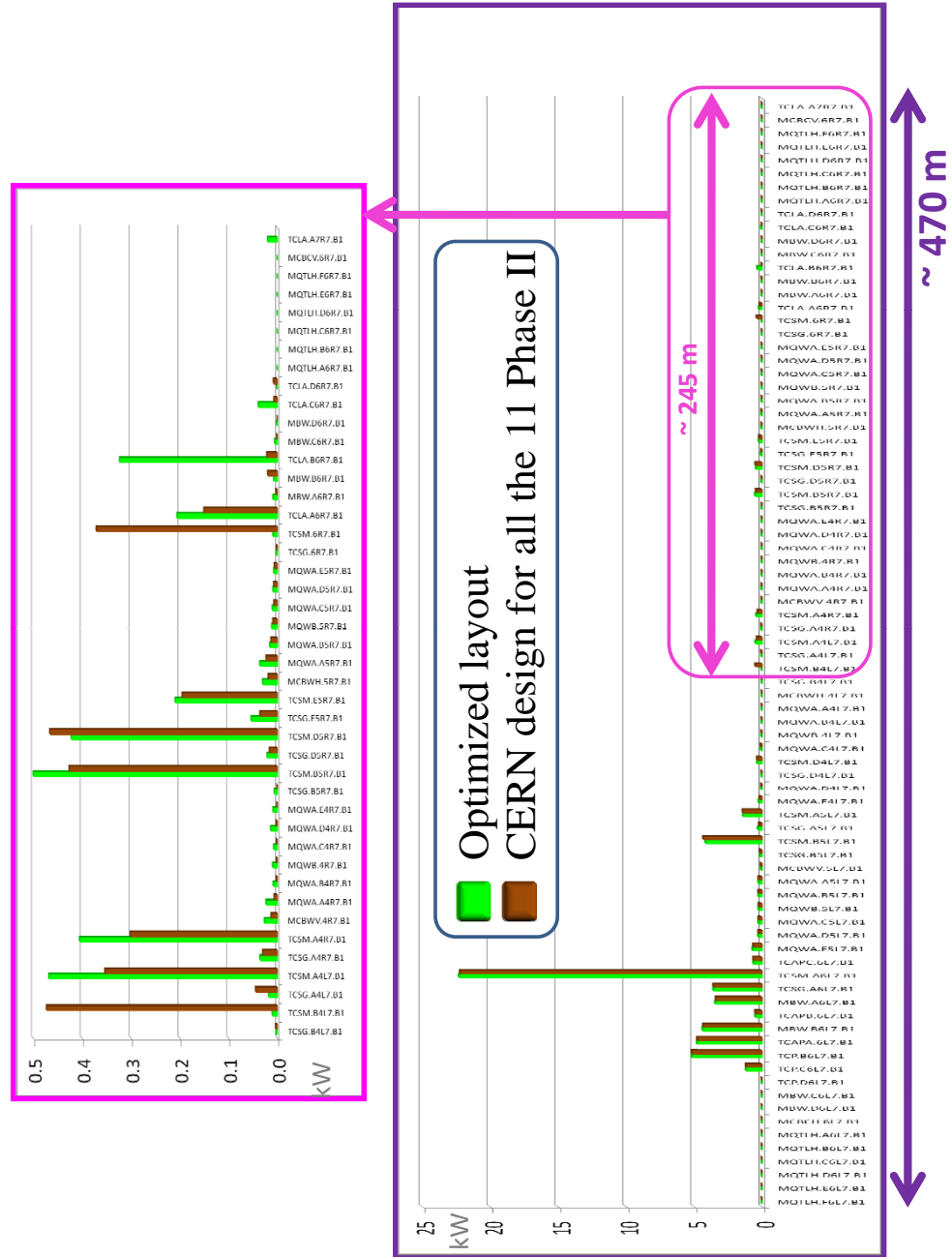


Figure 12.2: Optimized layout vs. layout envisaging 11 Phase II CERN design Cu jaw collimators: power deposition along the LSS7 (1 h beam lifetime).

12.3 Conclusion

The Phase II collimator system layout proposed in this chapter for IR7 has negligible effects on the re-distribution of power deposited along the Beam 1 elements. Indeed, changing the jaw material from Glidcop to CFC for 2 Phase II collimators, located in the middle and at the end of LSS, introduces variations on thermal loads which do not bring to a functionality reduction of any IR7 beam device.

However, it could have consequences on Cleaning Efficiency and induced Impedance, limiting the beam Intensity. These possible limitations have to be evaluated but they are not a subject of these PhD studies.

In addition, prompt radiation in the tunnel alcoves in which electronics is located, that is UJ76 and RR77 (see Fig. 12.3) is affected. The effects in these regions will be evaluated in the following Chapter.

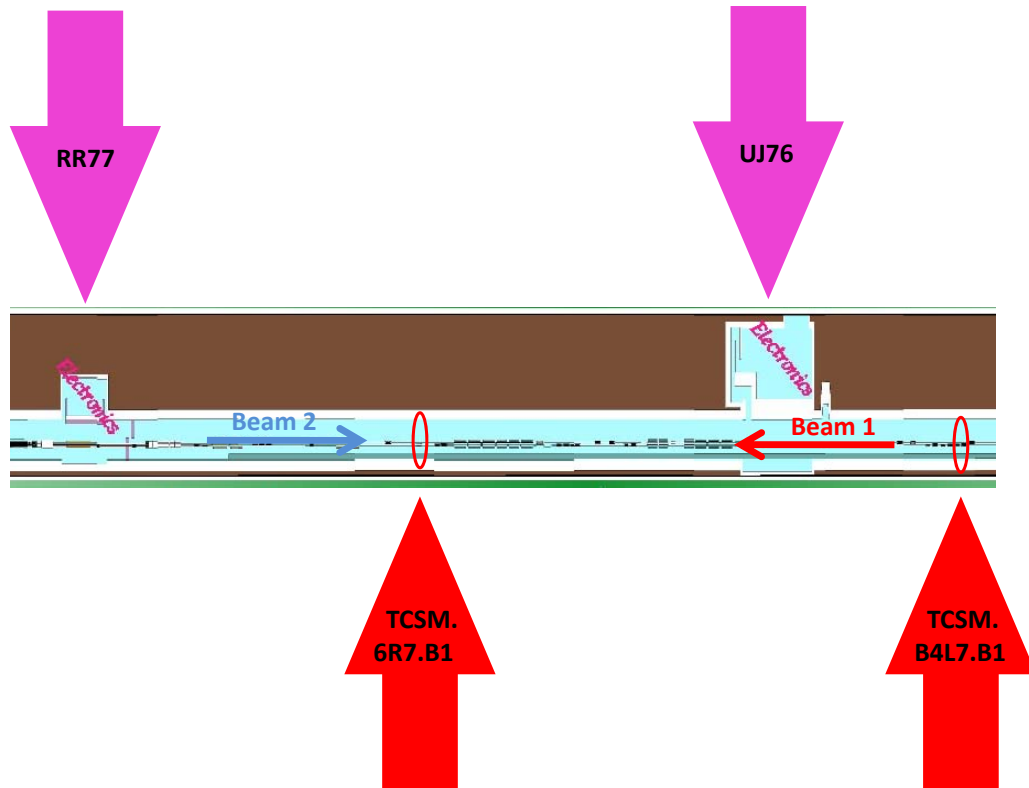


Figure 12.3: Sketch of IR7 line in which the tunnel service areas UJ76 and RR77 are shown.

Chapter 13

The prompt radiation effects

The prediction of the radiation environment for the LHC machine is a very complex issue that strongly depends on many specific LHC parameters e.g residual gas densities, collimation settings, beam losses and beam-beam effects in the experiments.

The LHC radiation field varies between the different underground locations. The prompt radiation, generated in the LHC main ring when the machine is on, could lead to damage not only of the beam elements but also of electronic equipment installed in the tunnel and in the adjacent service caverns.

Radiation damage to electronics is an important concern for the LHC operation. Both, in the LHC tunnel, as well as in adjacent caverns, electronics is exposed to a mixed radiation field. Whereas the equipment in the tunnel was specifically designed according to the radiation requirements, most systems situated in the partly shielded adjacent areas are based on Commercial Off the Shelf (COTS) components.

Given the short time of LHC operation at low Intensities and Luminosities, the knowledge of radiation levels to support the integration of instrumentations in the Phase II collimators as well as to evaluate the effect on the control system installed in the most LHC critical alcoves, such as UJ76 and RR77, is based on FLUKA simulations.

On the basis of these results, possible scenarios to mitigate the risk will be taken into account by the CERN management in order to avoid future problems.

13.1 Overview of LHC critical areas

Already in the early phase of the design of the LHC (1991-1996), it became clear that different areas of the rings would be exposed to high levels of radiation. In particular, for almost all the LHC experiments, it was decided to build custom designed rad-hard electronic circuits for the detectors, in order to resist to a total dose of 10 *Mrad* and fluence of 10^{14} *neutrons/cm²* per 10 years [84]. These electronics are based on a technology which is using deep submicron processes with enclosed transistor topologies and guard rings [85].

For what concern the LHC main ring, it has to be noted that even if the total annual dose is quite low, control electronics in the tunnel can be exposed to high levels of high energy hadrons. For this reason, in the LHC all the system directly set up in the tunnel (i.e. Quench Protection System (QPS) power converters, BLMs, BPMs, some cryogenic monitoring devices, etc.) have been tested in the CERN Neutrinos to Gran Sasso (CNGS) or in TCC2 facilities.

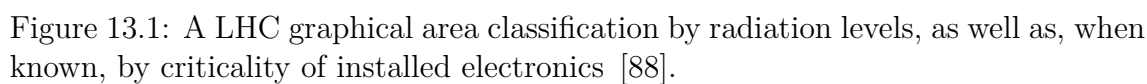
However, for what concerns the electronic equipments in some of the service caverns, their radiation tolerance was not considered. Following the failure in the ventilation system installed in the CNGS service gallery due to radiation effects in the electronics (i.e. Single Event Upset (SEU) due to high energy hadron fluence), a task force was formed to evaluate the risk of possible damages in the LHC underground regions and to reduce it by means of shielding, relocation of electronics, creation of new safe areas or redesign certain critical systems.

According to the radiation levels and to the control system sensitivity and criticality, different LHC regions were identified. Fig. 13.1 shows the critical areas during nominal operation scenarios, where the Point 7 and its adjacent caverns are put in evidence.

In particular, the UJ76 (i.e. the region underlined with a red circlet in Fig. 13.1) has been the first area in which an action plan was put in place, when the risk of failure, due to the high particle losses at collimators during the Betatron Cleaning, was evaluated in 2008 after the CNGS accident. A partial relocation of the most sensitive equipment has already been prepared by enlarging the TZ76 (i.e. the region underlined with a green circlet in Fig. 13.1) and installing part of the needed infrastructure. The necessary relocation is planned to take place in the next long LHC shutdown (2012). In addition, in order to shield the instrumentation that for their specificity cannot be moved from UJ76, further improvements were already performed during 2009, including a lateral shielding iron wall for the UJ76 (see Fig. 13.2).

The mobile shielding plugs in Point 7, close to the RRs, were also finalized in 2009 (see Fig. 13.2). Furthermore, different additional solutions were proposed for the RR73 and RR77 caverns (i.e. the regions put in evidence with two blue circlets in Fig. 13.1) in which are installed the not radiation tolerant 120 A and 600 A power converters. The options of re-designing the most sensitive parts or of their relocation using different technologies (i.e. warm cables, Superconducting Links (SCLs), etc [86]) are evaluated at this stage.

In addition, to assure a long term solution, R&D work is currently carried out at CERN for the development of new SCLs and associated cold powering system [87] which could enable the removal of the LHC power converters from the tunnel to underground or on surface radiation safe areas. In particular, the SCL technology can be envisaged as a candidate solution for removing to the surface the power converters located in critical positions at Point 1 and 5, using vertical SCLs for powering the SC magnets from surface. This option is not possible at Point 7, due



to integration and properly constraints, thus in terms of SCLs only a horizontal link is studied with its cryogenic connections to be installed in the TZ76.

The change of the collimation system has been also considered at this stage, in order to reduce the radiation effects in UJ76, RR73 and RR77. An option is a temporary operational move of the Betatron Cleaning to Point 3. However, it has to be pointed out that this solution could imply to use some of the positions reserved for the Phase II collimators, introducing a first longterm limitation in the intensity and spoiling therefore the objective to increase it to the nominal value within few years. Moreover, the use of additional Phase II collimators as absorbers, as well as their local installations and use for the collimation system upgrade, have been studied and are discussed in the following.

Many of these possible solutions imply not only high costs, but also important installation times (e.g. SCLs) for which could be required possibly long LHC shut-down periods (e.g. two years).

13.1.1 Radiation effects on electronics

Radiation effects in electronic devices can be divided into two main categories: cumulative effects and Single Event Effects (SEE) [89].

The steady accumulation of defects causes measurable effects that can ultimately lead to device failure. In particular, the Total Ionizing Dose (TID) is a cumulative effect of ionizing energy loss in the lattice by Coulomb scattering from energetic particles or by gamma radiation. It is a quite predictable effect and should be tested for equipment exposed to high level of dose ($> \text{few Grays}$), typically by exposing it to a ^{60}Co calibrated source. Standard electronic normally fails at levels starting from a few Grays up to hundreds of Grays for rad-tolerant equipment. The Non Ionizing Energy Loss (NIEL) is another cause of possible cumulative damages. It is mainly due to accumulation of displacement damage in the lattice following collision with neutrons or very low energy heavy ions. It represents a reproducible and thus predictable effect, expressed in fluence of 1 MeV equivalent neutrons. Equipments are usually tested in reactors with neutrons at a fixed energy.

Stochastic failures, so called SEE, form an entirely different group as they are due to the direct ionization by a single high energy hadron ($> 20 \text{ MeV}$) from nuclear reaction in the electronics itself, able to deposit sufficient energy through the ionization process in order to disturb the operation of the device. They can only be characterized in terms of their probability to occur, which will strongly depend on the device as well as on the flux and nature of the particles [90].

Apart for electronics installed directly in the tunnel, where the TID and displacement damage from NIEL may represent a serious issue, the main risk for exposure to electronics to radiation in LHC underground areas comes from stochastic SEE effects.

A distinction must be made between non-destructive and destructive SEEs events, as this has very different consequences on the accelerator operation. The first ones

refer to *recoverable* soft SEEs which cause data corruption (e.g. Single Event Upset (SEU), Multiple Bit Upset (MBU), Single Event Transient (SET) or Single Event Functional Interrupt (SEFI) events). The second ones are *non-recoverable* hard SEEs which cause permanent loss of the data and sometimes even permanent damage of the circuit (e.g. Single Event Latch-up (SEL), Single Event Gate Rupture (SEGR) or Single Event Burn-out (SEB) events).

In addition, a certain sensitivity to thermal neutrons has been observed, for example in devices without specific precautions powered with low voltage (e.g. 3 V). The low-energy neutron capture reaction (e.g. n-alpha) can create highly ionizing secondary particles that are then also the source of SEEs.

As general indications and in order to minimize the risk of occurrence of SEEs, currently employed mitigation aims to reduce the fluence of high energy hadrons ($> 20 \text{ MeV}$) below $10^7 \text{ hadrons/cm}^2$ for every year of operation, that is equal to about 200 days of machine on at nominal condition [91].

13.2 Radiation to electronics FLUKA results

The FLUKA results reported in this section refer to the *classical* collimation system with Phase II and its impact on the radiation level in IR7. The purpose is to show how it effects the dose levels and the particles fluencies at nominal condition when it performs a pure Betatron Cleaning at Point 7.

In particular, the high energy hadrons fluence is evaluated in the UJ76 and in the RRs and the shielding contribution of Phase II is put in comparison with a collimation system built up of only Phase I collimators used at the same nominal scenario condition.

The results are normalized to 1.15×10^{16} protons per year, which is the estimated lost primary protons of IR7 for each beam of the LHC machine during one year of operation (i.e. about 200 days of machine on) [11].

They refer to a horizontal halo loss maps for the 7 TeV low beta scenario, since it is demonstrated to be a conservative case [92]. In case, when operation data will be available, corrections can be introduced.

13.2.1 Radiation to electronics in UJ76 and RR77 (& RR73)

Fluencies of high energy hadrons ($> 20 \text{ MeV}$) are evaluated first outside the caverns at Point 7 to show the pure shielding effect of Phase II collimators and then inside both UJ76 and RR77.

Fig. 13.2 shows the results for Beam 1 simulations all along the IR7 LSS. The values of fluence are averaged in the orange region close to the caverns. The blue line refers to the case of only Phase I collimators implemented in the line. The red and green lines show the Phase II impact in both cases of collimators with Copper jaws and with the optimization layout proposed in Chapter 12.

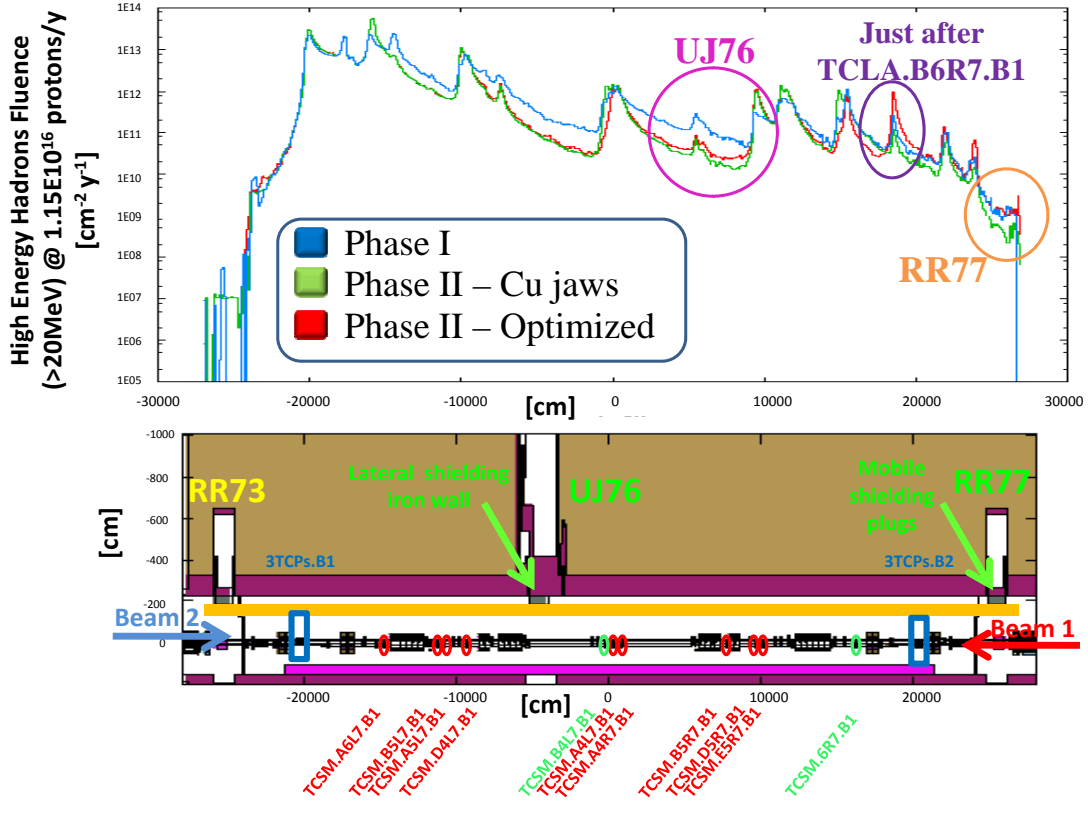


Figure 13.2: High Energy Hadrons Fluence ($> 20 \text{ MeV}$) along IR7 averaged in the orange area, close to the LHC tunnel wall. The 11 Phase II collimators implemented in the Beam 1 line are shown by name. The possible proposed Phase II with CFC jaws are indicated in green. The shielding walls for UJ76 and RRs mentioned in Section 3.1 are also shown.

The presence of Phase II collimators reduces significantly the fluence in the area close to the UJ76 and close to the RR77 entrance (see Fig.13.2), but for the latter only in the case of using Phase II collimators with Copper jaws. This is due to the fact that the last Phase II collimator in the line (i.e. TCSM.6R7.B1) is supposed to be with CFC jaws as a Phase I secondary collimator to maximize the protection against the asynchronous dump accident. The use of this material in this special location is comparable to a layout composed by only Phase I collimators. In addition, in this case, an increase of fluence is found upstream the RR77 cavern and in particular just after the second active absorber, that is the TCLA.B6R7.B1.

Inside the UJ76 service area, the values of fluence also include the effect of the

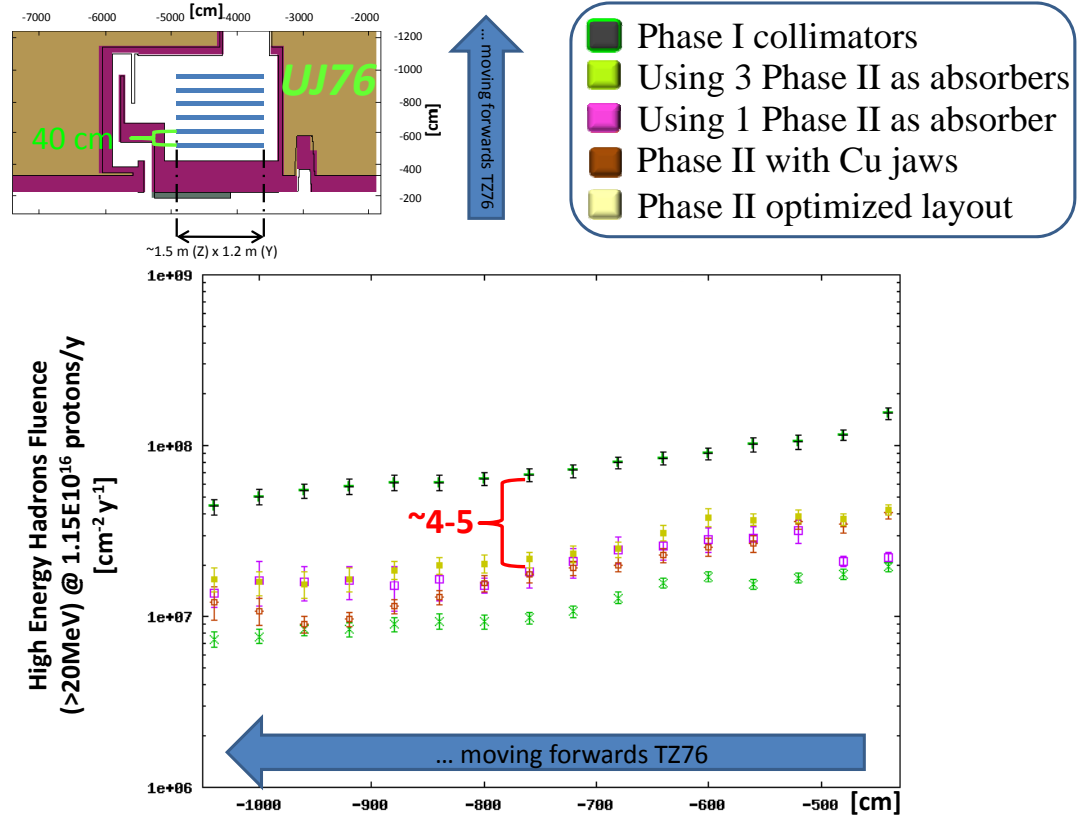


Figure 13.3: High Energy Hadrons Fluence (> 20 MeV) in the UJ76 cavern, resulting from to Beam 1 line simulations. The effect of Phase II collimators in the two layouts are compared to the Phase I collimators used at the same nominal condition. In addition, the effect of using Phase II as absorbers is also shown.

wall and iron shielding added in 2009, in addition to the effect of Phase II collimators. Fig. 13.3 shows the high energy particle fluence values calculated in average on a surface 1.5×1.2 m for each 40 cm step, starting close to the LHC tunnel wall and moving toward the TZ76 region.

Beam 1 simulation results, calculated using the Phase I layout, are compared with the fluence values with Phase II collimators installed for the nominal scenario. The fluence reduction of a factor 4-5 is shown for both cases of using Phase II with Copper jaws and Phase II optimized layout. A gain of the same order is also obtained by using as absorber the Phase II collimator with Copper jaws closest to the UJ76, i.e. the TCSM.A4R7.B1 (see pink dots in Fig. 13.3). In this case, the TCSM.A4R7.B1 is opened at 20σ (i.e. 13σ in addition to the nominal aperture

of 7σ) in order to intercept only shower particles. A bigger fluence reduction is obtained by using all the three Phase II collimators as absorbers, which are closest to the UJ76, i.e. the TCSM.B4L7.B1 and the TCSM.A4L7.B1 in addition to the TCSM.A4R7.B1 (see Fig. 13.3).

Maximizing the shielding power of Phase II collimators by opening them at 8σ (i.e. 1σ in addition to the nominal aperture of 7σ), the gain in the fluence reduction is of a factor 10-11 for Beam 1, however only a factor 2-3, considering the contribution of Beam 2 (see Fig. 13.4). The Phase II effect in UJ76 is thus dominated by Beam 2, since this service area is closer to the Beam 2 Phase I primary collimators, in which the initial particle shower is developed (i.e. UJ76 distance from Beam 2 Phase I primary collimators is about 140 m against 240 m from the Beam 1 ones). In addition, for Beam 2, a lower number of collimators, which could act as particle shower absorbers, are installed in the line before the UJ76 cavern.

The only insertion of Phase II collimators thus doesn't solve the SEEs problem in UJ76. Adding the contribution effects from the two beam lines, the fluence of high

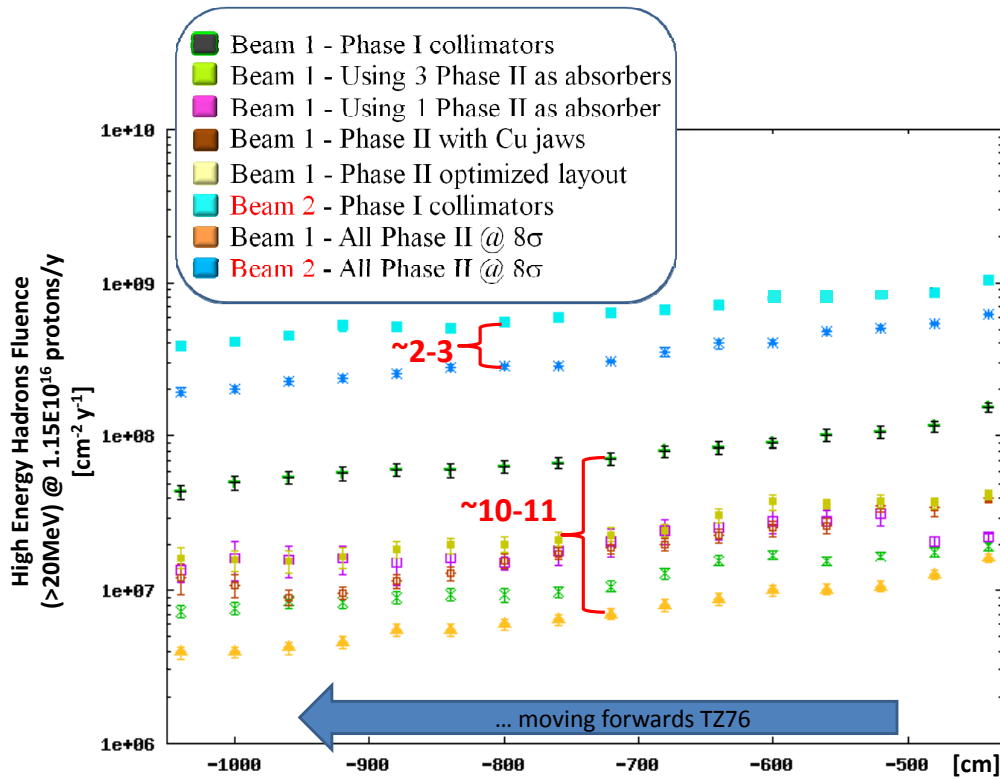


Figure 13.4: High Energy Hadrons Fluence ($> 20 \text{ MeV}$) in the UJ76 cavern, resulting from Beam 1 and Beam 2 line simulations.

energy hadrons ($> 20 \text{ MeV}$) is two order of magnitude higher than the maximum limit in fluence of $10^7 \text{ hadrons/cm}^2$, as reported above.

Fig. 13.5 shows the fluence values averaged on a $1 \times 1.2 \text{ m}^2$ surface each 40 cm inside the RR77 cavern. The Phase II installation reduces of 1 order of magnitude the fluence of high energy particles with respect of the nominal Phase I at 7 TeV (see Fig. 13.5). However, some of the gain could be lost with the introduction of possible asynchronous dump protections. It has to be pointed out that the reduction of a factor 6 as shown in Fig. 13.5 could be increased if, for example, non conductive Phase II collimators are used (see Chapter 9, Section 9.3). However, this possible increment, by using different than CFC suitable jaw materials, can not exceed the factor 10-11 gained with the Copper or Glidcop jaws. Addition calculations were performed in order to evaluate the contribution of dose and the fluence of 1 MeV equivalent neutrons in comparison to the high energy hadron fluence in the racks inside the caverns (see Fig. 13.6).

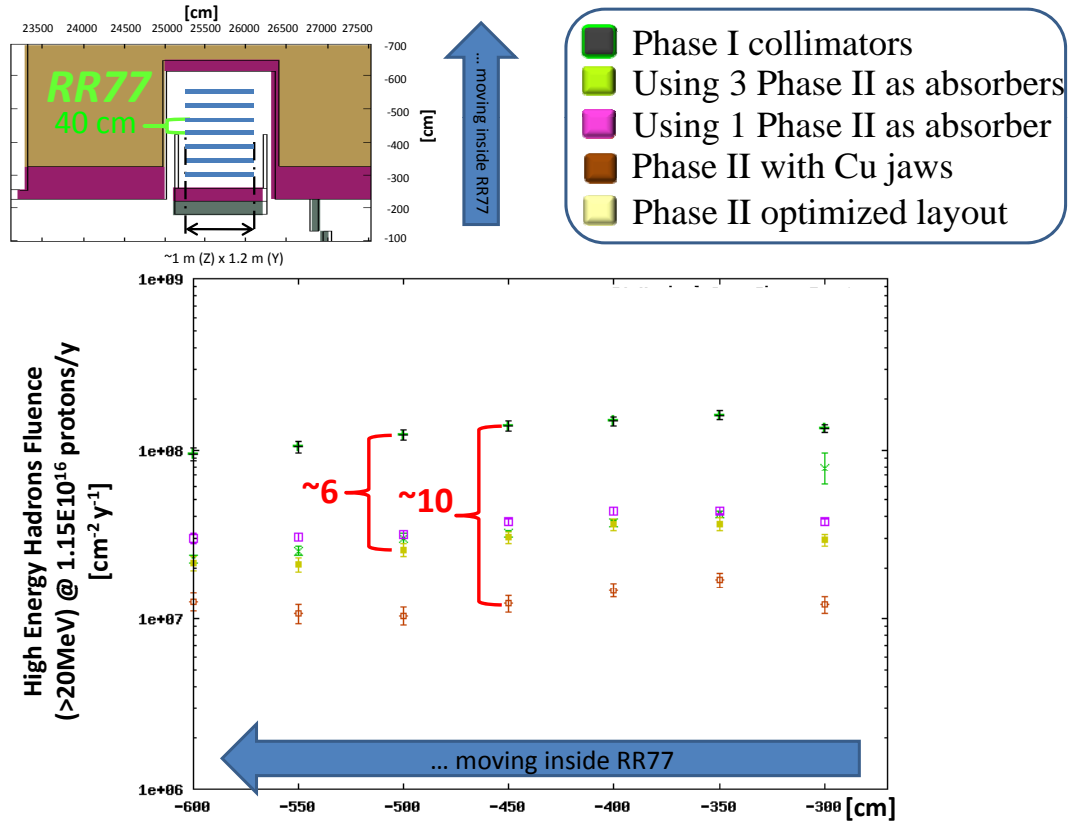


Figure 13.5: High Energy Hadrons Fluence ($> 20 \text{ MeV}$) in the RR77 cavern

The purpose is to produce a figure of merits to support the possible installation of different sensitive equipments in the appropriate rack locations.

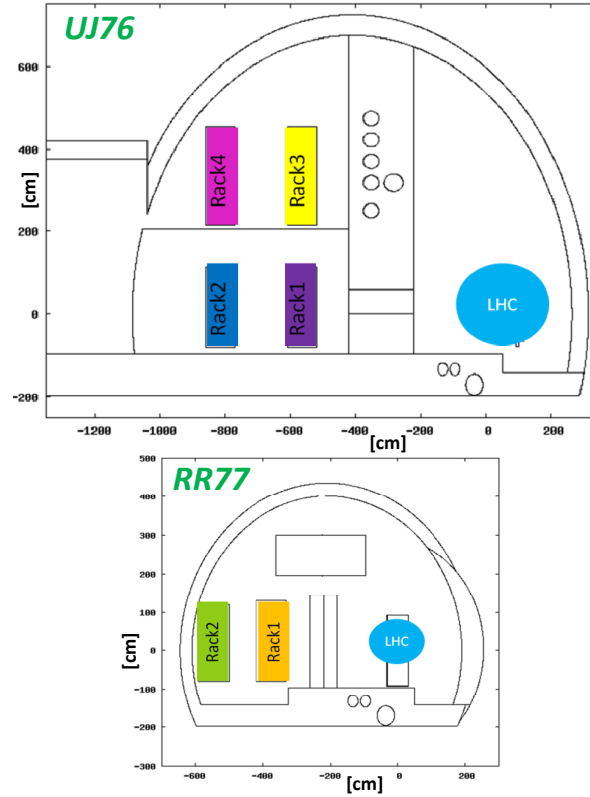


Figure 13.6: Location of electronic racks in the RR77 and UJ76 caverns.

Table 13.1 shows the values calculated with respect of a Phase II collimation system with Glidcop jaws.

Table 13.2 reports the values in the rack exposed to the strongest radiation field for Glidcop jaws and for the optimized proposed Phase II layout.

These results and in particular the ratio between the fluence of 1 MeV neutron equivalent over the fluence of high energy hadrons above 20 MeV , or between the fluence of high energy hadrons above 20 MeV and the dose are used as reference to qualify the radiation environment in the facilities, in which future LHC electronic equipments will be tested before expect to be installed in the foreseen service areas. The idea is to test the electronics in reproduced LHC realistic radiation fields.

Table 13.1: High Energy Hadrons Fluence ($> 20 \text{ MeV}$), 1 MeV equivalent neutron Fluence and Dose values in the UJ76 and RR77 racks (in reference to Fig. 13.6) resulting from Beam 1 simulations with Glidcop jaw Phase II collimators.

LHC cavern	Rack	$\Phi_{20\text{MeV}}$ [$\text{cm}^{-2}\text{y}^{-1}$]	$\Phi_{1\text{MeV}}$ [$\text{cm}^{-2}\text{y}^{-1}$]	Dose [y^{-1}Gy]	$\Phi_{1\text{MeV}}/\Phi_{20\text{MeV}}$	$\Phi_{20\text{MeV}}/\text{Dose}$ [$\text{cm}^{-2}\text{Gy}^{-1}$]
UJ76	<i>Rack1</i>	3E7 \pm 15%	6E7 \pm 11%	1E-1 \pm 14%	2.4	2.5E8
	<i>Rack2</i>	1E7 \pm 11%	3E7 \pm 9%	1E-2 \pm 17%	2.4	1.1E9
	<i>Rack3</i>	1E7 \pm 10%	5E7 \pm 23%	8E-3 \pm 22%	3.5	1.7E9
	<i>Rack4</i>	1E7 \pm 13%	4E7 \pm 24%	6E-3 \pm 18%	3.7	2.1E9
RR77	<i>Rack1</i>	1E7 \pm 17%	8E7 \pm 12%	5E-2 \pm 13%	5.6	3E8
	<i>Rack2</i>	1E7 \pm 18%	8E7 \pm 14%	3E-2 \pm 14%	8.2	3.1E8

Table 13.2: High Energy Hadrons Fluence ($> 20 \text{ MeV}$), 1 MeV equivalent neutron Fluence and Dose values in the most exposed Rack1 in both UJ76 and RR77 (in reference to Fig. 13.6) resulting from Beam 1 simulations with Glidcop jaw Phase II collimators and using an optimized proposed Phase II layout.

LHC cavern	Phase II layout	$\Phi_{20\text{MeV}}$ [$\text{cm}^{-2}\text{y}^{-1}$]	$\Phi_{1\text{MeV}}$ [$\text{cm}^{-2}\text{y}^{-1}$]	Dose [y^{-1}Gy]	$\Phi_{1\text{MeV}}/\Phi_{20\text{MeV}}$	$\Phi_{20\text{MeV}}/\text{Dose}$ [$\text{cm}^{-2}\text{Gy}^{-1}$]
UJ76	Cu jaws	3E7 \pm 15%	6E7 \pm 11%	1E-1 \pm 14%	2.4	2.5E8
	Opt.	4E7 \pm 11%	9E7 \pm 11%	8E-2 \pm 13%	2.5	4.4E8
RR77	Cu jaws	1E7 \pm 17%	8E7 \pm 12%	5E-2 \pm 13%	5.6	3E8
	Opt.	3E7 \pm 18%	2E8 \pm 10%	1E-3 \pm 26%	5.9	2.9E8

13.3 The BPMs integration studies

Calculations of prompt radiations also support the integration of the BPMs on the Phase II Glidcop jaws of the proposed CERN design (see Fig. 9.16). Annual dose evaluations are required to give indications about the feasibility of the beam position measurements provided by the devices.

High dose values on the BPMs could have effects on the output signals and on degradation of the electronic instrumentations. The estimations are strongly dependent by the BPMs position on the collimator jaw and by the surrounding material on which they are installed.

In particular, for the most loaded Phase II collimator, that is the first after the Phase I primaries in the Beam 1 line (i.e. TCSM.A6L7.B1), calculated values range from 270 MGy/y to 21 MGy/y , if the BPM is installed upbeam or downbeam on the Copper tapering bases of the most charged jaw respectively. Using Aluminum instead of Copper reduces the dose to 180 MGy/y and 40 MGy/y for the upbeam

and downbeam BPMs respectively. For this reason, the CERN Phase II collimator design employs Aluminum taperings.

Actually, tests on the BPMs signal are performed in the SPS accelerator at CERN. Experimental data will support the possible installation BPMs on the Phase II jaws.

13.4 Conclusion

The technological complexity of the LHC has required several control systems for the operation of the machine. Radiation tolerance has taken into account as a constraint for the functionality and reliability of all these electronic systems installed in the tunnel. The radiation monitoring is improved in particular in the LHC tunnel and surrounding areas in which important beam losses are intentionally generated by interactions of the primary beam with beam line component such as collimators. It shall to be noted that equipments installed in partly shielded adjacent areas are based on COTS and they were not tested for radiation.

All the results presented in this Chapter for Point 7 are based on considering only the effects due to the collimation.

The layout of the collimation system strongly affects the radiation fields in UJ76 and RRs. Maximum gain of a factor 10 could be obtained by using Phase II as absorbers. However, this solution is not sufficient to solve the problem. Indeed, in the UJ76, the radiation field is dominated by the Beam 2 effect, which brings the high energy particle fluence to values of two order of magnitude higher than the maximum limit of 10^7 hadron/cm^2 . In the RRs, only in the case of a Phase II collimation system with Glidcop or Copper jaws, the fluence is in the order of the limit value.

It has to be pointed out that radiation is also produced when protons interact with the nuclei of the residual gas atoms in the beam pipeline. In particular this effect becomes dominant in the RRs. Indeed, inside these caverns the radiation level due by beam gas, in terms of high energy hadron fluence, reaches the value of $5 \times 10^8 \text{ cm}^{-2} \text{ y}^{-1}$ [93] close to each shielding wall, becoming thus the major source of possible problems to electronics located there. The effect is negligible for what concerns UJ76, because each beam pipe close to it is coated with TiZrV non evaporable getter (NEG) [94].

The prompt radiation effect is also an important parameter, which has to be evaluated before integrating instrumentations in the Phase II collimators themselves. Dose evaluations in nominal conditions support not only the choice of the electronics to be implemented, but also their best locations in the device, which could bring in changes of the mechanical design or of the support materials, as was for the tapering parts of the Phase II jaw. Tests with beam are now on the way in the SPS to study the behaviour of the BPM buttons on a preliminary version of the Phase II jaws.

Chapter 14

Displacement Per Atom (DPA) calculations

Ideally, the performance of the LHC collimators in high radiation environment should not change with time. However, for long-term employment of collimators significant microstructural alterations occur in the jaw materials due to displacement of atoms from their nominal position.

Major phenomena affecting structural materials are void swelling, irradiation creep, phase stability and changes in mechanical properties such as the electrical resistivity. The latter is responsible for the collimator induced impedance that can modify in turn the LHC performance.

The influence of proton damage, in particular on the structure and property of the jaw material, provides an input for estimating lifetime of collimators complying with required specifications. The prediction of the collimation lifetime allows to avoid premature replacements of the whole collimators or its components. Such evaluation is rely upon models describing the structural damage due by radiation and is supported by test beam studies.

14.1 Brief description of theoretical background

The defects, that can develop in any crystalline lattice under irradiation by neutral or charged particles and ions, can be distinguished according to the topology of the defect formation. Points defects (i.e. vacancies and interstitials), 1D or line defects (i.e. dislocation lines), 2D or planar defects (i.e. dislocation loops) or 3D or volume defects (i.e. voids, bubbles, etc.) are considered as destructive elements which contribute both to changes in physical properties and visible deformations of irradiate material, ultimately leading to the material distruction.

The DPA is a measure of the ammount of radiation damage in the irradiated material. For example, 3 DPA means that each atom in the material has been displacement from its site within the structural lattice of the material an average of

3 times.

Displacement damage can be induced by all particles produced in the hadronic cascade, including high energy photons. The latter, however, have to initiate a reaction producing charged particles, neutrons or ions.

The DPA quantity is directly related with the total number of defects, or Frenkel pairs, N_F produced in the irradiated material. A Frenkel defect forms when an atom or ion leaves its place in the lattice (leaving a vacancy) and lodges nearby in the crystal (becoming an interstitial).

$$\mathcal{DPA} = \frac{1}{\rho} \sum_i N_i N_F^i \quad (14.1)$$

where ρ is the density of the material in unit of *atoms/cm³*, N_i is the total number of incoming particles involved in the interaction channel i .

The calculation of N_F in each channel is based on the Kinchin-Pease model [95], revised by Norgert, Robinson and Torrens [96]:

$$\mathcal{N}_F = k_{NRT} \frac{f(E_p) E_p}{2E_{th}} \quad (14.2)$$

where k_{NRT} is the displacement efficiency and $f(E_p)$ is the partition function introduced in the framework of the LSS theory [97] defining partition of E_p , that is the kinetic energy of the Primary Knock-on Atom (PKA), between electronic excitation and kinetic energies of atoms. Finally E_{th} is the value of the threshold displacement energy averaged over all crystallographic directions or a minimum energy to produce a defect.

The displacement efficiency k_{NRT} can be considered as independent of E_p only for $E_p < 1 \div 2$ keV. In this energy range, it is set equal to 0.8. At higher energies, the development of collision cascades results in defect migration and recombination of Frenkel pairs, due to overlapping of different branches of a cascade which translates into decay of $k(E_p)$. From Molecular Dynamic (MD) simulations of the primary cascade [100], the number of surviving displacement N_{MD} , normalized to the number of those from NRT model N_{NRT} decrease down to values about $0.2 \div 0.3$ at $E_p \approx 20 \div 100$ keV. The efficiency in question only slightly depends on atomic number Z and the temperature. An approximation of the [100] results are employed in the following form:

$$\mathcal{N}_{MD}/\mathcal{N}_{NRT} = 0.3 - 1.3 \left(-\frac{9.57}{X} + \frac{17.1}{X^{4/3}} - \frac{8.81}{X^{5/3}} \right) \quad (14.3)$$

where $X = 20E_p$.

The product $f(E_p)E_p$ describes the damage energy or the energy deposited by the PKA (i.e. the removed atom) into elastic collisions of particles and nuclear fragmentations with a nucleus of the irradiated material.

The partition function $f(E_P)$ gives the fraction of stopping power S that is transferred to nuclear recoils (S_n) :

$$f(E_p) = \frac{S_n}{S} \quad (14.4)$$

The stopping power S of a material is defined as the average energy loss per unit path length which charged particles suffer when traversing the material, as the result of Coulomb interactions with electrons and with atomic nuclei. Tables of stopping powers are available from the semi-empirical stopping power formulas given by the model developed by Ziegler, Biersack and Littmarkwith [98].

The nuclear stopping power S_n is due to elastic Coulomb collisions in which recoil energy is imparted to atoms. For a particle with energy E_0 , it is determined by the spectrum of recoil particles (atoms) $d\sigma/dE_p$ integrated within the interval of recoil energies from E_p^{min} to $E_p^{max} = 4EM_1M_2/(M_1 + M_2)^2$. The latter is the maximum fraction of energy transfer during collision between the projectile (1) of whichever charged particle and the medium (2).

$$S_n(E_0) = N \int_{E_p^{min}}^{E_p^{max}} \left(\frac{d\sigma}{dE_p} \right)_{E_0} dE_p \quad (14.5)$$

where N is the atomic density of the medium. S_n magnitude is called *restricted* when $E_p^{min} = E_{th}$ and *unrestricted*, when all the energy losses are also considered below the threshold E_{th} .

The nuclear stopping power is closely related to the frequently used magnitude Non Ionizing Energy Loss (NIEL). The NIEL describes the rate of energy loss due to atomic recoils as a particle traverses a material. NIEL and the nuclear stopping power S_n are equal only in the limiting case of $f(E_p) = 1$, which means that all of the recoil energy is deposited in the displacements:

$$NIEL(E_0) = N \int_0^{E_p^{max}} \left(\frac{d\sigma}{dE_p} \right)_{E_0} f(E_p) dE_p \quad (14.6)$$

For complex material, the NIEL is calculated for each recoil-kind and sum up the contribution.

Approximation of NIEL can be find in [97] including all the energy losses also those below the threshold E_{th} . In additional, in [97] are reported the Lindhard approximated formulas for $f(E_p)$, which can handle any particle projectile.

$$f(E_p) = \frac{1}{1 + F_L(3.4008\epsilon(E_p)^{1/6} + 0.40244\epsilon(E_p)^{3/4} + \epsilon(E_p))} \quad (14.7)$$

where:

$$F_L = 30.724Z_1Z_2\sqrt{Z_1^{2/3} + Z_2^{2/3}}\frac{A_1 + A_2}{A_2} \quad (14.8)$$

$$\epsilon(E_p) = \frac{E_p}{0.0793 \frac{Z_1^{2/3} \sqrt{Z_2}}{(Z_1^{2/3} + Z_2^{2/3})^{3/4}}} \frac{(A_1 + A_2)^{3/2}}{A_1^{3/2} \sqrt{A_2}} \quad (14.9)$$

with A_1 (A_2) and Z_1 (Z_2) are the projectile (target) atomic weight and number, respectively.

Table 14.1 shows the typical values of E_{th} used in the NJOY99 code. The Nuclear Data Processing System NJOY [99] is a modular computer code designed to read evaluated data in Evaluated Nuclear Data Formats (ENDF), transform the data in various ways, and output the results as libraries designed to be used in various applications. The ENDF are used all over the world to encode nuclear data evaluations for use in research and nuclear technology.

Table 14.1: Typical values used in NJOY99 code.

Element	E_{th} (eV)
Lithium	10
Carbon in SiC composite	20
Graphite	30÷35
Aluminum	27
Iron	40
Cobalt	40
Copper	40
Niobium	40
Molybdenum	60
Tungsten	90
Lead	25

From 2009, new routines are implemented in FLUKA [101] in order to estimate the DPA values in materials under radiation. During interactions, FLUKA calculates the recoil energy for all charged particles and heavy ions, which are then transported such as any other particle. During transport, FLUKA calculates the fraction of nuclear stopping power over the stopping power to estimate $f(E_p)$ for primary particles, with kinetic energies above the FLUKA particle thresholds which are fixed by the users. Below them and, in addition for secondary particles, the Lindhard approximated formulas for $f(E_p)$ is used. This is done because of a strong discrepancy for high energies between the Lindhard approximated formulas for $f(E_p)$ and the value of S and S_n obtained using the Ziegler semi-empirical approximation (see Fig. 14.1). For neutrons below 20 MeV, the NIEL estimation, used to calculate the DPA, is performed from the NJOY99 code during the library preparation. The particle thresholds introduced by the users are depending by the problem under study.

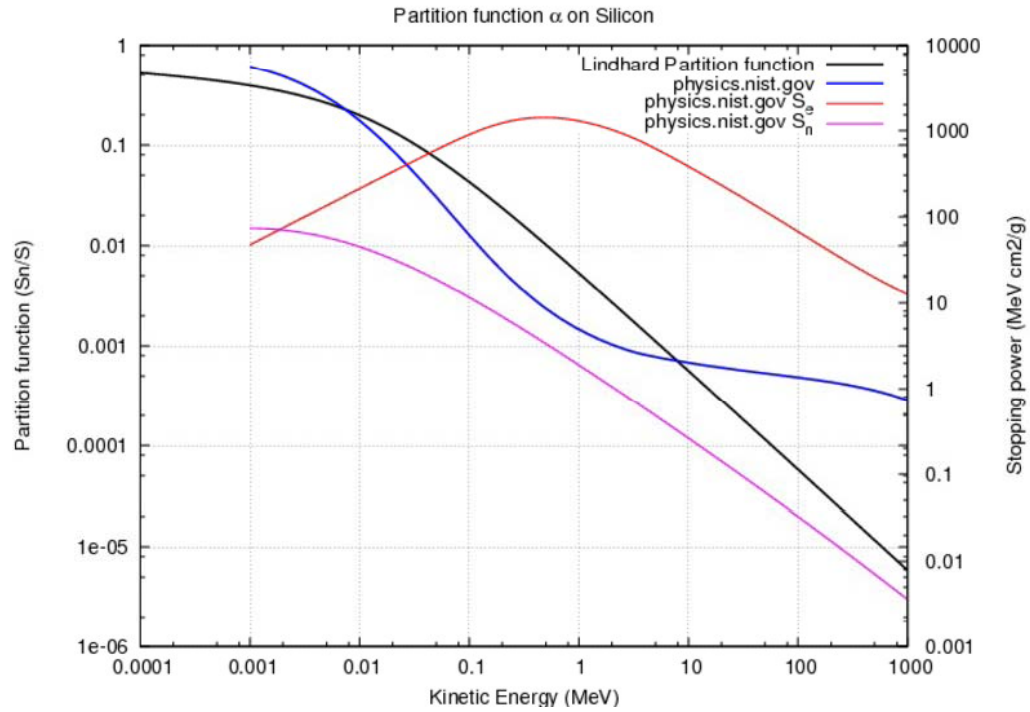


Figure 14.1: Comparison between the partition functions for α particles on Silicon, calculated using the Lindhard (black line) or the Zieler (blue line) approximations.

14.2 The BNL experiment

In order to validate the FLUKA DPA implemented model, results are compared to the DPA calculated with MCNPX MonteCarlo code [102] for the Brookhaven National Laboratory (BNL) experiment, in which the exact same material used for LHC Phase I collimator jaw was irradiated.

In March 2004 a 2 week irradiation of targets took place using the BNL accelerator complex. The 200 *MeV* proton beam at the end of the Brookhaven Linac Isotope Producer (BLIP) was directed towards the Isotope Production Facility (see Fig. 14.2), where a special target station submerged in about 9 *m* of water and with water flowing through the assemblies has been designed and installed. A precise tracking of the beam intensity at the Linac side led to the estimation of the total flux of 5.25×10^{20} *protons* (or a current of 23,454 $\mu A/h$).

The target array of interest were placed upstream of the isotope targets that typically operate at 112 *MeV*. It includes solid materials in the low-Z and mid-Z

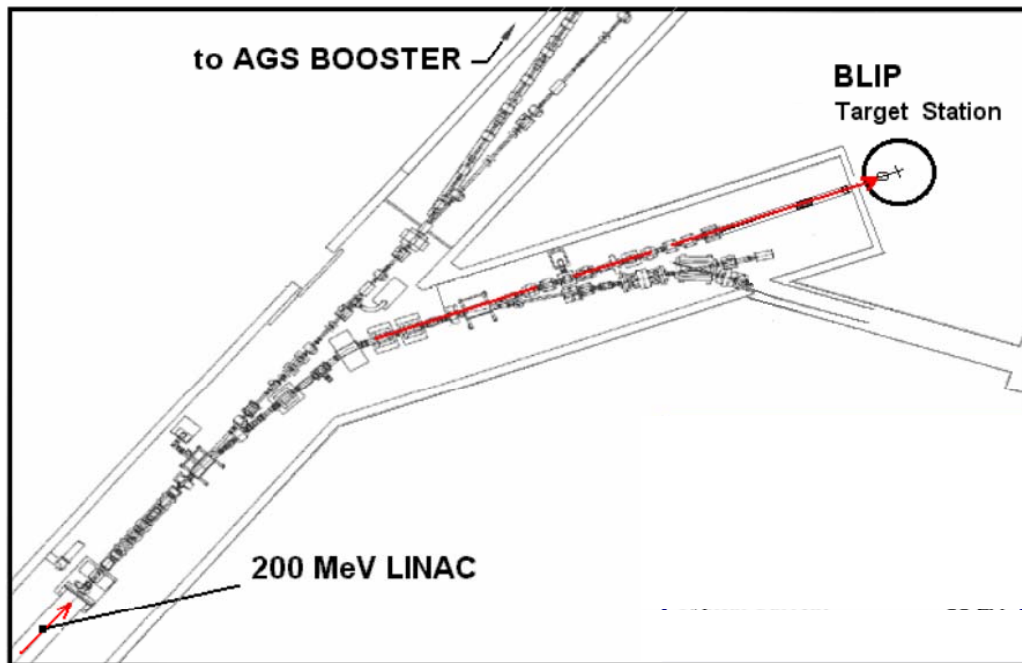


Figure 14.2: BNL experimental facility used in the material irradiation study.

regimes, specifically selected for their possible use as accelerator targets or collimator jaws. The special packaging of the different planes of irradiate material, which are in cascade Vascomax, Ti-alloy (Ti-6Al-4V), AlBeMet, Beryllium, Gum Metal, Graphite (IG-43), Carbon composite and the Ni-plated Aluminum, degrades the beam from 200 MeV down to what was desired by the isotope targets downstream. The requirement that the beam entering the assembly with 200 MeV must leave at a particular energy specified by the isotope production targets downstream, makes the arrangement a serious challenges.

Fig. 14.3 shows the general layout of the two sets. The material samples were located in the first three Aluminum target boxes (also see Fig. 14.6).

The packing arrangements are composed by different layers, most of which are 3 mm thick with between each a 1 mm water channel. Each $42 \times 42\text{ mm}$ cross section is made up by a tigh combination of 3 mm thick specimens arranged together in the same plane with three 1 mm thick tensile specimens. Fig. 14.4 shows the two types of specimens used during irradiation for the evaluation of the mechanical and physical properties. Their particular shape has been chosen to satisfy the requirements

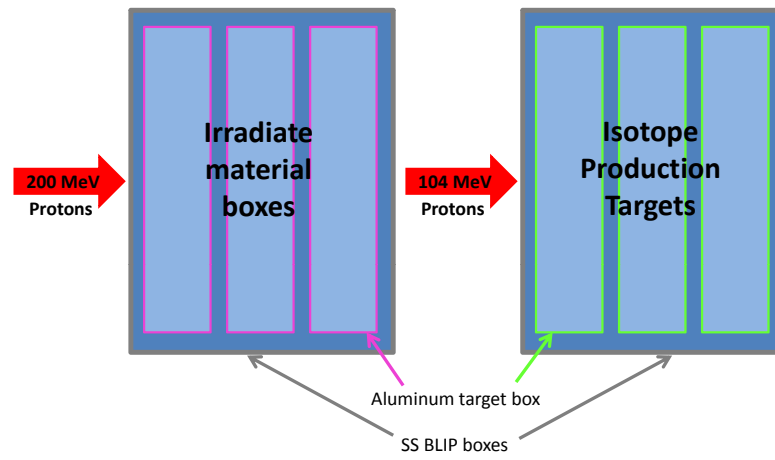


Figure 14.3: Cross section of the irradiated targets.

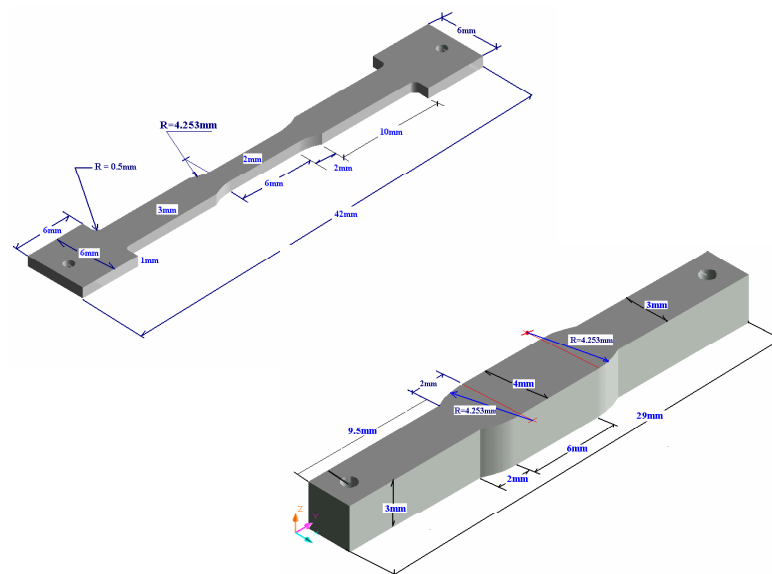


Figure 14.4: Specimen design for mechanical and physical property studies.

imposed by the isotope production. Only the Graphite and the Carbon composite formed 6 mm rather than 3 mm thick layers.

In order to not affect the isotope production downstream, the Gaussian shape of the beam entering the irradiation target must to be maintained. Special Nickel foils integrated into the irradiation assemblies help to establish the beam spot size, shape and location during irradiation. Beam spot sizes with full width at half maximum of about 15 mm are typical. The proton beam is purposely de-focused in order to expose as much as possible of the volume of the special targets for harvesting isotopes.

Fig. 14.5 shows an actual layer of the two types of specimens integrated and the position of the beam on the target plane. The downstream Nickel films positioned within the irradiation matrix were autoradiographed to establish the beam profile and its relative position to the specimens (horizontal and vertical rms beam σ equal to $7.2 \pm 0.3\text{ mm}$).

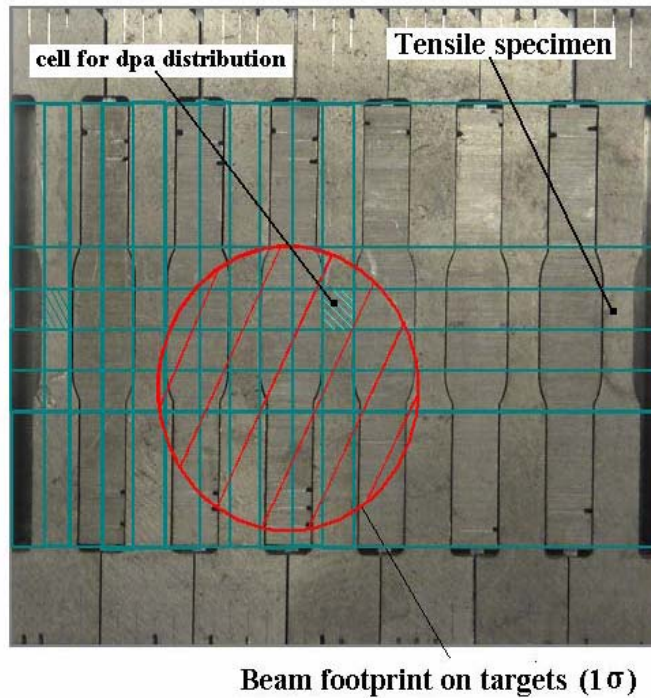


Figure 14.5: Front view of the target with the integration of different types of specimens into the irradiation space. Superimposed is shown the approximate location of the beam footprint and the discretization of the irradiation plane for the DPA calculations used by both MCNPX and FLUKA codes.

14.2.1 Simulation results with MCNPX

Following the irradiation, detailed DPA calculations were performed at BNL on all material involved using MCNPX MonteCarlo code. The DPA values have been estimated as average number over discrete volumes both from protons and the secondary neutrons. The $42 \times 42 \text{ mm}$ section was broken into unit volumes (i.e. 2 mm (x) \times 2 mm (y) \times 1 mm (z)). The importance of the space discretization is in that the location of rupture in the tensile specimens can be correlated with the distribution of the damage along the gauge length.

The analysis revealed that primarily the damage was the result of incident proton fluence. The contribution of neutrons was minimal.

For a total flux of $5.25 \times 10^{20} \text{ protons}$ in the irradiation phase, the DPA peaks calculated with MCNPX for some of the material layer are:

- *First Vascomax layer.*

The DPA peak values for Vascomax coming from protons was estimated to be 0.27 and from neutrons 0.014.

- *First Gum Metal layer.*

The DPA peaks estimated for the first 3 mm thick layer of Gum Metal was 0.23 DPA from protons and 0.015 DPA from neutrons.

- *First Carbon composite layer.*

For the first layer of the Carbon composite (i.e. first of the two 6 mm thick layer, where the beam is impacting at about 130 MeV) the DPA peak values from protons are 0.012 and from neutrons 0.0004.

14.2.2 The BNL experiment simulated with FLUKA

In order to validate the FLUKA DPA model implemented, the BNL experiment was simulated also with the FLUKA code. The geometry of the target layout as well as the Gaussian beam were *exactly* reproduced, including the windows before the target boxes (see Fig. 14.6).

The proton beam coming from Linac, goes through some upstream windows (i.e. the two 0.3 mm Beryllium and the 0.3 mm Aluminum layers) and the 0.8 mm thick SS box wall and the 1.59 mm water channel, before impinging the first Aluminum target box.

Fig. 14.7 shows the peak DPA values along the target assembly due to protons, to neutrons and to all particle showers respectively. In addition, the location of the layers for which results are available from MCNPX code are also indicated (i.e. first Vascomax, first Gum Metal and first Carbon composite layers). The impacting protons are the first cause of damages as already reported by the analysis of the MCNPX results.

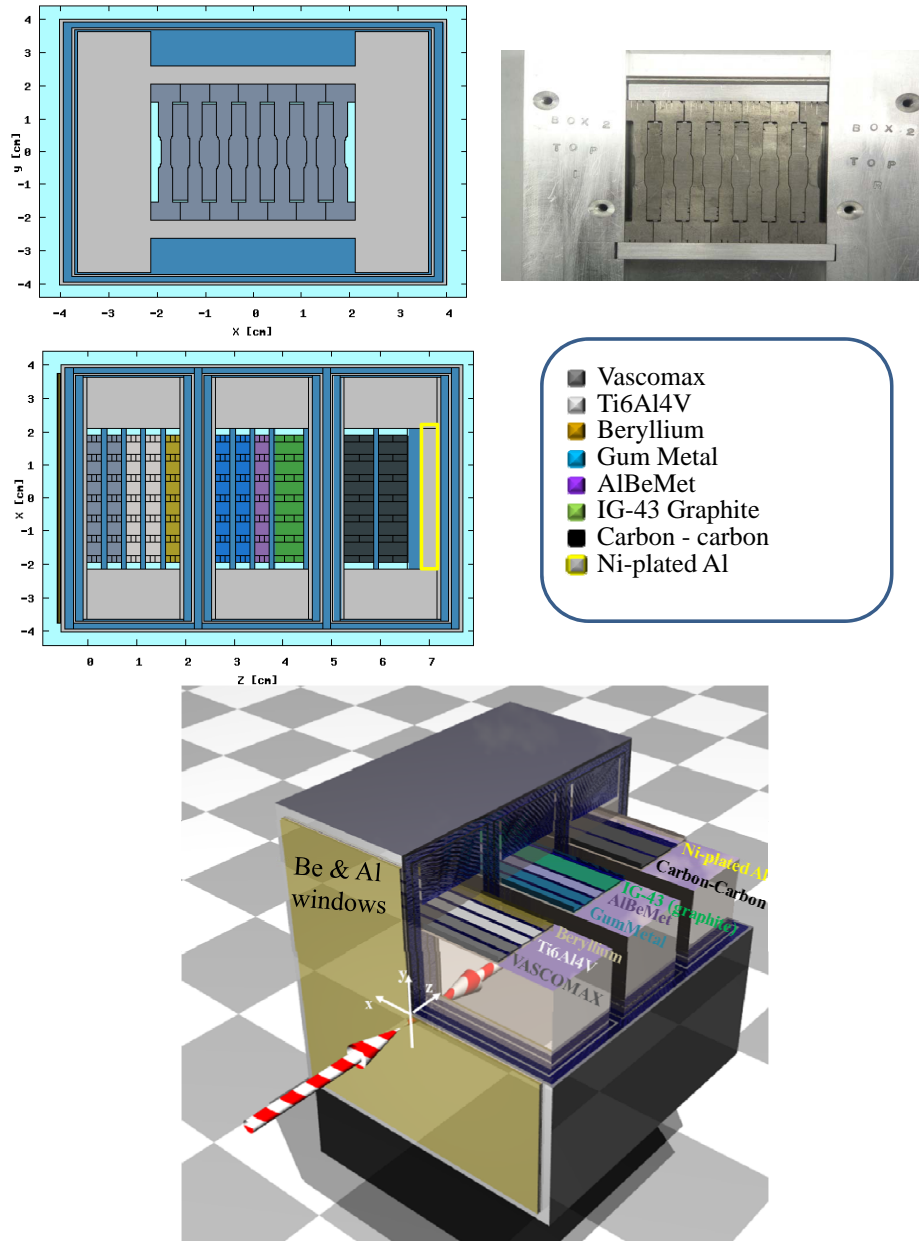


Figure 14.6: Real cross view of target irradiation assembly (right up corner) and the FLUKA model implemented. A 3D picture of the target assembly and the proton beam impacting position is also shown.

The FLUKA results are obtained using energy thresholds for electron and photon production set to 1 MeV in all the target materials, while cuts at 1 keV were fixed for protons, kaons and pions in all the regions. The kinetic energy transport cut-off settings are applied in order to stop the tracking of particles which give negligible contributions to DPA values, saving CPU time.

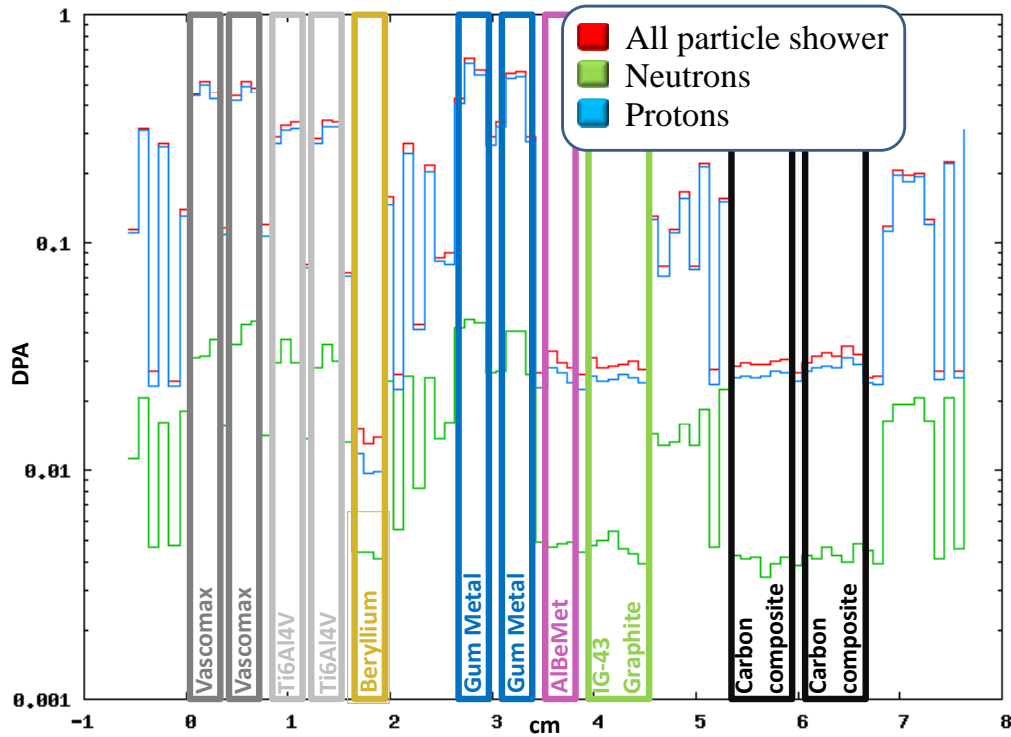


Figure 14.7: DPA peak values along the target assembly.

14.2.3 Results comparison

The DPA peak values from the MCNPX simulations are compared with the FLUKA ones in Table 14.2. A factor of 2 in the DPA values is shown for the first Vascomax layer both for protons and neutrons. For what concerns the first Gum Metal layer, a factor of 3 in both cases is in between the two simulation results. Finally for the first Carbon composite layer, a factor of 2 is shown for protons, while a factor 10 is obtained for neutrons.

Incertitudes in the stopping power thresholds of the target materials and in their chemical compositions used by the two codes, as well the particles thresholds

implemented could justify the factor 2 in the results. In particular the incertitude in the chemical composition of the Gum Metal used during the BNL irradiation experiment could justify the factor 3 found comparing the results. Since the carbon composite samples are installed at the end of the irradiated material boxes, the sum of the incertitude in the definition of each material layer, through which the proton beam have to pass before reaching them, could justify the factor 10 calculated between the DPA values due to neutrons in the first Carbon composite layer.

Summarizing, discrepancies of the order of 2 are found between the FLUKA and MCNPX results, due to different kinds of incertitudes.

Table 14.2: DPA values for the BNL irradiation experiment calculated by MCNPS and FLUKA MonteCarlo codes.

Target Material	Particles	DPA (MCNPX)	DPA (FLUKA)
Vascomax (first layer)	protons	0.27	0.498
	neutrons	0.014	0.037
Gum Metal (first layer)	protons	0.23	0.6
	neutrons	0.015	0.0045
Carbon composite (fist layer)	protons	0.012	0.0269
	neutrons	0.0004	0.0045

14.3 DPA calculations for LHC collimators

FLUKA simulations to evaluate DPA were performed for the CERN design Phase II collimator with Glicop jaws in the most loaded position, that is the TCSM.A6L7.B1 location.

Fig. 14.8 shows the DPA values along the Phase II collimator jaws due to neutrons, protons and all particles showers generated by primary proton beam interactions with the upstream primary collimators and with the TCSM.A6L7.B1 itself at 7 TeV . Results are normalized to 1.15×10^{16} proton losses per year.

Value of the order of 0.001 DPA in Copper/Glidcop could be already a critical issue for the Cleaning Efficiency and Impedance, since the radiation damages causes the increase of the cluster density and resistivity in the jaw material. However, in order to fix a limit in the DPA value, above which the Glidcop collimator has to be irremediably changed, DPA calculation has to be supported by experimental data. The incertitude in the DPA calculations and in the irradiation enviroment e.g. material properties and target temperature, could bring to errors if not supported by irradiation tests.

For this reason, different experimental tests on material resistance to beam-induced radiation are foreseen in the framework of the EuCard project to support the

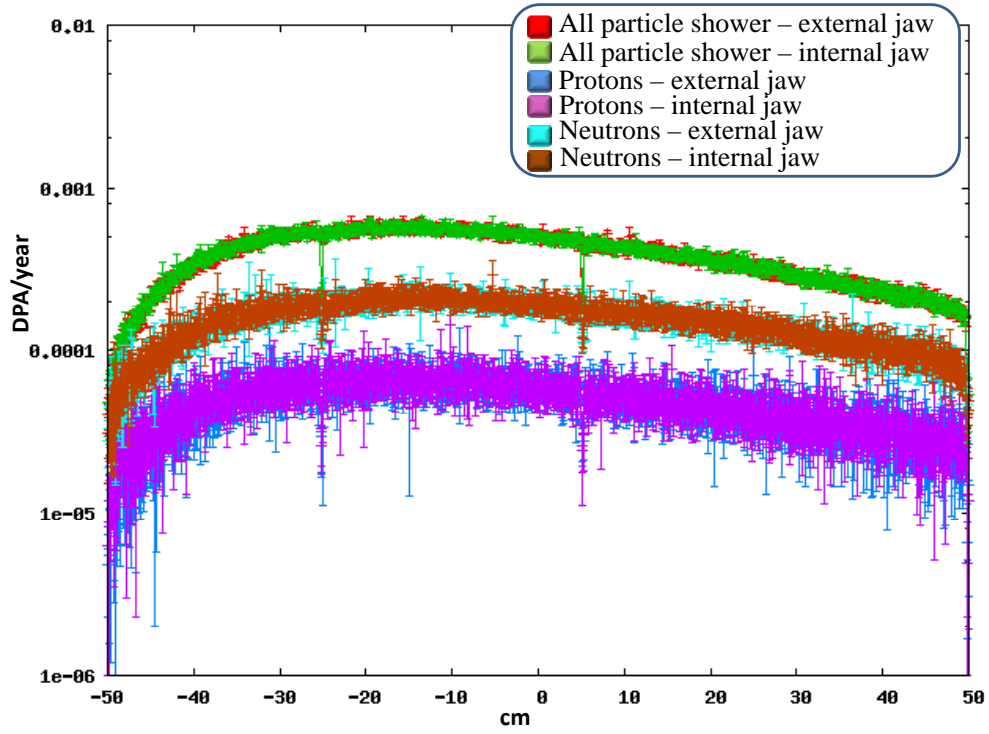


Figure 14.8: DPA values along the CERN design Glidcop jaws for the most loaded Phase II collimator location.

prediction of the material life expectancy in particular for the Phase II collimators jaws. The tests in irradiation facilities on the different material samples proposed for Phase II jaws are supposed to be coupled with MonteCarlo code simulations. Results will be used to fix the limits on the Phase II jaws without testing directly the whole device.

14.4 Conclusions on DPA calculations

The LHC performance at 7TeV are strongly dependent by its collimation system. Radiation damages on the Phase II jaws has to be evaluated in order to foreseen substitution actions in time.

In particular for metallic jaws, the DPA caused by radiation is a critical issue. In order to support the damage evaluations, the experimental results on irradiated material samples are coupling with MonteCarlo code simulations for the DPA calculations. This avoids to test the whole device for having predictions about the

possible changing in functionality.

However, incertitudes in the DPA dependences and in the model implemented could bring to different results, if different MonteCarlo code are used. Fig. 14.9 shows the DPA values calculated by FLUKA, TRIM_2 [103], PHITS [104] and MARS15 [105] codes, for a simple case of a 130 MeV/u ^{76}Ge beam impacting on 1.2 mm thick Tungsten target. Differences in the DPA results of 1 or 2 orders of magnitude are shown, when different codes are used. This underlines the necessity of knowing the MonteCarlo code used for the experimental tests on samples in order to apply it for the following DPA predictions on each complex accelerator device under study.

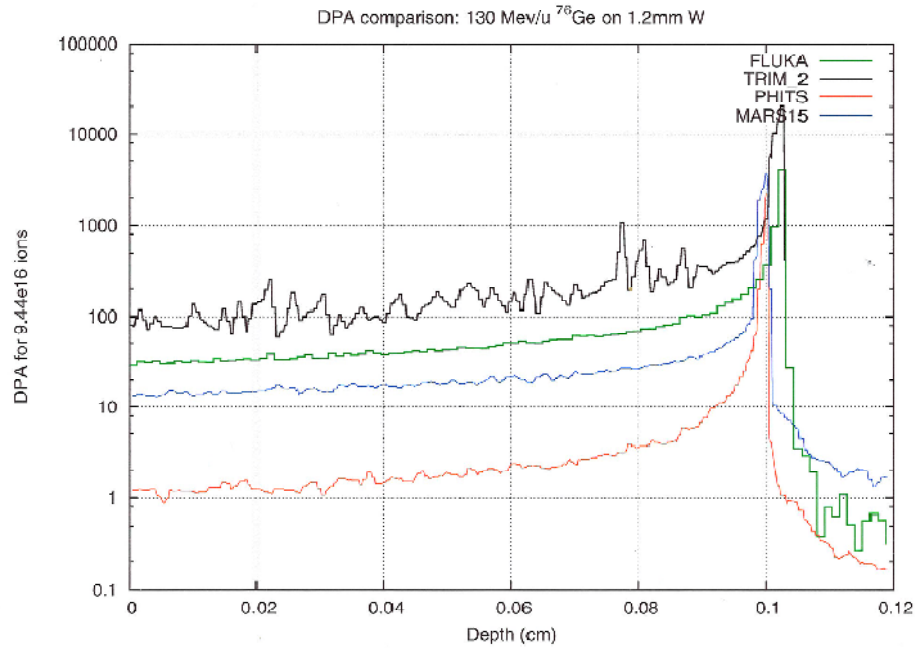


Figure 14.9: DPA results form different MonteCarlo code for 130 MeV/u ^{76}Ge impacting on 1.2 mm thick Tungsten target.

Chapter 15

Conclusions

The goal of this *doctoral thesis* was to provide directions on the final choice of the collimator jaw materials, which have to survive to the LHC 7TeV proton beam interactions. The calculations made in the frame of this PhD are not only used as the basis for the Phase II collimator mechanical integration studies, but also to evaluate the activation and radiation field on the surrounding areas due to the Phase II installation in the LHC main ring. In particular, they were focused in the Betatron Cleaning region, where the particle losses are about 7 times higher than in the Momentum Cleaning ones, in case of performing a pure Betatron Cleaning at IR7.

Starting from accelerator physics calculations, the FLUKA MonteCarlo code was extensively used to perform simulations, primary directed at identify materials and jaw geometries which would produce the best collimation surface, in terms of Cleaning Efficiency (better than 99.99%), jaw flatness (order of tens μm) and in order to provide jaw cooling with a reasonable water flow in both the steady state and transient conditions.

An iterative process between mechanical engineers and MonteCarlo experts follows the first phase of the preliminary material selection, to support the mechanical integration of all the device components with respect to the maximization of its working performance.

Two options in relation to the beam stabilization method used were in particular investigated for the jaw materials. The first one concerns the use of highly conductive jaws (e.g. Copper based materials), coupled with a Landau octupoles stabilization system, while the second option was focused on the investigation of jaw composed by a non conductive material (e.g. SiC) coupled with the transverse feedback stabilization method.

Copper based materials such as Glidcop were in particular studied since they have a good balance of Cleaning Efficiency performance, deflection and manufacturability, in addition to its good electrical conductivity.

If made of Copper, the most loaded Phase II secondary collimator in each beam line (i.e. the TCSM.A6L7.B1/B2), installed nearest to the Phase I primary collimators in the Betatron Cleaning region must survive head loading approximately 20

times than of its carbon Phase I secondary counterpart. Extensive FLUKA simulations of the power deposited at 7 TeV low beta condition in the most loaded location were performed during this PhD, in order to support the mechanical design evolution focusing on minimize the Copper based jaw deformations.

The option of increasing the aperture of this first secondary collimator in order to relax the cooling design and to pass the load to down-beam secondary collimators was also considered. In this particular case, the collimation efficiency would be maintained by the remaining collimators. However, since the peak heat load on this device is for the 90 % due to the particle showers coming from primary protons interaction with the Phase I primary collimators downstream, this solution is not effective. On the other hand, removing completely this first metal collimators or moving to a non conductive jaw materials or to a longitudinal multi-layer composition of different jaw materials for the Phase II have been shown to be promising options.

Based on the accident scenarios, other possible Phase II collimator improvements from Copper based jaw towards more transparent materials were proposed and evaluated in this PhD for the most exposed locations.

The PhD results, obtained on the hypothesis of ideal performance of the LHC collimation system, have oriented the mechanical development choices for the different components of the first two Phase II collimator prototypes with Glidcop jaws, one developed at CERN and the other at SLAC laboratories. They will be tested with beam at CERN in the next future (2011). A preliminary version of the design proposed by CERN implementing BPM buttons, for which the yearly nominal dose has been calculated, is already installed in the SPS to provide data on their possible integration on the tapering parts of the Phase II jaws.

The study in nominal conditions was completed by taking into account, for the first time, the impact of the misalignmet set-up collimator errors randomly selected for all the LHC collimation system within the alignment accuracy limit of $600\text{ }\mu\text{rad}$. Results have shown their limited effect on the variation of the integrated power deposited on the Phase II devices.

The impact on the tunnel environment of the different solutions proposed were estimated. In particular the studies were focused on the evaluation of the radiation to personnel in the tunnel and on the radiation to the electronic equipments in the adjacent service caverns. Close to the most loaded Phase II collimators, the ambient dose rate peaks calculated exceed the 2 mSv/h value at different cooling times. It triggers the highest level of ALARA precautions to be followed during works close to components. The importance of planning the foreseen interventions in the closest areas was thus underlined. Moreover, the shielding effect of the Phase II collimators was extensively studied to estimate the resulting protection to the electronic equipments. Unfortunately their installation is not sufficient to fix the problem. Additional solutions are on the way of evaluation, including moving part of the Betatron Cleaning to the Momentum region, in order to reduce the particle flux

towards the electronic equipments in the service areas. It includes the installation of the cryo-collimators with Tungsten jaws in the DS regions at IR3, at the place of the Copper ones in IR7 considered during this PhD. In addition, this option decrease the thermal loads on the Phase II collimators themselves.

Finally, the last effort of the thesis was directed on a better understanding of the functionality limits imposed by the DPA mechanism caused by the beam impact on jaw materials, in particular important for metal materials. For this purpose, the DPA model implemented in FLUKA was tested against the MCNPX calculations performed for the BNL experiments. Discrepancies of a factor 2 were found between the two code results, due to different kind of incertitudes (e.g. different DPA modeling, different geometry description, uncertainties in the chemical composition of special sample materials irradiated, etc). In addition, DPA calculations were also performed for the Phase II collimators with Glidcop jaws. Also taking into account the uncertainties, the DPA FLUKA results reach values which could be a critical issues after one year of nominal operation in the most loaded location. The need of supporting the FLUKA calculations with testing Glidcop samples in a similar LHC irradiation field was pointed out, in order to provide more realistic prediction of the Phase II lifetime as well as to plan possible substitution of the whole Phase II collimator only when necessary.

Agreements within 20 % are found between LHC BLM signals and FLUKA calculations during tests in the SPS in operation condition at 450 GeV , where a LHC Phase I collimator was installed with its downstream BLMs [106]. Studies are starting to benchmark the FLUKA results at different LHC operation energies at the beginning for the Phase I collimation system installed and in the future for the Phase II collimators. Only benchmark experiments and iterations between the computational and the engineering team can ensure high quality results and limit the range of uncertainties.

In particular, the results presented in this PhD thesis have to be benchmarked when experimental data will be available at 7 TeV . This implies that the biggest machine that mankind built will be into operation with the Phase II collimator system already installed.

Appendix A

The principle of 2 stage Betatron and Momentum collimation

Principle and optimization of secondary collimators are presented here for the one dimensional collimation. In this case, as a first approximation, the proton scattering is considered in the same plane of the analysed halo. It represents the theoretical limit for a realistic scenario, where the particles interacting with a jaw collimator are scattered isotropically in the transverse plane. However, already in this case it shows the need of two secondary per primary collimators. This is the minimum required in high intensity collider. More details about the two dimensional collimation can be found [23].

The analysis is performed in normalized phase space. Let n_1 and n_2 the normalized aperture, in units of rms transverse beam size, of primary and secondary collimators.

A.1 One-Dimensional Betatron Collimation

The Betatron cleaning allows to limit the transverse extension of the beam halo.

The proton, which drifts slowly outward, touches the collimators when being very close to its maximum spatial extension. Using the normalized coordinates (capitol letter):

$$\begin{pmatrix} Z \\ Z' \end{pmatrix} = \frac{1}{\sigma_z} \begin{pmatrix} 1 & 0 \\ \alpha_z & \beta_z \end{pmatrix} \begin{pmatrix} z \\ z' \end{pmatrix} \quad (\text{A.1})$$

this happens when $Z = n_1$ and $Z' = 0$, or in real coordinates when $z = n_1\sigma_z$ and $z' = (\alpha_z/\beta_z)z$. Thus, the coordinates in the real case are measured in units of σ and the divergences in units of σ' , where σ and σ' are transverse beam size and divergence.

If it is not absorbed, the particle is suppose to be scattered along the vertical line $Z = n_1$, receiving a positive or negative elastic kick (see Fig. A.1).

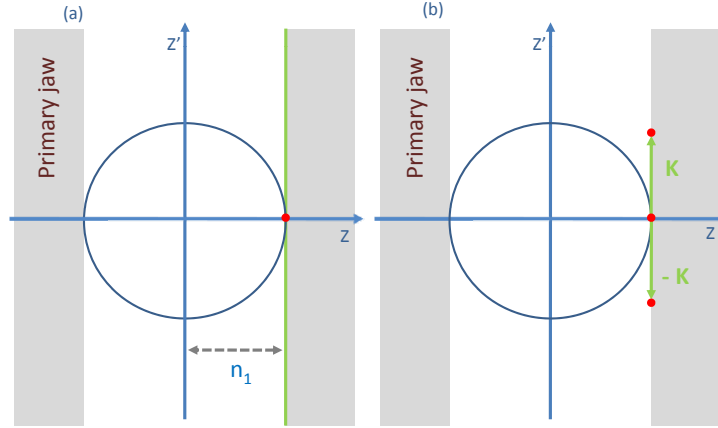


Figure A.1: Proton hitting the primary collimator receive a kick (b) along the line $Z = n_1$ (a).

In case of positive kick, the scattered particle has coordinates $Z_1 = (n_1, K)$. It propagates to the secondary collimators along the ring, through the normalized linear transport matrix. This matrix is reduced to a rotation one in the normalized coordinates:

$$\begin{pmatrix} Z_2 \\ Z_2' \end{pmatrix} = \begin{pmatrix} \cos\mu & \sin\mu \\ -\sin\mu & \cos\mu \end{pmatrix} \begin{pmatrix} n_1 \\ K \end{pmatrix} \quad (\text{A.2})$$

where μ is the betatronic phase advance between the first and the second collimators.

In order to catch as many as possible of the secondary particles, or in other words, to catch the smallest possible amplitude $A = \sqrt{n_1^2 + K^2}$ the secondary collimator jaws have to be placed in such a way that the absolute value of K gets a minimum.

The critical kick K_c , that a particle must receive at least in the primary jaw to be intercepted by the secondary one, can easily be calculated using A.2 ($Z_2 = n_2 = n_1 \cos\mu + K \sin\mu$):

$$K_c = \frac{n_2 - n_1 \cos\mu}{\sin\mu} \quad (\text{A.3})$$

the extreme value of the K_c is when $\mu = \mu_{opt}$ (see Fig. A.2) and this happens for:

$$\cos\mu_{opt} = \frac{n_1}{n_2} \quad (\text{A.4})$$

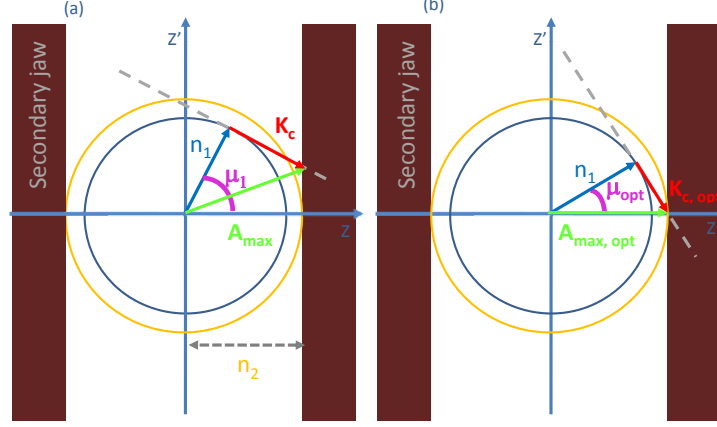


Figure A.2: Secondary particles intercepted by secondary collimators located at an arbitrary phase advance μ_1 (a) and at optimum phase advance μ_{opt} (b). Critical kick and maximum amplitude are indicated in both scenarios. Note that the particle could interact with the right jaw at $Z = n_2$ as well as with the left one at $Z = -n_2$.

Once n_1 and n_2 have been chosen, μ_{opt} is deduced and by using A.3

$$K_{c,opt} = \sqrt{n_2^2 - n_1^2} \quad (\text{A.5})$$

The maximum amplitude in phase space of particle escaping the secondary jaw is thus:

$$A_{max,opt} = \sqrt{n_1^2 - K_{c,opt}^2} = n_2 \quad (\text{A.6})$$

Summarizing, the phase advance between primary and secondary collimators is the critical quantity defining the maximum excursions of the secondary beam halo. One secondary collimator should be set at a phase advance μ_{opt} downstream of the primary collimator and one at its complement $\pi - \mu_{opt}$ on the opposite side of the beam. In such a way, it is guaranteed that only particles with amplitude $A_{max} < |n_2|$ do not interact with the secondary jaws.

An estimate of the real minimal deflection $\delta z'$ required by a deflected particle, such that it is intercepted by the secondary collimator, can be done using A.1 (i.e. coming back to the real coordinates) and A.5:

$$\delta z' \approx \frac{\sigma_z}{\beta_z} \sqrt{n_2^2 - n_1^2} \quad (\text{A.7})$$

Calculated values for LHC are for μ_{opt} of the order of 30° (both injection and top energy) and for $\delta z'$ of about $6 \mu rad$ for top energy and $23 \mu rad$ for injection.

A.2 One-Dimensional Momentum Collimation

The Momentum cleaning system is supposed to catch the particle with a large momentum deviation, to do this a certain value of dispersion is needed at the primary collimator. In general these particles will have some betatron emittance in addition. A combined momentum and betatron collimation is thus envisaged.

The horizontal transverse plane is usually the plane where dispersion is present, in normalized coordinates the dispersion is done by:

$$\begin{pmatrix} D_{norm} \\ D'_{norm} \end{pmatrix} = \frac{1}{\sigma_x} \begin{pmatrix} 1 & 0 \\ \alpha_x & \beta_x \end{pmatrix} \begin{pmatrix} D \\ D' \end{pmatrix} \quad (A.8)$$

where $D_{norm} = D/\sigma_x$ is the normalized dispersion at the primary collimator.

The particle reach the primary collimator with amplitude

$$n_1 = D_{norm}\delta + X_\beta \quad (A.9)$$

where X_β is the normalized betatronic contribution (see Fig. A.3), using the slow

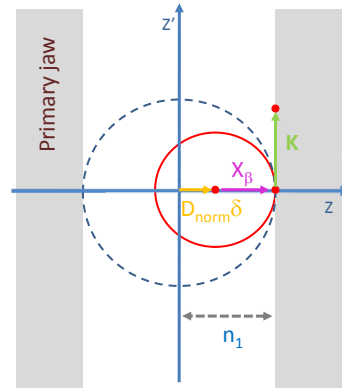


Figure A.3: Phase space at primary collimator for momentum collimation. The centre of the circular trajectory is shifted, due to the effect of the normalized dispersion D_{norm} and of the particle energy offset δ .

diffusion approximation (i.e. considering the impact points at the surface of the collimator while the betatronic oscillation is at its maximum).

If the particle touch the primary collimator with $D'_{norm} = 0$ (or in real coordinates $D' = -(\alpha_x/\beta_x)D$), as in Fig. A.3, the critical kick is independent of the momentum change (for the mathematical demonstration see [23]). This property is obtained by fixing a quantity at the primary jaw (namely $D'_{norm} = 0$) and the optimum phase advance of the secondary collimators respect to the primary is the same for all off-momentum particles. Thus the location of the secondary collimators can be chosen independently of momentum collimation considerations and the pure betatron cleaning considerations (i.e. 2 secondary collimators for each primary in one dimensional approximation) are applicable also in this case.

Appendix B

Phase I and Phase II collimator database

B.1 Beam 1

Table B.1: List of Phase I and Phase II (in red) collimators in the main ring for Beam 1. Name, length, azimuthal angle, material and nominal settings at injection and low beta energy are indicated. The devices both "out" at injection and low beta energies are used only to intercept particle showers. The jaw materials for Phase II are not indicated, because a final decision is still not taken as well as for the final aperture and material for the cryo-collimators jaws.

Name	Length [m]	Angle [deg]	Material	Half-gap[σ_z]	
				injection	low beta
TCL.5R1.B1	1.0	0.0	Cu	out	10.0
TCTH.4L2.B1	1.0	0.0	Cu-W	out	8.3
TDI.4L2.B1	4.0	90.0	C-C	6.8	out
TCDD.4L2	1.0	90.0	C	out	out
TCTVB.4L2	1.0	90.0	Cu-W	out	8.3
TCLIA.4R2	1.0	90.0	CFC	6.8	out
TCLIB.6R2.B1	1.0	90.0	CFC	6.8	out
TCP.6L3.B1	0.6	0.0	CFC	8.0	15.0
TCAPA.6L3.B1	1.0	0.0	W	out	out
TCSG.5L3.B1	1.0	0.0	CFC	9.3	out
TCSM.5L3.B1	1.0	0.0		out	18.0
TCSG.4R3.B1	1.0	0.0	CFC	9.3	out

continued from previous page

Name	Length [m]	Angle [deg]	Material	Half-gap[σ_z]	
				injection	low beta
TCSM.4R3.B1	1.0	0.0		out	18.0
TCSG.A5R3.B1	1.0	170.7	CFC	9.3	out
TCSM.A5R3.B1	1.0	170.3		out	18.0
TCSG.B5R3.B1	1.0	10.8	CFC	9.3	out
TCSM.B5R3.B1	1.0	11.4		out	18.0
TCLA.A5R3.B1	1.0	90.0	Cu-W	10.0	20.0
TCLA.B5R3.B1	1.0	0.0	Cu-W	10.0	20.0
TCLA.6R3.B1	1.0	0.0	Cu-W	10.0	20.0
TCLA.7R3.B1	1.0	0.0	Cu-W	10.0	20.0
TCTH.4L5.B1	1.0	0.0	Cu-W	out	8.3
TCTVA.4L5.B1	1.0	90.0	Cu-W	out	8.3
TCL.5R5.B1	1.0	0.0	Cu	out	10.0
TCDQA.A4R6.B1	3.0	0.0	CFC	8.0	8.0
TCDQA.B4R6.B1	3.0	0.0	CFC	8.0	8.0
TCSG.4R6.B1	1.0	0.0	CFC	7.0	7.5
TCRYO.BL7.B1	1.0	0.0	Cu	≥ 10.0	≥ 10.0
TCRYO.AL7.B1	1.0	0.0	Cu	≥ 10.0	≥ 10.0
TCP.D6L7.B1	0.6	90.0	CFC	5.7	6.0
TCP.C6L7.B1	0.6	0.0	CFC	5.7	6.0
TCP.B6L7.B1	0.6	127.5	CFC	5.7	6.0
TCAPA.6L7.B1	1.0	0.0	W	out	out
TCAPB.6L7.B1	0.1	0.0	W	out	out
TCSG.A6L7.B1	1.0	141.1	CFC	6.7	out
TCSM.A6L7.B1	1.0	142.5		out	7.0
TCAPC.6L7.B1	0.6	0.0	W	out	out
TCSG.B5L7.B1	1.0	143.5	CFC	6.7	out
TCSM.B5L7.B1	1.0	141.6		out	7.0
TCSG.A5L7.B1	1.0	40.7	CFC	6.7	out
TCSM.A5L7.B1	1.0	42.7		out	7.0
TCSG.D4L7.B1	1.0	90.0	CFC	6.7	out
TCSM.D4L7.B1	1.0	90.0		out	7.0
TCSG.B4L7.B1	1.0	0.0	CFC	6.7	out
TCSM.B4L7.B1	1.0	0.0		out	7.0
TCSG.A4L7.B1	1.0	134.6	CFC	6.7	out
TCSM.A4L7.B1	1.0	135.7		out	7.0
TCSG.A4R7.B1	1.0	46.3	CFC	6.7	out

continued from previous page

Name	Length [m]	Angle [deg]	Material	Half-gap[σ_z]	
				injection	low beta
TCSM.A4R7.B1	1.0	45.2	CFC	out	7.0
TCSG.B5R7.B1	1.0	141.5		6.7	out
TCSM.B5R7.B1	1.0	139.6		out	7.0
TCSG.D5R7.B1	1.0	51.4	CFC	6.7	out
TCSM.D5R7.B1	1.0	53.3	CFC	out	7.0
TCSG.E5R7.B1	1.0	130.5		6.7	out
TCSM.E5R7.B1	1.0	128.5		out	7.0
TCSG.6R7.B1	1.0	0.5	CFC	6.7	out
TCSM.6R7.B1	1.0	0.0	Cu-W	out	7.0
TCLA.A6R7.B1	1.0	90.0		10.0	10.0
TCLA.B6R7.B1	1.0	0.0		10.0	10.0
TCLA.C6R7.B1	1.0	90.0	Cu-W	10.0	10.0
TCLA.D6R7.B1	1.0	0.0	Cu-W	10.0	10.0
TCLA.A7R7.B1	1.0	0.0	Cu-W	10.0	10.0
TCRYO.AR7.B1	1.0	0.0	Cu	≥ 10.0	≥ 10.0
TCRYO.BR7.B1	1.0	0.0	Cu	≥ 10.0	≥ 10.0
TCTH.4L8.B1	1.0	0.0	Cu-W	out	8.3
TCTVB.4L8	1.0	90.0	Cu-W	out	8.3
TCTH.4L1.B1	1.0	0.0	Cu-W	out	8.3
TCTVA.4L1.B1	1.0	90.0	Cu-W	out	8.3

B.2 Beam 2

Table B.2: List of Phase I and Phase II (in red) collimators in the main ring for Beam 2. Name, length, azimuthal angle, material and nominal settings at injection and low beta energy are indicated. The devices both "out" at injection and low beta energies are used only to intercept particle showers. The jaw materials for Phase II are not indicated, because a final decision is still not taken as well as for the final aperture and material for the cryo-collimator jaws.

Name	Length [m]	Angle [deg]	Material	Half-gap[σ_z]	
				injection	low beta
TCTH.4R8.B2	1.0	0.0	Cu-W	out	8.3
TCDD.4R8	1.0	90.0	C	out	out
TDI.4R8.B2	4.0	90.0	C-C	6.8	out
TCDD.4R8	1.0	90.0	C	out	out
TCTVB.4R8	1.0	90.0	Cu-W	out	8.3
TCLIA.4L8	1.0	90.0	CFC	6.8	out
TCLIB.6L8.B2	1.0	90.0	CFC	6.8	out
TCRYO.BR7.B2	1.0	0.0		≥ 10.0	≥ 10.0
TCRYO.AR7.B2	1.0	0.0		≥ 10.0	≥ 10.0
TCP.D6R7.B2	0.6	90.0	CFC	5.7	6.0
TCP.C6R7.B2	0.6	0.0	CFC	5.7	6.0
TCP.B6R7.B2	0.6	127.5	CFC	5.7	6.0
TCAPA.6R7.B2	1.0	0.0	W	out	out
TCAPB.6R7.B2	0.1	0.0	W	out	out
TCSG.A6R7.B2	1.0	141.1	CFC	6.7	out
TCSM.A6R7.B2	1.0	142.5		out	7.0
TCAPC.6R7.B2	1.0	0.0	W	out	out
TCSG.B5R7.B2	1.0	143.5	CFC	6.7	out
TCSM.B5R7.B2	1.0	141.6		out	7.0
TCSG.A5R7.B2	1.0	40.7	CFC	6.7	out
TCSM.A5R7.B2	1.0	42.7		out	7.0
TCSG.D4R7.B2	1.0	90.0	CFC	6.7	out
TCSM.D4R7.B2	1.0	90.0		out	7.0
TCSG.B4R7.B2	1.0	0.0	CFC	6.7	out
TCSM.B4R7.B2	1.0	0.0		out	7.0
TCSG.A4R7.B2	1.0	134.6	CFC	6.7	out
TCSM.A4R7.B2	1.0	135.7		out	7.0

continued from previous page

Name	Length [m]	Angle [deg]	Material	Half-gap[σ_z]	
				injection	low beta
TCSG.A4L7.B2	1.0	46.3	CFC	6.7	out
TCSM.A4L7.B2	1.0	45.2		out	7.0
TCSG.B5L7.B2	1.0	141.5	CFC	6.7	out
TCSM.B5L7.B2	1.0	139.6		out	7.0
TCSG.D5L7.B2	1.0	51.4	CFC	6.7	out
TCSM.D5L7.B2	1.0	53.3		out	7.0
TCSG.E5L7.B2	1.0	130.5	CFC	6.7	out
TCSM.E5L7.B2	1.0	128.5		out	7.0
TCSG.6L7.B2	1.0	0.5	CFC	6.7	out
TCSM.6L7.B2	1.0	0.0		out	7.0
TCLA.A6L7.B2	1.0	90.0	Cu-W	10.0	10.0
TCLA.B6L7.B2	1.0	0.0	Cu-W	10.0	10.0
TCLA.C6L7.B2	1.0	90.0	Cu-W	10.0	10.0
TCLA.D6L7.B2	1.0	0.0	Cu-W	10.0	10.0
TCLA.A7L7.B2	1.0	0.0	Cu-W	10.0	10.0
TCRYO.AR7.B2	1.0	0.0		≥ 10.0	≥ 10.0
TCRYO.BR7.B2	1.0	0.0		≥ 10.0	≥ 10.0
TCDQA.A4L6.B2	3.0	0.0	CFC	8.0	8.0
TCDQA.B4L6.B2	3.0	0.0	CFC	8.0	8.0
TCSG.4L6.B2	1.0	0.0	CFC	7.0	7.5
TCTH.4R5.B2	1.0	0.0	Cu-W	out	8.3
TCTVA.4R5.B2	1.0	90.0	Cu-W	out	8.3
TCL.5L5.B2	1.0	0.0	Cu	out	10.0
TCP.6R3.B2	0.6	0.0	CFC	8.0	15.0
TCAPA.6R3.B2	1.0	0.0	W	out	out
TCSG.5R3.B2	1.0	0.0	CFC	9.3	out
TCSM.5R3.B2	1.0	0.0		out	18.0
TCSG.4L3.B2	1.0	0.0	CFC	9.3	out
TCSM.4L3.B2	1.0	0.0		out	18.0
TCSG.A5L3.B2	1.0	170.7	CFC	9.3	out
TCSM.A5L3.B2	1.0	170.3		out	18.0
TCSG.B5L3.B2	1.0	10.8	CFC	9.3	out
TCSM.B5L3.B2	1.0	11.4		out	18.0
TCLA.A5L3.B2	1.0	90.0	Cu-W	10.0	20.0
TCLA.B5L3.B2	1.0	0.0	Cu-W	10.0	20.0
TCLA.6L3.B2	1.0	0.0	Cu-W	10.0	20.0

continued from previous page

Name	Length [m]	Angle [deg]	Material	Half-gap[σ_z]	
				injection	low beta
TCLA.7L3.B2	1.0	0.0	Cu-W	10.0	20.0
TCTH.4R2.B2	1.0	0.0	Cu-W	out	8.3
TCTVB.4R2	1.0	90.0	Cu-W	out	8.3
TCTH.4R1.B2	1.0	0.0	Cu-W	out	8.3
TCTVA.4R1.B2	1.0	90.0	Cu-W	out	8.3
TCL.5L1.B2	1.0	0.0	Cu	out	10.0

Appendix C

Database of LHC Beam 1 collimators with tilt jaws

C.1 Operational conventions for the collimator jaws

The operational naming conventions are shown in figure C.1.

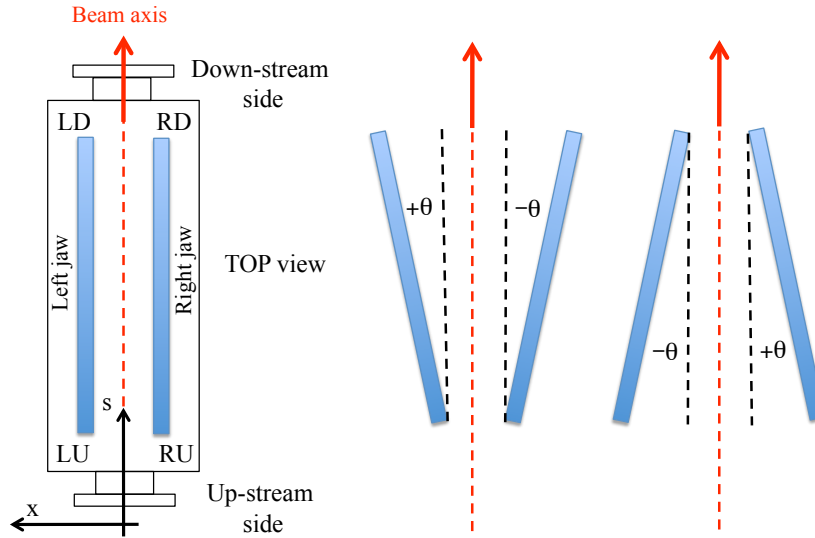


Figure C.1: Operational naming conventions for the collimator jaws.

For each jaw four corners are defined: the Left jaw Ustream end (LU), the Left jaw Downstream end (LD), the Right jaw Upstream end (RU) and the Right jaw Downstream end (RD).

A positive tilt angle θ_x for the left jaw correspond to having the LU corner closer to the beam axis. For the right jaw θ_x is positive if RU is further away from the beam axis.

C.2 Operational conventions for the collimator jaws

Table C.1: List of Beam 1 Phase I and Cu Phase II collimators (in red) with jaw tilted at low beta. In the following table are reported only collimators which are able to experience a tilt. Name, length, azimuthal angle, material, half-gap and tilt angles for each Left (L) and Right (R) jaw are indicated. The half-gaps refer to the minimum distance between the two jaws, which can be at the beginning or at the end of the collimator as consequence of the jaw tilt values.

Name	Length [m]	Angle [deg]	Material	Half-gap [mm]	Tilt angle [μ m]	
					Right	Left
TCL.5R1.B1	1.0	0.0	Cu	2.89	180	15
TCTH.4L2.B1	1.0	0.0	Cu-W	1.33	-60	283
TDI.4L2.B1	4.0	90.0	C-C	142.41	-75	440
TCTVB.4L2	1.0	90.0	Cu-W	1.41	-319	-66
TCLIA.4R2	1.0	90.0	CFC	226.87	9	73
TCLIB.6R2.B1	1.0	90.0	CFC	112.25	-545	169
TCP.6L3.B1	0.6	0.0	CFC	3.86	-157	369
TCSG.5L3.B1	1.0	0.0	CFC	5.97	135	-109
TCSM.5L3.B1	1.0	0.0	Cu	2.96	192	-57
TCSG.4R3.B1	1.0	0.0	CFC	4.13	-244	-115
TCSM.4R3.B1	1.0	0.0	Cu	2.09	139	194
TCSG.A5R3.B1	1.0	170.7	CFC	5.34	70	265
TCSM.A5R3.B1	1.0	170.3	Cu	2.78	3	200
TCSG.B5R3.B1	1.0	10.8	CFC	5.99	340	150
TCSM.B5R3.B1	1.0	11.4	Cu	3.11	-118	-187
TCLA.A5R3.B1	1.0	90.0	Cu-W	5.96	84	-123
TCLA.B5R3.B1	1.0	0.0	Cu-W	5.53	-62	100
TCLA.6R3.B1	1.0	0.0	Cu-W	5.11	163	87
TCLA.7R3.B1	1.0	0.0	Cu-W	3.65	274	-262
TCTH.4L5.B1	1.0	0.0	Cu-W	7.55	205	26
TCTVA.4L5.B1	1.0	90.0	Cu-W	4.77	-414	-59
TCL.5R5.B1	1.0	0.0	Cu	2.90	-133	-454
TCDQA.A4R6.B1	3.0	0.0	CFC	3.92	219	-29
TCDQA.B4R6.B1	3.0	0.0	CFC	3.97	165	-84
TCSG.4R6.B1	1.0	0.0	CFC	3.77	144	556

continued from previous page

Name	Length [m]	Angle [deg]	Material	Half-gap [mm]	Tilt angle [μ m]	
					Right	Left
TCP.D6L7.B1	0.6	90.0	CFC	1.18	130	78
TCP.C6L7.B1	0.6	0.0	CFC	1.67	13	-78
TCP.B6L7.B1	0.6	127.5	CFC	1.39	73	-115
TCSG.A6L7.B1	1.0	141.1	CFC	6.32	-249	92
TCSM.A6L7.B1	1.0	142.5	Cu	1.65	-337	34
TCSG.B5L7.B1	1.0	143.5	CFC	7.50	-101	-105
TCSM.B5L7.B1	1.0	141.6	Cu	2.01	293	-452
TCSG.A5L7.B1	1.0	40.7	CFC	7.65	148	92
TCSM.A5L7.B1	1.0	42.7	Cu	2.03	-254	72
TCSG.D4L7.B1	1.0	90.0	CFC	4.95	37	-221
TCSM.D4L7.B1	1.0	90.0	Cu	1.27	309	-169
TCSG.B4L7.B1	1.0	0.0	CFC	6.95	-2	22
TCSM.B4L7.B1	1.0	0.0	Cu	1.80	-106	1
TCSG.A4L7.B1	1.0	134.6	CFC	6.90	102	249
TCSM.A4L7.B1	1.0	135.7	Cu	1.82	50	-41
TCSG.A4R7.B1	1.0	46.3	CFC	6.93	264	-82
TCSM.A4R7.B1	1.0	45.2	Cu	1.83	-73	-113
TCSG.B5R7.B1	1.0	141.5	CFC	7.98	6	33
TCSM.B5R7.B1	1.0	139.6	Cu	2.13	-160	27
TCSG.D5R7.B1	1.0	51.4	CFC	8.01	-4	18
TCSM.D5R7.B1	1.0	53.3	Cu	2.09	74	147
TCSG.E5R7.B1	1.0	130.5	CFC	8.02	336	371
TCSM.E5R7.B1	1.0	128.5	Cu	2.09	-35	209
TCSG.6R7.B1	1.0	0.5	CFC	10.97	-197	-175
TCSM.6R7.B1	1.0	0.0	Cu	2.85	280	146
TCLA.A6R7.B1	1.0	90.0	Cu-W	1.54	-108	62
TCLA.B6R7.B1	1.0	0.0	Cu-W	2.84	266	225
TCLA.C6R7.B1	1.0	90.0	Cu-W	2.77	-37	-114
TCLA.D6R7.B1	1.0	0.0	Cu-W	1.79	42	267
TCLA.A7R7.B1	1.0	0.0	Cu-W	1.76	-377	-182
TCTH.4L8.B1	1.0	0.0	Cu-W	1.28	181	-14
TCTVB.4L8	1.0	90.0	Cu-W	1.35	215	-141
TCTH.4L1.B1	1.0	0.0	Cu-W	7.55	53	-258
TCTVA.4L1.B1	1.0	90.0	Cu-W	4.77	121	-99

Bibliography

- [1] L. Evans “*The Large Hadron Collider: A Marvel of Technology*”, EPFL Press, 2009.
- [2] <http://cms.cern.ch/iCMS/>, CMS Collaboration.
- [3] <http://atlas.web.cern.ch/Atlas/internal/tdr.html>, ATLAS Technical Design Reports.
- [4] <http://lhcb.web.cern.ch/lhcb/TDR/TDR.htm>, LHCb Technical Design Reports.
- [5] “*LHCf experiment : Technical Design Report*”, CERN Editorial Board, CERN-2006-004, 2006.
- [6] <http://totemtdr.web.cern.ch/totemtdr/>, TOTEM Technical Design Reports.
- [7] <http://alice.web.cern.ch/Alice/TDR/>, ALICE Technical Design Reports.
- [8] “*LHC Design Report, Volume I: The LHC Main Ring*”, CERN Editorial Board, CERN-2004-003, 2004.
- [9] J.B. Jeanneret, D. Leroy, L. Oberli and T. Trenckler, “*Quench levels and transient beam losses in the LHC magnets*”, LHC Project Report 44, 1996.
- [10] R. Assmann et al., “*Requirements for the LHC collimation system*”, proceedings of the European Particle Accelerator Conference EPAC02, Paris, France, 2002.
- [11] M. Lamont, “*Estimates of annual proton doses in the LHC*”, LHC Project Note 375, 2005.
- [12] R. Assmann et al., “*Designing and building a collimation system for the high intensity LHC beam*”, LHC Project Report 640.
- [13] R. Assmann, “*Collimators and cleaning: could that limit the LHC performance?*”, proceedings of the Chamonix XII Workshop, 2003.
- [14] G. Robert-Demolaize et al., “*A new version of SixTrack with collimation and aperture interface*”, proceedings of the 21st Particle Accelerator Conference PAC05, Knoxville, TN, USA, 2005.

- [15] E.B. Holzer et al., “*Generation of 1.5 million beam loss threshold values*”, proceedings of the European Particle Accelerator Conference EPAC08, Genoa, Italy, 2008.
- [16] B. Goddard et al., “*Protection of the LHC against unsynchronised beam aborts*”, LHC Project Report 916, 2006.
- [17] E. Metral et al., “*Transverse impedance of LHC collimators*”, LHC Project Report 1015, 2007.
- [18] F. Zimmermann et al., “*Tune shift induced by nonlinear resistive wall wake field of flat collimator*”, proceedings of the European Particle Accelerator Conference EPAC06, Edinburgh, UK, 2006.
- [19] J. Gareyte, J.P. Koutchouk, F. Ruggiero, “*Landau Damping, Dynamic Aperture and Octupole in LHC*”, LHC Project Report 91 (revised), 1997.
- [20] G. Kotzian, W. Höfle, E. Vogel, “*LHC transverse feedback damping efficiency*”, LHC Project Report 1156, 2008.
- [21] S. Calatroni, R. Perret, W. Vollenberg, “*RF contacts for the LHC collimators*”, Nuclear Instrumentation and Methods in Physics Research A566 (2006) 205-211.
- [22] H. Burkhard et al., “*Measurements of the LHC collimator Impedance with beam in the SPS*”, Nuclear Instrumentation and Methods in Physics Research A566 (2006) 205-211.
- [23] T. Trenkler and J.B. Jeanneret, “*The principles of two stage betatron and momentum collimation in circular accelerators*”, LHC note 312, 1995.
- [24] S. Redaelli, R. Assmann and G. Robert-Deomlaize, “*LHC aperture and commissioning of the collimation system*”, proceedings of the LHC Project Workshop “Chamonix XIV”, 2005.
- [25] J.B. Jeanneret, “*Optics of a two-stage collimation system*”, Physical Review Special Topics: Accelerators and Beams, 1998.
- [26] P. Sievers et al., “*Appropriate materials for LHC-Collimators*”, proceedings of the Chamonix XII Workshop, 2003.
- [27] R. Assmann, “*The Phased implementation of the LHC collimation*”, HHH-2008 Proceeding, 2008.
- [28] R. Assmann, “*Operational Experience with LHC Collimation*”, proceedings of the 23rd Particle Accelerator Conference PAC09, Vancouver, Canada, 2009.
- [29] A. Bertarelli et al., “*The mechanical design for the LHC collimators*”, LHC Project Report 786, 2004.

- [30] A. Masi, R. Losito, “*LHC Collimator Lower Level Control System*”, 15th IEEE NPSS Real Time Conference 2007.
- [31] V. Vlachoudis et al. “*Consequences of Regular and Irregular Beam Impact on the LHC Collimators*”, proceedings of the European Particle Accelerator Conference EPAC04, Lucerne, Switzerland, 2004.
- [32] C. Bracco, “*Commissioning Scenarios and Tests for the LHC Collimation System*”, PhD thesis, École Polytechnique Fédérale de Lausanne, 2008.
- [33] H. Braun et al. “*Collimation of Heavy Ion Beams in LHC*”, proceedings of the European Particle Accelerator Conference EPAC04, Lucerne, Switzerland, 2004.
- [34] V. Shiltsev et al., “*LHC particle collimation by hollow electron beams*”, proceedings of the European Particle Accelerator Conference EPAC08, Genoa, Italy, 2008.
- [35] R. Assmann, G. Bellodi, J.M. Jowett, E. Metral, T. Weiler, “*Accelerator physics concept for upgraded LHC collimation performance*”, proceedings of the 23rd Particle Accelerator Conference PAC09, Vancouver, Canada, 2009.
- [36] W. Scandale, “*Crystal collimation as an option for the LHC*”, proceedings of International Conference on Charged and Neutral Particles Channeling Phenomena, Frascati, Italy, 2006.
- [37] J. Resta Lopez, R. Assmann, S. Redaelli, G. Robert-Demolaize, D. Schulte, F. Zimmermann, A. Faus-Golfe “*An alternative non linear collimation system for the LHC*”, LHC-Project-Report-939, proceedings of the European Particle Accelerator Conference EPAC06, Edinburgh, UK, 2006.
- [38] J. Smith et al., “*Prospect for integrating a hollow electron lens into the LHC Collimation system*”, proceedings of the 23rd Particle Accelerator Conference PAC09, Vancouver, Canada, 2009.
- [39] H. Grote, F. Schmidt, “*MAD-X – an upgrade from MAD8*”, proceedings of the 20th Particle Accelerator Conference PAC03, Portland, OR, USA, 2003.
- [40] F. Schmidt, “*SixTrack, user reference manual*”, CERN SL/94-56, 1994.
- [41] T. Trenkler, J.B. Jeanneret, “*K2, a software package evaluating collimation systems in circular colliders (manual)*”, CERN SL/94105 (AP), 1994.
- [42] R. Assmann, S. Redaelli, “*Beam distribution on the collimators for various accident cases*”, <http://lhc-collimation-project.web.cern.ch/lhc-collimation-project/AccidentInput.htm>

- [43] G. Battistoni, S. Muraro, P.R. Sala, F. Cerutti, A. Ferrari, S. Roesler, A. Fassó, J. Ranft, “*The FLUKA code: Description and benchmarking*”, proceedings of the Hadronic Shower Simulation Workshop 2006, Fermilab 6–8 September 2006, M. Albrow, R. Raja eds., AIP Conference Proceeding 896, 31-49, 2007.
- [44] A. Fassó, A. Ferrari, J. Ranft, and P.R. Sala, “*FLUKA: a multi-particle transport code*”, CERN-2005-10, 2005, INFN/TC_05/11, SLAC-R-773.
- [45] M. Brugger, H. Khater, S. Mayer, A. Prinz, S. Roesler, L. Ulrici, H. Vincke, “*Benchmark studies of induced radioactivity produced in LHC materials, Part II: remanent dose rates*”, proceedings of the 10th International Conference on Radiation Shielding ICRS10, Maidera Island, Portugal, 2004.
- [46] M.E. Law et al., “*A compilation of Data on Inclusive Reactions*”, LBL-80 (1972).
- [47] M. Adamus et al., “*Charged Particle Production in $K+p$, $\pi+p$ and pp Interactions at 250 GeV/c*”, Z. Phys. C39 (1988) 311.
- [48] H.A. Bethe, “*Molière’s theory of multiple scattering*”, Physical Review 89, pp.1256-1266, 1953.
- [49] C. Amsler et al., “*Passage of particles through matter*”, Phys. Leet. B667,1 (2008).
- [50] J. Bak et al., NPB288 (1987) 681.
- [51] T. Enqvist et al., “*Primary-residue production cross sections and kinetic energies in 1AGeV 208Pb on deuteron reactions*”, Nuclear Physics A686 (2001) 481.
- [52] W. Guber, J. Nagel, R. Goldstein, P.S. Mettelman and M.H. Kalos, “*A geometric description technique suitable for computer analysis of both nuclear and conventional vulnerability of armored military vehicles*”, Mathematical Application Group, Inc. Report MAGI-6701 (1967).
- [53] H. Lichtenstein, M.O. Cohen, H.A. Steinberg, E.S. Troubetzkoy, M. Beer, “*The SAM-CE Monte Carlo system for radiation transport and criticality calculations in complex configurations (Revision 7.0)*”, RSIC Computer Code Collection CCC-187 (1979)-/Lic79
- [54] M. Santana Leitner et al., “*Energy deposition studies for the Betatron Cleaning insertion (IR7) of LHC*”, LHC-Project-Report-825, proceedings of the 21st Particle Accelerator Conference PAC05, Knoxville, TN, USA, 2005.

- [55] S. Russenschuck, “*ROXIE - A Computer Code for the Integrated Design of Accelerator Magnets*”, LHC-Project-Report-276, proceedings of the European Particle Accelerator Conference EPAC98, Stockholm, Sweden, 1998.
- [56] V. Vlachoudis, “*BRexx Overview*”, REXX Symposium 2001, Research Triangle Park, NC, USA, 2001.
- [57] D. Kramer, “*Design and Implementation of a Detector for High Flux Mixed Radiation Fields*”, p. 98, CERN-THESIS-2008-090, 2008.
- [58] D. Kramer et al., “*Very High Radiation Detector for the LHC BLM System Based on Secondary Electron Emission*”, IEEE Nuclear Science Symposium Conference Record, 2007.
- [59] F. Cerutti, “*Material choice from the point of view of energy deposition*”, talk presented at the 2nd Phase 2 Specification and Implementation meeting, CERN, Feb 8th, 2008.
- [60] L. Lari et al., “*Preliminary exploratory study of different Phase II collimators*”, LHC-Project-Report-1114, proceedings of the European Particle Accelerator Conference EPAC08, Genoa, Italy, 2008.
- [61] M. Brugger, D. Forkel-Wirth, S. Roesler, “*Generic studies of radioactivity induced by high energy beams in different absorber materials*”, talk presented at the 11th International Conference on Radiation Shielding, ICRS-11, Callaways Garden, GA, USA, April 13-18th, 2008.
- [62] M. Brugger, F. Cerutti, A. Ferrari, L. Lari, M. Mauri, S. Roesler, L. Sarchiapone, V. Vlachoudis, “*LHC Accelerator design studies on the example of Passive Absorbers*”, proceedings of the 11th International Conference on Radiation Shielding, ICRS-11, Callaways Garden, GA, USA, April 13-18th, 2008. Nuclear technology, ISSN 0029-5450, 2008.
- [63] F. Cerutti, “*Energy deposition studies for the LHC Phase II collimation*”, talk presented at the Conceptual Design Review LHC Phase II Collimation, CERN, 2009.
- [64] J. Frisch et al., “*Advanced collimator engineering for the NLC*”, proceedings of the 19th Particle Accelerator Conference PAC01, Chicago, IL, USA, 2001.
- [65] J. Amann, G. Anzalone, R. Assmann, C. Bracco, Y. Cai, E. Doyle, L. Keller, L. Lari, S. Lundgren, T. Markiewicz, T. Raubenheimer, R. Rogers, J. Smith, Th. Weiler, L. Xiao, “*LHC Phase II Rotary Consumable Collimator - RC1 Conceptual Design Report*”, Rev 4, SLAC (2009).

- [66] L. Lari et al., “*Evaluation of Beam losses and energy depositions for possible Phase II design for LHC collimation*”, LHC-Project-Report-1115, proceedings of the European Particle Accelerator Conference EPAC08, Genoa, Italy, 2008.
- [67] J. Smith et al., “*Mechanical and thermal prototype testing for a rotatable collimator for the LHC Phase II collimation upgrade*”, proceedings of the European Particle Accelerator Conference EPAC08, Genoa, Italy, 2008.
- [68] C. Hassler et al., “*Beam line design for the CERN HiRadMat test facility*”, sLHC-Project-Report-0012, proceedings of the 23rd Particle Accelerator Conference PAC09, Vancouver, Canada, 2009.
- [69] A. Dallocchio et al., “*Advanced material for future Phase II LHC collimators*”, proceedings of the 23rd Particle Accelerator Conference PAC09, Vancouver, Canada, 2009.
- [70] P. Collier, M. Ferro-Luzzi, N. Phinney, M. Seidel, P. Spiller, R. Van Weelden, F. Willeke, “*Conceptual design review of a Phase II collimation system for LHC - Report of the Review Committee*”, CERN, March 2009.
- [71] E. Metral et al., Minutes of the 6th Phase II Design Meeting, CERN, April 2008.
- [72] F. Caspers et al., Minutes of the 7th and 8th Phase II Design Meeting, CERN, April - June 2008. http://lhccollimationprojectmeeting_phase2_design.htm
- [73] A. Dallocchio, “*Phase II collimators: design status*”, talk presented at the 12th Phase 2 Design meeting, CERN, May 20th, 2009.
- [74] L. Lari et al., “*Energy deposition studies for possible innovative Phase II collimator designs*”, CERN-ATS-2009-128, proceedings of the 23rd Particle Accelerator Conference PAC09, Vancouver, Canada, 2009.
- [75] S. Redaelli et al., “*Operational experience with a LHC collimator prototype in the CERN SPS*”, proceedings of the 23rd Particle Accelerator Conference PAC09, Vancouver, Canada, 2009.
- [76] S. Redaelli et al., “*LHC aperture and commissioning of the Collimation system*”, ChamomixXIV, CERN-AB-2005-014, 2005 pp. 268-277.
- [77] Safety Code F, Radiation Safety Manual, Revision 2006, CERN.
- [78] Council Directive 96/29/EURATOM of 13 May 1996, Office Journal of the European Communities, Vol. 39, L159, 1996.
- [79] H. Vincke et al., “*Investigation of the radiation protection issues of the TI8 injection and TT40 material tests*”, CERN-SC-2005-038, 2005.

- [80] S. Roesler, G. R. Stevenson, “*deg99.f - A FLUKA user-routine converting fluence into effective dose and ambient dose equivalent*”, CERN-SC-2006-070-RP-TN, 2006.
- [81] M. Pelliccioni, “*Overview of fluence-to-effective dose and fluence-to-ambient dose equivalent conversion coefficients for high energy radiation calculated using the FLUKA code*”, Radiation Protection Dosimetry 88, 2000 pp. 279-297.
- [82] M. Brugger, D. Forkel-Wirth, S. Roesler, “*Radiological considerations for passive absorbers in the LHC betatron cleaning insertion*”, CERN-SC-2007-056-RP-TN, 2005.
- [83] P. Bonnal, D. Forkel-Wirth, “*Critères et exigences ALARA applicables aux interventions*”, Note d’information, RGE 9/S5-GSI1 (EDMS no. 810176), CERN 2006.
- [84] D.R. Alexander, “*Design issues for radiation tolerant microcircuits for space*”, short course presented at the Nuclear and Space Radiation Effects Conference NSREC, Indian Wells, Ca, USA, 1996.
- [85] P. Jarron et al., “*Deep Submicron CMOS technologies for the LHC experiment*”, proceedings of the 6th International Conference on Advanced Technology and Particle Physics, Villa Olmo, Italy, 1998.
- [86] V. Vuillemin, F. Faccio “*Summary of the Chamonix 2010 on Radiation to electronics*”, proceedings of Chamonix 2010 workshop on LHC performance, 2010.
- [87] A. Ballarino, “*Design of an MgB₂ feeder system to connect groups of Superconducting magnets to remote power converters*”, proceedings of the 9th European Conference on Applied Superconductivity Eucas 2009, Dresden, Germany, 2009.
- [88] Radiation to Electronic R2E study group, “*R2E Overview of Critical LHC Underground Areas*”, <http://r2e.web.cern.ch/R2E/>, Area Overview, 2010.
- [89] T. Wijnands, et al., “*Review of exposed equipment in the LHC: a global view*”, proceedings of Chamonix 2010 workshop on LHC performance, 2010.
- [90] M. Brugger et al., “*Review of critical radiation areas for LHC electronics and mitigation actions. Radiation monitoring and first results*”, proceedings of Chamonix 2010 workshop on LHC performance, 2010.
- [91] R. Losito, “*Where are we with the long-term plans and the CERN wide radiation policy*”, proceedings of Chamonix 2010 workshop on LHC performance, 2010.
- [92] L. Lari, “*Phase II collimation impact on IR7*”, presented at the R2E workshop, CERN, 2010.

- [93] M. Brugger, “*Update on Beam-Gas and Radiation Levels*”, presented at the R2E workshop, CERN, 2010.
- [94] C. Benvenuti et al., “*Vacuum properties of TiZrV non-evaporable getter films*”, published in Vacuum 60,2001 pp 57-65.
- [95] G.H. Kinchin, R.S. Pease, “*The Displacement of Atoms in Solids by Radiation*”, Rep. Prog. Phys. Volume 18, Issue 1, 1955.
- [96] M.J. Norgett, M.T. Robinson, I.M. Torrens, “*A proposed method of calculating displacement dose rates*”, Nuclear Engineering and Design Volume 33, Issue 1, 1974 pp 50-54.
- [97] J. Lindhard, V. Nielsen, M. Scharff, P.V. Thomsen, Mat. Fys. Medd. Dan. Vid. Selsk Volume 33, Issue 10, 1963.
- [98] “*Stopping powers and ranges for protons and alpha particles*”, International Commission on Radiation Unit (ICRU) and measurement Report 49, 1993.
- [99] Nuclear Energy Agency, NJOY General Nuclear Data Processing System for Files in ENDF Format, <http://www.nea.fr/dbprog/njoy-links.html>.
- [100] R.E. Stoller et al., “*Molecular Dynamics Simulations Of High Energy Cascades*”, Microstructure of Irradiated Materials, Materials Research Society, Pittsburgh, USA, 1995, pp. 21-26.
- [101] V. Vlachoudis et al., “*dpa for FLUKA*”, presented at the FLUKA user meeting, Nov., 2008.
- [102] L.S Waters et al., “*MCNPX 2.6.0 Manual*”, LA-CP-07-1473, LANL, Los Alamos, April, 2008.
- [103] J. F. Ziegler, M. D. Ziegler, J. P. Biersack, “*SRIM, The Stopping and ranges of Ions in Matter*”, Chester, MD, SRIM.com., 2007.
- [104] K. Niita, et al., “*PHITS, A particle and heavy ion transport code system*”, Radiat. Meas. 41, 2006.
- [105] N. V. Mokhov, C. C. James, “*The MARS Code System User’s Guide Version 15*”, published by the Fermi National Accelerator Laboratory, 2009.
- [106] T. T. Bohlen, “*Beam Loss Patterns at the LHC Collimators*”, CERN-THESIS-2008-092, 2008.

Curriculum Vitae

Luisella Lari

PERSONAL INFORMATION

<i>Name</i>	Luisella LARI
<i>E-mail</i>	luisella.lari@cern.ch luisella.lari@slac.stanford.edu
<i>Nationality</i>	Italian
<i>Date of birth</i>	June 15 th 1973

EDUCATION

<i>2010</i>	PhD in physics at the <i>École Polytechnique Fédérale de Lausanne (EPFL)</i> , Switzerland.
<i>Dec. 2008</i>	Project Management Professional (PMP) certification at <i>Project Management Institute (PMI)</i> , USA.
<i>Mar. 2003</i>	Attestation of Chartered Engineer in Italy at <i>Politecnico di Torino</i> , Italy.
<i>Mar. 2001</i>	Master degree in Nuclear Engineer at <i>Politecnico di Torino</i> , Italy. Thesis title “ <i>Cooling installations in living spatial systems: modelling and verifying of a hydraulic test stand</i> ” Supervisors: Magnifico Rettore 2001-2005 Prof. G. Del Tin, Prof. M. De Salve, Eng. M. Crivello. (Sept. 1998 - Sept. 1999) - Scholarship for Meritorious University Students at <i>Politecnico di Torino</i> , Italy.

WORK EXPERIENCE

From Nov. 2002

Physicist & Project Engineer

CERN - European Organization for Nuclear Research -
CH-1211 Geneva 23, Switzerland.

* Responsible for MonteCarlo calculations used to evaluate energy deposition and radiation loads related to the protection of the LHC machine (Collimation System Upgrade project).

* Invited for my experience in the collimation field at SLAC National Accelerator Laboratory, Stanford, USA from Feb. to May 2009.

* Responsible for specific cold and warm tests and measurements on LHC Superconducting magnets, in response to urgent concerns during fabrication.

* Supervision of technicians and definition of procedures for laboratory tests on accelerator magnets.

* Schedule Officer for the LHC construction and Installation General Co-ordination schedule (baseline cost-to-completion 3.3 BCHF).

* Responsible for Organization and Work Package planning, Follow-up, Review and Resource Management for several LHC main ring Installation sub-projects, including the General Services phase.

Nov. 1999 - Sept. 2002

Testing Engineer

Thales Alenia Space - Sede di Torino Strada Antica di Collegno, 253, 10146 Turin, Italy.

* Responsible for acceptance, verification and calibration of fluid supply line for the International Space Station ISS project.

* Two NASA awards obtained for outstanding performance of Node2 activities.

* Stage (Nov. 1999 - Jun. 2001). Practical training period to develop my Master's degree thesis.

MAIN PUBLICATIONS

As main author:

L.Lari et al. “*Energy Deposition studies for possible innovative Phase II collimator designs*” PAC09, Vancouver, Canada.

L.Lari et al. “*Preliminary exploratory study of different Phase II collimators*”, EPAC08, Genoa, Italy.

L.Lari et al. “*Evaluation of beam loss and energy deposition for one possible Phase II design for LHC collimation*”, EPAC08, Genoa, Italy.

L.Lari et al. “*Scheduling the installation of the LHC injection lines*”, EPAC04, Lucerne, Switzerland.

As co-author:

D. Wollmann et al. “*First cleaning with LHC collimators*”, IPAC10, Kyoto, Japan.

J.C.Smith et al. “*Recent Progress on the Design of a Rotatable Copper Collimator for the LHC Collimation Upgrade*” PAC09, Vancouver, Canada.

J. Amann, G. Anzalone, R. Assmann, C. Bracco, Y. Cai, E. Doyle, L. Keller, L. Lari, S. Lundgren, T. Markiewicz, T. Raubenheimer, R. Rogers, J. Smith, Th. Weiler, L. Xiao, “*LHC Phase II Rotatable Collimator - RC1 Conceptual Design Report*”, March 2009, SLAC, USA.

J.C.Smith et al. “*Design of a Rotatable Copper Collimator for the LHC Phase II Collimation Upgrade*” EPAC08, Genoa, Italy.

M.Brugger et al. “*FLUKA LHC Engineering studies on the example of Passive Absorbers*” ICRS-11 & RPSD-2008, Callaway Gardens, Pine Mountain, Georgia, USA.

K.Foraz et al. “*Scheduling the installation of the Large Hadron Collider*”, EPAC04, Lucerne, Switzerland.

Acknowledgments

It was a pleasure for me to work with all the wonderful people at CERN, EPFL and SLAC during this PhD time.

First of all I would like to thank my supervisors: Vasilis Vlachoudis at CERN and Leonid Rivkin at EPFL for their support, their interest in my research as well as for our fruitful discussions. Thanks for guiding me along all this period and for giving me the chance to participate in several interesting conferences.

Special thanks to Ralph Assmann, the project leader of the LHC collimation system, in particular for supporting my internship at SLAC laboratory in USA. My thanks for opening me the doors of the international collimation community and for teaching me all the secrets about collimation theory.

Special thanks to Tor Raubenheimer and Thomas Markiewicz, my SLAC supervisors, who made me feel part of the SLAC team from the first day of working at the laboratory.

Special thanks also to Alfredo Ferrari. My thanks for giving me the change of benefit from his amazing knowledge in Physics.

A huge “thank you!!” to Francesco Cerutti who always helped me in finding and solving errors in the FLUKA simulations. Thanks for your door always opened. A big thank also for the time you spent in reading this thesis and for providing helpful suggestions and remarks in order to improve it.

Many thanks also to Markus Brugger for supporting with your experience in the field my ambient dose rates & radiation to electronics calculations. Moreover I want to thank you for accepting to check my thesis chapters on these subjects.

Special thanks also to Chiara Bracco, who made “SixTrack” much less mysterious to my hears.

Thanks to all the EN department people with whom I have been working during these years. In particular I would like to thank my group leader Roberto Losito who hosted me in his group during this PhD and all the FLUKA team who made FLUKA simulation pleasant and also funny. Thanks to all to made me feel a part of the team!

Additionally, I would like to thank several people with whom I have been collaborating for the development of the CERN and SLAC Phase II design. In particular, special thanks to Stefan Roesler for your support in the radiation protection subjects. Many thanks to Alessandro Bertarelli and Alessandro Dallochio and the EN/MME design team at CERN. Many thanks also to Jeffry Smith, Luis Keller and Steven Lundgren and to the other members of the SLAC collimation team.

Last but not least, I wish to thank my family and my friends for enjoying life & PhD time together with me.

Thanks again sincerely to all of you!!

